The binarity of Massive Young Stellar Objects

Robert Geoffrey Shenton

University of Leeds

School of Physics and Astronomy

Submitted in accordance with the requirements for the degree of

Doctor of Philosophy

July 2023

The extraordinary is in what we do, not who we are.

Lara Croft

Declaration

I confirm that the work submitted is my own and that appropriate credit has been given where reference has been made to the work of others.

All science chapters made use of information from the Red MSX Source survey database at http://rms.leeds.ac.uk, which was constructed with support from the Science and Technology Facilities Council of the UK. They also make use of the SIMBAD database, operated at CDS, Strasbourg, France. Chapter 2 is based in part on data obtained as part of the UKIRT Infrared Deep Sky Survey, and the Vista Variables in the Via Lactea on data products from observations made with ESO Telescopes at the La Silla or Paranal Observatories under ESO programme ID 179.A-2010. It also uses data from the UKIRT telescope in Hawaii, owned by the University of Hawaii (UH) and operated by the UH Institute for Astronomy. When the data reported here were obtained, UKIRT was operated by the Joint Astronomy Centre on behalf of the Science and Technology Facilities Council of the U.K. Subsection 2.4.5 includes data from models created and simulated by Rebecca Houghton, a PhD stu-

dent, and Prof. Simon Goodwin, both from the University of Sheffield. Chapter 3 uses data from The Immersion Grating Infrared Spectrometer (IGRINS) which was developed under a collaboration between the University of Texas at Austin and the Korea Astronomy and Space Science Institute (KASI) with the financial support of the US National Science Foundation under grants AST-1229522, AST-1702267 and AST-1908892, McDonald Observatory of the University of Texas at Austin, the Korean GMT Project of KASI, the Mt. Cuba Astronomical Foundation and Gemini Observatory. It also uses data taken with the X-Shooter instrument through European Southern Observatory programs. Chapter 4 made use of data from the European Space Agency (ESA) mission *Gaia* (https://www.cosmos.esa.int/gaia), processed by the *Gaia* Data Processing and Analysis Consortium (DPAC, https://www.cosmos.esa.int/web/gaia/dpac/consortium). Funding for the DPAC has been provided by national institutions, in particular the institutions participating in the *Gaia* Multilateral Agreement.

Signed

Acknowledgements

Thank you to my family: Mum and Dad, you never stopped believing in me and always kept checking in on how things were going. Rosie-Mae and Heather, you always know how to make me laugh, and you're the best sisters I could ask for. Ruby, you're a daft dog and the best one. Especially during the pandemic, you all helped me through the stressful times.

Thank you to Lucy. You made the final year of my PhD so much better. You've always been there when I needed you, and when things got tough you never failed to make me smile again. I appreciate your love, kindness and support so much.

Thank you to my friends that helped me through the last four years, even if you didn't fully know it. James, Brandan, Jam, Matt, Ronan, Usama, Torr and Max: that silly group chat kept me going more than you realise! Harry, Liam, Lawrence and Dan: a night on Fifa or Warzone always helped take my mind off things. Kahlan: our collective raging at game-related stuff never gets old. Ben, James, Jodie, Callum, Sophie, Grace, Nathan and Jared: our annual-ish meetups are always a highlight of my year. Lara, Abigail, Rob, Adam: our year living together was crazy but great. Jacob, Julia and Hannah: living with you lot this last year has been nothing short of fantastic!

Thank you to everyone I've worked alongside during my PhD, especially Abi, James, Miguel, Alice B, Alice P, John, Evgenia, Sam, Joe, Suzi, Kingsley and Marcin: you were all so helpful through those early times. And thank you to all the current PhD students and postdocs, as you all kept the office alive and make lunchtimes much more interesting. I'll miss our Friday trips to the Fenton!

Thank you to Greg and Eve. Our PhD lives have been practically interwoven since all three of us started on that day four years ago. Our office conversations never ceased to entertain, amaze or just downright confuse me, and when I moved in with you both for our final year things got even wilder and better. Both of you made this project so much more bearable, and I hope I helped do the same for you. Good luck in both of your future careers, although I'm positive you won't need it!

And finally, thank you to the staff, supervisors and assessors. I can't close this off without giving a huge thank you to my supervisor, René. It's safe to say my PhD hasn't been plain sailing, but without your guidance, insight and wisdom, I don't know where I'd be. I'm grateful for your patience in me finishing my thesis, and for always finding the time to talk to me, even during a global pandemic! We've had some laughs too alongside the stressful times. Thank you so much for giving me the chance to do this project, and I'm excited for where you'll take it next.

Abstract

Multiplicity is known to be a common occurrence in massive stars ($>8M_\odot$), and is intrinsically linked to their formation. However the specific formation processes of multiple star systems are still in question. In order to study this phenomenon, massive stars must be observed and studied at an early a stage as possible, and Massive Young Stellar Objects (MYSOs) provide an ideal opportunity for this. Very few studies on MYSO multiplicity currently exist, and so our knowledge of the phenomenon is limited.

This thesis presents three studies into the multiplicity of MYSOs, covering all scales and multiple wavebands. Firstly, $K-$band imaging was used to search for companions around hundreds of MYSOs between 1000-100,000 au, comprising the largest MYSO multiplicity study to date. $\sim$50% of MYSOs have at least one companion, and a significant number of companions have mass ratios greater than 0.5. Monte Carlo simulations show that triple systems must be a common occurrence in order to explain the observed separation distribution. Secondly, high- and medium-resolution $K-$band spectra of MYSOs were used to search for radial velocity variations (an indication of a close-in companion), and multiplicity fractions of 0% and $\sim$8% were found respectively. Masses and separations of these companions were also estimated. Finally, Gaia DR3 data was used to search for MYSO companions in the optical regime for the first time, using parallaxes and proper motions to find companions comoving with MYSOs. A multiplicity fraction of $\sim$60% was found for this sample.

After factoring in observational limitations of these studies, it can be asserted that up to 100% of MYSOs form in multiple systems, with triple systems possibly forming a significant fraction of those multiples. Additionally, the relatively high mass ratios indicate that the capture scenario for binary formation is unlikely for MYSOs.

Abbreviations

2MASS	2 Micron All-Sky Survey
ALMA	Atacama Large Millimetre/submillimetre Array
AMBER	Astronomical Multi-Beam Combiner
AO	Adaptive Optics
A_V	V-band extinction
au	Astronomical Unit
CNO	Carbon-Nitrogen-Oxygen
CF	Companion Fraction
Dec	Declination
DECaPS	DECam Plane Survey
DR3	Data Release 3
ERIS	Enhanced Resolution Imager and Spectrograph
ESO	European Southern Observatory
FIR	Far-infrared
FWHM	Full-Width Half-Maximum
GLIMPSE	Galactic Legacy Infrared Midplane Survey Extraordinaire
GMC	Giant Molecular Cloud
H_2	Molecular Hydrogen
H-R	Hertzsprung-Russell
IGRINS	Immersion Grating Infrared Spectrometer
IMF	Initial Mass Function
IR	Infrared
IRAS	Infrared Astronomical Satellite
ISM	Interstellar Medium
K-S	Kolmogorov-Smirnov

kpc	kiloparsec
LSR	Local Standard of Rest
$M_\odot$	Solar Mass
MF	Multiplicity Fraction
MSX	Midcourse Space Experiment
MWB	Massive Wide Binary
MYSO	Massive Young Stellar Object
NACO	Nasmyth Adaptive Optics System
NIR	Near-infrared
Pan-STARSS	Panoramic Survey Telescope and Rapid Response System
PIONIER	Precision Integrated-Optics Near-infrared Imaging Experiment
PMa	Proper Motion Anomaly
PMS	Pre-main-sequence
PNe	Planetary Nebulae
RA	Right Ascension
RMS	Red MSX Source
RV	Radial Velocity
SD	Standard Deviation
SED	Spectral Energy Distribution
SINFONI	Spectrograph for Integral Field Observation in the Near Infrared
SNe	Supernovae
SNR	Signal-to-Noise Ratio
UCHII	Ultracompact HII (region)
UKIDSS	UKIRT Infrared Deep Sky Survey
UKIRT	United Kingdom Infrared Telescope
VIRCAM	VISTA Infrared Camera
VISTA	Visible and Infrared Survey Telescope for Astronomy
VLT(I)	Very Large Telescope (Interferometer)
VVV	Vista Variables in the Via Lactea
VVVX	VVV eXtended
WFCAM	Wide Field Infrared Camera
YSO	Young Stellar Object
ZAMS	Zero-Age Main Sequence

Contents

List of Figures

List of Tables

Chapter 1

Introduction

Stars are an extremely important part of astrophysics research. Stars, in particular massive stars, have a significant effect on their galaxy's evolution. Many factors are at play in the process of star formation, such as a star's initial mass, its evolutionary path, and whether or not it exists in a multiple system.

Massive stars have a mass greater than 8 $M_{\odot}$. Above this limit, stars can burn hydrogen more efficiently into helium thanks to the CNO cycle, and can also burn heavier elements than low-mass stars via rapid nuclear fusion. They produce high energy photons which can ionise their surroundings and may create HII regions (Churchwell, 2002). They also have strong stellar winds and outflows which transfer gas into the surrounding regions and may potentially trigger further star formation in the local vicinity, making them very important in the evolution of galaxies and the interstellar medium (Sugitani et al., 1989; Kennicutt, 2005). Massive stars end their lives as supernovae (SNe); powerful and hugely energetic explosions which distribute stellar material into the the surrounding galaxy.

Star formation has always been an intense point of astrophysics research, however the formation of massive stars is still not fully understood. The observation of these objects presents a difficult challenge; massive stars evolve onto the main sequence while still embedded in their natal dust cloud, restricting a clear view of the whole formation stage. Massive star formation is rapid compared to that of lower-mass stars, providing a relatively short window to observe this evolutionary stage. As predicted by the initial mass function (IMF), massive stars are rare (Salpeter, 1955). Their scarcity also means that they are generally situated at larger distances ($\sim$ kpc) than low-mass stars ($\sim$ 100s of pc). These factors hamper high-resolution studies of the early stages of massive stars, especially ones with large samples of objects.

A crucial part of the debate centres around whether the formation scenario for massive stars is simply a variation of the intermediate and low-mass theories, or whether they have a completely different origin. Many massive stars appear to be in binary or multiple systems, and there are unanswered questions around how these form too. Observations of Massive Young Stellar Objects (MYSOs) are key in trying to understand massive star formation and binary formation.

This thesis aims to study the multiplicity of MYSOs in multiple wavebands and spatial scales, to provide a comprehensive set of constraints which can inform formation theories and models. To gain a complete picture of the formation of massive multiple star systems, they must be studied as early in their lifetimes as possible. This chapter outlines the background of star formation in both low- and high-mass stars, as well as the formation theories for multiple systems, and finally discusses the current state of MYSO observational studies.

1.1 Low-mass star formation

Some theories of massive star formation suggest that a scaled-up version of low-mass star formation is one possible pathway. Therefore to understand massive star formation, an understanding of the formation of solar-mass stars is paramount. A detailed review of the processes of low-mass star formation can be found in Shu et al. (1987) and Larson (2003).

Stars form from dust and gas in Giant Molecular Clouds (GMCs). These clouds are initially stable against gravitational collapse, however a perturbation (such as stellar winds from nearby massive stars or a supernova shock) may trigger a collapse. To form a star, this gas and dust much reach the densities commonly found in stars through the compression that occurs during gravitational collapse. The minimum mass needed for collapse is known as the Jeans mass M_J (Jeans, 1902):

$$M_J = (\frac{5k_BT}{G\mu m_p})^{\frac{3}{2}}(\frac{3}{4\pi\rho})^{\frac{1}{2}} \tag{1.1}$$

where k_B is Boltzmann's constant, T is temperature, G is the gravitational constant, μ is the mean molecular weight, m_P is the mass of a proton and ρ is the density in kg/m^{-3}. If the mass of the GMC exceeds this mass, a runaway gravitational collapse will occur. During collapse, the GMC begins to produce filaments, which are dense elongated structures generally around ∼0.1 pc long (Könyves et al., 2015). As collapse continues, pre-stellar cores begin to form at the densest regions of the filaments. The collapse remains generally isothermal, and so the increased density causes the Jeans mass to decrease, potentially causing fragmentation.

This free-fall collapse is halted when a core is dense enough that it becomes optically thick and it cannot radiate away the gravitational potential energy generated from the contraction quickly enough. This heats the core up and prevents collapse. Eventually the core reaches a temperature of ∼2000K, at which point H_2 dissociation begins; this uses photon energy which would otherwise have been preventing gravitational collapse, and as a result of this reduction in pressure the second stage of collapse begins. The core becomes a 'protostar', and forms an accretion disc around its equator. This disc is the result of material in the surrounding envelope falling in; the centrifugal force of the protostar is more powerful than gravity at the equator due to the conservation of angular momentum by the envelope. Therefore material builds around the equator, whereas otherwise it falls into the star and is accreted.

As the core heats up and becomes convective, a magnetic field forms which allows material from the disc to be accreted by the protostar via magnetospheric accretion. Additionally, the magnetic field creates bipolar outflows and jets at the poles of the protostar (Figure 1.1), where material has been rapidly ejected from the central core (Machida, 2017), or from the disc (Blandford and Payne, 1982). This process transfers angular momentum away from infalling material (Pudritz and Norman, 1986). When the protostar begins to run out of material to accrete, it reaches its pre-main-sequence (PMS) phase and the accretion process slows down, reducing the strength of the jets and outflows. Eventually when accretion stops, radiative processes take over and the star begins the burning of hydrogen into helium via nuclear fusion. Here the star has reached its main sequence (MS) phase.

These formation stages can be classified when studied via observations, and are assigned a class based on how its flux is related to its wavelength, i.e. the form of its spectral energy distribution (SED). Class 0 is the youngest phase, where the first rapid accretion phase is beginning (Barsony, 1994). These objects are dust-rich and cold. Class I objects are undergoing the main accretion phase (Shu, 1977) and emit mainly in the far-infrared (FIR). These are heavily embedded in the prestellar envelope. Class II objects (Shu, 1977) are less obstructed by the envelope but are still undergoing accretion. This class of object are brightest in the near-infrared (NIR). Finally, Class III objects are post-accretion (Shu, 1977). The SED appear similar to that of an MS star as the flux is mainly from the star itself, but they have remnants of their circumstellar disc and may show substructures.

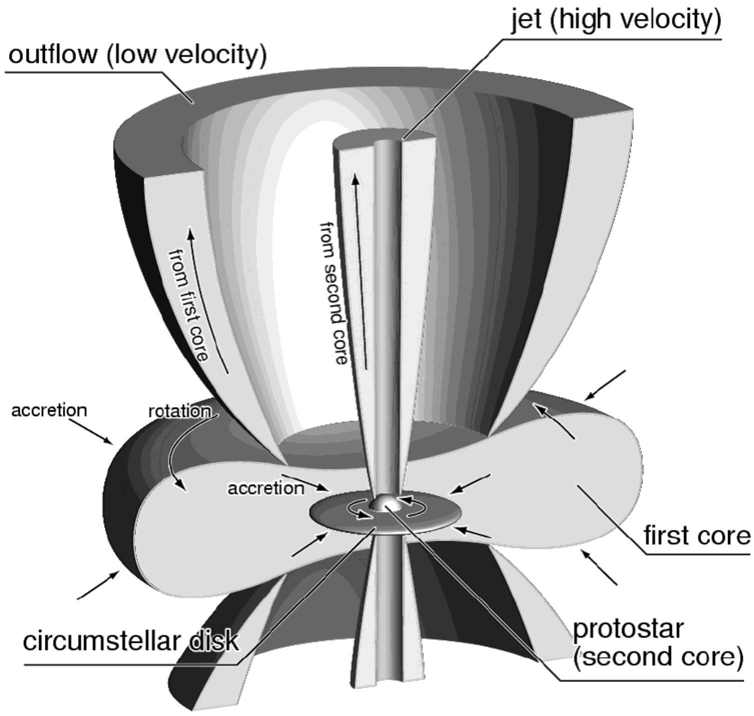

Figure 1.1: A diagram of the jet and outflow produced by a forming protostar. Taken from Machida et al. (2009).

1.2 High-mass star formation

Massive star formation occurs in cold, highly-dense regions of gas in molecular clouds. The formation of massive stars remains a topic of debate, namely whether their evolution mirrors that of low mass stars or not. Massive stars have a shorter Kelvin-Helmholtz timescale than its free-fall collapse timescale; gravitational potential energy is rapidly converted to luminosity while the central source is still obscured by its surrounding natal gas and dust. A massive star can also continue accretion after it has begun to burn hydrogen, i.e. it can accrete while on the MS and therefore can move on a Hertzsprung-Russell (H-R) diagram during its evolution.

Previously it was theorised that an upper limit on the mass existed for massive stars (Kahn, 1974), and that radiation pressure prevented further accretion. The outwards acceleration of radiation pressure from a protostar is given by:

$$a_{radiation} = \frac{L_*}{4\pi c r^2}\frac{n_d \sigma_d}{\rho} \tag{1.2}$$

where L_* is the luminosity of the protostar, c is the speed of light, r is the distance between the material and the protostar, n_d is the number density of dust grains, σ_d is the cross-sectional size of a dust grain and ρ is the density of the grain material (Ward-Thompson and Whitworth, 2015; Sivkova et al., 2021). The inwards acceleration of gravity due to an accreting star of mass M_* at a distance r is given by $a_{gravity} = \frac{GM_*}{r^2}$. By comparing the inward acceleration due to the protostellar gravity with the outward acceleration due to radiation pressure, an upper limit of approximately $20M_\odot$ should exist, beyond which accretion would cease. However, stars well above this mass limit have been observed (Hillier, 2008; Crowther et al., 2016).

To overcome this 'barrier' of radiation pressure, the accretion rate needs to be sufficiently high so that the gravitational force from accretion is higher than the outward luminosity/radiation pressure (Hosokawa and Omukai, 2009; Kuiper and Hosokawa, 2018). One explanation is that accretion does not occur spherically, and that disc accretion causes the infalling material to experience less radiation pressure (Bonnell et al., 1998; Yorke and Sonnhalter, 2002), allowing accretion to continue beyond $20M_{\odot}$. Additionally, the properties of the dust may not align with that of the ISM. Rosen (2022) performed 3D radiation-magnetohydrodynamic simulations of massive core collapse and found that feedback from stellar winds prevents accretion onto protostars with $\sim 30M_{\odot}$. Therefore $\gtrsim 30M_{\odot}$ stars require large dynamical inflows from their host cloud to combat the wind feedback and continue accretion.

Currently there is no clear-cut formation path for massive stars. The two central theories that aim to explain the process are monolithic collapse and competitive accretion. The details of each theory are discussed below.

1.2.1 Monolithic collapse

Monolithic collapse (also known as core accretion) is the theory that massive stars follow a scaled-up version of the low-mass formation path, where a single pre-stellar core forms a single massive star and its final mass is set only by the mass of the core. This theory infers that the pre-stellar core mass function is aligned with the stellar IMF, which is supported by observations (André et al., 2010).

McKee and Tan (2003) present a turbulent core model where the molecular cloud fragments into clumps which are in quasi-equilibrium. Kinetic energy is transferred from outflows, accretion shocks and the GMC to keep the clump in this state. These cores are turbulent on a supersonic scale, are significantly denser than the clump surrounding it, and have higher pressures than that of the average diffuse ISM pressure or the cloud pressure (Tan et al., 2014). From these models, timescales of order 10^5 years are estimated, with a larger dependence on the clump's surface density (t $\propto \Sigma_{clump}^{-3/4}$) than the stellar mass (t $\propto M_*^{1/4}$).

Similarly to the low-mass paradigm, an accretion disc forms to conserve the angular momentum of the system, and a magnetic field causes jets and outflows to be present at the poles which removes angular momentum. Radiation pressure is alleviated in two ways: self-shielding by the disc against radiation pressure, and the release of radiation pressure through optically thin bubbles (Krumholz et al., 2009). Consequently, accretion is not halted and so the upper limit on the stellar mass is nullified.

3D radiation-hydrodynamic simulations of core collapse by Rosen et al. (2016) found a solution for radiation pressure by simulating the absorption of the radiation field (with the caveat of excluding outflows, ionisation or magnetic fields). These simulations found that instabilities are caused by radiation bubbles which reducing radiation pressure, similar to that of Krumholz et al. (2009). These bubbles also cool down the disc and make it more likely to fragment, therefore increasing the likelihood of companions.

Hosokawa et al. (2010) modelled massive protostars with very high accretion rates. They found that the energy from accretion could not be dissipated effectively by radiative cooling, as the models had short timescales. The accretion becomes adiabatic, and as the stellar mass grows its opacity increases, resulting in cooling of the star. The Stefan-Boltzmann law states that the temperature is inversely proportional to the square root of the stellar radius, and so the models predict bloated stars with radii up to 100 $R_{\odot}$. The opacity eventually decreases, causing an increase in the luminosity and a shorter Kelvin-Helmholtz contraction timescale. Contraction occurs until it reaches the ZAMS when hydrogen burning begins. These models provide an explanation as to how massive stars can reach such high luminosities while not being hot enough to ionise their surroundings to create HII regions.

1.2.2 Competitive accretion

An alternative approach to massive star formation is competitive accretion: the idea that a cloud's fragmentation into clumps is non-uniform and inefficient. This theory has been simulated extensively (e.g. Bonnell et al., 1997; Bonnell and Bate, 2006). A large gas reservoir must be available and under the same gravitational acceleration as the cores, and it cannot be affected by magnetic fields. Cores located towards the centre of the cloud accrete more material faster than those found further out, as they experience its full gravitational potential; they compete for the material available in the cloud.

The accretion follows the Bondi-Hoyle law of spherical accretion on a compact object moving through the ISM. A star-dominated regime was argued as the better fit for massive star formation (Bonnell et al., 2001; a gas-dominated regime was also modelled). The accretion rate is initially low, only accreting gas in close proximity to the cores, but as they gain mass the gravitational pull increases, allowing gas in further out regions of the clump to be accreted onto the cores. Essentially, the core's final mass is influenced more by its location in the clump than the core's initial mass. Discs smaller than those found in the monolithic collapse model are predicted to exist, with their smaller size due to multi-core interactions in the dense cluster. Fragmentation or stellar feedback will eventually halt the accretion process. Competitive accretion alone is not enough to solve the radiation pressure problem, however additional hypotheses such as disc accretion, stellar collisions and binary mergers exist which are able to overcome this issue (Bonnell and Bate, 2006).

1.3 Multiplicity of massive stars

Single-star formation theories have been established for many years, but multiplicity is now known to be a very common phenomenon which has its own implications on the process of star formation. Multiplicity properties are established early on in the lives of stellar systems, particularly in the PMS stage (Mathieu, 1994; Duchêne and Kraus, 2013). Multiplicity also significantly affects the ongoing evolution of massive stars (Sana et al., 2012), such as changing the nature of stellar outflows (Sana, 2022). The frequency of multiples, and their properties and dependence on the primary star provide a unique insight into the origins of a multiple system. Large-scale studies into this phenomenon have been historically tricky, but within the last two decades all-sky surveys have made a comprehensive analysis of stellar multiplicity much more feasible. Multiplicity studies can inform star formation models with initial conditions and evolutionary changes, which in turn can help refine the theoretical picture of star formation. A large proportion of stars are thought to form in multiple systems (Duchêne and Kraus, 2013), and it is also known that up to 100% of OB-type stars are in multiple systems (Chini et al., 2012). King et al. (2012) and Marks and Kroupa (2012) suggested that multiplicity is higher in dense clusters.

An important statistic in this area of study is a measure of how commonly these multiple systems occur; this is represented by the multiplicity fraction of a population of stars, which is the percentage of multiple systems in that population. Another useful statistic is the companion fraction, which represents the average number of companions per system in that population; this value can exceed 100%. Additional important parameters include the the orbital semi-major axis (found using the apparent separation from a directly imaged binary) and the orbital period of a binary system (determined through spectroscopic analysis). The distribution of orbital periods can be parameterised by a power law, $f(P) \propto P^{\alpha}$, with α=-1 a common choice known as the logarithmically flat Öpik's law (Öpik, 1924) which suggests a scale-free process of binary formation; i.e. there is a constant number of binary systems per logarithmic interval. Duquennoy and Mayor (1991) shows a good fit for solar-mass stars to Öpik's law, but a system's orbital period may be affected through dynamical evolution, so

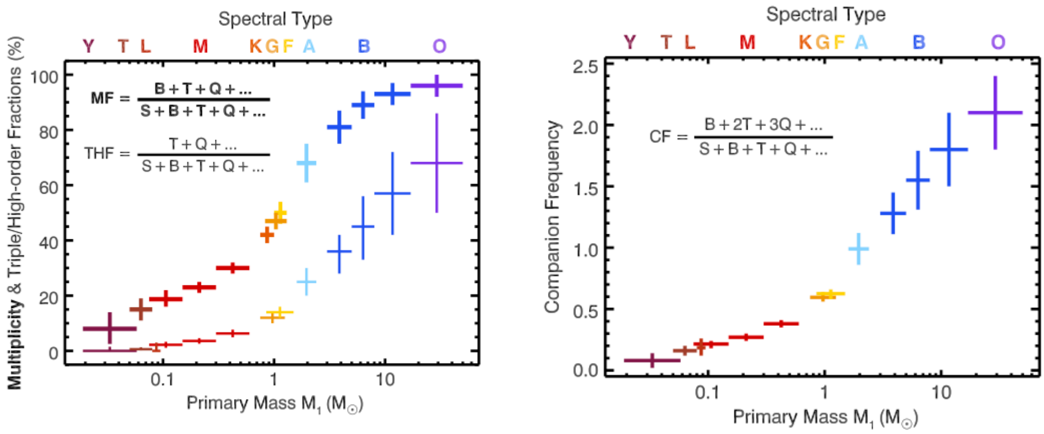

Figure 1.2: Multiplicity fraction (left, thick), triple/higher-order multiplicity fraction (left, thin) and companion frequency (right) against primary mass for brown dwarfs and main-sequence stars. Taken from Offner et al. (2022).

the observed and primordial period distributions may not be identical. The mass ratio of a primary source and its companion ($q = M_c/M_p$) can be derived from the ratio of their observed fluxes; for PMS objects this is model-dependent.

Multiplicity surveys should be as uniform and as complete as possible using a volume-limited sample, using multiple methods of observation depending on the separations of the systems being observed: imaging for wider binaries which can be individually resolved, and spectroscopy/interferometry for closer binaries which cannot be resolved using imaging. Biases can affect a survey through differential extinction or magnitude limitations, and these must be corrected for or at least taken into context with results. For a precision of ±5% in the multiplicity fraction, at least 100 targets are needed in a sample. To study orbital parameters effectively, a sample size many times larger than this is required (Duchêne and Kraus, 2013). Magnitude-limited surveys are susceptible to Malmquist bias - while correctable, this can be avoided using volume-complete samples with distance measurements or samples that are free from distance biases. Distances also introduce a resolution bias for distant rare objects (Duchêne and Kraus, 2013).

The frequency of massive binary systems (and the order of multiplicity) generally increases with stellar mass (see Figure 1.2). There are a large range of estimates for the frequency of companions detected through spectroscopy, as these methods are susceptible to bias and are commonly small and/or incomplete samples; the most recent estimate of the MF for spectroscopic companions is 70±9%. Imaging surveys can have an even wider range of results, thanks to differences in techniques and wavelength ranges, but a MF of ∼45±5% is generally accepted for visual companions (Duchêne and Kraus, 2013). In many cases, companions to massive stars are close enough to interact with the primary, via common envelope evolution, envelope stripping, spin-up (by accretion or coalescence) or binary mergers. Sana et al. (2012) found that at least 70% of massive star companions are close enough to exchange mass with the primary.

Duchêne and Kraus (2013) and Offner et al. (2022) summarise how massive stars may form in binary and multiple systems. Like with massive star formation, there are multiple theories which aim to explain how massive stars come to be in binary or multiple systems, and some theories favour different mass ranges. The theories also aim to address whether massive binary systems are primordial or are formed throughout the star's evolution.

1.3.1 Disc fragmentation

Disc fragmentation is when the accretion disc around a prestellar core experiences gravitational instability and fragments into clumps which may then go on to form companion stars. This theory has been discussed for more than 30 years (Adams et al., 1989; Shu et al., 1990). Two important criterion have been discussed for fragmentation; firstly the Toomre Q-criterion describes the relation between the sizes and masses of the disc and star, and how instability can occur (Toomre, 1964):

$$Q = f\frac{M_*}{M_d}\frac{H}{r} \leq 1, \tag{1.3}$$

where M_*/M_d is the star-disc mass ratio, H/r is the aspect ratio between the disc scale height H and its radius r, and f is a scale factor depending on the surface density power law chosen. The second criterion is a cooling criterion, which describes how radiating away heat from the disc can lead from instability to full fragmentation (Gammie, 2001): discs must rapidly cool on roughly the orbital timescale for fragmentation to occur. However these two criterion alone are not enough to predict fragmentation in massive discs (Takahashi et al., 2016), as they are too easily satisfied (Lau and Bertin, 1978; Kratter and Lodato, 2016). The most likely explanation for instability in discs is that the surface density increases without an increase in temperature, such as when material is accreted by a star more slowly than material falling onto the disc (Kratter et al., 2010; Zhu et al., 2012). For fragments to survive and become binary companions, they must cool and shrink rapidly otherwise they will fall victim to disc/fragment interactions.

Disc fragmentation is more common for massive stars than for the low-mass case as gravitational instability is more likely to occur in massive systems (Kratter et al., 2008; Krumholz et al., 2009), and it also favours closer (< 100au) binaries (Meyer et al., 2018) and equal mass binaries (Young and Clarke, 2015). Simulations by Tokovinin and Moe (2020) suggest that disc fragmentation creates companions around massive stars which then migrate inwards as they accrete from the disc, and the model predicts a large fraction of binary mergers early on in the accretion process. Their model also suggests that disc fragmentation (and subsequent migration driven by accretion) is the main formation path for close binaries and compact triple systems.

1.3.2 Core and filament fragmentation

The core fragmentation (or turbulent fragmentation) theory suggests that a prestellar core with a large amount of turbulence can cause irregularities in the core's density, some of which may be above the Jeans mass and therefore will lead to a secondary collapse away from the main core, producing potential companions (Goodwin et al., 2004). Even a low level of turbulence can cause secondary objects to form in the majority of cores. This scenario lends itself more towards the formation of low-mass binary systems, and binaries at wide separations (Offner et al., 2010). Wide binaries formed through turbulent fragmentation can initially form at up to 0.1pc, then tend to migrate inwards to $\leq 10^2$ au within 10^5 years (Offner et al., 2016; Lee et al., 2019). As a result of these wide initial separations, the differential angular momentum from accreted gas means that misalignment in accretion discs and outflows are common, with simulations exhibiting a random distribution (Offner et al., 2016; Lee et al., 2019), meaning that misalignment may be a signature of turbulent fragmentation.

Filament fragmentation follows a similar process to core fragmentation; overly dense regions of a filament will fragment into smaller separate structures which go on to form a multiple system. Filamentary structures are thought to be a result of turbulence, and so these two theories may go hand-in-hand. Models have been used to determine the relation between a filament's initial properties and the masses of fragments; André et al. (2019) determined that a filament fragment will collapse if its mass is greater than a critical mass known as the Bonnor-Ebert mass. The dependencies of this critical mass limit suggest that closely-spaced fragments can only form from dense, narrow filaments, and therefore strong magnetic fields must be involved in the filament fragmentation process.

1.3.3 Capture

In binary capture, two isolated stars form and then interact to become a gravitationally bound pair. This can be assisted by an accretion disc when a star is still in its protostellar stage; the disc effectively widens the interaction area which could result in a more efficient capture rate. Moeckel and Bally (2007) found that the rate of binary capture for massive stars is an order of magnitude greater than that of low-mass stars.

However these were likely to be soft binary systems that could easily break up; massive companions have more chance of holding on to their primary in a dense cluster in comparison to low-mass companions. Rozner et al. (2023) found that gas-assisted capture is a significant and efficient method of forming binaries in star-forming regions, with the capture rate increasing with gas density. The capture rate was found to be highest for more massive primary stars capturing less massive companion stars, suggesting that this theory lends itself to lower mass ratios.

Post-capture migration can also occur to form close binaries (or in some cases push companions further out). Possible migration processes include friction from the gas producing a torque that reduces the size of the orbit (Bate and Bonnell, 1997; Lee and Stahler, 2011), torques produced by circumstellar and circumbinary discs (Muñoz et al., 2019; Dempsey et al., 2021), and secular evolution caused by long-term orbital oscillations in triple systems (Fabrycky and Tremaine, 2007; Moe and Kratter, 2018).

1.3.4 Stellar multiplicity studies

Studies have shown how different factors in massive star formation can affect multiplicity. The binary fraction of a system has been shown to scale with the mass of the primary object, according to hydrodynamical simulations of stellar cluster formation (Bate, 2012). This is thought to occur because the more massive a core is initially, the more fragments it will generally produce. It has also been suggested that magnetic fields and radiative feedback play an important part in suppressing fragmentation, due to the low number of quadruple and higher systems in field stars. These mechanisms prevent the fragmentation process from becoming too violent, which would cause stellar ejections and reduce the overall multiplicity fraction (Bate, 2012).

Rosen et al. (2019) performed radiation-hydrodynamic simulations on massive prestellar cores to determine how their initial state affects binary formation. The virialised prestellar cores experience a slow, gradual gravitational collapse, along with significant

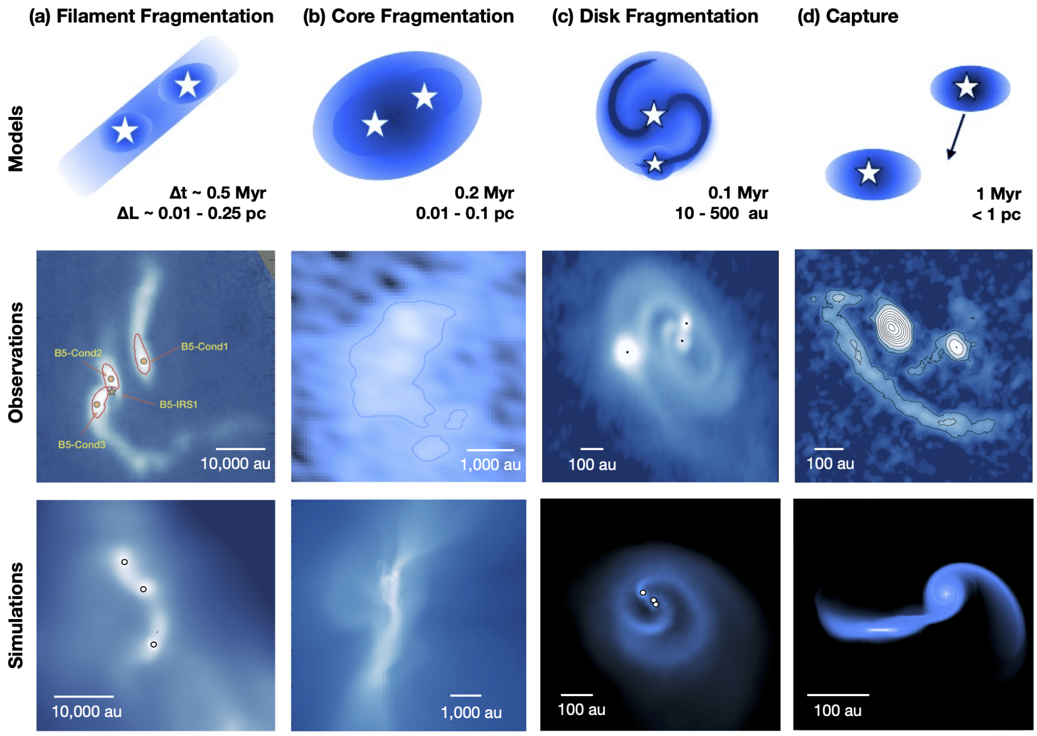

Figure 1.3: A summary of the possible binary formation mechanisms. Top: model of each formation theory with time and length scales. Middle: observational examples of each process. From left to right: Perseus B5 (Pineda et al., 2015), Ophiuchus SM1N (Kirk et al., 2017), L1448 IRS3B in Perseus (Reynolds et al., 2021) and RW Aurigae (Rodriguez et al., 2018). Bottom: Simulations of each formation mechanism. From left to right: Guszejnov et al. (2021), Offner et al. (2016), Bate (2018), and Muñoz et al. (2015). Summary diagram taken from Offner et al. (2022).

turbulent fragmentation early on. Conversely, subvirial cores are not supported by turbulence, and therefore are very unstable to collapse - their high accretion rate means that at early times, fragmentation is prevented. Regardless of their early virial state, accretion disks form around massive stars later on and eventually the disks fragment to form companions.

Primordial massive wide binaries (MWBs) with seperations larger than 10^2 au are more likely to survive in low-density regions with few surrounding stars; in high density regions they have a high risk of destruction. MWBs are more likely to form later in their lifetime in a dense cluster than in a low-density environment (Griffiths et al., 2018). Massive close binaries are thought to be a result of inward migration from wider separations, occurring through interaction with a disk remnant or another young stellar object (Ramírez-Tannus et al., 2021). Atacama Large Millimetre/submillimetre Array (ALMA) observations of high-mass star-forming regions at sub-50 au spatial scales have shown close-in substructures with masses and separations consistent with thermal Jeans fragmentation of a dense core, indicating that this fragmentation process occurs down to the smallest observable scales (Beuther et al., 2019; Meyer et al., 2019). In massive MS (O- type) stars, 53% of them have been reported to be in binary systems at separations less than 200 au, with the multiplicity fraction increasing to 90% when taking larger separations into account (Sana et al., 2014; Bordier et al., 2022).

1.4 Massive Young Stellar Objects

As a result of dynamical processes such as capture or magnetic braking (Lund and Bonnell, 2018) occurring during the evolution of a star, the multiplicity statistics of main-sequence (MS) stars may not be an accurate indicator of the primordial properties of a multiple system (Kratter, 2011); young stars are therefore the best windows into this primordial stage of binary star formation.

Massive Young Stellar Objects (MYSOs) represent a key point early on in a star's lifetime where the process of accretion can be observed and investigated. This phase lasts around 10^5 years, and heavy dust extinction is common during this phase which renders the majority of MYSOs effectively invisible at $< 1\mu m$ (Davies et al., 2011). They are bright in the mid-infrared which makes this wavelength range ideal for observing them. MYSOs commonly exhibit bipolar outflows, but despite their high bolometric luminosity they do not emit ionising radiation, indicating that they are still undergoing the accretion process (Oudmaijer and de Wit, 2014).

Small-scale gap-like substructures in MYSO disks have been connected to the high binary fractions of MYSOs and may be due to the presence of one or more companions (Frost et al., 2021). Accretion disc-like structures have been detected around MYSOs through ALMA observations (Johnston et al., 2015; Ilee et al., 2018a) and NIR disc tracers (Wheelwright et al., 2010; Cooper et al., 2013; Ilee et al., 2013) at large separations (1000-1500 au). More recently, direct evidence of discs around MYSOs has been found at scales of a few au (Kraus et al., 2010; GRAVITY Collaboration et al., 2020; Koumpia et al., 2021; Koumpia et al., 2023).

Observational studies of MYSOs are a difficult undertaking, due to their heavily extincted nature (A_V=42 mag, Cooper et al., 2013), rarity and large distances (of order kpc). Only the newest high-resolution instruments are able to study MYSOs in enough detail. One of the earliest attempts at creating a catalogue of MYSOs used data from the IRAS satellite (Neugebauer et al., 1984), and Campbell et al. (1989) identified 115 YSOs from the data based on their IR colors. This study was followed up by that of Molinari et al. (1996) and Molinari et al. (1998) who used radio and NH_3 observations of sources identified by IRAS, but the study was biased against sources in larger HII regions or SFRs due to the exclusion of sources less than 30° north of the celestial equator and sources within 1' of HII regions. Further follow-up studies by Sridharan et al. (2002) and Beuther et al. (2002) included molecular line data and FIR, radio continuum and maser observations, focusing on objects with gas densities and luminosities similar to that of UCHII (Ultracompact HII) regions. This focus led to a similar bias as Molinari et al. (1996); only some MYSOs exhibited maser emission and the nature of the transition varied between sources, which implies that during the MYSO phase, molecules which produce maser emission are being destroyed. This means that maser-based MYSO catalogues are unreliable.

Robitaille et al. (2008) used the GLIMPSE catalogue to identify 11000 YSO candidates using colour selection criteria, but no follow-up studies were performed. Therefore some of the detected YSOs may actually be different types of object with a similar colour; HII regions, planetary nebulae or evolved stars. Churchwell et al. (2006) and Churchwell et al. (2007) used GLIMPSE data to find 600 HII regions and bubbles, and determined that 10% had associated YSOs and 12% had a morphology which suggested that triggered star formation had occurred.

1.4.1 The RMS Survey

The Red MSX Source (RMS) survey (Lumsden et al., 2013) was constructed with the aim of creating a complete and unbiased database of the Galactic population of MYSOs. The RMS survey was initially derived from the MSX point source catalogue (Egan et al., 2003); as MYSOs are bright in the infrared, MSX was ideal due to its higher resolution and because bright objects do not saturate. The selection criteria were outlined in Lumsden et al. (2002); the inner $\pm 10^{\circ}$ of the centre of the galaxy was excluded so that issues with source confusion and distance estimates were avoided. The MSX bands A, D and E were used to classify MYSOs, and they correspond to wavelengths of 8, 14 and 21 μ respectively. Using the E-band of MSX, a lower flux limit of $F_{21\mu m} = 2.7$ Jy was set due to the 95% completeness rate of the MSX catalogue at this sensitivity. Sources had to have a signal-to-noise ratio (SNR) of > 5 in the E-band.

MYSOs have a red rising continuum due to their dust extinction, and so the primary colour selection criterion was that flux must increase with wavelength ($F_{8\mu m} < F_{14\mu m} < F_{21\mu m}$). Colour-colour plots in Lumsden et al. (2002) (an updated version of these plots from Lumsden et al., 2013 is shown in Figure 1.4) showed that MYSOs segregate from evolved stars, and that younger sources had the limit $F_{21\mu m}/F_{8\mu m} > 2$. Additionally, the planetary nebulae (PNe) lie towards the blue end of the plots as they are not obscured by a molecular cloud. As a result of this, the limits of $F_{8\mu m}/F_K > 5$ and $F_K/F_J > 2$ were added to the selection criteria. Objects that showed extended

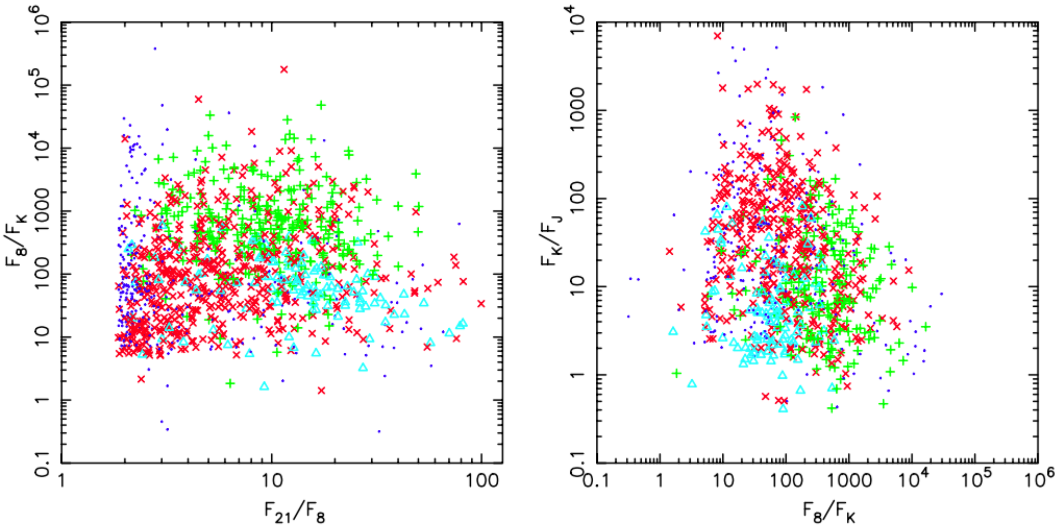

Figure 1.4: Colour-colour plot from Lumsden et al., 2013 showing distributions of YSOs (red ×s), HII regions (green +s), planetary nebulae (cyan △s) and evolved stars (blue dots).

emission larger than the MSX beam size were rejected, and classified as 'diffuse HII regions', background emission or simply erroneous image artifacts. Follow-up radio observations and CORNISH survey data (Urquhart et al., 2009; Purcell et al., 2013) were used to distinguish HII regions and YSOs that did not segregate on the colour-colour plots, and to exclude evolved stars that had not been excluded by the earlier selection criteria. Additional multi-wavelength data (including radio, infrared and millimetre CO observations) was used to form a spectral energy distribution and determine the luminosity of the sources.

1.5 Multiplicity studies of massive protostars

Until recently, there had been no dedicated studies into the multiplicity of MYSOs; there have been serendipitous discoveries of companions (e.g. Caratti o Garatti et al., 2015), and stars of similar masses and ages have been studied for companions, such as in the Herbig Ae/Be studies of Baines et al. (2006) and Wheelwright et al. (2011).

Both studies found multiplicity fractions over 70% and high mass ratio, which disagrees with the IMF random sampling that the capture theory predicts. They also found a similar mass-multiplicity relation to MS stars, and coplanarity between the binary orbits and disc axes. These findings suggest an agreement with the formation theory of disc fragmentation. However Herbig Ae/Be stars are of lower masses than MYSOs (2-8 $M_{\odot}$). Sana et al. (2012) investigated a sample of 71 massive Galactic O-type stars and found that at least 70% of them orbit a companion in close enough proximity for mass exchange, or in some cases for a binary merger to occur. Kraus et al. (2017) conducted a NIR survey of the MYSO IRAS 17216-3801 using VLTI observations and found it to be a binary system with masses of 20 and 18 $M_{\odot}$ with both components showing evidence of misaligned circumstellar discs (the masses are rough estimates as the SED model used did not incorporate the companion). However, no comprehensive study of MYSOs existed until a few years ago.

The first dedicated study into MYSO multiplicity from Pomohaci et al. (2019) was performed on a sample of 32 MYSOs from the RMS survey (Lumsden et al., 2013). Using K-band adaptive optics (AO) observations from NACO, 18 previously undiscovered companions were found within 3" of their primaries. The multiplicity fraction was determined to be 31 $\pm$ 8% and the companion fraction was 53 $\pm$ 9%, although it was asserted that the total multiplicity fraction could be up to 100%. Mass ratios for the sample were generally found to be greater than 0.5. This is consistent with multiplicity studies on Herbig AeBe stars (Wheelwright et al., 2011). However, caveats of this survey include the small sample size, and the shallow limiting magnitude (between K = 12 and K = 15). Additionally, the mass ratios had a relatively large error ($\pm$30%) due to significant uncertainties in the primary flux, secondary photometry and secondary extinction.

More studies on the multiplicity properties of MYSOs have since been performed. Koumpia et al. (2019) investigated two MYSOs, PDS 27 and PDS 37, using H-band

VLTI/PIONIER observations (with a maximum angular resolution of ∼3.3 au and 2.5 au respectively) and discovered that both were each part of a binary system. A companion was detected at 30 au for PDS 27, and one at 42-54 au for PDS 37, making these some of the closest MYSO companions ever resolved. There were issues constraining the model parameters for both objects (particularly for PDS 27), and so this method would benefit from a more detailed model. Koumpia et al. (2021) presented the first interferometric K-band survey of MYSOs, using VLTI observations of six objects, and found a binary fraction of 17±15% at separations between 2-300 au (shown in Figure 1.5). The very small number of objects means this result is highly uncertain, and the limited UV coverage across the sample means that up to 50% of close-in (<4 mas) companions may have been missed.

In summary, while multiple studies of MYSO multiplicity have been conducted, each one is subject to caveats due to their relatively small size; a large-scale study (∼ 100s of objects) is yet to be performed.

1.6 Thesis outline

This introduction has summarised the current state of our knowledge of the formation and multiplicity of massive stars, specifically MYSOs. Thanks to near-infrared and ALMA observations, MYSOs which were once thought of as deeply embedded and difficult to observe can now be studied in detail. To gain a complete understanding of the multiplicity properties of the MYSO stage, these objects must be observed in multiple wavebands and using multiple observing techniques to probe as much of the parameter space as possible. The aim of this thesis is to do just that: to study MYSOs at both wide and close separation ranges, and in different wavebands, to gain a clearer picture of where companions form around MYSOs, how massive these companions are and how often they form. Although this thesis will not provide a definitive answer to every question surrounding MYSO multiplicity, it will provide vital new information which can inform simulations and models of massive star formation to find those answers.

Chapter 2 presents an imaging study of MYSO multiplicity, using the UKIDSS and VVV K-band surveys (as well as RMS UKIRT K-band images) to search for wide-separation companions around YSOs across the entire RMS survey using statistical methods. This chapter serves as a successor to the MYSO multiplicity pilot study of Pomohaci et al. (2019), using a much larger sample size.

Chapter 3 presents a K-band spectroscopic study of MYSOs, using both high-resolution (R$\sim$45000) IGRINS and medium-resolution (R$\sim$11000) X-shooter spectra to search for radial velocity variations in the Brackett γ emission line. These variations are an indication of close-in companions which could not have been resolved through imaging.

Chapter 4 presents a survey of MYSO multiplicity in the optical regime using Gaia DR3 data. Despite previous assumptions that no YSOs would be visible at optical wavelengths, around a quarter of YSOs in the RMS catalogue are present in Gaia thanks to its unprecedented depth compared to other optical surveys. By comparing proper motions and parallaxes between primary YSOs and nearby objects, companions can be found in the vicinity.

Chapter 5 brings together all the results of the previous chapters and discusses the entire picture of MYSO multiplicity that they form, and highlights potential future studies that could further this work.

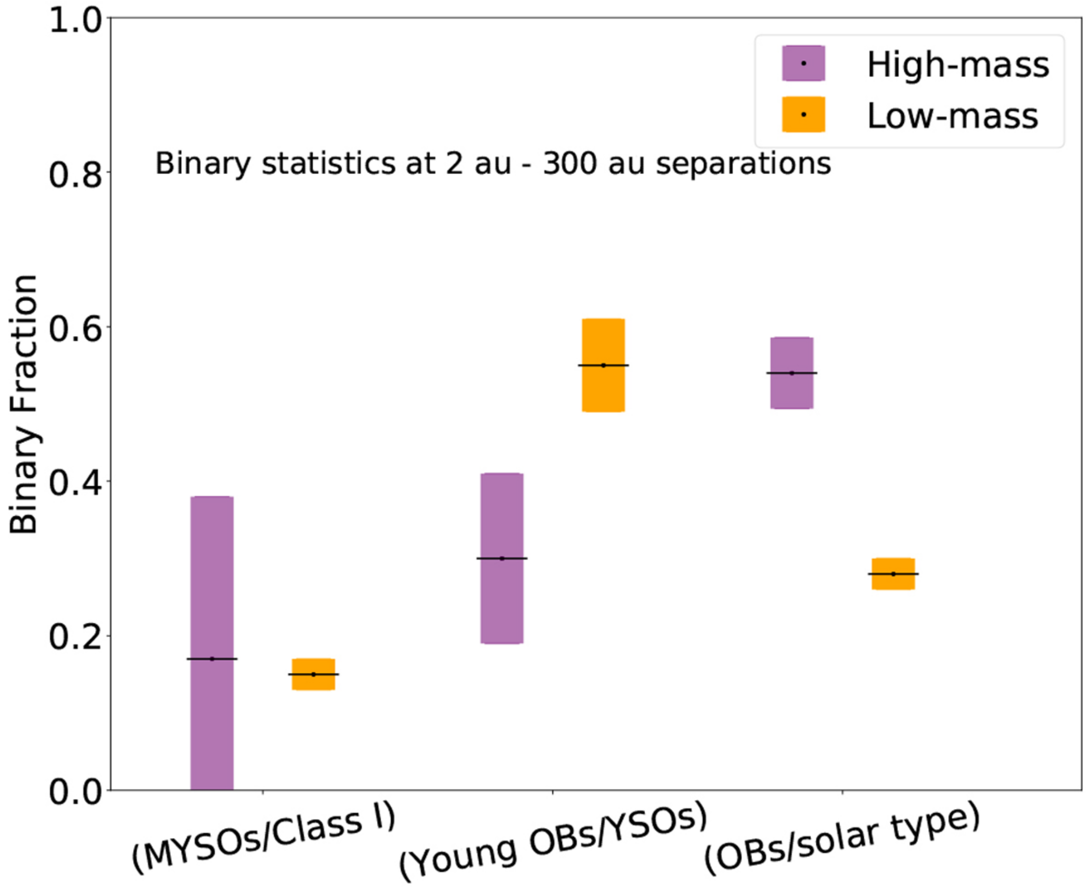

Figure 1.5: A comparison of binary statistics for companions located between 2 - 300 au for both low- and high-mass stars at various evolutionary stages: (i) embedded objects: low-mass Class I vs. MYSOs ($> 8 M_\odot$), (ii) pre-main-sequence: YSOs (0.25–2.5 $M_\odot$) vs. young OBs, (iii) main-sequence: OBs vs. solar mass. Taken from Koumpia et al. (2021).
References: Connelley et al. 2008 (Class I), Koumpia et al. 2021 (MYSOs), Kraus et al. 2011 (YSOs), Gravity Collaboration et al. 2018 (young OBs), Sana et al. 2014 (MS OBs), Raghavan et al. 2010 (MS solar type).

Chapter 2

Searching for MYSO companions in K-band imaging surveys

2.1 Introduction

Multiplicity properties of massive stars are established early on in their lives, particularly in the pre-main-sequence (PMS) stage (Mathieu, 1994; Duchêne and Kraus, 2013), and it also affects their evolution (Sana et al., 2012). The phenomenon of multiplicity has multiple theorised origins: disc fragmentation (Kratter et al., 2008; Krumholz et al., 2009), binary capture (Moeckel and Bally, 2007) and turbulent fragmentation (Goodwin et al., 2004) are three key theories. Many stars are thought to form in multiple systems (Duchêne and Kraus, 2013), with the fraction rising to up to 100% for OB-type stars (Chini et al., 2012).

When investigating stellar multiplicity, two key parameters of interest are the multiplicity fraction (MF) and the companion fraction (CF), which represent the fraction of stars in multiple systems and the average number of companions per systems respectively.

The multiplicity statistics of main-sequence (MS) stars may not be an accurate indicator of the primordial properties of a multiple system, due to processes such as capture or magnetic braking (Kratter, 2011; Lund and Bonnell, 2018). Thanks to the early stage of MYSOs, accretion and early multiplicity properties can be observed and investigated. Heavy dust extinction is common during this phase which renders the majority of MYSOs effectively invisible at $< 1\mu m$ (Davies et al., 2011), making the mid-infrared the ideal wavelength range for observations. Small gaps in MYSO disks may be due to the presence of one or more companions (Frost et al., 2021).

An important recent investigation into massive young binaries comes from Pomohaci et al., 2019 in which the very first MYSO multiplicity study was performed on a sample of 32 MYSOs from the RMS survey (Lumsden et al., 2013). Using K-band observations, 18 previously undiscovered companions were detected within 3" of their primaries. The multiplicity fraction was found to be $31 \pm 8\%$ and the companion fraction was $53 \pm 9\%$. From these findings it was asserted that the total multiplicity fraction could be up to 100%. Mass ratios for the sample were generally found to be greater than 0.5. This is consistent with multiplicity studies on Herbig AeBe stars (Wheelwright et al., 2010). However, caveats of this survey include the small sample size, and the shallow limiting magnitude (between $K = 12$ and $K = 15$). Additionally, the mass ratios had a relatively large error ($\pm 30\%$) due to significant uncertainties in the primary flux, secondary photometry and secondary extinction. This chapter aims to further the work done by Pomohaci's pilot survey, using a larger sample of MYSOs.

This chapter is structured as follows. Section 2.2 outlines the nature of the observations used in the sample of MYSOs. Section 2.3 explains the results of the multiplicity analysis, including the details of completeness and accounting for chance projections. In Section 2.4 I discuss the multiplicity statistics achieved from this sample and compare them to other previous studies, and I also explore mass ratios of the potential companions detected. Section 2.5 summarises the findings of this chapter.

2.2 Observational Data

2.2.1 Sample selection

The master sample consists of 681 YSOs, 402 of which are MYSOs ($> 8M_{\odot}$). All of the targets are drawn from the Red MSX Source (RMS) survey (Lumsden et al., 2013). This survey was constructed with the aim of creating a complete and unbiased database of the Galactic population of Young Stellar Objects (YSOs), by using multiwavelength data to discern YSOs from other similar objects, including HII regions and evolved stars (see Subsection 1.4.1 and references therein for more details). The full catalogue can be found at http://rms.leeds.ac.uk. The survey is complete for massive protostellar objects brighter than $2 \times 10^4 L_{\odot}$ out to 18 kpc, and is restricted to $10° < l < 350°$ to avoid source confusion towards the Galactic centre. The final selection of targets was effectively any YSO in the RMS catalogue that was present in the surveys described below, minus a few objects which had to be discarded due to poor data (e.g. corrupted/low quality images). The YSOs in this sample have distances ranging between 1.4-11.2 kpc; for the chosen detection range of 0.5-10 arcsec, this places any detected companions between 700-100,000 au away from the primary.

2.2.2 Galactic Plane Surveys

Point source catalogue data from the UKIRT Infrared Deep Sky Survey Galactic Plane Survey (UKIDSS GPS, Lucas et al. 2008) was used for targets in the Northern sky. We used the $K-$band so that YSOs are visible at short wavelengths despite high extinction. The WFCAM instrument used for UKIDSS has a pixel size of 0.4", and the limiting magnitude of the data is $K \sim 18.2$. The GPS survey has a spatial resolution of 0.8-1". From the UKIDSS DR11 catalogue, 395 YSOs were found, with 221 classed as MYSOs.

Alongside UKIDSS, point source catalogue data from the Vista Variables in the Via Lactea (VVV, Saito et al. 2012) survey was used. VVV focuses on the Southern part of the Galactic plane, and DR5 contains data on 279 YSOs with 181 of them classed as MYSOs. The VVV DR5 catalogue does not yet cover the entirety of the Southern sky, and so there is a region of the galactic plane left uncovered by either of these surveys; the VVV Extended Survey (VVVX, Minniti 2018) has since been conducted which includes observations of the regions left uncovered by VVV. There is an overlap of two YSOs between UKIDSS and VVV for these samples. VVV's VIRCAM has a pixel size of 0.34" and an average limiting magnitude of K_s=18.5, with a spatial resolution of ∼0.9".

The main advantage of using these surveys is their coverage of the RMS catalogue and their deep limiting magnitudes, as well as the availability of multi-colour data (specifically J- and H-bands) which is useful in determining interstellar extinction. This data allows deeper probing than that of the NaCo images used in Pomohaci et al. (2019) which had an average limiting magnitude of K=14. The main trade-off of this study compared to NaCo is the lower spatial resolution of these surveys. These differences are visible in Figure 2.1, where the four resolved bright objects in the centre of the RMS and UKIDSS images appear as one extended luminous object in the 2MASS image. UKIDSS/VVV are able to resolve objects almost as well as the RMS images, due to their similar resolution, but are deeper and have multi-colour information as mentioned above.

In addition, the 2MASS survey was used for photometry brighter than the saturation limit of UKIDSS/VVV ($K \sim 12$). The 2MASS survey is the only existing database of near-IR images of the whole sky and while it was an unprecedented project at the time, advancements in observational technology since then have vastly enhanced our view of the sky. 2MASS uses a pixel size of 1" and has a spatial resolution of ∼2", meaning it has only half of the resolution of UKIDSS/VVV.

2.2.3 UKIRT/RMS K-band imaging

K-band imaging data was obtained for a sample of 88 RMS objects (referred to from here onwards as the 'RMS images') taken in the K-band by the United Kingdom Infra-Red Telescope (UKIRT) in Hawaii between 2001 and 2006. 38 images were taken using the UIST instrument and 50 were taken with the UFTI instrument as a follow-up.

These 88 YSOs were sampled from the RMS catalogue. The RMS images taken were acquisition images used for obtaining spectra (Clarke et al., 2006; Cooper, 2013), and were calibrated using flat field frames and sky subtraction and had their astrometry corrected. This sample is therefore brighter on average compared to the entire YSO sample, hence their use in spectroscopy. The field of view of each of the images is 2.3 arcminutes. The images have an average limiting magnitude of K=17.5, and a seeing of ∼0.7" on average. The UIST and UFTI instruments of UKIRT have pixel sizes of 0.12" and 0.09" respectively. The main benefit of these images is the better resolution compared to UKIDSS/VVV. UKIDSS/VVV data was used as a reference to calibrate the K-band flux in the RMS images. There is no overlap with the VVV catalogue but 75 of the YSOs in the RMS image sample are also in the UKIDSS sample. The whole sample of YSOs is listed in Table A.1.

2.3 Binary detection

To determine companions, two methods were used for the two different types of survey. The RMS $K-$band images did not have a pre-existing point source catalogue, and so one had to be constructed. The UKIDSS and VVV surveys have point source catalogues readily available, and instead of using images the data was taken straight from the catalogues. The point source catalogues were tested against both the UKIDSS survey's own imaging and the RMS images, to determine the reliability of the catalogued sources. From the tested objects, there were no significant omissions or erroneous entries in the catalogue that could not be filtered out using flags or by simple visual inspection.

2.3.1 Point source catalogues

For each YSO in the sample, a region of 1.5 arcminute radius surrounding it (to cover the same FoV of the RMS images) was retrieved from the WFCAM Science Archive (http://wsa.roe.ac.uk) or the VISTA Science Archive (http://vsa.roe.ac.uk), depending on whether it was in the Northern or Southern sky respectively. The RMS coordinates were cross-matched with the catalogue data of the regions corresponding to each primary. The closest target to the inputted coordinates was initially assumed to be the primary, and a manual check was done for objects which had a significant separation between the coordinates of the RMS target and the UKIDSS target. In a few cases where a different point source had been selected instead of the primary, the primary was manually selected.

One issue with the point source catalogues was the existence of duplicated or saturated sources. Objects brighter than K=11-12 could potentially be saturated (according to UKIDSS and VVV documentation), with some exhibiting ring-like artifacts which then are registered as multiple detections around the ring. Also in rare cases, some non-saturated point sources are entered more than once in the UKIDSS point source catalogue (due to the existence of primary and secondary detections in the catalogue). To overcome this, the UKIRT and VVV catalogues have additional quality flags that allow for most of the saturated and duplicate objects to be removed from the analysis; some visual inspections had to be done afterwards to manually remove some outlying sources and ensure no false detections were still included.

To detect objects in the RMS images, a point source catalogue was constructed using the source detection program DAOphot (Stetson, 1987) along with Astropy (Astropy Collaboration et al., 2013; Price-Whelan et al., 2018). Objects with a brightness 3σ

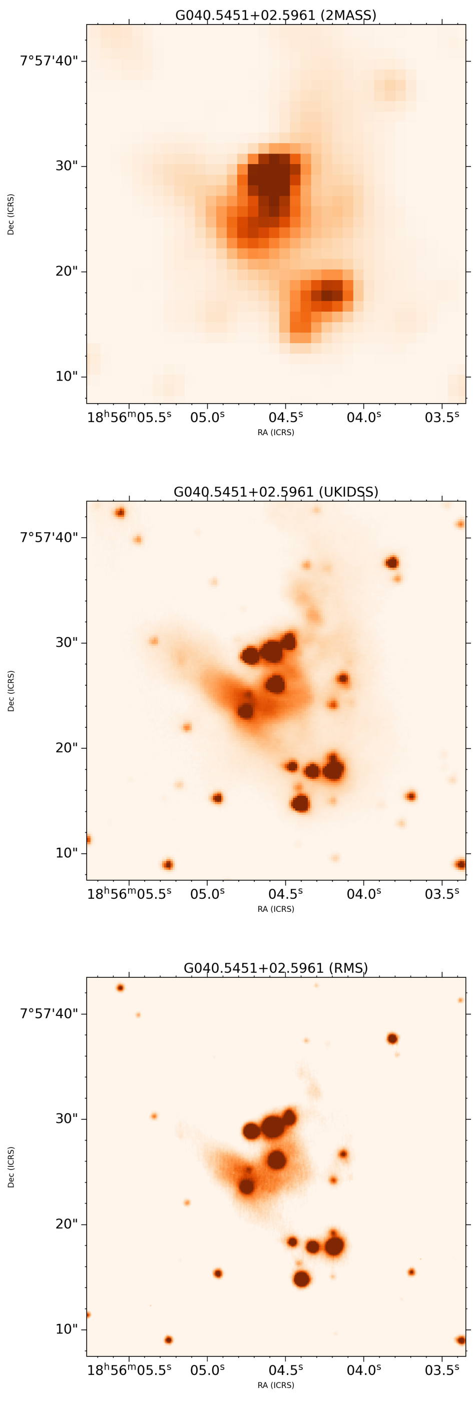

Figure 2.1: A comparison between 2MASS (top), UKIDSS (middle) and RMS (bottom) infrared K-band images for the YSO G040.5451+02.5961. The superior resolution of the RMS and UKIDSS/VVV images allows for the detection of companions which were previously unresolved in 2MASS.

above the image's background value were classed as true detections. DAOphot also provides estimates for the magnitude of each source along with its uncertainty, which were calibrated using UKIDSS K-band photometry. This calibration was verified by checking known UKIDSS magnitudes against DAOphot flux-calibrated magnitudes.

Pomohaci et al. (2019) used 2MASS photometry to calibrate magnitudes, however due to the relatively poor resolution of 2MASS the flux from multiple objects is sometimes erroneously interpreted as a single source; a good example of this is in Figure 2.1, where the four resolved bright objects in the centre of the RMS and UKIDSS images appear as a single luminous object in the 2MASS image. This is reflected in the 2MASS point source catalogue, as these four objects are grouped together as a single source with a presumable overestimate of the magnitude. UKIDSS is able to resolve objects almost as well as the RMS images, but has the added benefit of multi-colour information.

2.3.2 Completeness

To determine the completeness of the data, the limiting magnitude of the images was determined by injecting multiple artificial Gaussian sources of varying intensity and distance from the parent object into the images, using Astropy's Gaussian2DKernel function (Astropy Collaboration et al., 2013). For each image, four copies were created which then had $\sim$10 artificial sources injected into them; the results of the analysis for each copy were compiled together into a single data set for each image. These artificial sources were set to the same FWHM as the average seeing of the sources in the images. The minimum intensity at which the artificial sources would be detected by DAOphot would correspond to the limiting magnitude of the images; the distance was also varied to see how closeness to the central MYSO would affect this limit. A hindrance of detecting faint close-in companions will affect the accuracy of the companion statistics. The results for two objects can be seen in Figure 2.2, with the detected artificial stars shown in blue and the undetected artificial stars in red. It was concluded that in the

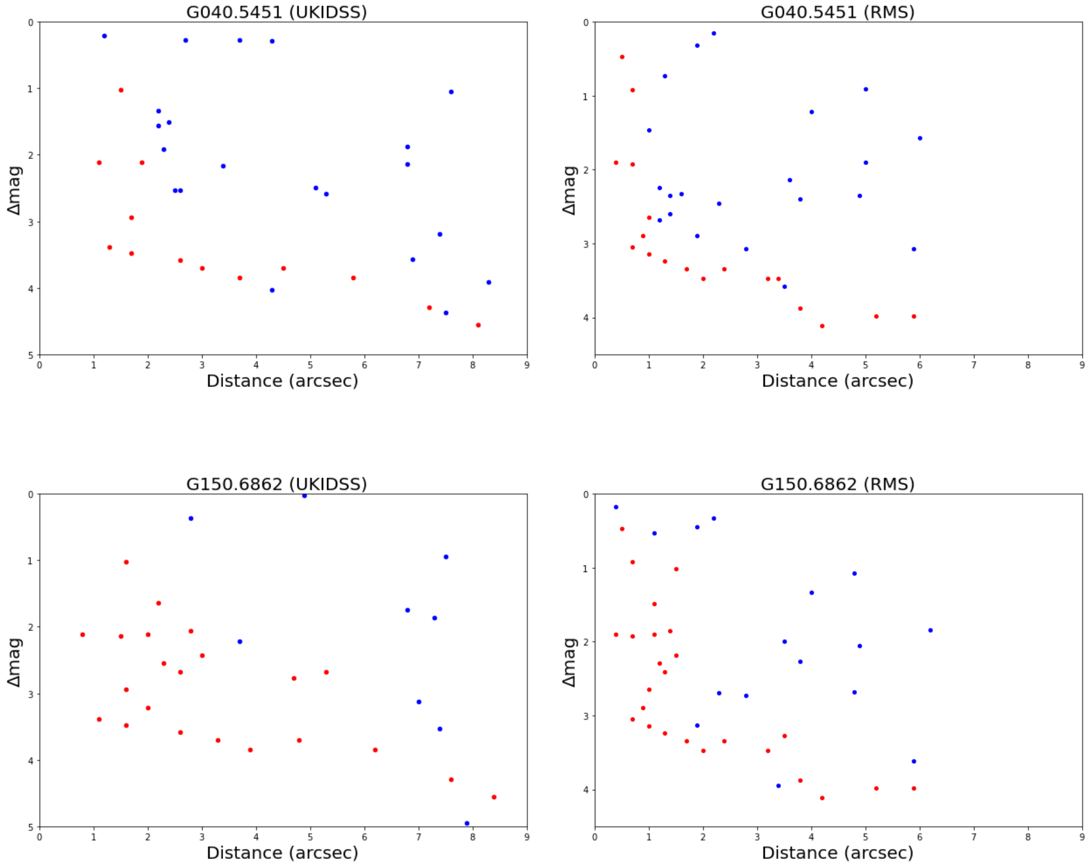

Figure 2.2: Artificial star analysis on two MYSOs, G040.5451+02.5961 and G150.6862-00.6887, for the UKIDSS K-band image and the corresponding RMS K-band image. The blue dots represent detected fake stars and the red dots show undetected fake stars.

RMS images, close-in binaries at distances within ~1.5 arcsec of the primary would not be consistently detected, and the limiting magnitude in these inner regions can increase to up to ~3 magnitudes brighter. This is due to extended emission or crowded regions leading to source confusion or obfuscation. At ~2 arcsec and beyond, the sensitivity improves and stars around 3.5 mag fainter than the primary are detected. Artificial star analysis was also performed on the UKIDSS/VVV images to show the difference in the detection ability of DAOphot for each survey. UKIDSS/VVV struggle more within 2 arcsec of the primary but perform similarly to the RMS images beyond that.

These comparisons demonstrated the benefits and caveats of each of these surveys: the RMS, UKIDSS and VVV surveys can probe deeper than the NaCo images used in Pomohaci et al. (2019), allowing fainter objects to be detected (the UKIDSS limiting magnitude is $K \sim 18.2$, making it the best tool for the faintest objects and a large improvement over the K=14 of the NaCo images). However, the NaCo images have a much better resolution meaning that objects within 1 arcsecond of the primary (or other nearby objects) may not be resolved in the RMS/UKIDSS/VVV survey data. The RMS image data takes the middle ground, having a better resolution than UKIDSS/VVV but worse than NaCo, and a slightly worse limiting magnitude than UKIDSS/VVV but better than NaCo. UKIDSS/VVV have the added benefit of full J-, H- and K-band photometry, providing more information on the companion candidates.

2.3.3 Visual binary probability

An important factor to take into account is the fact that any detected potential companion may simply be a chance projection on the sky, and not a physical binary. For each primary YSO, the density of background objects ρ within 1.5 arcminutes was assessed to quantify how many objects laid in the nearby line of sight. This was done by sorting every background object in the region by its $K-$band magnitude, and then determining the number of background objects brighter than each object (i.e. every object above the one in question) by the total observed area in arcseconds^2. This allows us to assign a background source density to each background object which effectively scales with the brightness of the object in question; a bright object amongst more numerous fainter sources is more likely to be a companion than a faint source among equally faint background sources. Therefore the likelihood of an object being a physical companion has three dependencies in total: a) the further away an object is from the primary, b) the fainter an object is in relation to background objects, or c) the denser the background, the less likely the object will be a physical companion.

The Poisson distribution (van Albada 1968; Correia et al. 2006, see also Halbwachs 1988) defines this probability:

$$P = 1 - e^{-\pi d^2 \rho} \tag{2.1}$$

where d is the distance from the primary to the potential companion in arcseconds and ρ is the background density of objects brighter than the potential companion in arcsec^{-2}. In this equation, the right-hand side is the probability that no sources from a random background are projected within the given radius d. The full 1.5 arcminute radius of the retrieved catalogue data was used to determine the background density. Spot checks were performed to ensure that the chance projection probability of objects scaled correctly with each of the different dependencies.

2.3.4 Physical companions

For each primary in the sample, objects in their neighbourhood were investigated to see if they could be classed as probable companions. The probability of each candidate being a visual binary was calculated using Equation 2.1, and those with $P_{chance} > 20\%$ were disregarded as probable chance projections. The multiplicity and companion fractions (MF and CF) were calculated for the potential companions detected within

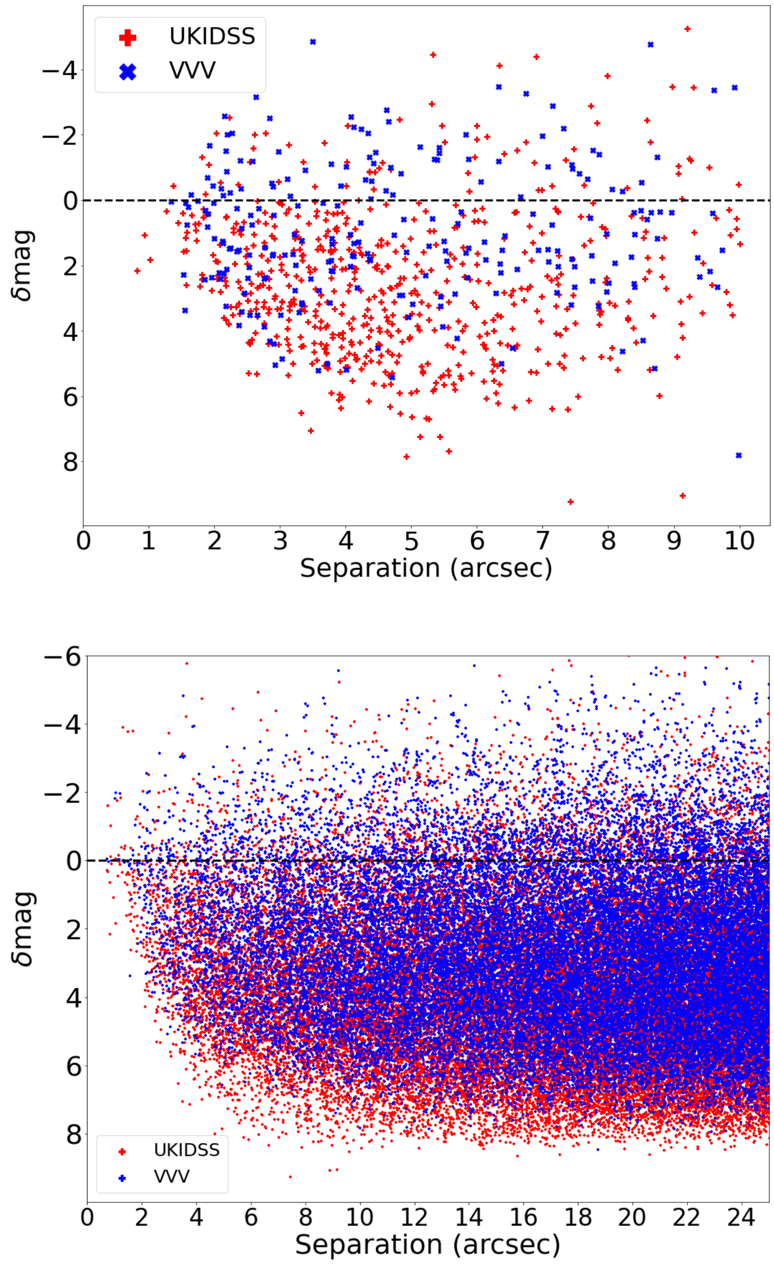

Figure 2.3: Top: Separation between the companion and its primary in arcseconds plotted against the $K-$band magnitude difference between the companion and the primary. The UKIDSS companions are shown with red crosses while the VVV companions are shown with blue pluses. It is also apparent that very few VVV objects have a δmag greater than 3, while numerous UKIDSS objects have δmag up to and greater than 6. Objects with δmag<0 are brighter than the primary. Bottom: the same plot but including objects with $P_{chance} > 20\%$ and to 25 arcseconds.

this limit, defined by the formulae: MF $= \frac{N_m}{N_{tot}}$ and CF $= \frac{N_b+2N_t+3N_Q+...}{N_s+N_b+N_t+N_q+...}$, where N_m is the number of multiple systems, N_{tot} is the total number of systems, N_s is the number of single systems, N_b is the number of binary systems, N_t is the number of triple systems, N_q is the number of quadruple systems, and so on.

A plot of the detectability of binary sources can be seen in Figure 2.3, showing how companion brightness relative to the primary (δmag) relates to proximity to the primary. A clear dearth of fainter detected sources is visible at <2 arcseconds, demonstrating that only the brightest objects can be detected at very close separations. Additionally, there seems to be a binary "sweet spot" with more companions between 3-6 arcseconds, and a drop-off at >7 arcsec. This drop-off can be understood when exploring Equation 2.1, as a fainter object at a large separation is much less likely to be registered as a probable binary companion at all. It therefore makes sense that companions of any brightness are more likely to be found at a mid-point, such as this "sweet spot".

10 arcseconds was the chosen upper limit for companion detection because there is a distinct flattening in the number of objects in the field beyond this point in each of the samples; this is where the random distribution of background stars is being probed. Distances larger than this upper limit were tested in order to ensure that the method was not overly sensitive to small clusters or other small-distance effects.

A table of all companions detected in the IR surveys is presented in Table B.1. The multiplicity fractions for each sample can be found in Table 2.1. A histogram showing the number of detected companions depending on their separation is shown in Figure 2.4. I investigate these findings further in Section 2.4.

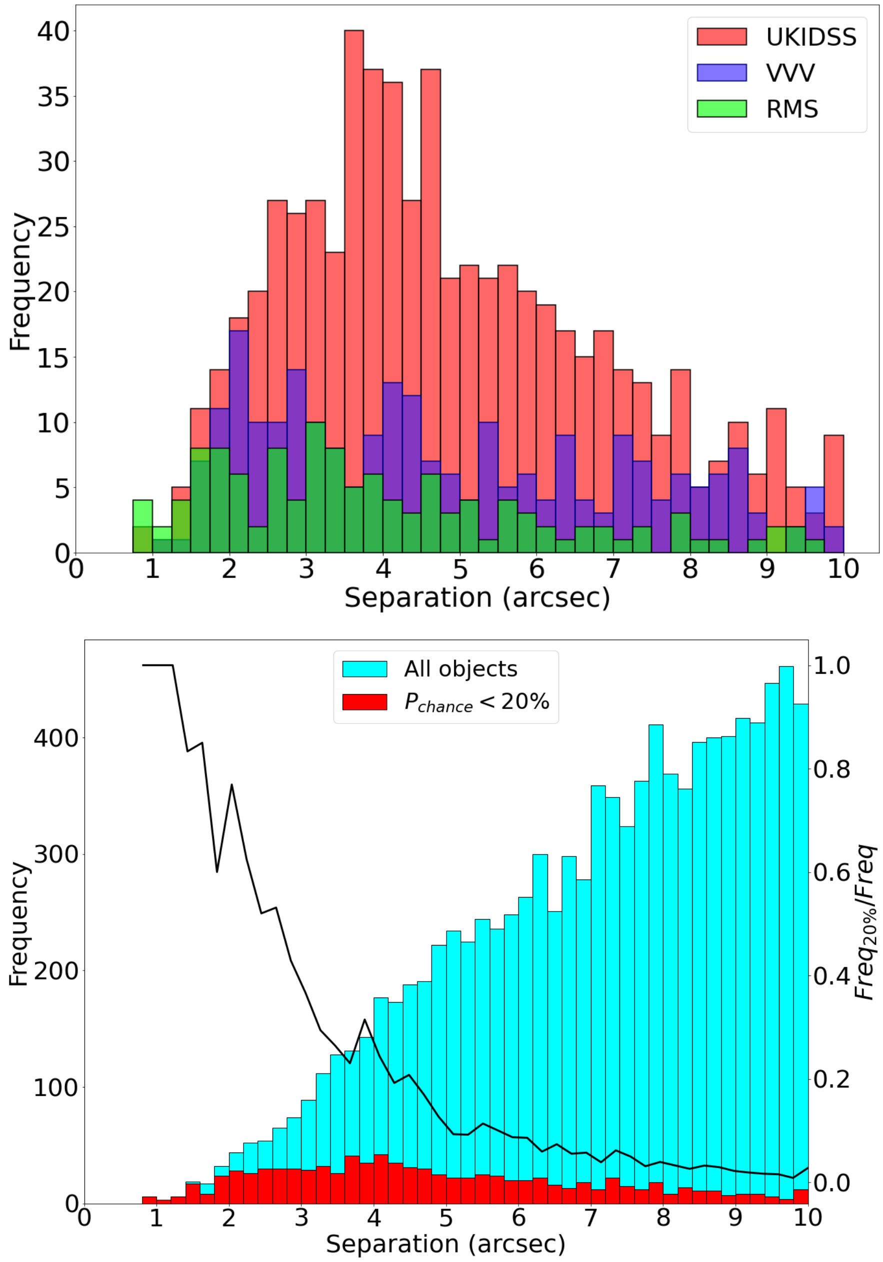

Figure 2.4: Top: a histogram of the separation between the detected companions and their primaries. Bottom: a histogram of the separation between all detected companion candidates and their primaries. The red objects have a P_{chance} less than 20%. The black line represents the ratio between the frequency of $P_{chance} < 20\%$ objects and the whole sample at each separation.

Table 2.1: Multiplicity results for each sample, separated into subsets based on YSO mass. The uncertainties are determined through binomial confidence intervals.

Sample	Subset	MF (%)	CF (%)
UKIDSS	All	65 ± 4	147 ± 6
	High-mass	67 ± 5	
	Low-mass	66 ± 6	
VVV	All	53 ± 4	84 ± 5
	High-mass	54 ± 8	
	Low-mass	54 ± 5	
UKIRT/RMS	All	64 ± 8	139 ± 9
	High-mass	60 ± 11	
	Low-mass	69 ± 14	

2.3.5 Mass ratios

Primary YSO masses were determined using the bolometric luminosities from the RMS catalogue[1] along with mass-luminosity relations from Davies et al. (2011). To determine the ratio of masses between a primary and its companions, previous studies have used the K-band magnitudes as a proxy for companion masses under the assumption of them being an MS star, once corrected for extinction (Oudmaijer and Parr, 2010). In Pomohaci et al. (2019) lower and upper limits for binary mass ratios were determined using both the foreground extinction and primary 'total' extinction (foreground + circumstellar extinction) respectively, from extinction maps and comparing with expected colours.

This is taken a step further as I estimate mass limits for YSO companions across the entire RMS catalogue. The multi-colour information available in the UKIDSS/VVV point source catalogues allows estimations of the total extinction of the companion itself.

The dust map chosen for the foreground extinction estimates was Bayestar19 (Green

[1]The primary YSO luminosities and masses used in this chapter are from an older version of the RMS catalogue; later chapters use the most recent version of the catalogue as of June 2023.

et al., 2019), a three-dimensional map of dust reddening across most of the Galaxy. However, Bayestar19 does not cover the Southern sky at $\delta < -30$. For these objects, dust maps of Stilism (Capitanio et al., 2017) were instead used, which cover the whole Galactic plane but have a lower distance cutoff than Bayestar19. Therefore Bayestar19 was used as the main dust map, while Stilism was used for the regions that Bayestar19 does not cover.

To determine the total extinction towards a companion, $J - H$ photometry from UKIDSS and VVV was used to estimate A_V as in Cooper et al. (2013), where the photometry was compared to the expected colours of a MS B0 star. Not every YSO in UKIDSS and VVV has $J-$band photometry; where $J-H$ photometry was unavailable, $H-K$ was used instead. Once the companion's $K-$band photometry was corrected for extinction, the distance to the primary was used to convert from apparent to absolute (K_{abs}) magnitude; the distances were retrieved from the RMS catalogue. Using the K_{abs} estimates found through the foreground A_K, the total A_K to the companion and the total A_K to the primary, estimates of the companion mass could be determined using the main-sequence assumption of Oudmaijer and Parr (2010):

$$log(M/M_{\odot}) = -0.18K_{abs} + 0.64 \tag{2.2}$$

Using the same method as Oudmaijer and Parr (2010), the $J-$band magnitude could also be used as a proxy for the mass:

$$log(M/M_{\odot}) = -0.16J_{abs} + 0.65 \tag{2.3}$$

Using the primary mass determined from the RMS luminosities, estimates of the mass ratios could then be made. The mass ratio estimates for each companion can be found in Table B.1.

2.4 Results & Discussion

2.4.1 Statistical differences in surveys and galactic regions

The companion statistics vary when comparing the UKIDSS and VVV surveys with each other (see Table 2.1). The existence of these differences is counter-intuitive as the surveys are highly comparable, however when comparing different regions of the galactic plane, there is variation in the statistics of the UKIDSS survey alone. It is good to keep in mind that a physical binary has a larger chance of being identified in a lower density region than a higher density region. When considering the inner Galaxy, the stellar background appears more dense, and so according to Equation 2.1 the YSOs in this region are less likely to have companions. Conversely, when looking towards the outer Galaxy the stellar background appears to be less dense. This will increase the likelihood of nearby objects meeting the criteria of a physical companion and therefore driving up the observed multiplicity fraction.

Figure 2.5 shows the different regions of the Galaxy and the surveys that probed them. The outer section of the Galactic plane was surveyed by UKIDSS and has a binary fraction of 91%. The Northern inner part of the Galaxy, also surveyed by UKIDSS, has a binary fraction of 55%, much lower than the outer galaxy. The UKIDSS inner region aligns statistically with the VVV fraction of 53%, which only surveys the Southern inner galaxy. This shows that the outer, less dense region of the Galaxy as surveyed by UKIDSS is responsible for the significantly larger binary fraction in UKIDSS compared to VVV, and that a large number of objects are missed in the inner Galaxy due to observational bias.

2.4.2 Multiplicity statistics

Despite the similar limiting magnitudes and resolutions between UKIDSS and VVV, the MF and CF of the VVV sample are significantly lower than that of the UKIDSS

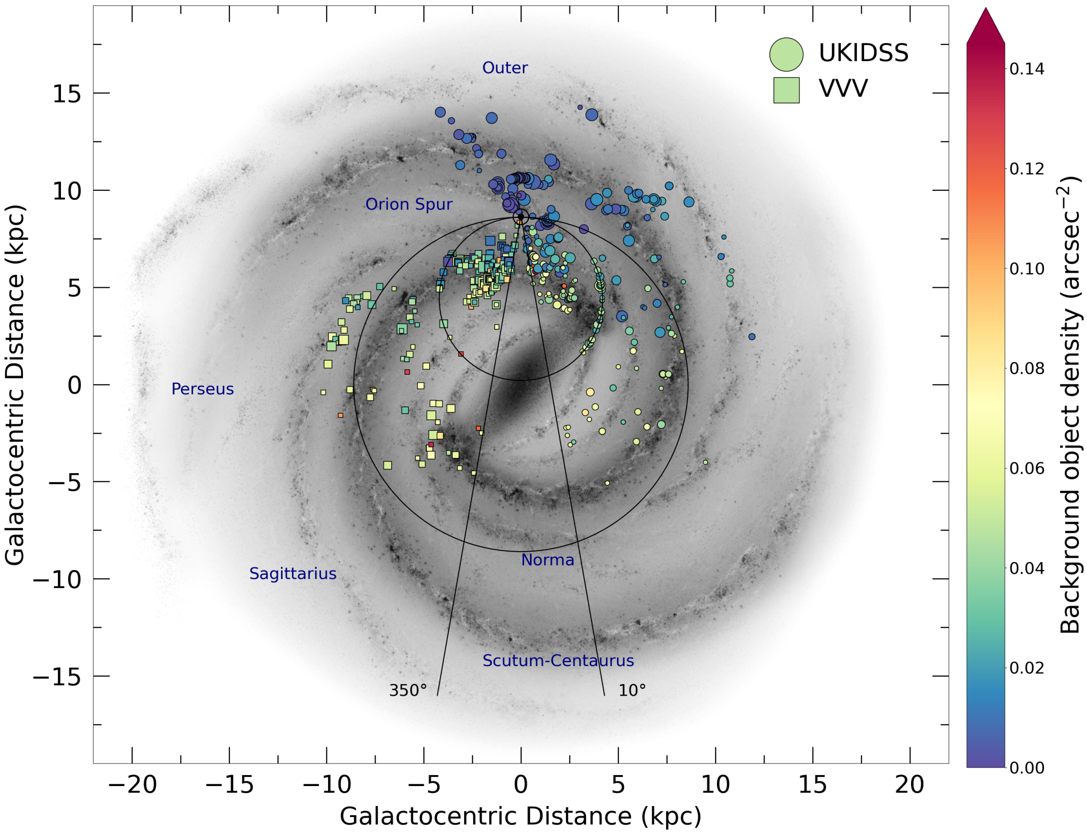

Figure 2.5: A diagram of the Galactic plane showing the position of the YSOs in the UKIDSS (circle) and VVV (square) samples. The larger ring represents the Solar circle and also shows the divide between the 'inner' and 'outer' Galaxy. The points are coloured based on the YSO's surrounding background object density, and also are sized depending on the number of detected companions; larger points are YSOs with more companions. The two black lines show the Galactic centre region which was not included in the RMS survey due to confusion regarding the sources and their distances.

sample (and the RMS imaging sample). As mentioned above, this can be attributed to differences in survey background density. When accounting for this by only including the 'inner' region of UKIDSS with similar average background density to VVV, the multiplicity fractions of the two samples are within agreement, showing uniformity between the two samples. Across the UKIDSS and VVV surveys, the detected companions have a mean angular separation of 4.8", with a minimum of 0.8", a maximum of 9" and a standard deviation of 1.9". The companions have a mean physical separation of 17900 au, ranging from 910-121,000 au with a SD of 15500 au.

Although the MF of the RMS imaging sample is within the uncertainties of that of the VVV survey, the CF is significantly higher. This can once again be explained by the survey density discrepancies mentioned above leading to more companions being detected in the 'outer' regions.

The average $H-K$ colour of the companions is 1.4, compared to nearby field stars which have an average $H-K$ of 0.6. The companions are redder than surrounding field stars, supporting their status as companions. When considering $J-H$, the same conclusion applies (1.5 and 1.2 respectively).

The effect of primary mass on a YSO's multiplicity can be seen in Figure 2.6. It is clear that the primary YSO mass does not have a significant effect on whether the YSO forms at least one companion, save for a relatively small peak between 5-12 $M_{\odot}$ which can be accounted for by the uncertainty. Therefore it can be asserted that primary mass does not affect whether a companion is formed during the birth of a star. However it is apparent from the bottom plot of Figure 2.6 that the frequency of companions per system drops off $\sim 10\ M_{\odot}$.

The fractions calculated for all three of the high-mass subsets are higher than that in Pomohaci et al. (2019), which gave MF $= 31\pm8\%$ and CF $= 53\pm9\%$ for their sample of MYSOs. However this is due in part to the improved magnitude depth of these samples over the NaCo sample, meaning fainter companions not picked up by Pomohaci are more likely to be detected in the IR surveys or the RMS images. Also the separations probed in each sample are different; the NaCo survey was able to probe closer to the primaries but it was only complete out to 3 arcseconds, as opposed to 10 arcseconds in this survey. By using the survey limits of Pomohaci et al. (2019) with this survey, a like-for-like comparison can be made. A separation limit of 3 arcsec and a magnitude limit of 4.5mag fainter of the primary were used to match the two surveys. At these limits, fractions of MF $= 38 \pm 7\%$ and CF $= 48 \pm 7\%$ were calculated, which are well within the uncertainties of the Pomohaci et al. (2019) survey. The inner 0.6 arcsec

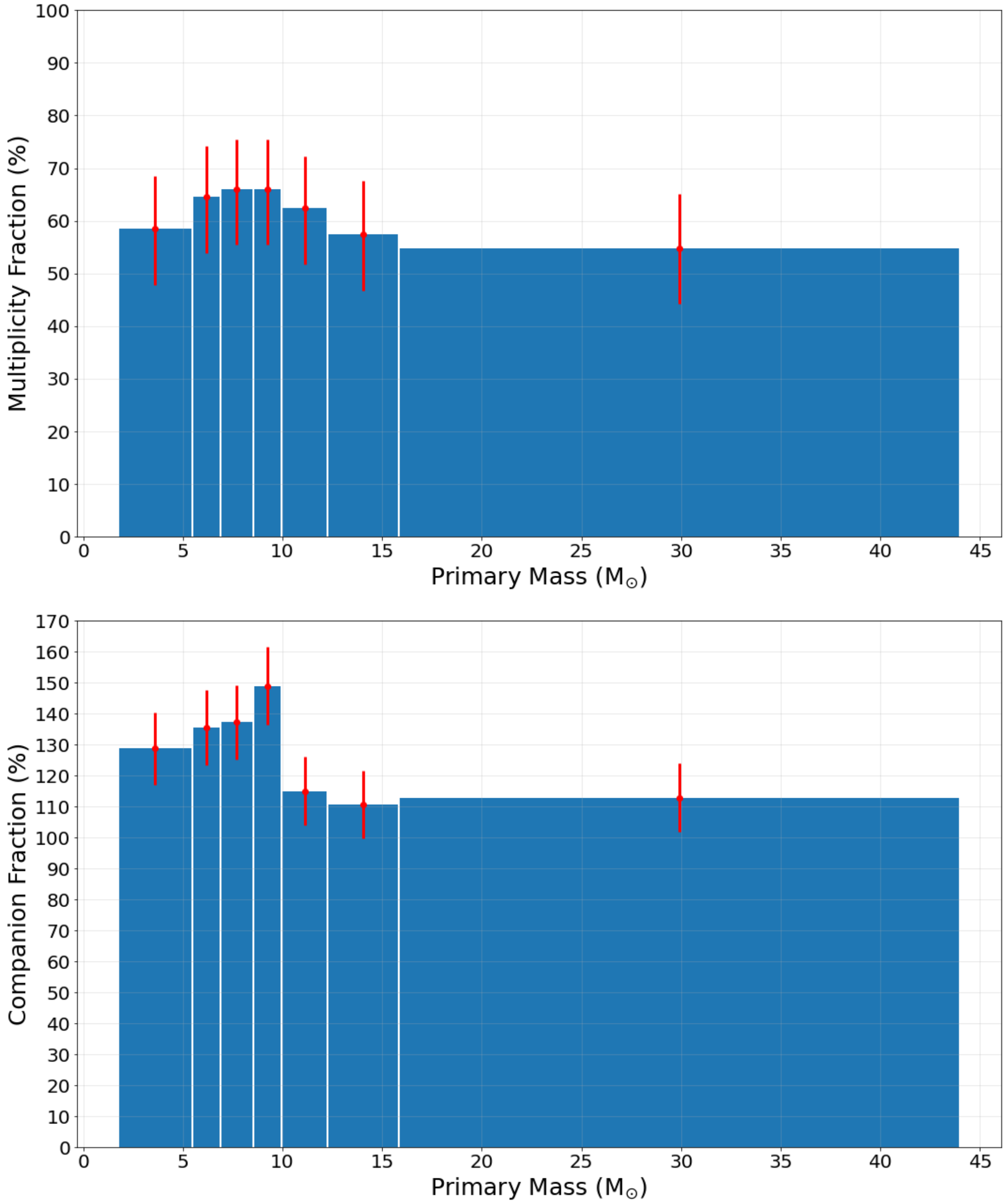

Figure 2.6: Top: The multiplicity fraction of different primary mass bins. Each bin contains an equal number of objects. The red error bars are derived from binomial confidence intervals. This shows a relatively flat distribution, and demonstrates that multiplicity generally is not affected by primary mass. Bottom: The companion fraction of different primary mass bins. Here there seems to be a marked drop-off in the number of companions formed per system around 10 $M_{\odot}$.

of the Pomohaci sample contains no companions, which aligns with the fact that the closest detected companion here is at 0.8". This suggests that there may be a dearth of close-in MYSO companions, however future work will probe the inner regions of MYSOs using spectroscopy to determine the true binary fraction at these separations.

A recent interferometric MYSO survey by Koumpia et al. (2021) found a binary fraction of 17±15% in a sample of six MYSOs between ∼2 and 300 au, a lower fraction than reported in this work; however their separation range is smaller and the observational technique used has biases.

Previous surveys have also investigated binarity in massive stars. Sana et al. (2012) studied the multiplicity of O and B main-sequence stars and found them to have a MF = 70 and 52%, and CF = 130 and 100%, between 2-200 au. Oudmaijer and Parr (2010) found that a sample of B stars and a sample of Be stars had binary fractions of 29 ± 8% and 30 ± 8% respectively at separations between 20-1000 au. Looking at more recent surveys, Banyard et al. (2021) studied binarity in B-type stars in the young open cluster NGC 6231 and found a binary fraction of 52 ± 8% when correcting for observational bias, agreeing with the MF found here. Bordier et al. (2022) found a MF of 100% from a sample of young O-stars within 120au, which is much higher than the binary fraction determined here but also probes much closer separations.

Direct comparison between these surveys is not an easy task due to significant differences in separations probed, as well as the observational conditions, sensitivities and techniques used, as well as the differences in evolutionary status. The resolution of the data used here means that the inner ∼1-1.5 arcsec of each YSO is essentially a blank spot, and so it is not possible to probe regions in which other surveys have found varying levels of multiplicity.

Compact groups of objects have a complicated distinction between a multiple system and a cluster. When considering the IMF, it is expected that MYSOs will largely be in clusters. The binary systems found here are most likely physical but in terms of higher order systems such as quadruple systems, these are harder to distinguish from compact clusters. Further investigation is required on higher order systems in order to determine whether they should be classified as clusters.

To conclude, the multiplicity fraction of the YSOs investigated here agrees with previous MYSO multiplicity studies at similar separation ranges, and generally agrees with previous studies into the binarity of B stars.

2.4.3 Mass ratios

The total extinction (a combination of foreground and circumstellar extinction) towards the primaries was estimated in a similar fashion to Pomohaci et al. (2019), and these values were compared to the extinctions estimated in Cooper et al. (2013), where a good agreement was found. However, the extinction towards the companions themselves are the favoured mass ratio estimates as they provide a more accurate correction for the $K-$ and $J-$band magnitudes of the companions, especially ones at larger separations which are unlikely to share the same extinction as their primary.

A histogram of the mass ratio distribution can be found in Figure 2.7. Here the mass ratio is defined as $q = M_{comp}/M_{prim}$, where M_{comp} is the mass of the companion and M_{prim} is the mass of the primary. Using the $K-$band estimation of foreground extinction ($A_{K,fg}$), the average mass of the companions is 6 $M_{\odot}$ and the average mass ratio is 0.5. Using the total extinction ($A_{K,tot}$), I find an average companion mass of 12 $M_{\odot}$ and an average mass ratio of 1.3. A significant fraction of companions have a mass ratio $q > 0.5$.

When instead using the $J-$band as the proxy for companion masses, I find that the average companion masses and mass ratios are smaller than for the $K-$band estimates of foreground extinction (3 $M_{\odot}$, $q = 0.3$) and total extinction (11 $M_{\odot}$, $q = 1.6$). This is likely to be due to excess emission from hot dust in the $K-$band causing an

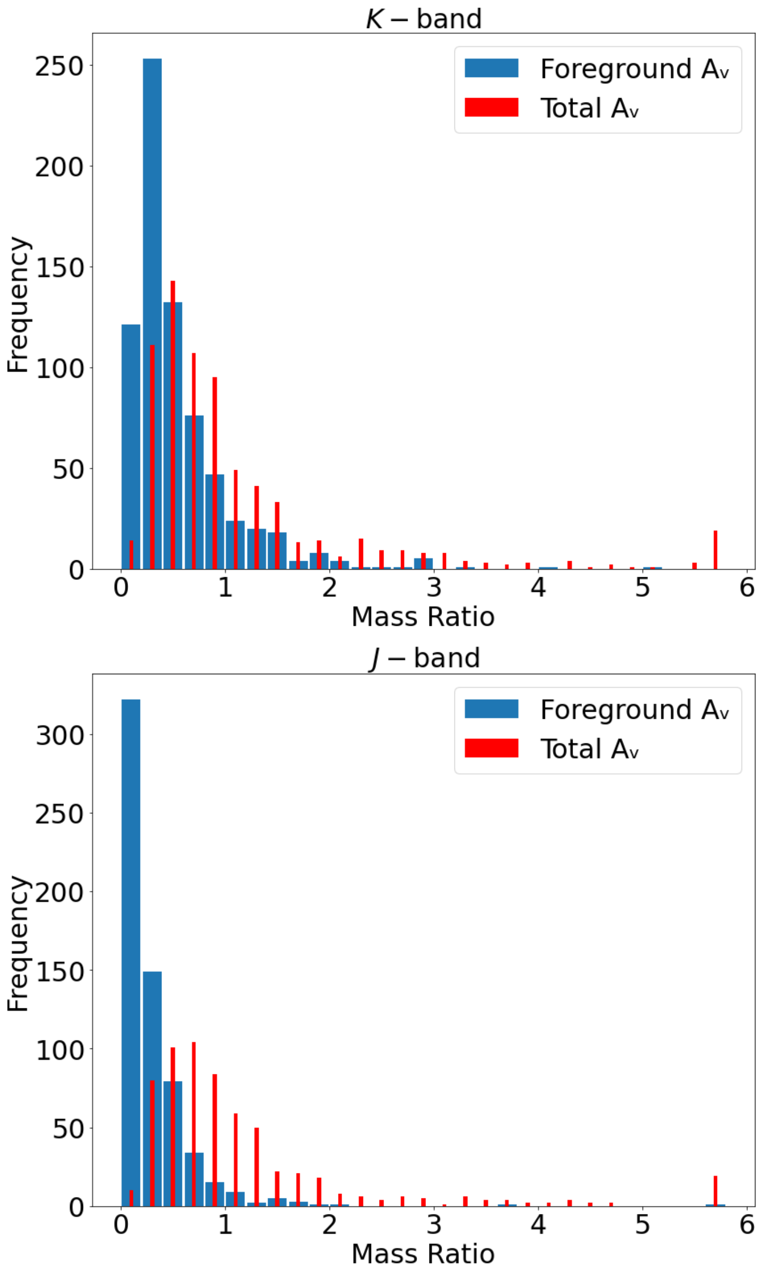

Figure 2.7: A histogram of the mass ratios of the detected companions with $P_{chance} = 20\%$. The thick blue bars represent the mass ratios determined using only foreground extinction, while the thin red bars show the estimates using total extinction. For triples/higher order systems, each companion is included against its primary. Only objects with both extinction estimates are shown. Objects with mass ratios > 6 are collected in the last bin.

overestimation of the extinction and therefore the mass.

The masses determined for the companions are simple estimates from Equation 2.2, which assumes the star is a MS star as well as the fact that the entire $K-$band brightness is a result of photospheric emission. Companions generally have large mass ratios (>0.5), especially from $A_{K,tot}$ estimates. Mass ratios significantly greater than 1 are likely due to excess emission leading to mass overestimates. The errors on the mass ratios are of order ∼20%, mostly as a result of uncertainty in the bolometric flux of the objects (Mottram et al., 2011). Distance uncertainty is insignificant when taking the mass ratio as the same distance uncertainty applies to both the primary and secondary.

This proportion of mass ratios suggests an inconsistency with the binary capture formation scenario, which favours low mass ratios (Salpeter, 1955). Moe and Di Stefano (2017) found MS mass ratios consistent with random IMF sampling at large separations (similar to the separations probed here) but large mass ratios for close binaries. This also leads to a potential situation where the distribution of secondary separations in MYSOs may not be constant, and changes over time. Migration could be an explanation for this, as Ramírez-Tannus et al. (2021) suggest that stars may form in wide binary systems and migrate inwards over time to form tighter pairs.

More accurate estimates for extinction could be made using infrared excess determinations (e.g. through SED fitting, Frost et al., 2019) but the very large sample size used here would make this a long process; this is therefore outside of this work's scope.

2.4.4 Are binary MYSOs significantly different?

To see whether binarity has an effect on an MYSO, the samples were studied to look for differences in the properties of single MYSOs and MYSOs with one or more companions.

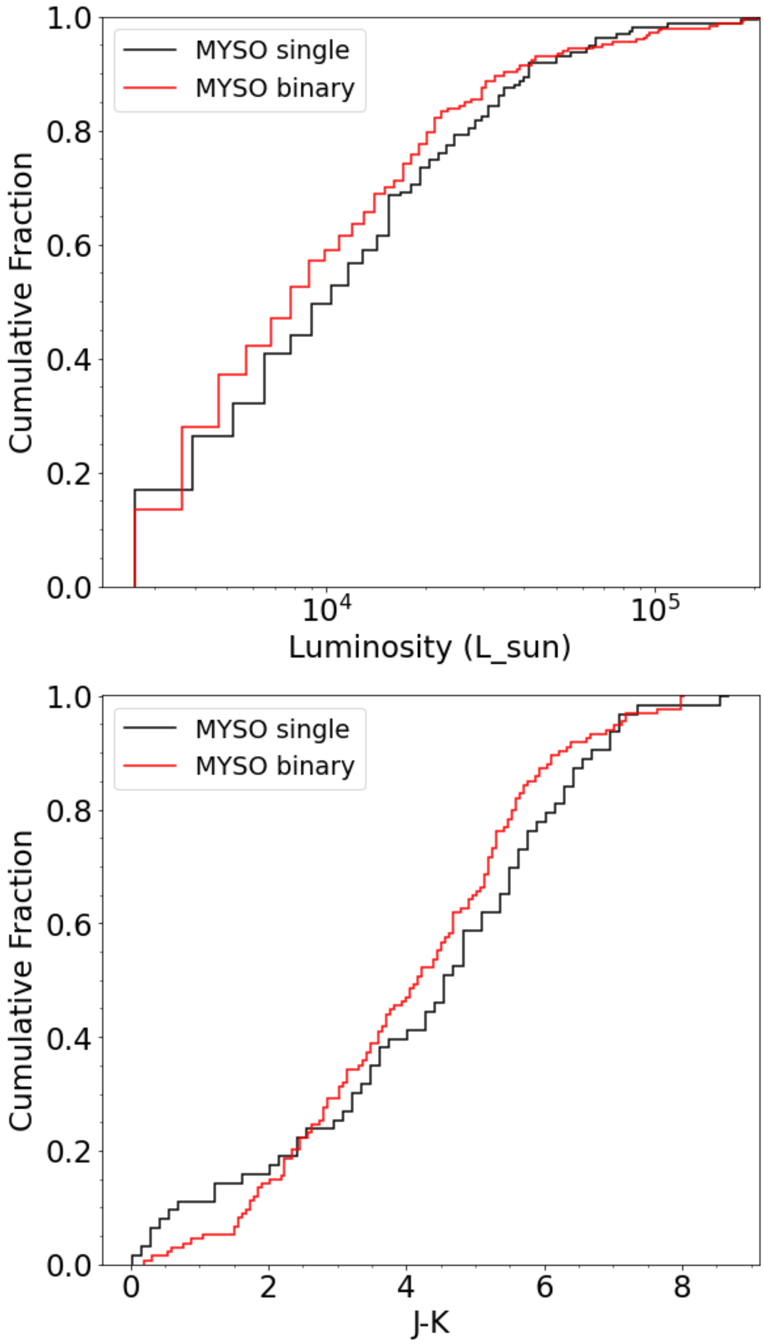

Figure 2.8: The cumulative distribution of (a) luminosity and (b) J-K colour in the MYSO primaries. Single MYSOs are represented by the solid black line and binary MYSOs are represented by the dashed red line.

For single MYSOs, the average luminosity is 19000 $L_{\odot}$ and the average distance is 6.7 kpc. The average luminosity of binary MYSOs is 18000 $L_{\odot}$, with an average distance of 5.7 kpc. For comparison, the entire sample of UKIDSS/VVV MYSOs has an average luminosity and distance of 19000 $L_{\odot}$ and 6.1 kpc respectively. Additionally, the whole YSO population of the RMS catalogue has averages of 18000 $L_{\odot}$ and 5.9 kpc. Kolmogorov-Smirnov (K-S) two-sample tests were performed to see whether the single and binary MYSO samples could be deemed to come from the same population. For the luminosity distribution, the K-S statistic was 0.08 and it was judged that there is a 58% chance that the single and binary stars were drawn from the same distribution. The K-S test was also performed with respect to distance to the primary MYSOs, and resulted in a K-S value of 0.11 and a P-value of 0.18, also indicating a similar distribution. Therefore there appears to be no significant difference in the distribution of luminosity or distance of primary MYSOs with companions or without them.

A K-S test for luminosity in the UKIDSS and VVV surveys concluded that there was no significant difference between the luminosity distributions in either survey. The cumulative distribution of luminosity in the sample can be seen in subplot (a) of Figure 2.8. When the same test was performed for distance it was apparent that they were not drawn from the same sample; however this may be a result of the different regions of the sky that UKIDSS and VVV target (discussed in Subsection 2.4.1). UKIDSS targets objects in both the inner and outer galactic spiral arms, with peaks in object frequency at ∼1.5 and ∼5 kpc. VVV focuses on primarily the inner regions of the galaxy, with a peak at ∼3.5 kpc. It is therefore reasonable to assume that this is why the K-S test deems them to have separate distance distributions.

Subplot (b) of Figure 2.8 shows the cumulative distribution of the $J - K$ colour of the MYSOs, separated into both single and binary systems. A K-S test resulted in a P-value of 0.26, indicating that the binary and single MYSO primaries share the same distribution. The binaries appear to be slightly less red in general compared to the singles, implying a lesser extinction which may have allowed companions to be detected more easily.

2.4.5 Total multiplicity

The multiplicity statistics found here are limited by the observations. The companions found lie at separations ranging from $\sim 10^3$-10^5 au, and companions at smaller separations than this will not be resolved in the UKIDSS, VVV or UKIRT/RMS data due to the spatial resolution. Additionally, the quality of the observations between the surveys are not constant, with selection effects arising due to varying observing conditions. With magnitudes being the only method of determining masses, the uncertainties on the mass ratios are high. However, these results significantly improve on the first MYSO multiplicity survey of Pomohaci et al. (2019), with a larger sample size and an improved method of determining mass ratios.

These restrictions suggest that a significant number of companions may be being missed. Almost all of the MYSOs are expected to have a companion within 10^3 au which is not being observed (see Offner et al., 2022 and references therein). It is therefore possible that a wide tertiary component is being detected in a large number of these observations.

To estimate the unaffected, unbiased total multiplicity fraction, Monte Carlo simulations were performed using an artificial binary population, having applied the same selection effects as the observations. The following method is explained in detail in Houghton (2023). Underlying distributions of a lognormal semi-major axis distribution and a flat eccentricity distribution were assumed. The simulations draw the instantaneous orbital properties of the true anomaly, the inclination of the system, and the relative orientation of the system relative to the observer randomly (such that the inclination is distributed as sin i and the true anomaly is uniformly distributed in time). By using these orbital properties along with the distance distribution of the observed sample, the separation in arcseconds of each artificial companion could be calculated. The simulations also draw a magnitude difference between the primary and the companion from a normal distribution which is truncated at the minimum and maximum observed δmag values. Due to this truncation, at higher standard deviations the δmag distribution appears flat which allows models with a flat uniform δmag distribution to also be included.

The selection effects from the observed sample were applied to the artificial sample, including the gradual decrease in binary detections below ~2 arcseconds and the corresponding limiting magnitudes. An artificial background density was generated and this was used to assign each binary a value of P_{chance} as from before.

The results of the models were compared to the observed YSO separation and δmag distributions. In the top panel of Figure 2.9 the results of the best fitting simulation are shown, along with a comparison of a distribution of $\sim 10^4$ simulated systems in grey, to the actual data in red. Above and to the right of this plot are histograms of the simulated (grey) and real (red) data distributions.

The resulting models imply an extremely wide separation distribution is required for the detected companions, peaking at $\sim$ 9000 au. In reality, it is expected that the observed separation distribution would be ~85-90 per cent lower than the semimajor axis distribution, but a population of binaries with a semimajor axis distribution only slightly higher than the separation distribution would be heavily weighted towards small separations compared to the observed sample.

As companions are regularly found at 10-100s of au around MYSOs, this suggests that the observed phenomenon is either the extremely high separation tail of the binary distribution or a vast number of triple companions to binaries too close to be resolved. MYSOs frequently form as triple systems: a primary MYSO with a close companion and a wide companion. The difference in semimajor axis between the two companions

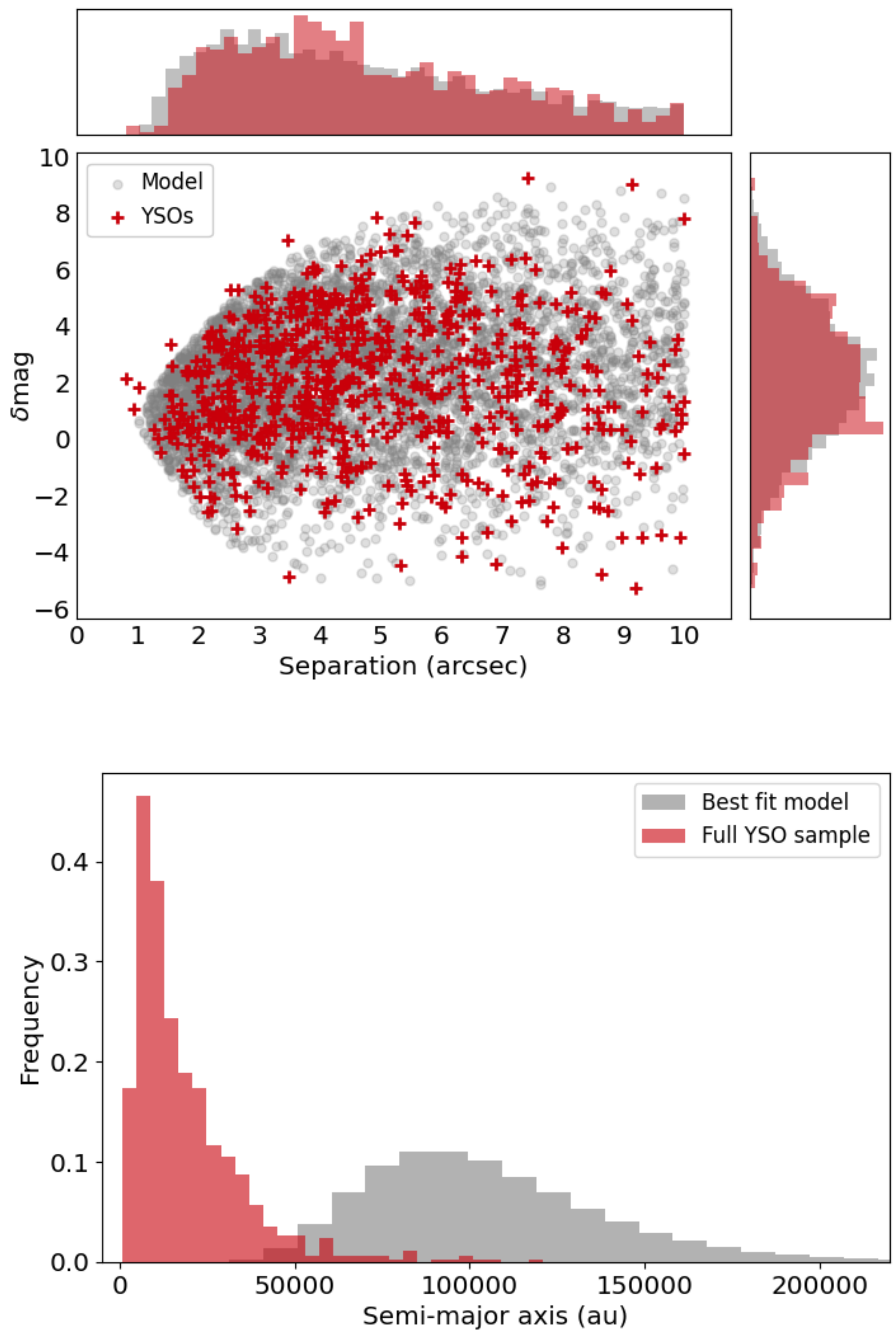

Figure 2.9: Top: comparison of the separation vs δmag distribution from the best fit binary population model (grey) and the combined YSO sample (red). Bottom: the intrinsic semi-major axis distribution of the binary population from the best fit model (grey) compared to the separation distribution in au from the YSO sample.

is sufficient to keep the system stable; if the wide companion were closer in, the system would likely break up. Due to the limitations of these observations, only the wide companion can be detected, explaining the wide companion distribution needed for the Monte Carlo models.

These models also suggest that only $\sim 1-3$ per cent of all binaries would have been observed when taking the observational biases and selection effects present in this sample into account. This provides further evidence that the large separation tail of the binary/triple distribution may be being observed; if ~99 per cent of companions are much closer than the mean separation of 17900 au, which is likely, then they would not be detected through these methods.

The trends found for the best fit binary population model of the entire YSO sample (very high separation and low multiplicity fraction) as presented in Figure 2.9 also apply to the MYSO sample.

This presents an interesting conclusion: not only do up to 100% of MYSOs exhibit multiplicity, but a significant fraction of MYSOs (possibly up to 100%) form in triple systems. As it has been previously stipulated that up to 100% of massive stars form in binary systems (Chini et al., 2012), this work suggests that these objects are frequently found with a higher order of multiplicity than originally thought.

2.5 Conclusions

I have investigated the binary properties of 683 YSOs (402 of which are MYSOs) across the RMS catalogue using UKIDSS and VVV point source data, and a sample of 88 YSOs were investigated using K-band RMS images. Using statistical methods, the probability of companions being real rather than chance projections was used to determine the multiplicity statistics of the sample.

1. For the RMS-wide sample using UKIDSS/VVV data, the fractions are MF =

$65 \pm 4\%$ and CF $= 147 \pm 6\%$ for the UKIDSS sample, and MF $= 53 \pm 4\%$ and CF $= 84 \pm 6\%$ for the VVV sample. These agree with previous YSO multiplicity studies at similar separation ranges.

2. The multiplicity statistics for the sample of 88 YSOs investigated with the RMS UKIRT images are MF $= 64 \pm 8\%$ and CF $= 139 \pm 9\%$.

3. A large fraction of companion mass ratios are larger than 0.5.

4. There appear to be no significant differences in binary and single YSO properties.

5. Primary YSO mass does not have any significant effect on multiplicity.

6. The total multiplicity fraction of MYSOs is $\sim$100%, with a large fraction of these likely to be at least triple systems.

This is one of the first studies, and so far the largest, looking specifically at MYSO multiplicity. Future spectroscopic observations will be paramount in learning more about the identified companions, including classifying their spectral types and investigating their environments.

Chapter 3

Spectroscopic MYSO binaries: looking for radial velocity variations

3.1 Introduction

As explained in Chapter 1, multiplicity is an integral factor in the formation of massive stars, and binarity characteristics are set early on in a massive star's lifetime (Mathieu, 1994; Duchêne and Kraus, 2013). Up to 100% of OB-type stars are thought to be in multiple systems (Chini et al., 2012). Studies suggest that the most likely binary formation scenarios are fragmentation during core collapse for larger (>100 au) separations (Krumholz et al., 2012; Myers et al., 2013), with accretion disc fragmentation or orbital decay through interactions (e.g. magnetic braking, stellar capture) responsible for closer (<100 au) binary systems (Meyer et al., 2018; Lund and Bonnell, 2018). To study massive star binarity in more detail, studies at the pre-main-sequence (PMS) phase are key; however there are some significant barriers to studying the binarity of young stellar objects: they are embedded in their own natal dust clouds, which renders most of them effectively invisible unless observed in the infrared. Also they tend to form at large distances (generally at kpc distances), making direct imaging of close binaries difficult. In this chapter, close binaries are the focus.

Apai et al. (2007) studied the close binarity of young massive stars using near-infrared spectra and found that at least 20% were radial velocity variable. Moe and Di Stefano (2017) investigated the relation between binary separation and mass ratio in O- and B- type stars, finding that very small separations ($\lesssim$ 0.4 au) favour mass ratios of $\sim$0.5, while separations of around 10 au result in smaller mass ratios ($q \sim$ 0.1-0.2). Gravity Collaboration et al. (2018) found a binary fraction of 100% from 16 MYSOs, with mass ratios declining with primary mass. Koumpia et al. (2019) presented an interferometric and spectroscopic study of two MYSOs, PDS 27 and PDS 37, using $H-$band observations from VLTI/PIONIER and VLTI/X-shooter. They found that both MYSOs had companions within tens of au, making these some of the closest and most massive MYSO companions ever spatially resolved. Later, the interferometric survey of MYSOs in the K-band from Koumpia et al. (2021) was the first of its kind and found MF$=17 \pm 15$% for six MYSOs at separations of 2-300 au.

To probe the closer-in parameter space not covered by imaging or interferometry, I aim in this chapter to investigate binarity at much smaller separations using multi-epoch $K-$band spectroscopy from two sources: IGRINS for high spectral resolution, and X-shooter for medium spectral resolution. A particularly useful emission line in the $K-$band is the Brackett gamma (Brγ) line at 2.166 μm, due to its strong nature and because it is almost unaffected by telluric absorption. In MYSOs, Brγ is commonly one of the brightest features.

The Brackett series of hydrogen recombination lines trace ionised gas from stellar winds in the near-infrared (as modelled by Simon et al., 1981), making it a common indicator of MYSOs. The profile of the lines can provide an insight into the nature of the emission region. Cooper et al. (2013) investigated 247 RMS survey objects, 131 of which were MYSOs, using emission lines such as Brγ and CO bandhead. The majority of MYSOs exhibited Brγ emission, while others showed P Cygni or inverse P Cygni profiles, suggesting outflow or infall respectively. Additionally Brγ line luminosities indicated there may be a case for massive star formation as a scaled-up version of low-mass formation scenarios. Pomohaci et al. (2017) investigated the Brackett series of a sample of 36 MYSOs and found similar conclusions, while also finding Brγ/Br12 line ratios which may suggest the presence of various types of stellar winds.

A word of caution: YSOs are known to exhibit variability; for example, YSOs with discs can be seen to vary in both brightness and CO emission due to changes in accretion rate (Ilee et al., 2018b; Lakeland and Naylor, 2022). Additionally, circumstellar discs around MYSOs have shown variability in emission lines on timescales of days, months and years (Derkink et al., 2021). This variability may be due to disc inhomogeneities, magnetic fields, jets/outflows or the presence of one or more companions. This variability has the potential to affect the determination of radial velocities, and so should be taken into consideration when performing an analysis.

The main objective in this work is to use Brγ to determine the radial velocity (RV) of MYSOs at each epoch to look for RV variability. An investigation of whether the RV of an MYSO varies between epochs will allow us to infer the presence, or lack thereof, of a close-in companion. Section 3.2 outlines the observations and the spectra used in this work. Section 3.3 covers the results of the radial velocity study as well as an estimation of separations and mass ratios. Conclusions are presented in Section 3.4.

3.2 Observational Data

This work consists of two samples: high-resolution multi-epoch $K-$band spectra for a sample of two MYSOs, and medium-resolution dual-epoch $K-$band spectra for a

Table 3.1: Log of the IGRINS spectroscopic observations used in this chapter.

Object name	Coordinates (J2000)	Observatory	t_{int} (s)	Observation Time
G076.3829-00.6210	20:27:26.77	McD	120	2015-06-12 UT 09:14
	+37:22:47.7	McD	150	2016-06-12 UT 10:24
		McD	60	2016-07-22 UT 05:46
		McD	60	2016-07-22 UT 07:49
		McD	60	2016-07-24 UT 07:11
		McD	60	2016-07-26 UT 08:29
		McD	60	2016-07-26 UT 10:06
		Lowell	120	2017-09-08 UT 02:56
G033.3891+00.1989	18:51:33.82	McD	120	2015-06-11 UT 06:05
	+00:29:51.0	McD	120	2016-05-22 UT 06:14
		McD	120	2016-07-20 UT 06:52
		McD	180	2016-07-20 UT 08:55
		McD	120	2016-07-22 UT 06:19
		Lowell	60	2017-09-07 UT 05:04

larger sample of MYSOs.

3.2.1 IGRINS

I use echelle spectra from the Immersion GRating INfrared Spectrometer (IGRINS, Yuk et al. 2010; Park et al. 2014), taken at different epochs between June 2015 and August 2017 covering varying timescales: hourly, daily and yearly. All but the final epoch were taken while IGRINS was installed on the Harlan J. Smith Telescope at the McDonald Observatory; the 2017 observations were taken while IGRINS was on the Discovery Channel Telescope at the Lowell Observatory. I focus on two MYSOs: G076.3829-00.6210 (also known as SH 2-106) and G033.3891+00.1989. IGRINS has a resolving power of ∼45,000, covering both the $H-$ and $K-$ infrared bands with a range of 1.45-2.45 μm; here the main focus is on the $K-$band. IGRINS has a slit width of 0.34" and a slit length of 5". A log of the observations can be found in Table 3.1. Data was retrieved from the IGRINS Raw Data Archive (https://igrinscontact.github.io/RRISA_raw/). The observations were originally intended for investigating

CO bandhead emission, but this project repurposed the data as the Brγ line. At first only pipeline-reduced data was used, however additional epochs were retrieved from the raw data archive and manually reduced to effectively double the observed timescale.

G076.3829 exhibits extended emission and so additional subtraction of the nebular emission had to be performed on top of regular background subtraction; G033.3891 is compact enough that a simple ABBA nodding sequence along the slit was sufficient to remove the sky background. More detailed descriptions of each object can be found in Section 3.3. There are two telluric absorption lines either side of Brγ (2.1635 and 2.1687 μm). To remove this effect from the spectra, telluric standards were observed alongside the MYSOs. A0V stars were used as telluric standards in order to provide relatively featureless spectra, and were observed at similar airmass to that of the target MYSOs. The target spectra were divided by the spectra of a corresponding telluric standard to remove these absorption lines.

3.2.2 X-shooter

In addition to the IGRINS multi-epoch spectra for two objects, reduced NIR medium-resolution spectra from an ongoing program on the VLT's X-shooter spectrograph was used, with the data used here obtained between November 2016 and April 2022. The original master sample contained 68 MYSOs with $K \leq 13$, once again selected from the RMS catalogue (Lumsden et al., 2013). They were selected with the aim of forming a complete sample of objects in the Southern hemisphere with luminosities between 1000 - 200,000 $L_{\odot}$. The completeness of the RMS catalogue is dependant on the luminosity; the sample is complete galaxy-wide for objects with $L >$ 10,000 $L_{\odot}$, The sample of objects observed with X-shooter is much larger than the IGRINS sample; 39 YSOs were observed at least twice.

The objects are bright in the K-band so they were observed as a filler program, hence

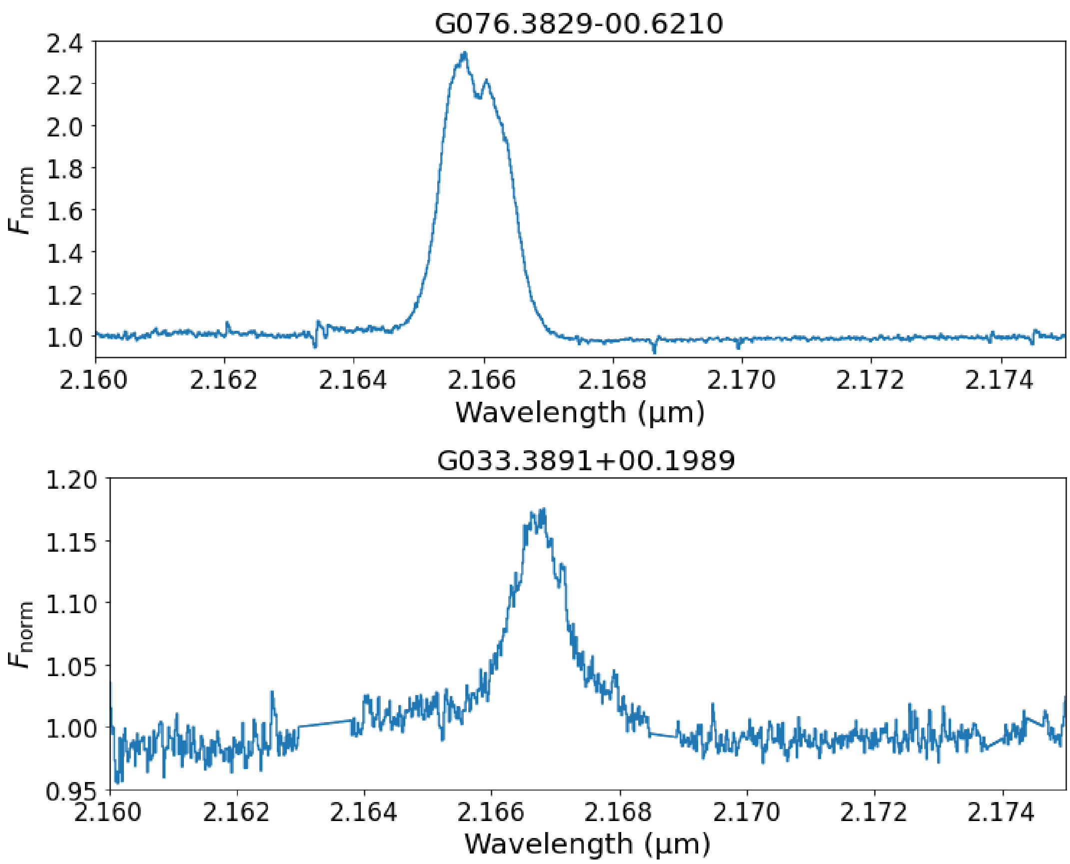

Figure 3.1: Example of an IGRINS spectra for G076.3829 (top) and G033.3891 (bottom) showing the Brγ line. The spectra have been continuum normalised.

they were not all observed at photometric conditions. The spectra were taken with a slit width of 0.4" and a slit length of 11". The observations cover a range of 1-2.5μm at a spectral resolution of R$\sim$11400 and were pipeline reduced (`xshoo/2.4`, Modigliani et al., 2010). As the main focus of this study is RV variability, I checked the precision of the wavelength calibration manually; this is detailed further in Subsection 3.3.3.

The Brackett γ emission line at 2.16μm was once again the focus for the X-shooter sample. In some cases, alternate emission lines were looked at to confirm an object's status as RV variable: Br12 at 1.64μ m, the molecular hydrogen (H_2) transition at 2.12μm and Paschen β at 1.28μm. Some spectra had to be excluded for quality reasons, as detailed in Subsection 3.3.2. An example of the X-shooter Brγ emission line spectra for the MYSO G332.8256-00.5498A can be found in Figure 3.2.

3.3 Results

3.3.1 Description of objects and spectra: IGRINS

G076.3829 is a MYSO situated at a distance of 1.3 kpc with L_{bol} = 34000 $L_{\odot}$ (corresponding to ∼19 $M_{\odot}$) and v_{LSR} = -1.7 kms^{-1}, as measured from Lumsden et al. (2013) using the CS (2-1) transition. It is tied to the closest bipolar HII region SH 2-106, and sits at the centre of a large star formation nebula. The system is seen at an inclination of $< 60°$ (Comerón et al., 2018). G033.3891 is an MYSO found at a distance of 5 kpc, with L_{bol} = 13000 $L_{\odot}$ (corresponding to ∼13 $M_{\odot}$) and v_{LSR} = 85.3 kms^{-1} as measured from Lumsden et al. (2013). It is a compact object with very little extended emission.

Both objects exhibit Brγ emission at 2.166 μm, with it being much stronger in G076.3829. The spectra for both objects centered on Brγ are shown in Figure 3.3. Additionally the 2.12 μm molecular hydrogen line is present in G076.3289. At 2.29 and 2.32 μm the first and second CO first overtone bandhead transitions are observed in emission in both objects, but are of too poor quality to analyse.

The spectra of G076 shown in Figure 3.3 show that the line profile is not a simple Gaussian; instead a double-peaked line is shown, and is due to nebular emission around the YSO. Lumsden et al. (2012) previously investigated G076.3829 and found a single-peaked Brγ emission line, possibly due to differences in how nebular emission was handled.

3.3.2 Description of objects and spectra: X-shooter

The sample of 39 YSOs have distances ranging between 0.7-9.5 kpc, with an average distance of ∼3.4 kpc. 33 of the YSOs are massive ($> 8M_{\odot}$), and the remaining 6 are

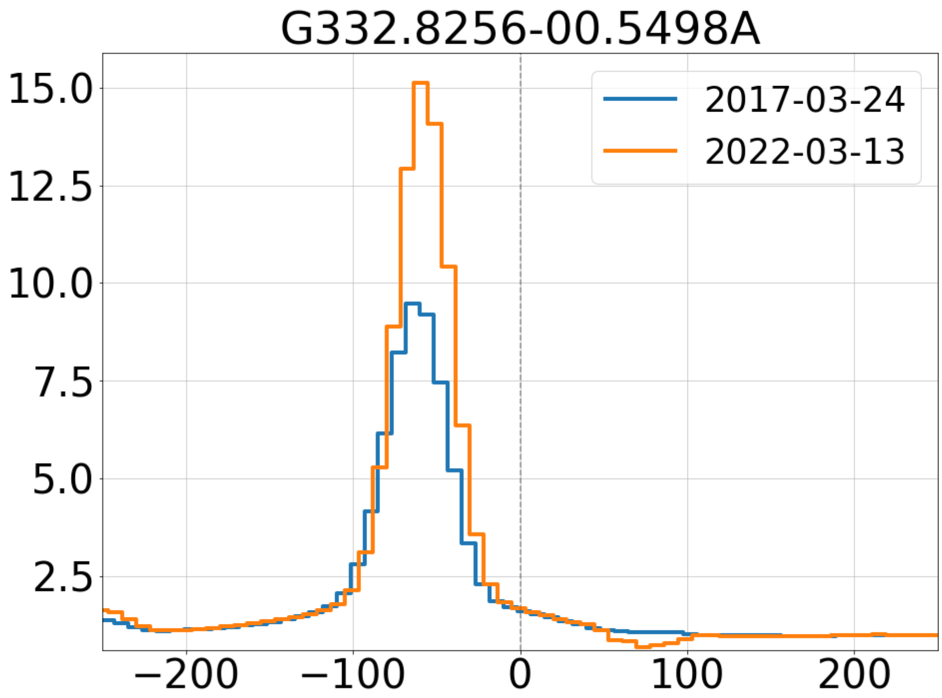

Figure 3.2: Brγ emission line spectra for the MYSO G332.8256-00.5498A. The spectra are plotted as a function of LSR-corrected velocity. Two epochs are presented, with March 2017 shown in blue and March 2022 shown in orange. This object was determined to be non-variable in terms of radial velocity.

classified as low-mass. The MYSO masses range between 8-34 $M_{\odot}$ with an average mass of 15.7 $M_{\odot}$.

Brγ is present in 82% of the sample. Additionally, Br12 is present in 62%, H_2 present in 74% and Paβ found in 67% of the sample. The average SNR of the sample is 78, with a maximum of 356. Some spectra were not usable, due to poor signal-to-noise or the lack of Brγ emission/absorption, rendering 7 objects unusable. An additional 6 objects which exhibited variable Brγ line profiles were excluded, as they could not provide reliable and comparable RV measurements. After these exclusions, there were 26 objects which comprised the final X-shooter sample. The details of the observations for these 26 objects can be found in Table 3.4.

Two objects have multiple spectra taken within the same hour on the same day: G305.6327+01.6467 and G308.9176+00.1231A. Both were excluded from the RV analysis due to the variable line profile issues mentioned above with the other epoch. However they do provide a lower limit to the uncertainty in the quality of the spectrum, as the objects are unlikely to exhibit any RV variations in such a short timescale. Both objects show a deviation of ∼0.2 kms^{-1} within the hour.

G231.7986-01.9682 shows some corruption in the spectra in the centre of the Brγ emission line. However enough of the wings either side of the line centre are present in order to fit a Gaussian and determine a radial velocity, therefore this object was retained in the final sample.

3.3.3 Radial velocity variations

Variations in the RV of each object were investigated in order to search for close-in companions. To do this, the RV of each epoch was determined using the Brγ lines. Using the python package `specutils` (Earl et al., 2022), the spectra were first continuum fitted, and then wavelength-calibrated using the telluric lines either side of Brγ. The telluric line to the blue side of Brγ (2.16348 μm, Mendigutıéa et al., 2015) was used to anchor all of the spectra at its known wavelength (telluric lines should by definition not vary in wavelength). The Brγ line was fitted in each epoch using a Gaussian and the central wavelength was used to calculate the radial velocity. The radial velocities were additionally corrected for heliocentric and Local Standard of Rest (LSR) motions. Following the method of Sana et al. (2012), any radial velocity variations of >20 kms^{-1} between epochs were deemed significant enough to infer the presence of a companion. Variations in Brγ due to physical processes (as opposed to binary orbital motion) are relatively small compared to this value (Derkink et al., 2023).

For IGRINS, the uncertainty in the RV calculations can be inferred from IGRINS's spectral resolution of $\sim 45,000$. As a rule of thumb the uncertainty is a tenth of the RV resolution of 6.7 km s^{-1}, giving a rough uncertainty of ~ 0.7 km s^{-1}. The Gaussian fitting procedure of `specutils` yields a relatively negligible uncertainty itself, however the noisy and uneven nature of the Gaussian (especially in G033.3891) proved difficult to fit perfectly. To ensure the RVs measured from the fits were reliable, the flux-weighted mean wavelength (i.e. the first moment of the distribution) was also measured for each epoch as a secondary check.

The uncertainties for the RVs were derived from the quality of the wavelength calibration, and can be found in Table 3.2 and Table 3.3. The wavelength of the telluric line to the red side of Brγ (2.16869 μm, Mendigutıéa et al., 2015) was used to determine the accuracy of the wavelength calibration, and gives an indicator of the uncertainty of any RVs measured. The G033.3891 spectra were resampled due to the low SNR, effectively reducing the spectral resolution and therefore increasing the uncertainty in the RV by a factor of ∼2. Around Brγ the spectra of G076.3829 have a high SNR (>80) whereas the G033.3891 spectra have a lower SNR (>40).

For X-shooter, a similar technique was applied. The telluric lines either side of Brγ were fit using Gaussians and the difference between their expected and observed wavelengths provided an indicator of the quality of the wavelength calibration and the data itself. By measuring the telluric lines, the combined uncertainty of the measurement error and the wavelength calibration was deemed to be ∼4 kms^{-1} (the measurement error on its own was determined to be ∼2 kms^{-1}).

IGRINS

The measured RVs for G076.3829 can be found in Table 3.2. Thanks to the high signal-to-noise in the spectra for G076.3829 variations can be seen in its RV, especially in the 2015 epoch as can be seen in Figure 3.3. The 2015 epoch shows a difference in its line profile compared to the other epochs, in that the redder peak is stronger, whereas

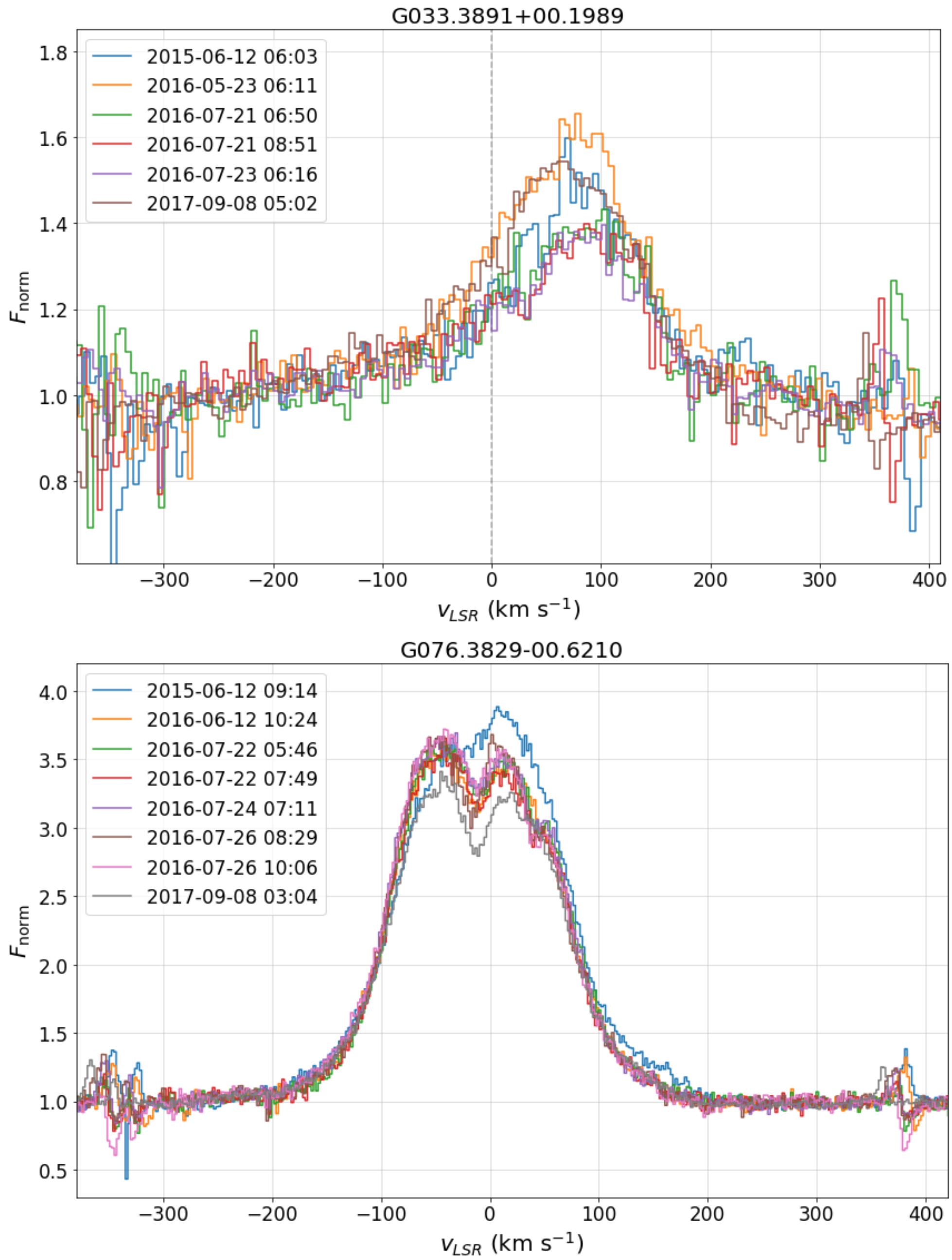

Figure 3.3: Spectra showing the Brγ emission line in G033.3891+00.1989(top) and G076.3829-00.6210 (bottom) at each epoch, having been heliocentrically- and LSR-corrected. For G033 the spectrum is noisier with a weaker Brγ line, while G076 has a much brighter and clearly defined line with a double-peaked feature. The G033 spectra have been resampled to improve the SNR and velocity determinations.

Table 3.2: LSR-corrected radial velocities of the Brγ, Br12 and H_2 lines in G076.3829, with FWHMs of the Brγ line. Some measurements are unavailable due to spectral issues.

Date/Time (UT)	v_{Br_γ} (kms^{-1})	Δv_{Br_γ} (kms^{-1})	FWHM (kms^{-1})	v_{Br12} (kms^{-1})	v_{H_2} (kms^{-1})
2015-06-12 09:14	-7.6	1.4	142.2	-0.1	-17.5
2016-06-12 10:24	-11.6	1.7	140.9		
2016-07-22 05:46	-11.2	1.3	138.6		-17.5
2016-07-22 07:49	-12.0	1.6	138.2		-18.8
2016-07-24 07:11	-12.5	2.2	138.6	-10.3	-18.1
2016-07-26 08:29	-13.7	1.2	138.8	-12.5	-15.6
2016-07-26 10:06	-13.5	1.8	139.0	-11.4	-16.1
2017-09-08 02:56	-10.7	1.3	139.7		

on the other epochs the bluer peak is stronger; however the profile of the wings appear unchanged. This line profile difference is also visible in the Br12 emission line. The FWHM of the Brγ lines are relatively similar, ranging from 138.2-142.2 kms^{-1}. This corresponds to an RV uncertainty of $\sim$4 kms^{-1}, the same uncertainty as measured by the telluric lines. Therefore, despite this small deviation in FWHM, these line profiles should be considered consistent with each other.

Also present in the spectra of this object is the Br12 line at 1.64 μm, and the shocked 2.12 μm H_2 line which traces shock activity; both are shown in Figure 3.4. Both lines also show some subtle variation, specifically in the 2015 epoch for Br12.

For the benefit of later sections I focus on the strongest line, Brγ. The mean LSR-corrected RV is -11.6 kms^{-1} with a standard deviation of 1.9 kms^{-1} (excluding the 2015 epoch, the mean RV is -12.2 kms^{-1} with an SD of 1.1 kms^{-1}). The RV of the 2015 epoch clearly exhibits some variation compared to the 2016/17 epochs, as the RV of every epoch is within 1.5σ of the mean apart from 2015, which differs by 3σ. Despite this variation, it is not significant enough to consider a binary companion. The plot of v_{LSR} against time is shown in Figure 3.5.

G033.3891 also exhibits some variation in its RV; this is reflected in the LSR-corrected

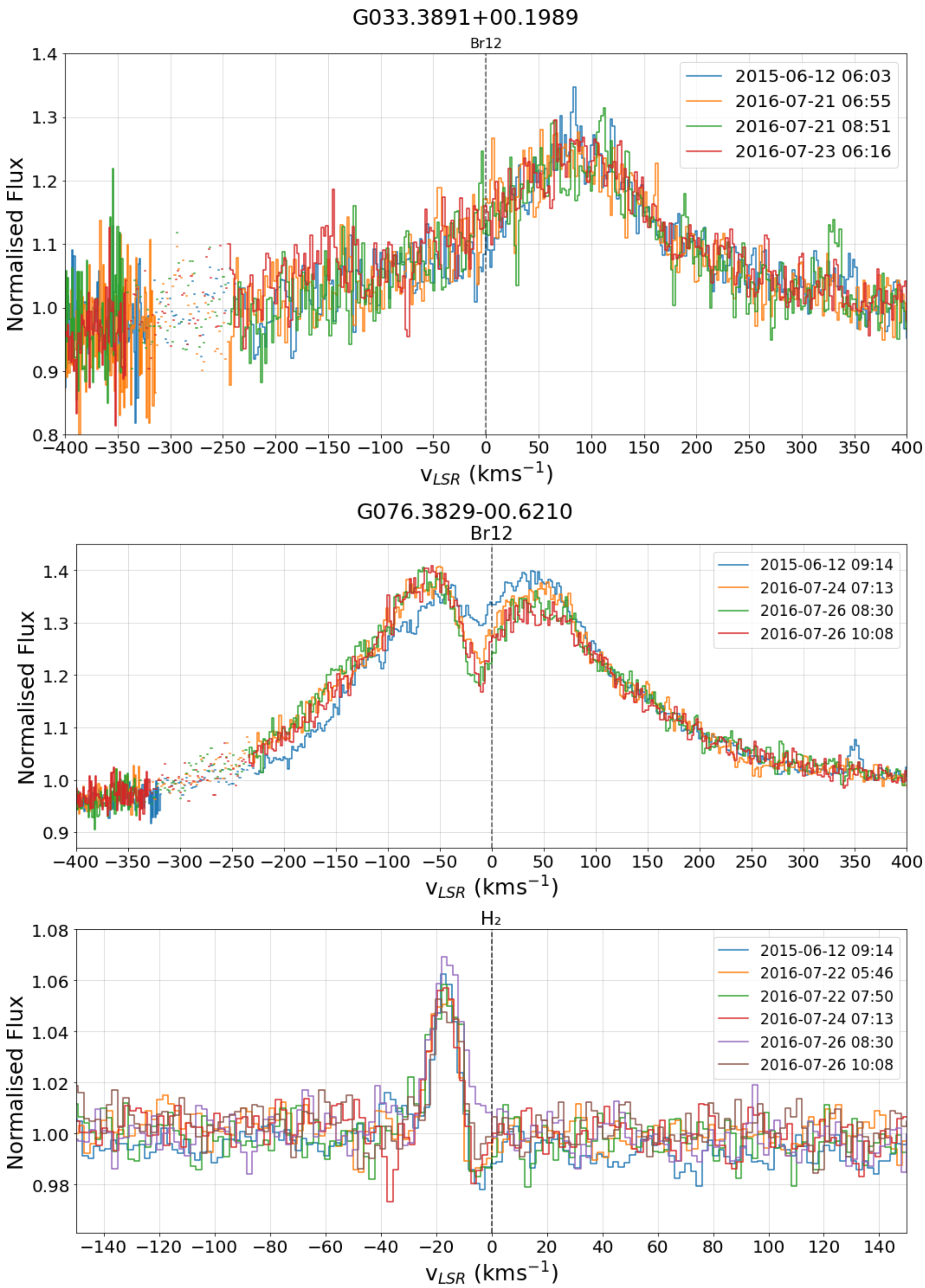

Figure 3.4: Spectra showing the Br12 line in G033.3891+00.1989 (top) and the Br12 and H_2 emission lines in G076.3829-00.6210 (middle and bottom) at each epoch, having been heliocentrically- and LSR-corrected. The H_2 line in G033 was of too poor quality to use.

Table 3.3: Measured radial velocities of the Brγ and Br12 lines in G033.3891, with FWHMs of the Brγ line. Some Br12 measurements are unavailable due to spectral issues, and the H_2 line was of too poor quality to obtain RVs.

Date/Time (UT)	v_{LSR} (kms^{-1})	Δv_{LSR} (kms^{-1})	FWHM (kms^{-1})	v_{Br12} (kms^{-1})
2015-06-12 06:03	76.5	1.2	152.1	88.1
2016-05-23 06:11	71.9	2.8	150.9	
2016-07-21 06:50	73.7	1.9	150.3	75.8
2016-07-21 08:51	72.4	0.8	149.0	79.0
2016-07-23 06:16	72.1	1.8	150.4	80.6
2017-09-08 05:02	62.3	1.4	150.7	

radial velocity values in Table 3.3. It seems to exhibit some line profile variation, but more subtly than G076.3829. The May 2016 epoch and Sept 2017 epochs have slightly broader lines than the rest, and the May 2016 epoch shows an asymmetrical peak. However the FWHMs are consistent, ranging between 149-152.1 kms^{-1}. The Br12 line at 1.64 μm and the 2.12 μm H_2 line are present; both are shown in Figure 3.4. The Br12 line appears to vary with RV, while the H_2 line is of too poor quality to determine any variations.

When considering the Brγ line, the mean RV is 71.5 kms^{-1} with a standard deviation of 4.8 kms^{-1}. Excluding the 2017 epoch, the mean RV is 73.3 kms^{-1} with an SD of 1.9 kms^{-1}. The RV of every epoch is within 1σ of the mean except for June 2015 and Sept 2017, the latter of which is more than 4σ away. The maximum variation between epochs is 14.2 kms^{-1}, therefore this is not significant enough to consider the presence of a binary companion. The plot of v$_{LSR}$ against time is shown in Figure 3.5.

X-shooter

For this sample I once again focus on the strongest line, Brγ, to determine any RV variability. These objects only have two (or in a single case, three) main epochs of data available. Once again, the RVs were determined by using `specutils` to fit a Gaussian to the Brγ line in each epoch and determining its central wavelength, then correcting

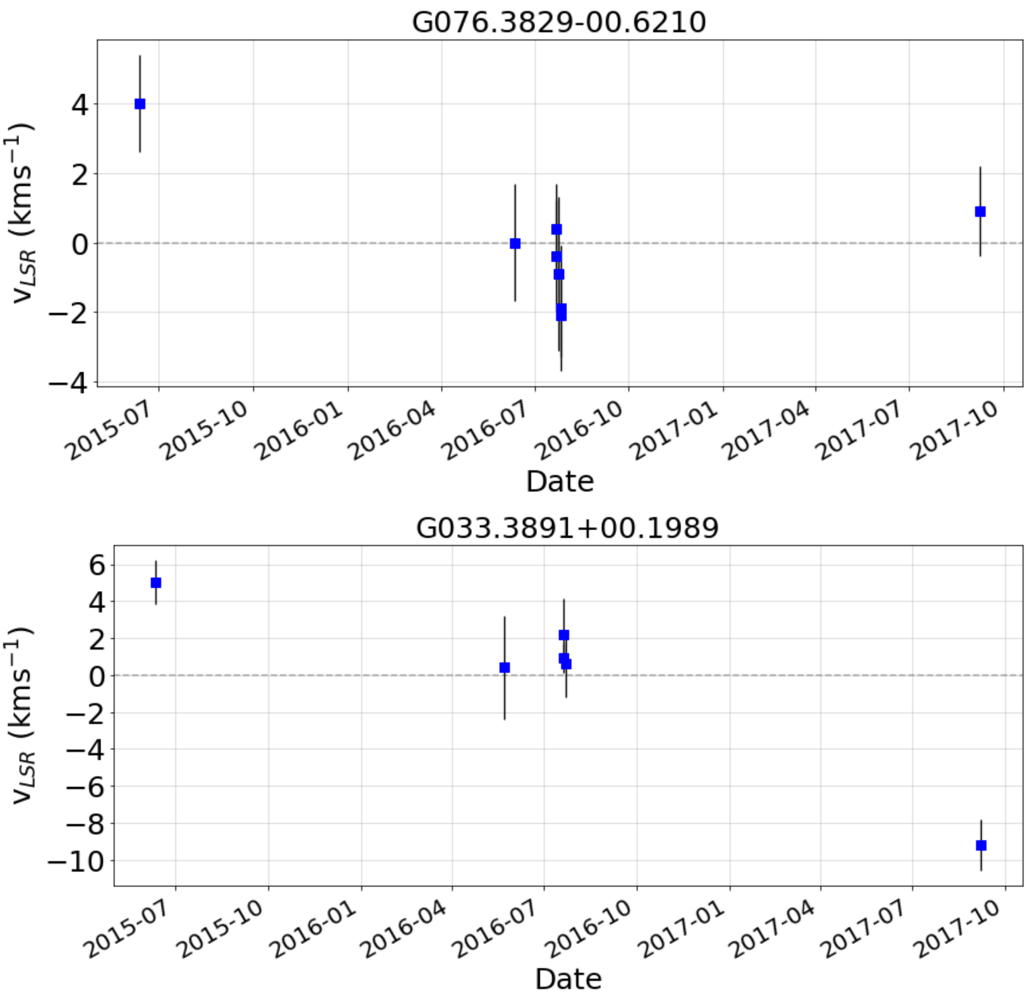

Figure 3.5: A plot showing v_{LSR} for Br_{γ} against time for G076.3829-00.6210 (top) and G033.3891+00.1989 (bottom), having been heliocentrically- and LSR-corrected.

for LSR to find the radial velocity.

The spectra can be found in Figure 3.6 and Figure 3.7. Some objects had spectra which exhibited artifacts; for example, the 2016 epoch of G231.7986-01.9682 seems to show corruption around the Brγ line, however enough of the wings were intact to deem that this object was not RV variable. Any unusable spectra from which a reliable RV measurement could not be taken were discarded earlier on.

Details of the observations and the measured RVs for the X-shooter sample can be found in Table 3.4. Of the YSOs in this sample, 2 out of 26 were found to have variability in their RV (G290.3745+01.6615 and G298.2620+00.7394), corresponding to a MF of 8^{+17}_{-7}%. The high-mass subset ($> 8M_{\odot}$) has 2 out of 23 objects labelled as RV variable, giving MF=9^{+19}_{-8}%, and the low-mass subset has 0 out of 3 objects deemed to be RV variable, giving MF=0^{+71}_{-0}%. Errors were calculated using binomial confidence intervals. The measured RVs were checked using the flux-weighted mean wavelength, which also showed that the two objects are RV variable.

Table 3.4: Details of the X-shooter observations for the sample of YSOs. v_{RMS} is the radial velocity of the YSO as recorded in the RMS catalogue (Lumsden et al., 2013). d_{RMS} is the RMS catalogue kinematic distance. L_{bol} is the bolometric luminosity taken from the RMS catalogue. t_{exp} is the exposure time of the X-shooter observation, and SNR is the signal-to-noise ratio of that observation around Brγ. $v_{Br\gamma}$ is the LSR-corrected radial velocity determined from the Brγ emission line in the X-shooter observations. The uncertainty of $v_{Br\gamma}$ is $\sim$4 kms^{-1}. The objects marked with ^{HII} were classed as YSOs in an earlier version of the RMS catalogue (and were observed with this in mind) but have since been reclassified as HII regions.

YSO Name	RA (deg)	Dec (deg)	v_{RMS} (kms^{-1})	d_{RMS} (kpc)	L_{bol} ($L_\odot$)	Obs. Date	SNR	t_{exp} (s)	$v_{Br\gamma}$ (kms^{-1})	Variable?
G207.2654-01.8080A	98.6568	4.2125	12.6	1.0	9100	2017-01-30 02:54	91	560	12.7	N
						2020-10-20 07:32	47	280	20.8	
						2020-12-07 05:34	73	280	18.5	
G207.2654-01.8080B	98.6554	4.2127	12.6	1.0	1300	2017-01-30 03:17	164	560	1.6	N
						2020-12-09 04:08	98	560	-1.9	
G212.0641-00.7395	101.8055	0.4352	45.0	4.7	16200	2017-01-30 03:32	64	2400	36.9	N
						2020-11-18 06:50	61	1200	45.3	
G231.7986-01.9682	109.8992	-17.6552	43.5	3.2	5600	2016-11-19 07:00	152	560	44.6	N
						2020-11-27 05:38	263	560	43.4	
G233.8306-00.1803	112.5687	-18.5976	44.6	3.3	13100	2016-11-04 08:20	16	280	37.2	N
						2019-10-11 08:50	15	280	36.3	
G232.6207+00.9959	113.0400	-16.9706	16.6	1.7	11270	2016-11-05 08:15	41	560	11.2	N
						2020-02-20 04:39	14	600	9.8	
G251.2337-01.9535	120.6783	-34.5296	54.4	4.6	8200	2016-11-19 07:43	21	2400	53.3	N
						2020-02-13 04:59	48	2400	52.4	
G263.7759-00.4281	131.6449	-43.9075	4.3	0.7	1270	2017-01-30 02:21	33	560	2.5	N
						2019-10-16 08:54	46	600	7.2	
G263.2283+01.5712^{HII}	133.2894	-42.2188	5.4	0.7	1200	2017-01-31 00:49	21	2400	-0.2	N
						2020-11-16 07:35	22	1200	-3.9	
G268.3957-00.4842	135.8538	-47.4740	11.6	0.7	3000	2017-01-30 01:51	105	560	8.1	N
						2020-11-02 07:29	109	300	6.4	
G281.0472-01.5432^{HII}	149.8152	-56.9101	-8.7	7.0	145160	2017-01-30 02:36	89	560	1.1	N
						2020-12-27 06:23	116	600	0.8	
G282.8969-01.2727	152.8808	-57.7839	-4.3	7.0	17100	2017-01-31 02:36	40	560	-19.9	N
						2020-12-31 07:18	45	600	-10.0	

YSO Name	RA (deg)	Dec (deg)	v_{RMS} (kms^{-1})	d_{RMS} (kpc)	L_{bol} ($L_\odot$)	Obs. Date	SNR	t_{exp} (s)	$v_{Br\gamma}$ (kms^{-1})	Variable?
G290.3745+01.6615	168.0745	-58.7723	-18.7	2.9	15100	2017-01-31 04:50	33	560	-10.3	Y
						2020-12-27 08:19	21	300	-31.9	
G298.2620+00.7394	182.9480	-61.7717	-30.6	4.0	15300	2017-01-31 05:13	19	2400	3.9	Y
						2022-01-21 05:21	18	1200	-33.4	
G301.8147+00.7808A	190.4737	-62.0708	-37.1	4.4	21580	2017-03-31 04:26	131	560	-34.9	N
						2021-03-01 03:50	110	280	-35.4	
G305.2017+00.2072A	197.7925	-62.5767	-41.0	4.0	48500	2020-02-13 07:18	59	600	-44.7	N
						2021-03-01 04:30	66	600	-52.2	
G309.9206+00.4790B	207.6755	-61.5856	-56.7	5.4	11000	2017-03-25 04:08	73	2400	-69.1	N
						2020-02-13 05:48	35	2400	-70.5	
G309.9796+00.5496	207.7608	-61.5028	-42.4	3.5	7600	2020-02-16 08:33	23	600	-52.0	N
						2022-01-16 07:57	40	2400	-50.4	
G310.0135+00.3892	207.9069	-61.6514	-39.7	3.2	67100	2017-02-25 09:10	136	280	-47.4	N
						2020-02-16 09:04	161	280	-33.9	
G320.2437-00.5619	227.7565	-58.6591	-52.2	9.5	31300	2020-02-13 07:35	67	600	-55.7	N
						2022-01-21 08:25	82	600	-59.6	
G330.8768-00.3836	242.5989	-52.1148	-63.3	3.9	7600	2017-04-01 08:36	223	2400	-70.3	N
						2022-02-03 08:15	209	2400	-70.0	
G332.0939-00.4206	244.0682	-51.3059	-56.5	3.6	92800	2017-02-03 08:56	92	280	-44.3	N
						2020-02-13 09:05	86	280	-62.6	
G332.8256-00.5498A	245.0454	-50.8871	-57.3	3.6	130100	2017-03-24 06:51	42	560	-60.1	N
						2022-03-13 09:16	56	600	-56.4	
G336.4917-01.4741B	250.0038	-48.8647	-23.4	2.0	12300	2017-03-23 09:12	89	560	-26.0	N
						2022-03-17 06:17	111	900	-28.4	
G338.9196+00.5495	250.1415	-45.7024	-64.1	4.2	32030	2017-04-01 09:25	28	560	-52.2	N
						2020-02-20 08:50	25	600	-49.0	
G347.0775-00.3927	258.1075	-39.9217	-12.0	1.7	2960	2017-03-23 08:56	63	560	-35.0	N
						2019-10-12 23:58	28	600	-15.9	

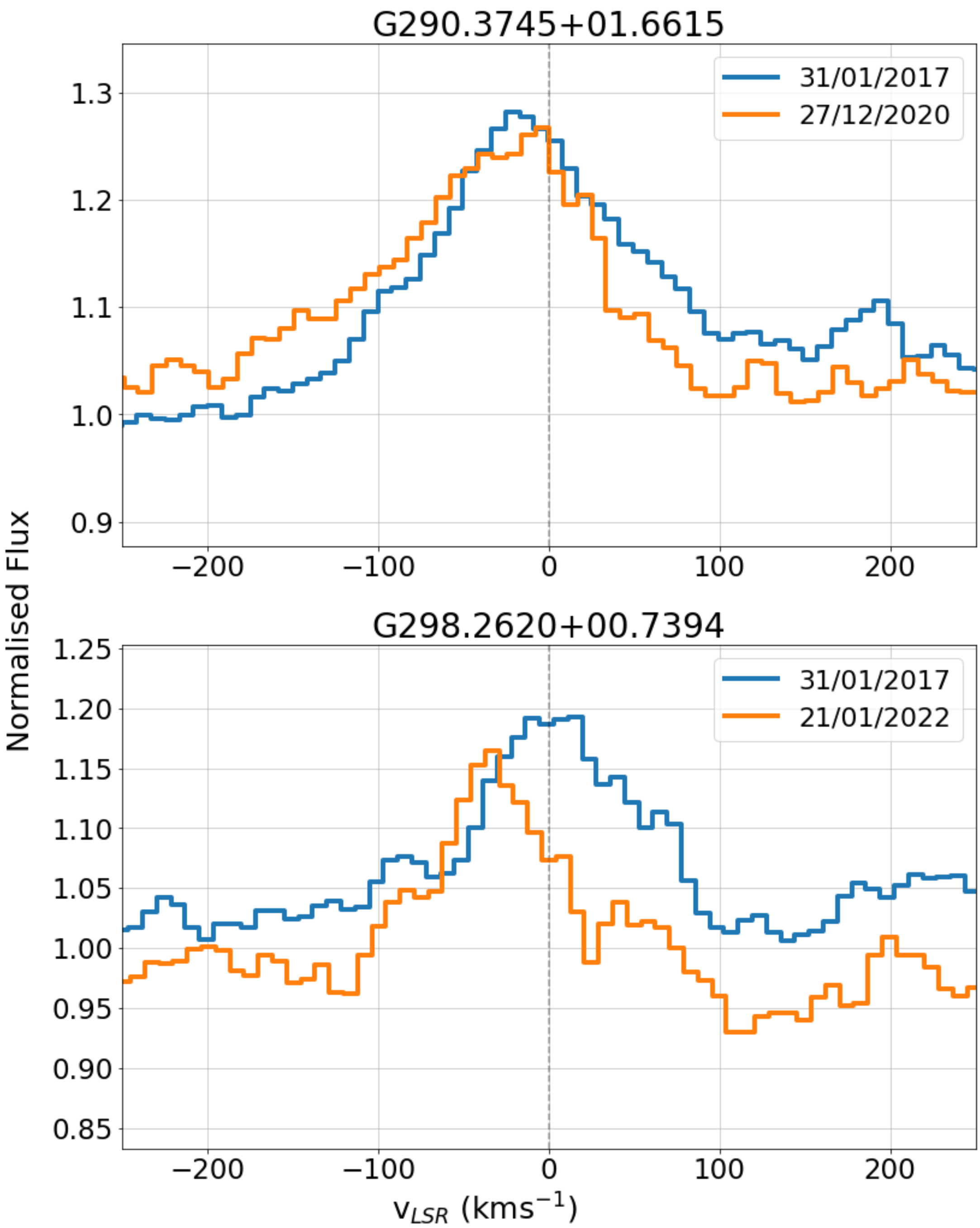

Figure 3.6: X-shooter spectra of the Brγ emission line for both MYSOs determined to be RV variable. The first and second epochs have been shown in blue and orange respectively.

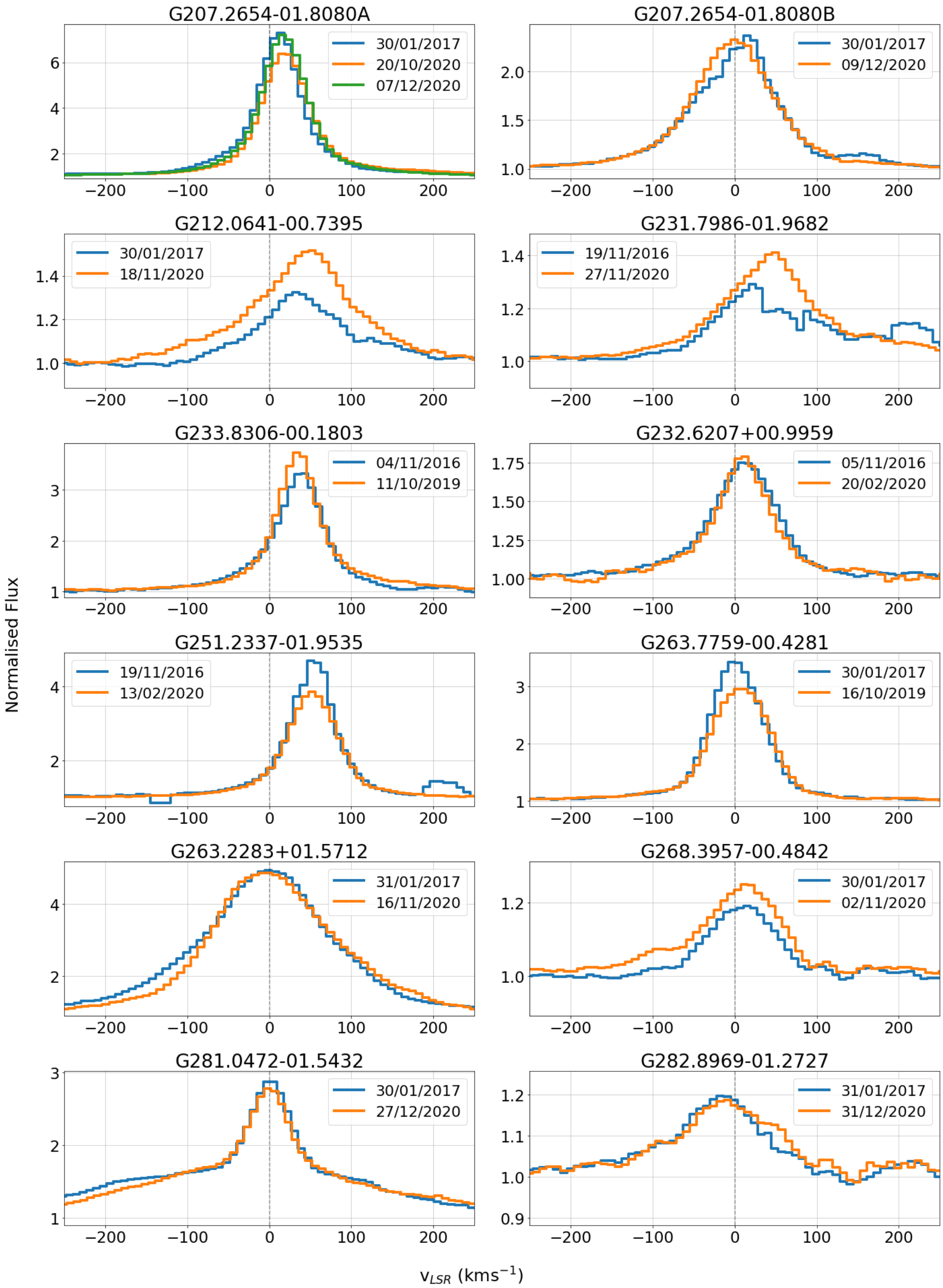

Figure 3.7: X-shooter spectra of the Brγ emission line for MYSOs determined to not be RV variable. The first and second epochs have been shown in blue and orange respectively. G207.2654-01.8080A has a third epoch shown in green.

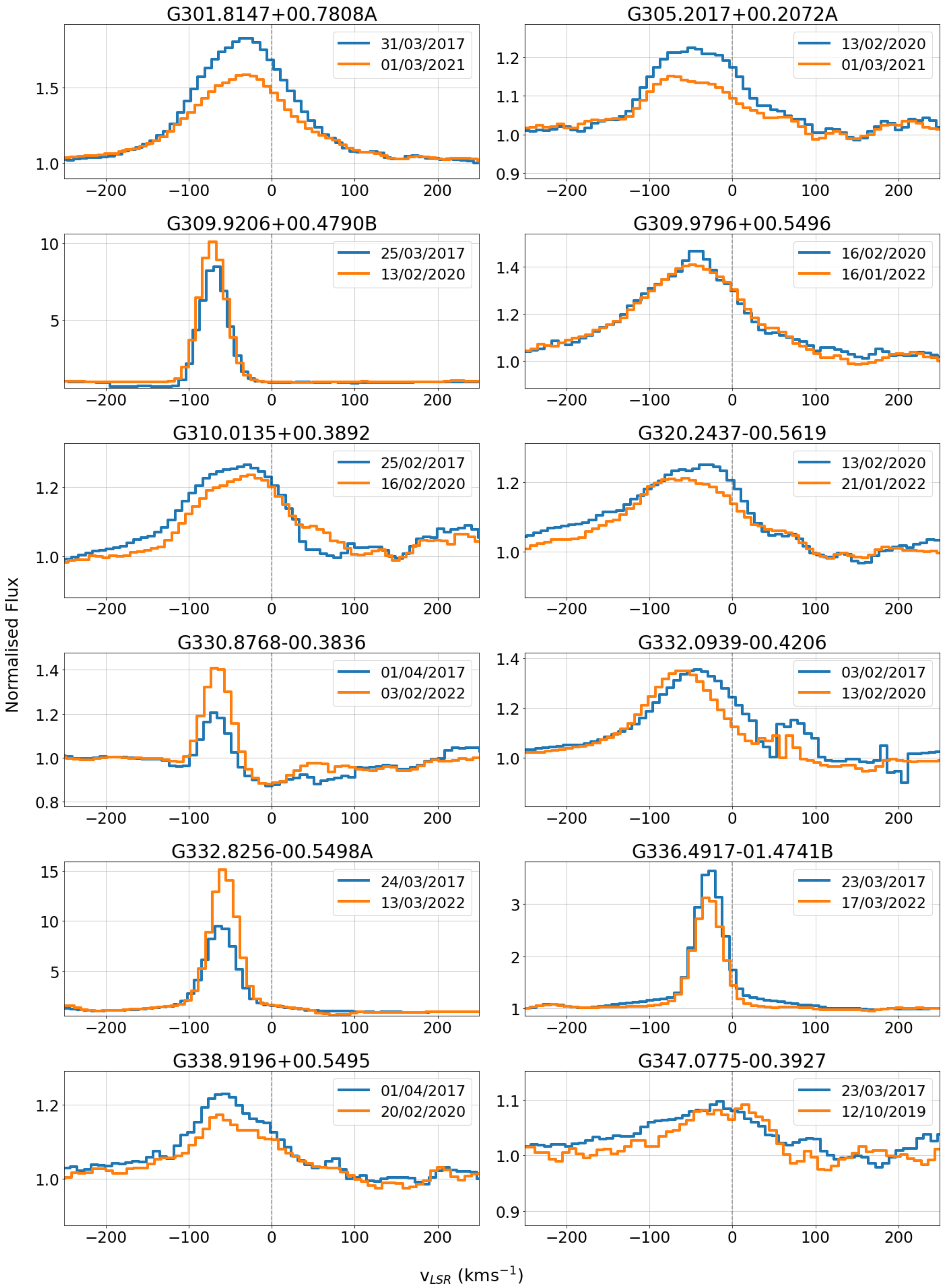

Figure 3.7: continued

One object, G207.2654-01.8080A, has three available epochs as opposed to the two that every other object has. Therefore it is possible to do a marginally more detailed analysis on this object. The January 2017 epoch was recorded to have an RV of 12.7 kms^{-1}. The October 2020 epoch has an RV of 20.8 kms^{-1}, and the December 2020 epoch has an RV of 18.5 kms^{-1}. This shows that the minimum RV difference of this object is at least 8.1 kms^{-1}, but may be larger seeing as only three epochs have been observed.

3.3.4 Masses and separations

Despite the RV variations of the IGRINS objects not being significant enough for the existence of a binary companion according to the >20 kms^{-1} criteria of Sana et al. (2012), this criteria is noted to be a conservative limit due to the possibility of photospheric variability (Sana and Evans, 2011). Therefore I pose a 'what-if' scenario; if the RVs measured here were instead deemed significant enough to indicate the presence of companions, their masses and separations can be estimated. The mass of the primary (m_1) can be estimated using luminosity data from the RMS catalogue (Lumsden et al., 2013). To determine possible masses and separations of the binary systems, Kepler's Third Law can be used:

$$\frac{P^2}{a^3} = \frac{4\pi^2}{G(m_1 + m_2)} \tag{3.1}$$

and:

$$\frac{m_2^3 sin^3 i}{(m_1 + m_2)^2} = \frac{P v_{obs}^3}{2\pi G} \tag{3.2}$$

where m_1, m_2 are the masses of the primary and secondary object respectively, a is the separation between the binary objects, P is the period of the binary orbit, i is the inclination of the system in degrees, and v_{obs} is the observed radial velocity of the system in ms^{-1}. The radial velocities of the binary orbits (v_{obs}) have been estimated in Subsection 3.3.3. These RVs are lower limits because they do not necessarily measure the maximum RV. Also G076 and G033 are assumed to be at an inclination of 60° and

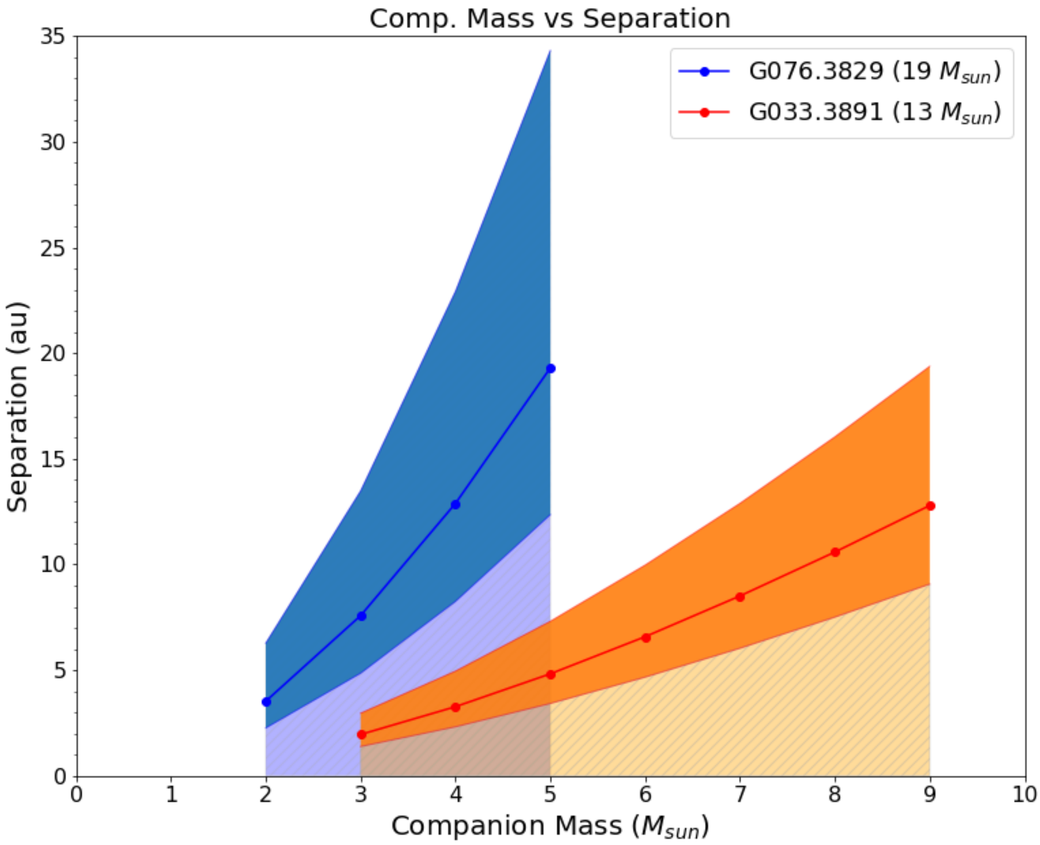

Figure 3.8: Plot showing the possible binary separations against companion mass for G076.3829-00.6210 (blue) and G033.3891+00.1989 (red) at each epoch. The solid blue line represents the mean estimate of the mass, and the darker shaded regions represent the uncertainty with respect to the determined radial velocity. The lightly-shaded hatched regions show the possible separation and magnitudes below the upper limit.

90° (edge-on) respectively, whereas in reality the systems may be at smaller inclination angles. Therefore the true RV value may again be larger. Nevertheless, by using these RVs with Equation 3.1 and Equation 3.2 limits can be placed on the mass of the secondary object (m_2) and the separation between them (a). A plot of companion mass against separation is presented in Figure 3.8.

For G076, a low-mass ($< 5M_{\odot}$) companion at separations up to ∼35 au would be possible. Companion masses and separations greater than this would be unlikely due to the fact that long periods are necessary which would be difficult to constrain the

Table 3.5: Possible separations and masses for each MYSO companion detected using RV variations in X-shooter spectra.

MYSO Name	Separation Range (au)	Mass Range ($M_\odot$)
G290.3745+01.6615	<20	3-14
G298.2620+00.7394	<6	6-14

RVs to. The upper limit of this binary orbit would have been around ∼25 years, as Figure 3.5 shows that a longer orbital period would again be difficult to produce from these observations.

The variability in G033's radial velocity also indicates the possibility of a binary companion, however the larger variations points to a closer separation or a more massive companion. Assuming a simple sinusoidal curve for this orbit leads to an upper limit to the period of ∼10 years, meaning a companion of mass $< 9M_\odot$ at a separation range of ∼2-20 au is possible; again longer periods are difficult to model from these observed RVs. As before, the existence of an extremely close binary or contact binary is possible due to the lower limit of ∼1 month on the orbital period. Additionally the unknown inclination of this object means that larger RV variations are possible, which would also reduce the separations.

Determinations of the masses and separations of objects in the X-shooter sample is more difficult due to the availability of only two epochs per object. However it is possible to determine limits for these parameters using the same approach as described above. For the two RV-variable objects, if it is assumed that the upper mass limit of the companion is the mass of the primary and that the inclination of the system is edge-on, the companion must lie somewhere between 1-20 au with a mass anywhere between 3 $M_\odot$ and the mass of the primary. More massive companions require larger separations to be consistent with the observed RVs. Details of each MYSO's possible companion separations and masses can be found in Table 3.5.

3.4 Discussion

3.4.1 IGRINS

Overall, the results found here suggest that neither MYSO has a binary companion. The RVs of both MYSOs are relatively stable within the observed epochs, with the 2015/2017 RV deviating slightly in the G076 and G033 cases respectively. There is also some subtle variation in the line profiles; double-peaked lines traced from MYSO discs have been known to exhibit line profile variation with a binary companion as a possible explanation (Derkink et al., 2021). I find zero out of two MYSOs to be in a small-separation binary system, giving a multiplicity fraction of $0^{+84}_{-0}\%$. When considering the large error bar, this result still agrees with Pomohaci et al. (2019) and Koumpia et al. (2019) which both suggest that most, if not all, massive stars form in binary or multiple systems.

If these variations were hypothetically enough to consider the MYSOs as binaries, the two systems would have different limits on their companion masses. G076.3829's companion would be likely to be less massive, due to the smaller fluctuations in the RV (however this is a lower limit). Any companion larger than $\sim 8M_{\odot}$ would not be likely as the orbital period necessary would be inconsistent with the variability in the RV. G033.3891's larger RV variations would allow for a slightly more massive companion at a closer separation. The small separations deduced here would suggest a closer agreement with the accretion disc fragmentation scenario, especially for G033.3891 as it would be consistent with a close-in companion which disc fragmentation suggests (Meyer et al., 2018). Core fragmentation is a less likely scenario (it suggests larger separations than are found here), as is binary capture (in which mass ratios are generally thought to be closer to 1).

3.4.2 X-shooter

The X-shooter sample has a MF of 8^{+17}_{-7}%. This is larger than the MF found for the IGRINS objects, however the two results are consistent within the uncertainties. Additionally, only two epochs were observed for each object in this sample. RV variations on longer timescales may not have been found, meaning that close-in companions may not be detected; the determined binary fractions are a lower limit to the true fraction. Additionally the inclinations of these systems are not known, and any binary systems that are face-on will likely not have been detected using this method.

The small number of epochs means that limits on the companion separations and masses are not very well constrained, however of the companions were estimated to lie at separations $\leq$ 20 au. This also agrees with the disc fragmentation scenario and its stipulation of small separations. However, the masses determined here are not constrained enough to point towards any particular binary formation scenario, as mass ratios may range from anywhere between $0 < q < 1$.

Considering the small separation ranged probed in this sample, the unknown inclinations of these objects, and the fact that some of the YSOs observed with X-shooter were determined to have a varying RV from just two epochs, it is almost certain that the true binary fraction is higher.

The binary fraction found here is not in agreement with the results found in Chapter 2 for all three samples. However the binary fraction of MYSOs in this sample, 9^{+19}_{-8}%, is in agreement with the MYSO binary fraction of 31$\pm$8% from Pomohaci et al. (2019). It should be noted that those two studies probe larger separation ranges than this chapter, and both studies suggest a much higher binary fraction is likely. Therefore this may provide evidence to the fact that MYSOs have companions at both small and large distances, i.e. triple systems, as also asserted in Subsection 2.4.5.

3.5 Conclusions

Here I have presented high-resolution NIR spectra of two MYSOs from the IGRINS spectrograph, and medium-resolution NIR spectra of a larger sample of YSOs from the X-shooter instrument. Multi-epoch observations were used to investigate whether their radial velocities are variable, and whether any observed variability is due to a possible binary companion. The main findings are as follows:

(i) Neither of the two MYSOs surveyed using IGRINS were determined to have a binary companion, giving a binary fraction of 0^{+84}_{-0}%. The MYSOs are relatively RV stable, but on longer timescales they both exhibit some RV variability.

(ii) 8^{+17}_{-7}% of the YSOs in the X-shooter sample were determined to be RV variable. The MF of the high- and low-mass subsets of YSOs are 9^{+19}_{-8}% and 0^{+71}_{-0}% respectively, agreeing with previous assertions that multiplicity increases with mass. Assuming an upper mass ratio limit of 1, the companions detected are thought to be between 1-20 au and are at least 3 $M_{\odot}$.

(iii) Judging by the small parameter space probed and the relatively low number of epochs observed, it is likely that the true binary fraction is higher.

(iv) The small separations suggest an agreement with the accretion disc fragmentation theory of massive binary formation.

To determine the multiplicity state of these YSOs with more certainty, interferometric observations should be conducted to probe the close-in regions where these potential companions may lie. Additionally, further spectroscopic observations at additional epochs should be made, increasing the number of observed epochs and therefore the possibility of binary detections.

Chapter 4

Optically visible MYSO binaries in Gaia DR3

4.1 Introduction

As previously mentioned in Chapter 1, when studying massive star formation and multiplicity, MYSOs are a crucial type of object to observe. They evolve onto the zero-age main sequence (ZAMS) and begin fusion while still embedded in their natal dust envelope. This is due to the fact that the Kelvin-Helmholtz timescale of these young massive stars is significantly shorter than the gravitational free-fall timescale (Zinnecker and Yorke, 2007). Strong stellar winds and bipolar molecular outflows are present and are much more powerful than lower-mass objects (Oudmaijer and de Wit, 2014). They are bright in the infrared due to their embedded nature; a large amount of their radiative output is absorbed and re-emitted at IR wavelengths by the surrounding envelope.

MYSOs have been infamously difficult to observe for a number of reasons. Their aforementioned embedded nature means that MYSO emission has high levels of extinction (average of $A_V \sim 42$, Cooper et al., 2013); as a result it had been widely thought that MYSOs are effectively invisible at shorter wavelengths (Davies et al., 2011). They are relatively rare, and generally lie at large distances (of order kpc), needing instruments with high spatial resolution to resolve them. Additionally, they are usually situated in dense stellar environments meaning that source confusion can be a problem. Consequently there have been very few MYSOs which have been studied comprehensively.

Most previous studies of MYSOs have been at IR wavelengths, and a large-scale deep optical survey has yet to be carried out which could provide a whole new insight into massive star formation. The Gaia survey represents the most comprehensive survey of the Galaxy to date, conducted using the Gaia satellite launched in 2013. Its high sensitivity ($G \sim 21$) means that it can measure the astrometry - particularly the parallaxes and proper motions - of sources with unprecedented precision ($<$ mas). The Gaia Data Release 3 (DR3, Gaia Collaboration et al., 2022) is the newest edition of the Gaia catalogue, with full astrometry for over 1.4 billion sources.

Despite the fact that MYSOs had generally been thought to be effectively invisible at optical wavelengths, as I will demonstrate below a significant fraction of YSOs from the RMS catalogue are present in the Gaia catalogue. This revelation, which has led to the construction of an optical catalogue of every MYSO in the Galaxy, means that MYSOs can be studied in the optical for the first time. From this catalogue, the first optical study of MYSO multiplicity has been conducted.

In this chapter I will outline the construction of the optical MYSO catalogue in Section 4.2, and then I will investigate the multiplicity of the MYSOs in this catalogue by comparing their parallaxes and proper motions to nearby objects in their vicinity in Section 4.3. In Section 4.4 I will discuss the results and how they factor into the conversation of MYSO binarity. I summarise my findings in Section 4.5.

4.2 Construction of the Catalogue

The catalogue was constructed using data from the third data release (DR3, Gaia Collaboration et al., 2022) of the Gaia mission. The purpose of the Gaia mission is to determine positions, parallaxes, proper motions and radial velocities for over a billion sources across the whole sky. Additionally it has determined G, G_{BP} and G_{RP} magnitudes for $\sim$1.5 billion sources. It is independent of previous surveys, and was launched in 2013. The data in DR3 was collected between July 2014 and May 2017.

From this data, a catalogue of YSOs present in Gaia was constructed. This work was carried out as part of a University of Leeds MSc project by Daniel Valentine, Jack English and Harry Turner (with me as co-supervisor). Each of the YSOs in the RMS catalogue were cross-referenced with the Gaia catalogue using their MSX coordinates, to find any optical counterparts. A maximum radius of 5 arcseconds was chosen to allow for any misalignments between the MSX and Gaia coordinates. To assess any detections, visual inspections were conducted using the Aladin Sky Atlas (Bonnarel et al., 2000) in multiple different wavebands, from imaging surveys such as 2MASS, Pan-STARSS DR1 and DECaPS DR1. This helped in differentiating between optical YSO detections and nearby unrelated objects, with Gaia points overplotted on the images. Firstly 2MASS was used to view a source in the IR, but the bright IR emission of YSOs and the survey's relatively low resolution meant that source confusion became a common issue, especially in crowded regions. Sources were then viewed in the optical surveys of Pan-STARSS and DECaPS to provide better interpretation of close sources. The combination of higher resolution images and a lesser amount of extended emission in the optical meant this was an effective way of pinpointing optically visible YSOs.

The difference between the RA and Dec of the MSX and Gaia coordinates were plotted to determine how consistent the two surveys are, shown in Figure 4.1. The FWHMs of the RA and Dec discrepancies are both 0.6 arcsec, showing that generally the surveys

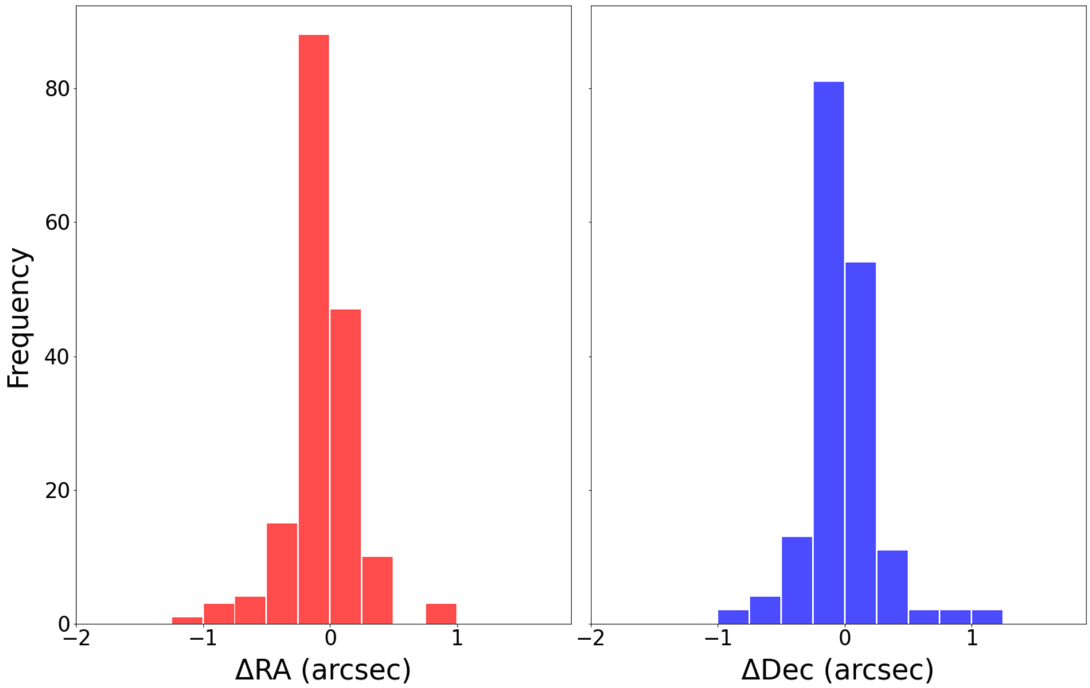

Figure 4.1: Histograms of the difference between Gaia and RMS right ascension (left) and declination (right) for all YSOs in the optical catalogue. The FWHM for the differences in RA is 0.6 arcsec and there is an average RA difference of -0.05 arcsec. The FWHM for the differences in Dec is 0.6 arcsec and there is an average Dec difference of -0.006 arcsec.

align very well with each other. Two reasons for large coordinate shifts were either crowded regions of the sky causing source confusion, or differences in emission morphology when comparing the different wavelength images due to the IR-bright dust (examples can be found in Figure 4.2 and Figure 4.3). Any outliers were ultimately found to be simple coordinate discrepancies and not incorrectly matched objects. The completed Gaia YSO catalogue consists of 172 YSOs (out of a total of 863 objects labelled YSO or HII/YSO), giving a detection rate of 20%. Luminosities of the YSOs were taken from the RMS catalogue (Lumsden et al., 2013), and the corresponding masses were determined using the mass-luminosity relations of Davies et al. (2011).

With the completion of the optical YSO catalogue, an analysis of the binarity of these YSOs could be performed and their mass ratios were determined using a similar

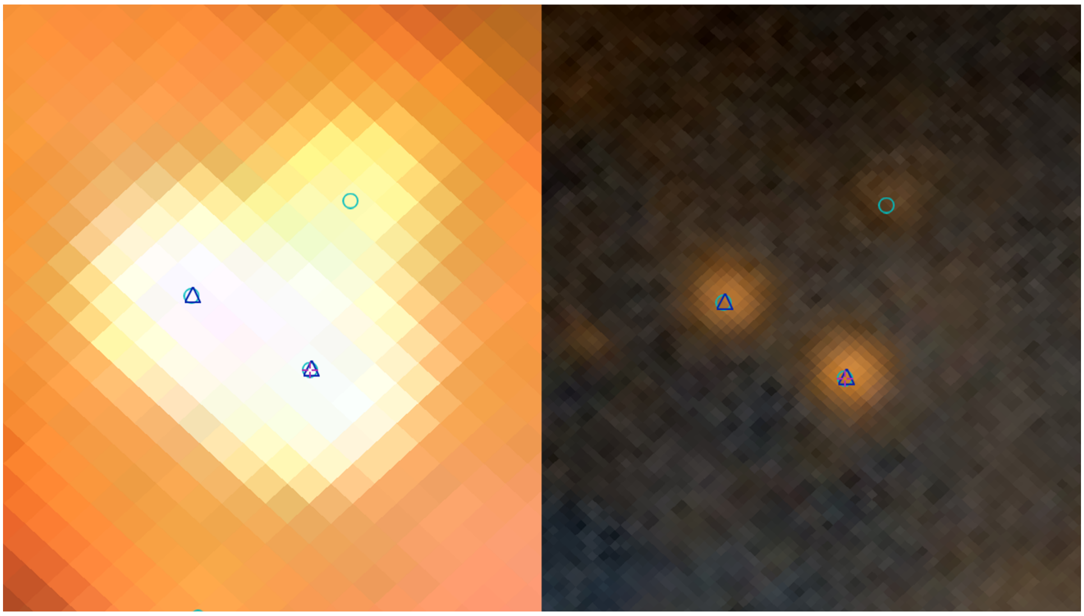

Figure 4.2: 2MASS (left) and Pan-STARSS DR1 (right) colour images of the YSO G015.1288-00.6717, with a field of view of ∼15″x15″. RMS coordinates are shown as a purple cross-hair. Gaia DR3 detections are shown as dark blue triangles, while 2MASS detections are represented as light blue circles. The 2MASS image shows how the bright infrared emission of YSOs regularly causes source confusion issues in 2MASS, but these objects are clearly distinguishable in the optical Pan-STARSS survey.

method to that of Subsection 2.3.5. The whole catalogue of YSOs detected in Gaia can be found in Table C.1.

4.3 Results

4.3.1 RMS catalogue assessment

In the RMS catalogue, distances were determined kinematically from velocities. By combining the Galactic rotation with the radial velocity, a distance for each object was be inferred (Busfield et al., 2006; Urquhart et al., 2011). For Gaia objects, parallax data provides an estimate of the distance simply by inverting the parallax. Additionally, distances to 1.47 billion stars in Gaia DR3 were estimated in Bailer-Jones et al. (2021), which accounted for the galactic anisotropy and inhomogeneity in the distri-

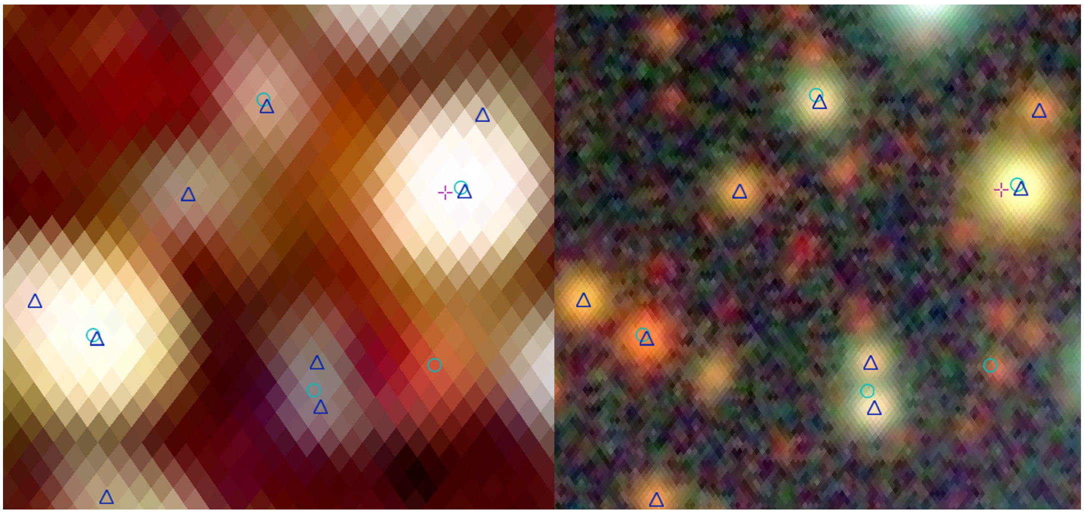

Figure 4.3: 2MASS (left) and DECaPS DR1 (right) colour images of the YSO G320.2878-00.3069A, with a field of view of $\sim$20″x20″. RMS coordinates are shown as a purple cross-hair. Gaia DR3 detections are shown as dark blue triangles, and 2MASS detections are represented as light blue circles. Both images show the RMS coordinates shifted to the left of the Gaia and 2MASS detections.

bution of objects. This method uses a distance prior along with Gaia parallax data to provide improved distances. Due to the differing nature of these distance estimates, an assessment of the YSOs present in Gaia will help in determining how accurate the RMS distances are compared to Gaia-derived distances.

One important decision was whether or not to use the Bailer-Jones geometric distances for binary detection. Many of the YSOs detected in Gaia have relatively large parallax uncertainties due to their faint magnitudes and large distances. Poor parallax data leads to poor distance determinations where the prior dominates over the parallax (Bailer-Jones et al., 2021), meaning the Bailer-Jones distance derived for these objects may be dominated by the prior and so may be unreliable. To investigate, I compared the Bailer-Jones distances and the raw Gaia parallaxes with the RMS catalogue distances.

For the YSOs in the optical catalogue, the average Bailer-Jones distance is $2.9^{+1.1}_{-0.8}$ kpc. For the same objects, the average RMS distance is 3.9 ± 1 kpc. A plot of RMS

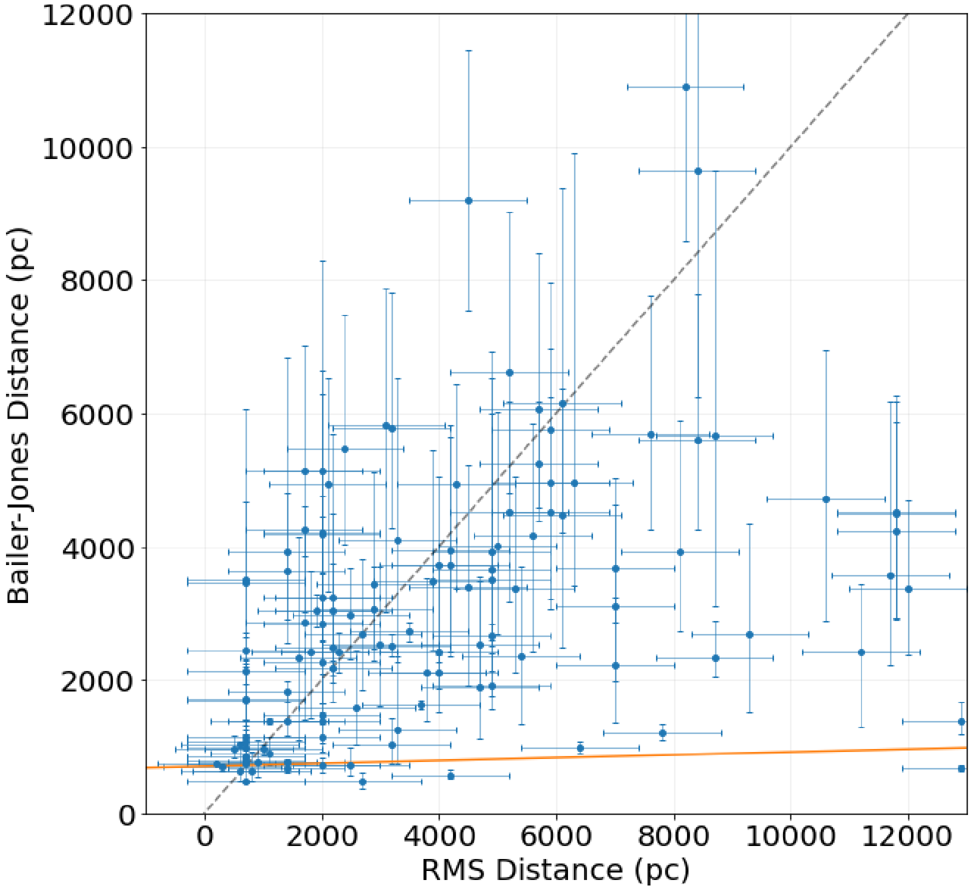

Figure 4.4: RMS distance against Bailer-Jones geometric distance. The orange line is the least squares best fit, weighted by the inverse of the Bailer-Jones distance uncertainty.

distance against Gaia Bailer-Jones distance is shown in Figure 4.4. The distances have been fitted using a least-squares fit, weighted depending on the uncertainty in the Gaia distance ($\frac{1}{\Delta d_{B-J}}$, where Δd_{B-J} is the uncertainty in the Bailer-Jones distance). The uncertainty in the RMS distances is set at a flat ± 1 kpc (Urquhart et al., 2008, with the exception of some sources with $d < 1$ kpc) and so are not calculated statistically, but through the kinematic determinations of distances as in Urquhart et al. (2011). As a result these errors were not considered for the fitting process. The correlation between the RMS kinematic distances and the Bailer-Jones distances had a coefficient of 0.26, which indicates a weak relationship between the two distance estimates.

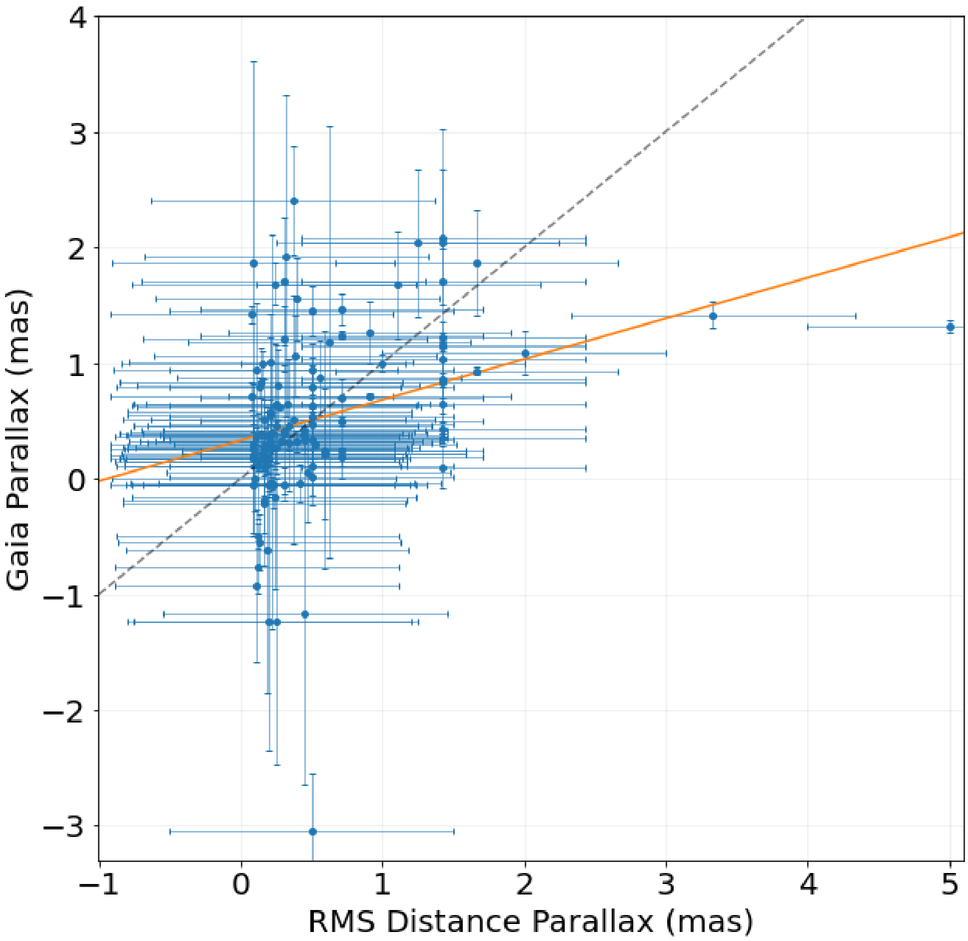

Figure 4.5: RMS parallax (derived from the RMS distance) against Gaia parallax for all YSOs in Gaia. The orange line is the least squares best fit, weighted by the inverse of the Gaia parallax uncertainty.

Instead, to determine how well RMS distances correlate to the raw Gaia parallaxes, the RMS distances were inverted to convert them to a parallax, and compared to the Gaia parallaxes. Figure 4.5 shows the comparison between the two parallax values. The data have been fitted with with a linear regression, weighted by $\frac{1}{\Delta\varpi_{Gaia}}$, where $\Delta\varpi_{Gaia}$ is the uncertainty in the Gaia parallax. The average Gaia parallax uncertainty is $\sim$0.34 mas. The uncertainties on the RMS parallaxes were derived using the uncertainty in the RMS distances of $\sim$1 kpc.

The RMS and Gaia parallaxes have a correlation parameter of 0.49, an almost 2x

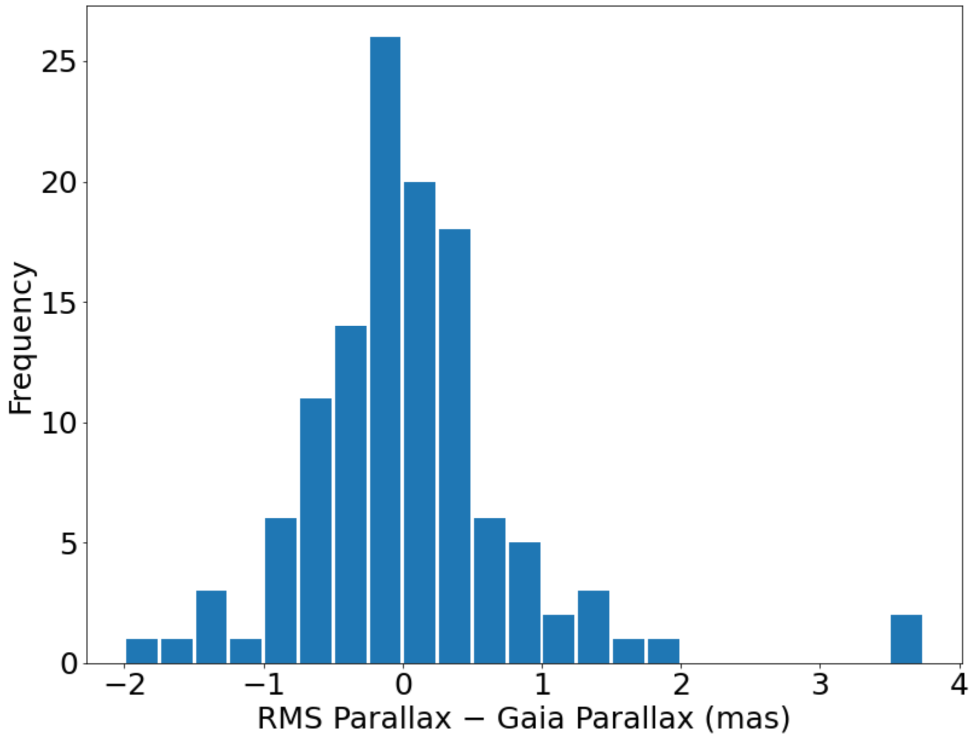

Figure 4.6: Histogram of the difference between Gaia and RMS parallax for the optical catalogue YSOs. The average value is 0.03 mas, and the FWHM of the differences is ~1.9 mas.

improvement over the correlation parameter of 0.26 of the Bailer-Jones and RMS distances. A histogram of the differences between the two parallax values for each object can be found in Figure 4.6.

Combined with the aforementioned fact that the Bailer-Jones distances are likely to be dominated by the prior for this sample, this means that using the raw parallax data is a safer and more authentic approach. Therefore, going forward the parallax data was used for binary determination instead of the Bailer-Jones prior-derived distances. RMS distances were retained for the luminosity/mass determinations due to the large amount of information available for determining these properties. RMS distances were not used for binary determination, due to the fact that no corresponding distance is available for the potential companions, and using different distance sources between primary and secondary may introduce issues.

4.3.2 Optical survey of MYSO multiplicity

Once the properties of the optical MYSO catalogue were compared against the entire RMS catalogue, I investigated the binarity of these optically-detected MYSOs. In Chapter 2 I used the primary-secondary separation and the density of background objects to analyse whether two or more objects were gravitationally bound. A different approach can be used with Gaia data; if a YSO has a true companion, that companion will lie at practically the same distance as the primary, and will have a very similar proper motion with the position vectors having the same orientation and magnitude. Non-physical binaries will deviate from the primary in at least one of these parameters. Therefore binarity can be inferred through proximity to the MYSO and a consistent parallax and proper motion, indicating the presence of a co-moving companion. Parallaxes were used instead of Bailer-Jones distances due to their aforementioned unreliability at typical YSO distances.

All YSOs in the catalogue, not just MYSOs, were analysed to allow for a comparison between the multiplicity statistics of the high- and low-mass subsets. Firstly, all objects within a radius of $15''$ of each YSO primary were found in the Gaia archive. For any of these nearby objects to be considered a physical companion, they had to meet the following criteria:

1. Both the primary and the object must have values for parallax (ϖ), proper motion along the RA axis (μ_α) and proper motion along the Dec axis (μ_δ).
2. The object must overlap with the primary in all three of the parameters mentioned above within 1σ error.

From the 172 primary YSOs in the catalogue, 139 had adequate astrometry available to be able to perform a companion analysis. This master sample consists of 58 MYSOs

(>8 $M_\odot$, Davies et al., 2011) and 69 low-mass YSOs (<8 $M_\odot$), along with 12 YSOs with an unknown mass. The average mass is 9 $M_\odot$ and the average distance is 4 kpc, with distances ranging from 0.2 - 13 kpc. From Gaia's resolution limit of 0.7" (Gaia Collaboration et al., 2021) and the maximum radius probed of 15", the physical separation range probed in this survey is 200 - 200,000 au.

As an example of the position and motion of the YSOs and their nearby objects, sky plots were made for each YSO, showing the parallax of each nearby object via colour coding and the proper motion via arrows. These sky plots were used to visualise companion status, and also provide a simple way to theorise whether the YSO is part of a cluster of comoving objects or whether a group of objects exhibit strong Galactic motion. An example sky plot can be seen in Figure 4.7, and the sky plots for the entire sample can be seen in Appendix D. In the example plot in Figure 4.7, G082.5682A can be seen to have one companion with a parallax and proper motion consistent with that of itself.

Pomohaci et al. 2019 verification

To determine the viability of this method, it was used to verify the results of Pomohaci et al. (2019). Four of the YSOs surveyed in that work which were determined to have a nearby object were found in Gaia along with at least one of those nearby objects. The results generally showed that four nearby objects deemed to be chance projections by Pomohaci et al. (2019) were also disregarded by the Gaia method, but one object discarded by Pomohaci et al. (2019) was determined to be a companion using Gaia data. This indicates that both methods may be effective at discarding chance projections but the overlap of physical companions between these methods could be small. The results of this work are compared with the larger sample of Chapter 2 later.

4.3.3 Multiplicity statistics

A total of 77 companions were detected from the sample of 139 YSOs. There are 31 binaries, 7 triples, 3 quadruples and 5 higher order systems. The multiplicity fraction MF=$\frac{N_{mult}}{N_{tot}}$ for this survey was determined to be 33±8%, with N_{mult} =46. The companion fraction CF was determined to be 55±6%. The uncertainties on the fractions were determined using binomial confidence intervals, which usually assume Gaussian errors. A table of all detected companions in Gaia is presented in in Table 4.1.

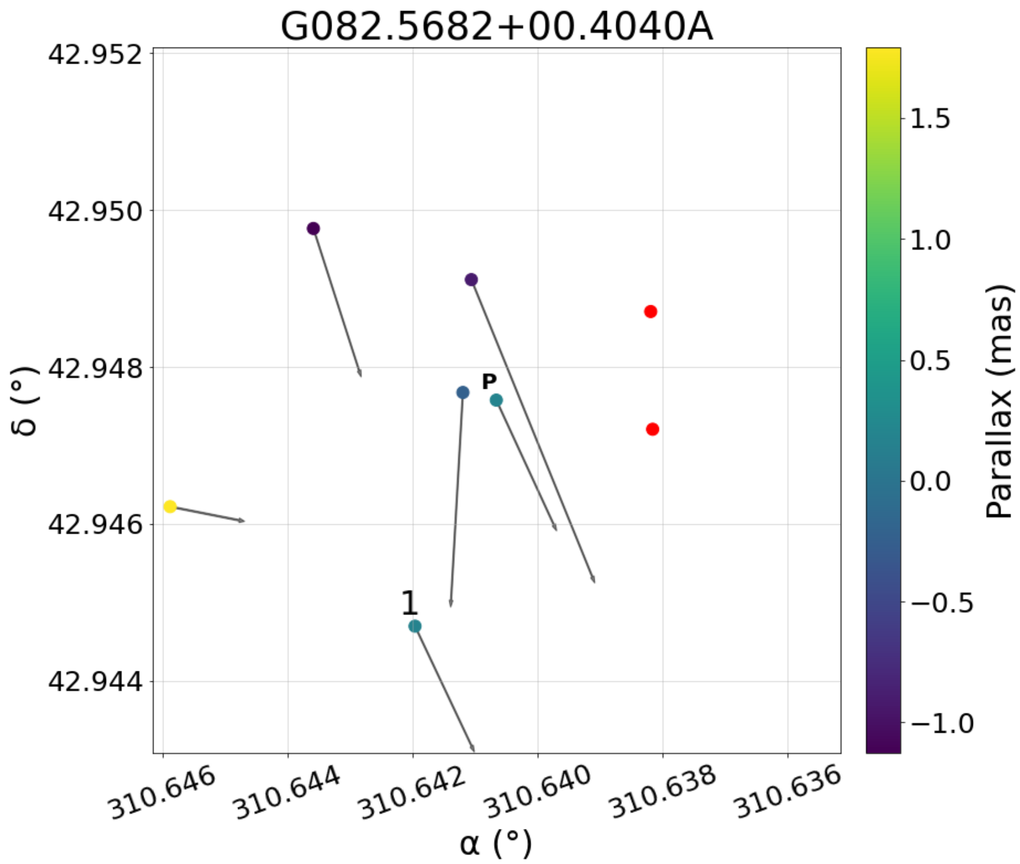

Figure 4.7: An example of a sky plot for the YSO G082.5682+00.4040A. Each point is a source detected in Gaia. Each valid point is colour-coded by its parallax, and has an attached arrow showing its proper motion. Sources with no valid astrometry are shown as red points with no arrow. The primary YSO is labelled with 'P', and any nearby objects that have been determined to be companions to the primary have been numbered. In this case, G082.5682A was found to have one companion, labelled '1', with a consistent proper motion and parallax. The typical parallax error for the YSOs is ∼0.2 mas or less.

Table 4.1: Table of all companions detected in Gaia. Positions, parallaxes and proper motions taken from Gaia DR3. Parallaxes and proper motions have been given to up to three decimal places, as some detected companions had very little parallax or proper motion overlap between themselves and the primary; rounding could make them appear as if they would not overlap at all.

Primary RMS ID	Companion Gaia ID	RA (deg)	Dec (deg)	ϖ (mas)	μ_α (mas yr^{-1})	μ_δ (mas yr^{-1})	G (mag)	BP-RP (mag)	Separation (arcsec)
G015.1288-00.6717	4098003634866306560	275.1451	-16.1073	0.939±0.729	-1.031±1.084	-2.316±0.847	20.0	3.4	3.8
G020.7617-00.0638B	4154942501642616960	277.2973	-10.8459	0.525±0.351	-0.236±0.492	0.997±0.46	19.0	2.6	14.9
G023.8176+00.3841	4156713844934255232	278.3318	-7.9253	0.249±0.16	-0.306±0.174	-4.642±0.152	18.3	3.6	6.1
G023.8176+00.3841	4156713849228449792	278.3307	-7.9292	0.767±0.91	-2.029±0.828	-4.311±0.7	20.2		8.5
G023.8176+00.3841	4156713844931953536	278.3311	-7.9293	0.864±0.213	-1.467±0.237	-3.795±0.203	17.4	2.5	8.9
G023.8176+00.3841	4156713849228461184	278.3292	-7.9287	0.137±0.407	-1.554±0.491	-6.379±0.423	19.5	2.3	9.6
G032.0518-00.0902	4266059696498179456	282.5382	-0.8233	-1.115±1.329	-0.843±1.105	-3.005±1.048	20.6		4.8
G049.5993-00.2488	4319862060333763200	290.8599	14.6737	1.135±1.002	-1.477±1.04	-5.147±0.736	20.7	2.4	9.1
G051.3617-00.0132	4322379362139148416	291.5094	16.3331	0.021±0.185	-2.729±0.169	-5.797±0.172	18.2	4.7	11.9
G056.4120-00.0277	1826022731928753024	294.0872	20.7525	0.76±1.5	-3.001±1.292	-7.959±1.665	20.8	2.7	12.1
G059.4657-00.0457	2020102717670678144	295.7315	23.4065	0.258±0.43	-1.634±0.229	-4.926±0.376	19.9		11.9
G073.6525+00.1944	2057379224166044416	304.0965	35.6015	0.436±0.014	-2.411±0.015	-2.599±0.016	13.9	1.6	15.0
G073.6525+00.1944	2057379219863846272	304.0916	35.6054	0.574±0.38	-2.48±0.369	0.342±0.406	19.9	2.2	13.2
G078.1224+03.6320	2062619354845085440	303.6125	41.2246	0.132±0.482	-4.084±0.552	-5.588±0.639	20.2	3.4	15.0
G080.9340-00.1880	2066325842897208448	309.9203	41.2894	0.596±0.764	-1.203±0.706	-3.399±1.128	20.6	2.4	14.2
G082.5682+00.4040A	2066562306616624512	310.6420	42.9447	0.178±0.109	-2.716±0.117	-4.588±0.126	18.0	2.7	10.9
G100.2124+01.8829	2198977355244330624	328.2337	56.6654	0.249±0.298	-2.369±0.343	-2.307±0.285	19.6	2.1	9.0
G100.2124+01.8829	2198977144784776704	328.2437	56.6669	0.03±0.1	-2.679±0.12	-2.152±0.098	18.0	2.0	12.6
G100.2124+01.8829	2198977149093332992	328.2369	56.6648	0.17±0.171	-2.672±0.207	-2.193±0.179	18.8	2.2	2.9
G100.2124+01.8829	2198977149093333120	328.2383	56.6655	0.079±0.099	-2.539±0.123	-2.23±0.101	17.9	2.2	1.2
G101.2490+02.5764	2199376233149055872	328.9343	57.8509	-0.415±0.191	-2.254±0.22	-3.578±0.242	18.7	2.0	10.6
G101.2490+02.5764	2199376237445137408	328.9416	57.8547	0.056±0.351	-2.491±0.38	-2.882±0.411	19.9	2.2	11.9
G101.2490+02.5764	2199376237446614656	328.9397	57.8505	0.203±0.61	-3.249±0.783	-4.036±0.909	20.4	2.6	3.6
G107.6823-02.2423A	2010087747286916992	343.8758	57.1608	-0.413±1.258	-4.894±1.445	-2.468±0.992	20.4	1.7	14.2

Primary RMS ID	Companion Gaia ID	RA (deg)	Dec (deg)	ϖ (mas)	μ_α (mas yr^{-1})	μ_δ (mas yr^{-1})	G (mag)	BP-RP (mag)	Separation (arcsec)
G107.6823-02.2423A	2010084796644075648	343.8763	57.1599	0.431±0.557	-3.097±0.597	-3.869±0.548	20.2	2.0	11.6
G111.2980-00.6606	2013835535748589952	349.0509	60.0427	0.5±0.158	-2.886±0.172	-1.617±0.17	18.8	1.6	14.0
G120.1483+03.3745	527470435478103424	5.9956	66.0986	-0.445±0.739	-3.392±0.833	-0.645±0.819	20.5	2.7	11.9
G121.3479-03.3705	425522617841329920	9.7457	59.4658	-0.106±0.539	-3.531±0.514	-0.081±0.721	20.3	2.0	9.5
G123.2836+03.0307	526085527569561216	13.7245	65.8977	-0.942±1.065	-0.841±1.034	-0.696±1.695	20.9	2.3	8.8
G123.8059-01.7805	426650029577697920	14.6700	61.0778	0.253±0.121	-2.366±0.111	-1.032±0.138	18.1	2.5	6.1
G123.8059-01.7805	426650029578600704	14.6706	61.0787	-0.507±1.383	-3.668±1.55	-1.357±2.639	20.7	2.4	6.4
G123.8059-01.7805	426650029578396672	14.6715	61.0778	0.653±0.721	-2.048±0.612	-1.163±0.747	20.4	2.3	8.4
G123.8059-01.7805	426650025277470592	14.6595	61.0787	0.979±0.958	-2.751±0.975	-0.714±1.137	20.5	2.1	12.8
G123.8059-01.7805	426650029583408512	14.6658	61.0789	0.238±0.103	-2.322±0.091	-1.123±0.123	17.7	2.3	2.4
G123.8059-01.7805	426650029583407232	14.6602	61.0793	0.4±0.096	-2.481±0.084	-0.956±0.111	17.5	2.9	11.9
G150.6862-00.6887	250753316161780096	61.2122	51.4489	0.312±0.378	-0.906±0.564	-1.432±0.353	19.5	2.4	12.2
G168.0627+00.8221	188633249951112576	79.3086	39.3750	-0.589±0.895	-0.22±1.296	-0.128±0.845	20.5	1.8	11.6
G174.1974-00.0763	3449181243489228160	82.6908	33.7977	-1.211±1.929	2.766±2.748	-1.938±1.333	20.9	1.8	4.3
G202.9943+02.1040	3326715847386516736	100.1881	9.7984	1.27±0.264	-1.53±0.335	-3.619±0.263	19.0	2.5	10.8
G212.9626+01.2954	3113711170591097600	104.0268	0.5616	0.717±2.174	-1.905±2.595	1.737±2.217	20.7	1.6	6.1
G217.0441-00.0584	3102590783001485440	104.6862	-3.6878	1.422±1.066	0.569±1.505	0.012±1.203	20.5		7.9
G231.7986-01.9682	2931756358561613312	109.9033	-17.6570	0.56±0.482	-1.534±0.434	2.702±0.524	19.9	2.8	14.0
G233.8306-00.1803	3026531825639762432	112.5701	-18.6003	1.531±0.629	-2.218±0.621	0.057±0.703	20.3	2.2	11.9
G263.5994-00.5236	5523960750255191552	131.3867	-43.8288	-0.037±0.911	-4.321±1.108	4.416±1.288	20.8	1.9	5.2
G267.7336-01.1058A	5330100765626318080	134.5162	-47.3822	0.95±0.527	-4.95±0.594	4.431±0.499	20.1	2.7	14.4
G282.2988-00.7769	5258914710657579904	152.4993	-57.0365	1.207±0.901	-5.135±0.964	2.041±1.232	19.7	2.7	5.6
G287.3716+00.6444	5350910367528142080	162.0189	-58.4523	0.332±0.333	-5.125±0.403	2.718±0.355	19.9	2.1	6.6
G287.6790-00.8669	5350302131442512128	161.1910	-59.9304	0.285±0.09	-6.996±0.106	1.758±0.091	17.6	1.7	4.6
G287.6790-00.8669	5350302131421243904	161.1939	-59.9345	1.229±1.082	-5.949±1.151	2.3±0.987	20.4	1.4	12.7
G289.1447-00.3454	5338323501993331328	164.2726	-60.1208	-0.628±0.763	-6.104±1.066	2.015±0.849	20.6	1.3	14.0
G289.1447-00.3454	5338323501993342720	164.2741	-60.1192	-0.423±0.845	-5.79±1.215	1.521±0.85	20.6	1.4	12.0
G289.1447-00.3454	5338323501993386880	164.2836	-60.1222	-0.907±0.636	-4.947±0.758	2.994±0.696	20.4	1.4	8.9
G289.1447-00.3454	5338323501993373056	164.2804	-60.1199	-0.017±0.363	-5.737±0.513	2.484±0.341	19.6		1.4

Primary RMS ID	Companion Gaia ID	RA (deg)	Dec (deg)	ϖ (mas)	μ_α (mas yr^{-1})	μ_δ (mas yr^{-1})	G (mag)	BP-RP (mag)	Separation (arcsec)
G289.1447-00.3454	5338323501993351424	164.2760	-60.1197	-0.177±0.274	-5.978±0.331	2.068±0.307	19.6	1.7	8.2
G290.0105-00.8668A	5337957158479302400	165.4444	-60.9566	0.467±0.347	-5.756±0.417	2.121±0.363	19.7	1.5	13.4
G290.0105-00.8668A	5337957227198755968	165.4348	-60.9604	0.335±0.305	-6.126±0.336	2.349±0.32	19.4		12.0
G290.0105-00.8668A	5337957227198753792	165.4321	-60.9580	0.391±0.444	-5.785±0.532	2.013±0.449	20.0	1.9	8.8
G296.2654-00.3901	5334625054151276288	178.2997	-62.5027	0.319±1.248	-8.139±2.213	0.764±1.762	20.8	1.7	12.4
G296.2654-00.3901	5334625015485489920	178.2866	-62.5059	0.086±0.334	-5.195±0.38	1.891±0.387	19.8	2.1	14.8
G296.2654-00.3901	5334625019789727744	178.2937	-62.5064	-0.44±0.777	-5.595±0.854	0.358±0.835	20.1		4.2
G296.2654-00.3901	5334625054149502848	178.3004	-62.5047	0.135±0.35	-5.989±0.402	1.547±0.381	19.9	2.1	8.7
G300.3412-00.2190	6053804576075120128	187.1503	-62.9785	0.068±0.319	-6.612±0.327	0.477±0.376	19.6	3.1	7.5
G300.3412-00.2190	6053804580395068800	187.1523	-62.9789	0.587±0.251	-6.183±0.258	1.651±0.287	19.3	2.3	10.5
G301.1726+01.0034	6054731537391513600	189.1394	-61.8145	-1.564±1.94	-6.085±1.587	-1.774±1.767	20.9	1.0	15.0
G304.3674-00.3359A	5862383385556531456	196.0357	-63.1734	-0.075±0.744	-7.55±0.637	-0.715±1.057	20.5	2.5	10.7
G308.7008+00.5312	5865765242816849536	205.1402	-61.7878	1.963±1.384	-4.288±1.561	-1.972±1.022	20.8	2.1	8.3
G308.7008+00.5312	5865765208456472576	205.1306	-61.7920	0.33±0.31	-5.404±0.239	-1.362±0.238	19.6	2.0	14.4
G308.7008+00.5312	5865765208456472704	205.1364	-61.7912	0.91±0.395	-5.971±0.31	-1.38±0.308	20.0	2.2	8.0
G326.7249+00.6159B	5885649150368871552	236.2451	-54.0401	1.669±0.672	-2.97±0.729	-3.447±0.651	20.1	2.8	8.9
G328.3442-00.4629	5980805834440030336	239.5371	-53.8543	0.5±0.45	-3.513±0.434	-2.783±0.301	19.5	2.6	6.9
G328.3442-00.4629	5980805800080290560	239.5349	-53.8574	0.225±0.289	-3.226±0.299	-3.008±0.245	19.2	2.7	13.8
G328.9842-00.4361	5980832944277564672	240.3240	-53.4201	0.318±0.196	-2.5±0.224	-2.002±0.157	18.6	2.2	14.3
G338.9377-00.4890B	5943066304696403072	251.2871	-46.3748	1.216±0.585	-1.416±0.647	-0.614±0.452	19.3	2.1	10.1
G339.7602+00.0530A	5943223908530897536	251.4629	-45.3896	0.684±0.48	-3.88±0.576	-3.957±0.401	19.5	4.3	11.7
G339.7602+00.0530A	5943212161789159296	251.4696	-45.3925	0.287±1.458	-3.461±2.101	-2.697±1.331	20.4		12.0
G340.1537+00.5116	5943270813887664640	251.3377	-44.7996	-0.474±1.117	-3.259±2.026	-3.961±1.213	20.4		13.2
G340.1537+00.5116	5943264938352568320	251.3294	-44.7985	-0.918±1.711	-4.318±2.458	-1.539±1.586	20.6	1.3	12.0

4.3.4 Mass ratios

To determine masses of the Gaia-detected companions, the extinction towards the companions was determined in a similar fashion to that of the companions detected using $K-$band imaging in Subsection 2.3.5. The two methods of determining extinction used are the same as in that chapter: an interstellar extinction map providing a lower limit (foreground extinction), and a comparison between the intrinsic and expected infrared colour of the object acting as the upper limit (total, or foreground + circumstellar extinction).

Firstly infrared photometry was retrieved for as many objects in the catalogue as possible, using a combination of the UKIDSS (Lucas et al., 2008), VVV (Saito et al., 2012) and 2MASS (Skrutskie et al., 2006) infrared surveys. When a source was likely to be saturated in UKIDSS/VVV ($J \lesssim 12.8$, $H \lesssim 12.3$, $K \lesssim 11.5$), the 2MASS photometry was used instead. Of the 77 YSO companions detected in Gaia, 49 (64%) had adequate JHK photometry for a mass ratio analysis.

For the foreground extinction estimates, a combination of the Bayestar19 (Green et al., 2019) and Stilism (Capitanio et al., 2017) dust maps were used, with Bayestar19 being able to handle larger distances better, but Stilism covering the entire sky. Bayestar19 was the prioritised dust map with Stilism covering the remaining uncovered regions.

For the estimates of total extinction, the JHK photometry was used to determine the observed colours of the companions, which were then compared to the intrinsic/-expected colours of a MS B0 star (which corresponds to the typical RMS MYSO in terms of mass) to determine A_V as in Cooper et al. (2013). $J-H$ was the preferred colour due to the effect of $K-$band excess which leads to overestimates of the extinction. However in a few cases where $J-$band photometry was not available, the $H-K$ colour was used instead.

Using these extinction estimates, the $K-$ and $J-$band magnitudes of the companions were converted to intrinsic magnitudes (also using the RMS distances of the primary YSOs). These estimates of K_{abs} and J_{abs} were used as a proxy for the mass as in Oudmaijer and Parr (2010) (see also Subsection 2.3.5), which assumes an MS star. Equation 2.2 and Equation 2.3 were used to determine masses for the companions. The next step would be to use optical data from Gaia to better determine the extinctions and masses, but this requires further investigation and is outside the scope of this thesis.

4.4 Discussion

4.4.1 RMS catalogue

From the comparisons performed earlier in Subsection 4.3.1, while it is clear that RMS distances and Gaia parallaxes do not exhibit a 1:1 correlation, they share a strong enough correlation to be used in tandem with each other. Additionally, prior distances determined from parallaxes by Bailer-Jones et al. (2021) are not reliable for YSOs, as the errors of the parallaxes for the objects in question are generally large, which leads to the prior dominating the determined distance. Therefore the parallax has less impact on the derived distance than the prior itself for these objects. For this survey, Gaia parallaxes were used as the distance indicator for detecting companions, while RMS distances were used for determining extinctions and mass ratios. In the future, Gaia could be used to help improve the determination of distances towards YSOs.

4.4.2 YSO multiplicity

The results of the multiplicity survey of MF=33±8% and CF=55±6% are lower than that of the results in Chapter 2 and Chapter 3. This is likely due to the embedded nature of YSOs; while the primaries detected in Gaia are sufficiently luminous to be detected despite their surrounding dust cloud, any companions may also be susceptible to this dust cloud and therefore may not be bright enough to be detected in the Gaia survey.

The master sample was split into subsets based on primary mass; the MYSO subset has an average mass of 12.9 $M_\odot$ and an average RMS distance of 5.7 kpc, while the low-mass/unknown mass subset has an average mass of 5.4 $M_\odot$ and an average distance of 2.1 kpc. The MF of the MYSO subset is 50±13% (29 multiples out of 58 total), and the MF of the low-mass/unknown mass subset was found to be $21\pm^{10}_{8}$% (17 multiples out of 81 total). This agrees with the stipulation that multiplicity increases with mass (Offner et al., 2022). When looking at the massive subsample only, the multiplicity fraction of 50±13% is in agreement with that of the high-mass subsets of Chapter 2. Therefore between these two methods, the frequency of MYSO multiplicity is found to be very similar, but the multiplicity of low-mass YSOs is significantly lower in the Gaia study.

120 of the companions detected in Chapter 2 are associated with MYSOs that are also studied in this chapter; only 5 of those companions were determined to be companions in Gaia as well, giving a retrieval rate of ∼4%. This is a tiny fraction of the binaries found through the imaging method, and is most likely down to the different approaches used. Additionally, 315 of the 874 total detected companions in Chapter 2 are present in the Gaia DR3 catalogue within 1 arcsec. 4 of these were also determined to be companions in this chapter.

The imaging sample of Chapter 2 does not have any measure of distance or motion, and is a statistical approach using only object separation, brightness and background density. The Gaia method allows for more of a three-dimensional approach thanks to parallax and proper motion data which can rule out chance projections more effectively. The majority of companions detected by Gaia but missed by UKIDSS/VVV are not sufficiently bright in the infrared and did not have photometry available, and so they could not be assigned a companion probability. Other reasons are that some companions were in very dense regions of the sky, and so the statistical method of

Chapter 2 discarded them but the Gaia method kept them as companions. This optical study should therefore be seen as complementary to that of an infrared study; relatively few companions detected in one regime are also detected in the other.

The results found here for the entire sample are in strong agreement with the multiplicity statistics of Pomohaci et al. (2019), which found MF=31±8% and CF=55±9%. The separations probed in this study are wider than that of Pomohaci et al. (2019), so the similar multiplicity statistics are an indication that companions exist in large numbers at both small and large separations. De Rosa et al. (2014) found that the separation distribution of A star companions maxes out to around 400 au when probing between 30-45,000 au, suggesting that there are many close companions missed by Gaia and the methods of Chapter 2. Additionally, the fact that only 20% of YSOs are detected in Gaia in the first place may suggest that a similar fraction of the total number of companions are detected optically; this could reaffirm the statement made in Subsection 2.4.5 that up to 100% of YSOs have companions, and that a large amount of these may be triple systems with a close-in companion and a companion further out.

4.4.3 Distance/luminosity comparison

The average luminosity of the Gaia sample is 7800 $L_\odot$, and it has an average distance of 3.3 kpc. In comparison, the entire YSO population of the RMS catalogue has an average luminosity of 11000 $L_\odot$ and an average distance of 4.3 kpc. This suggests that the YSOs detected by Gaia are generally the closer YSOs, as objects further away will generally be too faint for Gaia to pick up.

Using the typical distance of the primary, the companions have an average physical separation of ∼33,000 au, ranging from 12,000-50,000 au (using the total distance range, the extremes of detectable separations are 3600-120,000 au). This is smaller than the average distance between stars in clusters (on average ∼1 pc, down to ∼40,000 au in the very densest regions). Additionally, the companions are on average redder than nearby field stars. These points support the idea that these companions are genuine and not simply members of the same cluster. Companions were generally found at larger separations which gives support to the core and/or filament fragmentation theories for binary formation (Offner et al., 2010), and goes against the close binary predictions made in the disc fragmentation model (Meyer et al., 2018). However this study is biased against close companions due to the resolution of Gaia, with companions closer than 0.7" (corresponding to ∼2000 au) unable to be detected, and therefore cannot be taken on its own as evidence for any formation theory. As mentioned earlier, this should be taken as complementary with the previous chapters as a combined study across multiple separation ranges and wavebands. The results of previous chapters are brought together with this work in Chapter 5.

4.4.4 Mass ratios

The masses (M) and mass ratios (q) for all companions with adequate infrared photometry are presented in Table 4.2. Figure 4.8 shows histograms of mass ratios for foreground and total extinction estimates, using both $K-$ and $J-$band photometry. There are four main sources for the determination of the mass: foreground $K-$band ($M_{fg,K}$), foreground $J-$band ($M_{fg,J}$), total $K-$band ($M_{tot,K}$) and total $J-$band ($M_{tot,J}$). A table of the average, minimum and maximum masses and mass ratios for each extinction source can be found in Table 4.3.

Table 4.2: JHK magnitudes, masses and mass ratios for all detected YSO companions in Gaia. d_{prim} is the RMS distance for the primary YSO and M_{prim} is the derived primary mass from its RMS bolometric luminosity. J, H and K represent the infrared magnitudes of the source; the magnitudes tagged with ^{2M} have been taken from 2MASS, and the rest have been retrieved from UKIDSS or VVV. $M_{fg,X}$ represents a mass derived using foreground extinction, and $M_{tot,X}$ represents a mass derived using total extinction, labelled with the waveband X. q is the mass ratio of the corresponding companion mass and d_{prim}.

Gaia DR3 Source ID	Primary RMS ID	d_{prim} (kpc)	M_{prim} ($M_\odot$)	J (mag)	H (mag)	K (mag)	$M_{fg,K}$ ($M_\odot$)	$M_{fg,J}$ ($M_\odot$)	$M_{tot,K}$ ($M_\odot$)	$M_{tot,J}$ ($M_\odot$)	$q_{fg,K}$	$q_{fg,J}$	$q_{tot,K}$	$q_{tot,J}$
4098003634866306560	G015.1288-00.6717	2.0	13.1	13.3	11.1^{2M}	10^{2M}	8.6	2.5	24.8	23.0	0.7	0.2	1.9	1.8
4154942501642616960	G020.7617-00.0638B	11.8	13.4	15.6	15.1	14.8	7.9	8.5	8.0	8.6	0.6	0.6	0.6	0.6
4156713844934255232	G023.8176+00.3841	4.5	9.1	14.1	13.1	12.6	6.8	4.8	10.1	10.9	0.8	0.5	1.1	1.2
4156713844931953536	G023.8176+00.3841	4.5	9.1	14.1	13.5	13.1	5.4	4.6	7.0	7.8	0.6	0.5	0.8	0.9
4156713849228461184	G023.8176+00.3841	4.5	9.1	16.6	15.8	15.6	1.9	1.9	2.4	3.0	0.2	0.2	0.3	0.3
4156713849228449792	G023.8176+00.3841	4.5	9.1											
4266059696498179456	G032.0518-00.0902	4.2	8.7		15.6	15.3	2.1		2.6		0.2		0.3	
4319862060333763200	G049.5993-00.2488	5.4	7.1	16.1	15.1	14.6	3.8	3.2	4.8	5.3	0.5	0.5	0.7	0.7
4322379362139148416	G051.3617-00.0132	5.2	10.1	13.1	11.6^{2M}	11.1^{2M}	15.0	8.0	26.3	25.6	1.5	0.8	2.6	2.5
1826022731928753024	G056.4120-00.0277	9.3	16.1	16.2	15.1	14.6	6.1	4.9	8.2	8.8	0.4	0.3	0.5	0.5
2020102717670678144	G059.4657-00.0457	2.2	6.0	15.8	14.8	14.1	2.0	1.5	3.0	3.4	0.3	0.2	0.5	0.6
2057379224166044416	G073.6525+00.1944	11.2	28.9	11.8^{2M}	11.3^{2M}	11.1^{2M}	32.9	33.9	29.0	26.0	1.1	1.2	1.0	0.9
2057379219863846272	G073.6525+00.1944	11.2	28.9	16.6	15.8	15.3	6.2	5.8	6.9	7.1	0.2	0.2	0.2	0.2
2062619354845085440	G078.1224+03.6320	1.4	9.1	15	13.5	12.6	2.1	1.1	4.3	4.9	0.2	0.1	0.5	0.5
2066325842897208448	G080.9340-00.1880			15.1	14	13.3								
2066562306616624512	G082.5682+00.4040A	1.4	8.2	14.5	13.8	13.3	1.8	1.7	2.2	2.6	0.2	0.2	0.3	0.3
2198977144784776704	G100.2124+01.8829	5.9	11.6	15.5	15	14.6	3.6	3.3	4.1	4.4	0.3	0.3	0.4	0.4
2198977355244330624	G100.2124+01.8829	5.9	11.6	16.7	16.2	15.8	2.3	2.1	2.7	3.0	0.2	0.2	0.2	0.3
2198977149093332992	G100.2124+01.8829	5.9	11.6	15.6	14.8			3.1		5.9		0.3		0.5
2198977149093333120	G100.2124+01.8829	5.9	11.6	15.1	12.3	10.8^{2M}	18.0	3.8	66.5	57.9	1.6	0.3	5.7	5.0
2199376237445137408	G101.2490+02.5764	6.1	9.3	17.2	16.7	16.2	1.8	1.8	2.3	2.7	0.2	0.2	0.2	0.3
2199376233149055872	G101.2490+02.5764	6.1	9.3	16.2	15.6	15.3	2.7	2.6	3.3	4.0	0.3	0.3	0.4	0.4

Gaia DR3 Source ID	Primary RMS ID	d_{prim} (kpc)	M_{prim} ($M_\odot$)	J (mag)	H (mag)	K (mag)	$M_{fg,K}$ ($M_\odot$)	$M_{fg,J}$ ($M_\odot$)	$M_{tot,K}$ ($M_\odot$)	$M_{tot,J}$ ($M_\odot$)	$q_{fg,K}$	$q_{fg,J}$	$q_{tot,K}$	$q_{tot,J}$
2199376237446614656	G101.2490+02.5764	6.1	9.3	17.2	16.1			1.8		5.0		0.2		0.5
2010087747286916992	G107.6823-02.2423A	4.7	9.2	15.5	15.8	14.1	3.5	2.7	2.8	1.7	0.4	0.3	0.3	0.2
2010084796644075648	G107.6823-02.2423A	4.7	9.2											
2013835535748589952	G111.2980-00.6606	3.5	8.6	16.6	16	14.5	2.2	1.2	2.9	2.2	0.3	0.1	0.3	0.3
527470435478103424	G120.1483+03.3745	5.6	15.9											
425522617841329920	G121.3479-03.3705	3.0	6.2											
526085527569561216	G123.2836+03.0307	4.9	9.3	16.5	15	13.6	4.6	2.1	8.6	7.7	0.5	0.2	0.9	0.8
426650025277470592	G123.8059-01.7805	2.2	7.8											
426650029583407232	G123.8059-01.7805	2.2	7.8	13.6	12.6	12.1	3.9	2.6	6.6	7.6	0.5	0.3	0.8	1.0
426650029578396672	G123.8059-01.7805	2.2	7.8											
426650029578600704	G123.8059-01.7805	2.2	7.8											
426650029577697920	G123.8059-01.7805	2.2	7.8	14.6	13.1	11.8	4.5	1.8	9.5	8.6	0.6	0.2	1.2	1.1
426650029583408512	G123.8059-01.7805	2.2	7.8											
250753316161780096	G150.6862-00.6887	1.9	3.7	16.2	15.1	14.3	1.4	1.0	2.2	2.6	0.4	0.3	0.6	0.7
188633249951112576	G168.0627+00.8221	2.0	12.7	18	17.8	18	0.3	0.5	0.3	0.5	0.0	0.0	0.0	0.0
3449181243489228160	G174.1974-00.0763	2.0	10.3	16.2	14.8	14.1	1.5	0.9	3.0	3.6	0.1	0.1	0.3	0.3
3326715847386516736	G202.9943+02.1040	0.3	2.1	15.5	15	14.6	0.2	0.2	0.3	0.4	0.1	0.1	0.1	0.2
3113711170591097600	G212.9626+01.2954	4.2	6.5	16.7	15.6	14.8	2.5	1.5	4.2	4.4	0.4	0.2	0.7	0.7
3102590783001485440	G217.0441-00.0584	5.3	11.7		15.8	15.1	2.6		3.8		0.2		0.3	
2931756358561613312	G231.7986-01.9682	3.2	10.2	16.2	15.1	14.6	1.9	1.3	3.2	3.8	0.2	0.1	0.3	0.4
3026531825639762432	G233.8306-00.1803	3.3	13.4											
5523960750255191552	G263.5994-00.5236	0.7	3.8											
5330100765626318080	G267.7336-01.1058A	0.7	3.7	15	13.5	12.5	1.2	0.6	2.5	2.8	0.3	0.2	0.7	0.8
5258914710657579904	G282.2988-00.7769	3.7	9.1											
5350910367528142080	G287.3716+00.6444	4.5	15.0											
5350302131421243904	G287.6790-00.8669	2.5	6.6											
5350302131442512128	G287.6790-00.8669	2.5	6.6	14.5	13.5	13	3.1	2.0	5.3	6.1	0.5	0.3	0.8	0.9
5338323501993331328	G289.1447-00.3454	7.6	8.8											
5338323501993342720	G289.1447-00.3454	7.6	8.8											

Gaia DR3 Source ID	Primary RMS ID	d_{prim} (kpc)	M_{prim} ($M_\odot$)	J (mag)	H (mag)	K (mag)	$M_{fg,K}$ ($M_\odot$)	$M_{fg,J}$ ($M_\odot$)	$M_{tot,K}$ ($M_\odot$)	$M_{tot,J}$ ($M_\odot$)	$q_{fg,K}$	$q_{fg,J}$	$q_{tot,K}$	$q_{tot,J}$
5338323501993386880	G289.1447-00.3454	7.6	8.8											
5338323501993351424	G289.1447-00.3454	7.6	8.8											
5338323501993373056	G289.1447-00.3454	7.6	8.8											
5337957158479302400	G290.0105-00.8668A	8.4	11.0											
5337957227198755968	G290.0105-00.8668A	8.4	11.0	16	14.6	14.1	5.8	3.0	11.5	12.5	0.5	0.3	1.1	1.1
5337957227198753792	G290.0105-00.8668A	8.4	11.0											
5334625054151276288	G296.2654-00.3901	8.1	9.7	18.3	17.7			1.2		2.5		0.1		0.3
5334625054149502848	G296.2654-00.3901	8.1	9.7	17.6		16.2	2.2	1.6			0.2	0.2		
5334625015485489920	G296.2654-00.3901	8.1	9.7	17.2	16.7	16.3	2.1	1.9	2.8	3.4	0.2	0.2	0.3	0.3
5334625019789727744	G296.2654-00.3901	8.1	9.7											
6053804580395068800	G300.3412-00.2190	4.2	10.4	16.6	15.8	15.6	1.7	1.4	2.4	3.1	0.2	0.1	0.2	0.3
6053804576075120128	G300.3412-00.2190	4.2	10.4	14.6	13.1	11.8	7.7	2.9	16.7	14.5	0.7	0.3	1.6	1.4
6054731537391513600	G301.1726+01.0034	4.3	15.9	17.8	17.1	16.6	1.1	0.9	1.7	2.0	0.1	0.1	0.1	0.1
5862383385556531456	G304.3674-00.3359A	11.8	28.1	16.5	15.6	15.3	5.0	3.7	7.0	7.6	0.2	0.1	0.3	0.3
5865765242816849536	G308.7008+00.5312	4.0	5.9	17.2	16.6	16.2	1.3	1.1	1.8	2.3	0.2	0.2	0.3	0.4
5865765208456472576	G308.7008+00.5312	4.0	5.9	17	16.3	16.2	1.2	1.2	1.6	2.2	0.2	0.2	0.3	0.4
5865765208456472704	G308.7008+00.5312	4.0	5.9	17.1	16.3	16.2	1.2	1.2	1.7	2.2	0.2	0.2	0.3	0.4
5885649150368871552	G326.7249+00.6159B	1.8	6.9	16.2	15.3	14.6	1.2	0.8	1.8	2.2	0.2	0.1	0.3	0.3
5980805834440030336	G328.3442-00.4629	2.9	7.8	15.6	14.6	11.5^{2M}	6.7	1.5	10.5	3.9	0.9	0.2	1.3	0.5
5980805800080290560	G328.3442-00.4629	2.9	7.8	15.6	14.8	14.3	2.0	1.6	2.9	3.5	0.3	0.2	0.4	0.5
5980832944277564672	G328.9842-00.4361	4.7	7.1	15.8	15.3	15.1	2.3	2.1	2.9	3.4	0.3	0.3	0.4	0.5
5943066304696403072	G338.9377-00.4890B	2.9	5.8	16.6	16	15.6	1.2	1.1	1.5	1.8	0.2	0.2	0.3	0.3
5943212161789159296	G339.7602+00.0530A	12.0	11.1	15.3	14.3	14	8.3	5.3	13.5	14.5	0.7	0.5	1.2	1.3
5943223908530897536	G339.7602+00.0530A	12.0	11.1	14	13	12.5	15.8	8.8	26.1	25.1	1.4	0.8	2.3	2.3
5943270813887664640	G340.1537+00.5116	3.8	6.2											

Table 4.3: A summary of the mass statistics for the companions detected in Gaia. Masses are in units of $M_{\odot}$.

Property	Mean	Min	Max
$M_{fg,K}$	4.6	0.2	32.9
$q_{fg,K}$	0.4	<0.1	1.6
$M_{fg,J}$	3.1	0.2	33.9
$q_{fg,J}$	0.3	<0.1	1.2
$M_{tot,K}$	7.8	0.3	66.5
$q_{tot,K}$	0.7	<0.1	5.7
$M_{tot,J}$	7.8	0.4	57.8
$q_{tot,J}$	0.8	<0.1	5.0

These masses are simple estimates from Equation 2.2 and Equation 2.3 which assume the companion is a main-sequence star and that the entire brightness of the star is due to photospheric emission. A significant number of systems have mass ratios greater than 0.5, especially using the total extinction estimates. The masses and mass ratios found are very similar between using the $K-$ and $J-$band, with the $K-$band masses generally being slightly larger due to the aforementioned overestimate from $K-$band excess.

As also asserted in Subsection 2.4.3, these mass ratios suggest a disagreement with the low mass ratio regime of the binary capture formation scenario (Salpeter, 1955), and could lead to the idea of companions forming at wide separations and migrating inwards (Moe and Di Stefano, 2017; Ramírez-Tannus et al., 2021).

4.4.5 Are binary YSOs different from single YSOs?

To see whether the properties of the Gaia sample matches that of the entire RMS catalogue, Kolmogorov-Smirnov (K-S) tests were performed using distance and luminosity. As in Subsection 2.4.4, these tests were used to determine whether the two samples were drawn from the same population, i.e. whether the YSOs detected by Gaia differ substantially in luminosity or distance from the whole RMS catalogue. The cumula-

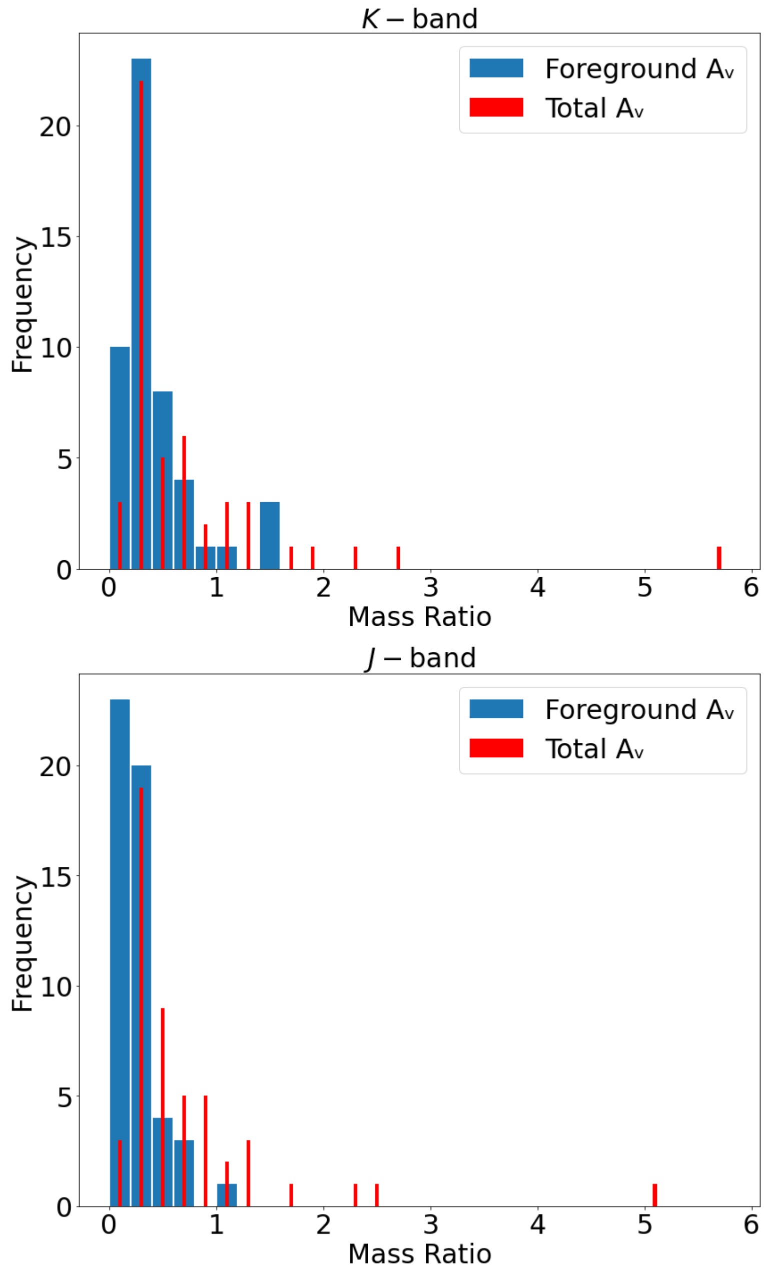

Figure 4.8: Histograms of the mass ratios for YSO companions detected in Gaia, using $K-$band (top) and $J-$band (bottom) magnitudes as proxies for the companion mass. The thick blue bar represents the mass ratios derived using foreground extinction, and the thin red bar represents masses derived through total extinction estimates. Primary mass was derived using RMS bolometric luminosity.

tive distribution histograms can be found in Figure 4.9. For MYSOs, the comparison of luminosity gave a P-value of 0.23, and comparing distance gave a P-value of 0.58. Comparing low-mass YSOs gave P-values of 0.93 and 0.39 respectively. This suggests that there are no significant differences in the properties of primary YSOs detected by optical means.

The luminosities and distances of the MYSOs surveyed in this work were compared to the MYSOs surveyed in Chapter 2, i.e. found in UKIDSS/VVV. The cumulative histograms for these properties can be found in Figure 4.10. The K-S for luminosity gave a P-value of 0.19, showing agreement, while the distance K-S test gave a P-value of 0.59. This indicates that there are no significant differences in MYSO luminosity or distance distributions between the two samples.

Additionally, the Gaia YSOs with and without companions were compared in terms of luminosity, distance, Gaia magnitude and BP-RP colour. A K-S test was conducted on the high-mass subset of Gaia YSOs found in multiple systems compared to those found in single systems. These K-S tests give a P-value of 0.57 for luminosity, 0.22 for RMS distance, 0.63 for BP-RP colour and 0.99 for G magnitude. A similar test for low-mass YSOs gives 0.17 for luminosity, 0.06 for distance, 0.7 for BP-RP colour and 0.95 for G magnitude. These values suggest that there are no significant differences between single and binary YSOs detected in Gaia, save for a discrepancy in the distances of the low-mass subset. This may be explained through the fact that lower-mass YSOs are less luminous and so are less likely to be detected at larger distances, and so companions (which would primarily be less massive than the primary) would also be less likely to be detected.

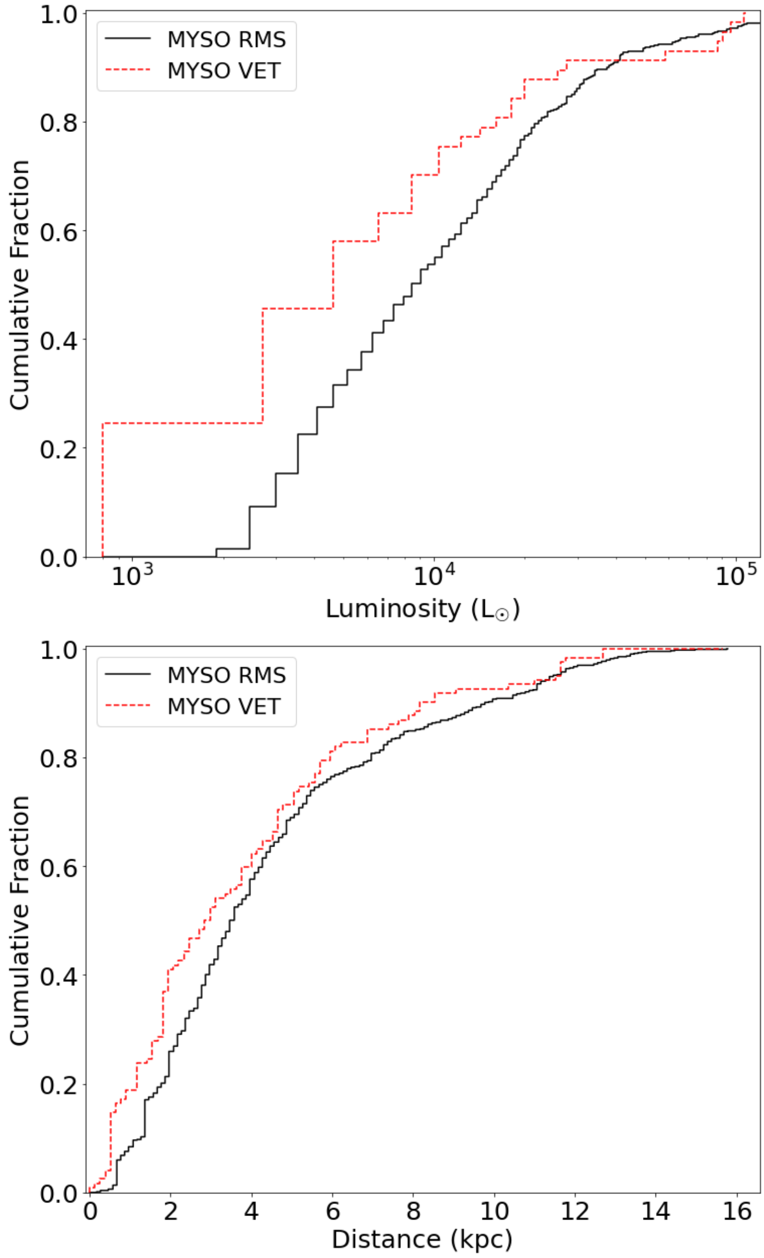

Figure 4.9: The cumulative distribution of luminosity (top) and RMS distance (bottom) of the MYSOs found in Gaia (red dashed) compared to all the MYSOs in the RMS catalogue (black solid). The K-S tests for these properties gave P-values of 18% and 55% respectively, indicating they come from the same distribution.

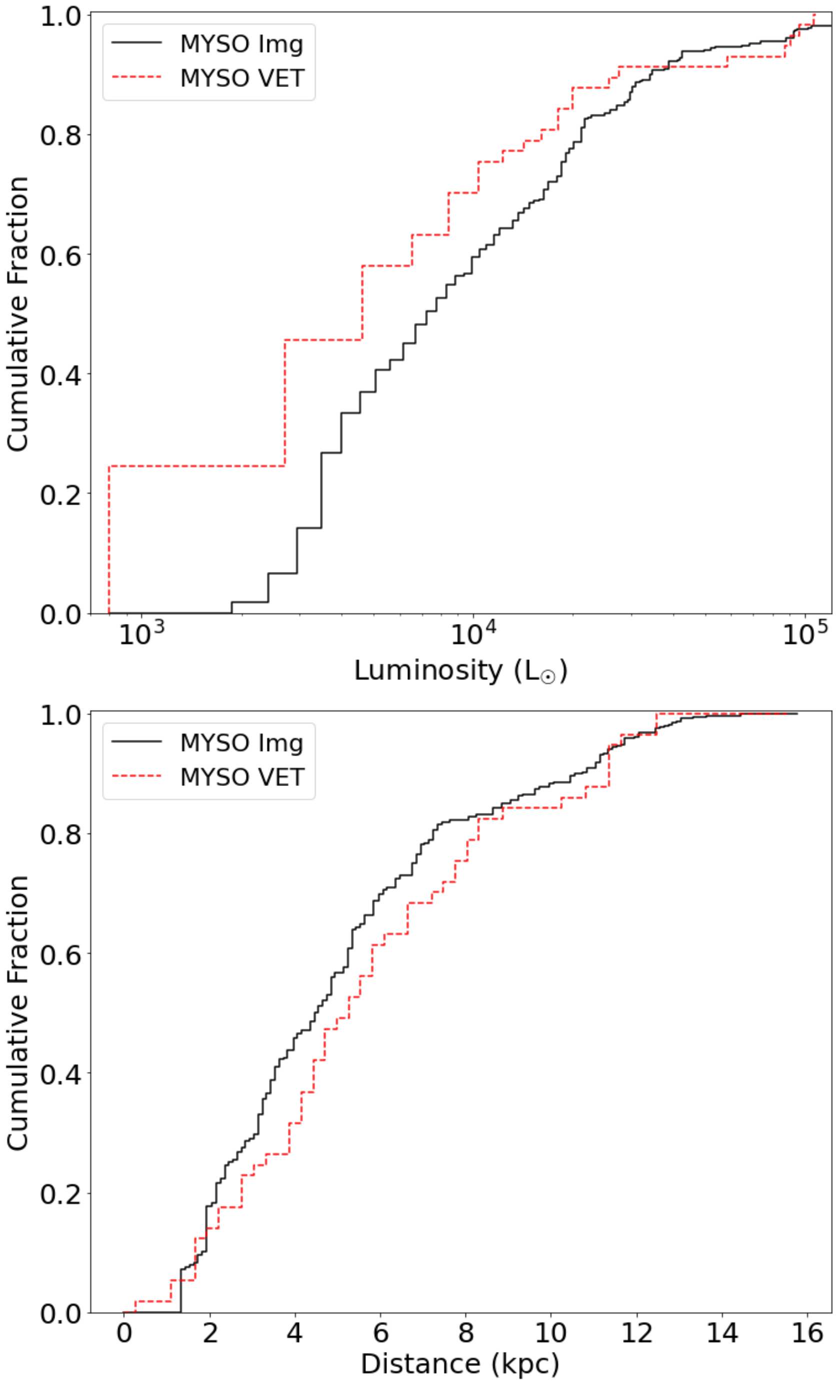

Figure 4.10: The cumulative distribution of luminosity (top) and RMS distance (bottom) of the MYSOs found in Gaia (red dashed) compared to the MYSOs surveyed using the imaging method of Chapter 2 (black solid). The K-S tests for these properties gave P-values of 47% and 3% respectively, indicating the luminosities appear to be drawn from the same distribution but the distances do not.

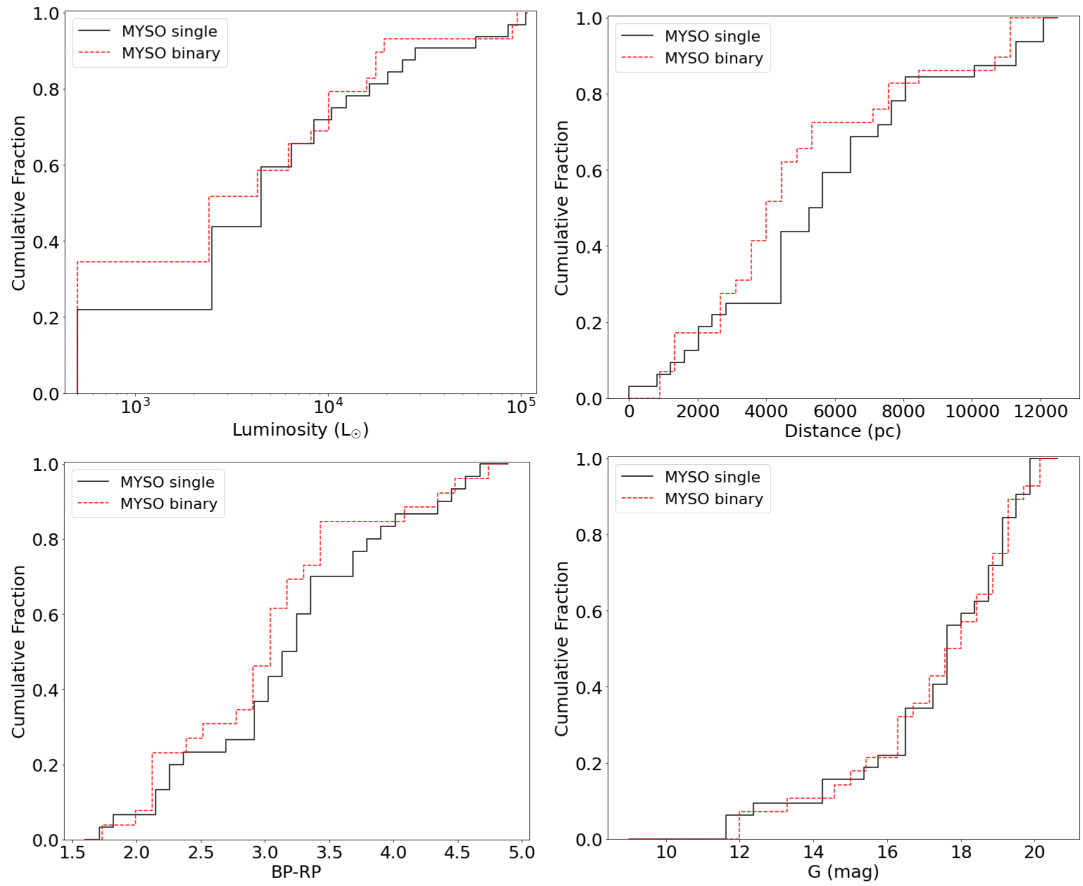

Figure 4.11: The cumulative distribution of luminosity (top left), distance (top right), Gaia BP-RP colour (bottom left) and Gaia magnitude (bottom right) of the MYSOs found in the Gaia survey. The two lines represent MYSOS with companions (red dashed) compared to single MYSOs (black solid). K-S tests show that MYSOs are drawn from the same distribution when testing all of these properties.

4.5 Conclusions

I present a study of YSO multiplicity using data from the Gaia DR3 survey. YSOs were previously thought to be practically absent from optical surveys, but the unprecedented depth of the Gaia survey allows for a fraction of YSOs to be studied optically. By using the parallax and proper motion data of Gaia DR3, a search for companions around these YSOs was performed.

(i) From the 863 YSOs in the RMS catalogue, 172 are present in Gaia DR3, giving an optical detection rate of 20%. 139 of these YSOs have parallaxes and proper motions in Gaia.

(ii) 77 companions were detected in Gaia around the 139 usable YSOs, giving a multiplicity fraction of 33±8% and a companion fraction of 55±6%. The MYSO subset has a multiplicity fraction of 50±13%.

(iii) The separations of these companions suggest agreement with the filament or core fragmentation scenarios, although there is a bias against smaller separations.

(iv) A significant fraction of the detected multiple systems have mass ratios greater than 0.5, suggesting that binary capture is not responsible for their formation.

(v) The true multiplicity fraction is likely to be up to 100%.

(vi) From the Gaia sample, there are no significant differences in distance, luminosity, colour or magnitude between MYSOs with companions and single MYSOs (low-mass YSOs do exhibit a slight skew of distance). There are also no significant differences in distance or luminosity between YSOs detected in Gaia and the entire YSO population of the RMS catalogue.

Further work would include determining improved masses of companions using Gaia data; specifically the spectral typing of companions, determining the extinction towards them using Gaia BP-RP colours, and the use of these corrected magnitudes as a proxy for the mass. Additionally, further Gaia data releases would provide improved data to perform companion analysis with.

Chapter 5

Conclusions

In this thesis, the multiplicity of MYSOs has been studied to help determine the primordial multiplicity properties of massive stars. MYSOs are a precursor stage to the main-sequence, where accretion is occurring but HII regions have not yet been created. All YSOs studied in this thesis were drawn from the RMS catalogue (Subsection 1.4.1, Lumsden et al., 2013), a catalogue built to be unbiased across the Galactic plane and which is 90% complete for objects $> 10^4 L_{\odot}$. See Section 1.4 or Oudmaijer and de Wit (2014) for more information on MYSOs.

Multiplicity is an intrinsic part of massive star formation, and studying this phenomenon at the earliest possible stage is key to fully understanding it. The multiplicity of these objects was studied using three specific techniques, covering a wide range of separations and multiple wavebands.

In Chapter 2 I studied a sample of 683 YSOs, 402 of which are MYSOs, using infrared images and the point-source catalogues of UKIDSS and VVV. I used statistical methods to detect nearby objects and determine the probability of them being a chance projection, based on the separation between a nearby object and the primary, and the density of the region of space the primary was found in. This method probed the widest binaries, with most found between 900-50,000 au. The YSOs in this sample have a multiplicity fraction of 65% in UKIDSS and 53% in VVV, and a companion fraction of 147% in UKIDSS and 84% in VVV. The stellar background densities were seen to vary across the Galaxy and this affected the likelihood of detecting companions in the UKIDSS data; when correcting for this, the UKIDSS multiplicity fraction falls to 55%, much more aligned with that of the VVV survey. Mass ratios of the companions are generally greater than ~0.5, and the properties of the primaries do not differ between single and multiple systems. Monte-Carlo simulations suggest that observational limitations result in the observed multiplicity statistics being a lower limit; the true multiplicity fraction is up to 100%, and the wide separation distribution of the models suggest a significant number of the systems must be at least triples in order to maintain stability in the systems.

In Chapter 3 I conducted an analysis of the multiplicity of MYSOs at smaller separations, by investigating radial velocity variability in infrared spectra. MYSOs that show variability in their radial velocity may harbour a companion at small separations which cannot be resolved through direct imaging methods. I used two main samples in this chapter: a sample of two MYSOs which each had between 6-8 epochs of high-resolution IGRINS $K-$band spectra, and a sample of 26 YSOs (23 of which were MYSOs) which each had two epochs of X-shooter medium-resolution $K-$band spectra. Neither of the MYSOs observed by IGRINS were determined to be RV variable. 8^{+17}_{-7}% of the MYSOs observed with X-shooter were determined to be RV variable. Taking the results into account with observational biases, the true binary fraction at these separations is also likely to be high.

In Chapter 4 I used optical data from the third data release of the Gaia mission to search for YSO companions through the use of proper motions and parallaxes. YSOs were originally thought to be invisible in optical surveys because of their heavily embedded nature, but a catalogue was constructed showing that approximately 20% of known Galactic YSOs are detected in Gaia DR3. By comparing their proper motions and parallaxes with nearby objects in their vicinity, companions can be found. A total of 77 companions were detected around 139 YSOs in Gaia, giving a multiplicity fraction of 33% (with an MF of 50% for MYSOs). These companions were found at separations from 3600 up to an extreme of 130,000 au. There are no major differences in luminosity, distance and magnitude between the YSOs with and without companions, and between YSOs that are optically detected and those that are not. Once again, accounting for observational restrictions, the true multiplicity fraction is close to 100%.

5.1 Combined view of MYSO multiplicity

Between the three studies performed in this thesis, a multi-scale, multi-waveband picture of MYSO multiplicity has been formed. Chapter 2 covered medium-to-wide companions of MYSOs observed in the $K-$band, Chapter 3 covered close-in companions also in the $K-$band, and Chapter 4 covered wide companions in the optical. A number of objects studied in this thesis have been covered by two or more methods, meaning that for the first time, we can summarise the multiplicity state of MYSOs across different regimes. Additionally, MYSO multiplicity information from the interferometry studies of Koumpia et al. (2019) and Koumpia et al. (2021) and the upcoming proper motion anomaly study of Dodd et al. (in prep) provide further insight to the total multiplicity of MYSOs.

5.1.1 Interferometry

Two recent studies have used interferometry to study MYSO multiplicity. Koumpia et al. (2019) used VLTI/PIONIER interferometry and X-shooter spectra to investigate the multiplicity of two MYSOs, G231.7986–01.9682 and G282.2988–00.7769 (also known as PDS 27 and PDS 37 respectively). G231.7986 was found to have a companion at 30 au, and G282.2988 was found to have a companion at 42-54 au. Koumpia et al.

(2021) studied 6 MYSOs using GRAVITY and AMBER long-baseline interferometry on the VLTI, in order to investigate their multiplicity status, among other properties of interest. 1 of the 6 MYSOs, G282.2988-00.7769, required a binary model to fit the interferometric observations. This study traced separations of 2-300 au.

5.1.2 Proper motion anomaly

Proper motion anomalies (PMas) are another method of indirectly detecting companions around stars. The short-term proper motion of an object measured by two separate surveys is compared to the long term proper motion of the object, which is determined by the change in the object's position between the two survey epochs. For a single star these proper motions will not change. However for a multiple star system, the companion's orbital motion will add an additional component to the observed proper motions. The difference in these proper motions, i.e. the PMa, is therefore an effective indicator of the binarity of said object (Kervella et al., 2022).

The first use of the PMa technique was the detection of Sirius B (Bessel, 1844), and more recently Kervella et al. (2022) used the long baseline of ∼25 years between the Hipparcos catalogue and Gaia EDR3 to detect companions of Hipparcos catalogue stars. The work of Dodd et al. (in prep) uses the proper motions of Gaia DR2 and Gaia DR3 to determine PMas for Herbig Ae/Be stars and MYSOs. MYSOs are generally too faint for Hipparcos, therefore the two Gaia epochs are instead used. The initial PMa findings for MYSOs are included in the table below.

5.1.3 Complete MYSO multiplicity statistics

A summary of all MYSOs that have been studied in more than one chapter of this thesis is presented in Table 5.1. The 'IR?', 'RV?' and 'Gaia?' columns represent whether companions were detected for an MYSO in Chapter 2, Chapter 3 and Chapter 4 respectively, with the first and third of these listing the number of companions detected.

The PMa? column represents whether a PMa has been detected using Gaia data from the work of Dodd et al. (in prep). The InF? column shows whether a companion has been detected using interferometry by Koumpia et al. (2019) or Koumpia et al. (2021).

The last five columns of Table 5.1 increase in separation range from left to right: The RV method of Chapter 3 covers separations of a few au up to ∼100 au. The interferometric studies of Koumpia et al. (2019) and Koumpia et al. (2021) probe separations of a few au up to ∼300 au. The PMas of Dodd et al. (in prep) cover separations between approx. 200-1000 au. The infrared imaging study of Chapter 2 and the Gaia parallax/proper motion study of Chapter 4 cover separations from 1000s of au to ∼100,000 au.

57 MYSOs have been studied in more than one chapter of this thesis. Of these 57 objects, 47 of them (82%) have at least one companion, with only 10 singles. This suggests a very high level of multiplicity in MYSOs, and signifies that previous stipulations of a binary fraction of 100% are very possible without observational bias. Additionally, 21 of the above MYSOs have been studied for RV variability, meaning a multi-scale analysis can be performed at both large and small separations. 14 of these objects have at least one companion, and 1 of them (G298.2620+00.7394) has a companion at both large and small separations. This provides further evidence to the idea in Subsection 2.4.5 of triple systems in MYSOs, with a companion at small separations and one at large separations to maintain orbital stability.

Including the objects observed using the PMas of Dodd et al. (in prep), and the interferometric studies of Koumpia et al. (2019) and Koumpia et al. (2021), 61 MYSOs have been observed in more than one study. Of these, 49 objects (80%) have at least one companion. 59 MYSOs have been studied at both large and small separations: 49 (83%) have at least one companion, and 6 (10%) have a companion in more than one separation range.

Table 5.1: All MYSOs that have been observed in more than one chapter of this thesis or another MYSO study. 'RV?' shows whether RV analysis found variability and the possible presence of a companion. 'InF?' shows whether a companion has been detected using interferometry by Koumpia et al. (2019) or Koumpia et al. (2021). 'PMa?' shows whether a proper motion anomaly was detected by Dodd et al. (in prep). 'IR?' shows the number of companions found via the IR imaging method, if any. 'Gaia?' shows the number of companions found using the Gaia method, if any. The last five columns increase in separation range from left to right.

RMS ID	d_{RMS} (kpc)	L_{bol} ($L_\odot$)	RV?	InF?	PMa?	IR?	Gaia?
G012.7879-00.1786	2.4	5624			✗	2	0
G015.1288-00.6717	2.0	12191			✗	2	1
G018.1968-00.1709	10.6	5636			✗	1	0
G020.7617-00.0638B	11.8	13395			✗	1	1
G020.7617-00.0638C	11.8	13103			✗	1	0
G023.8176+00.3841	4.5	3920				0	4
G032.0518-00.0902	4.2	3402			✗	0	1
G033.3891+00.1989	5.0	13000	✗			1	
G034.0126-00.2832	12.9	31473			✗	0	0
G034.0500-00.2977	12.9	22570			✗	2	0
G034.8211+00.3519	3.5	23878		✗		3	
G035.3778-01.6405	3.3	5891			✗	1	0
G051.3617-00.0132	5.2	5415			✗	0	1
G053.5343-00.7943	5.0	7348			✗	0	0
G053.5671-00.8653	7.8	6926			✗	0	0
G056.4120-00.0277	9.3	22243			✗	0	1
G064.8131+00.1743	8.2	89444			✗	0	0
G073.6525+00.1944	11.2	101843			✗	1	2
G076.3829-00.6210	1.3	34000	✗			4	
G077.5671+03.6911	5.7	4533			✗	5	0
G078.1224+03.6320	1.4	3967			✗	2	1
G078.8699+02.7602	1.4	6505			✓	2	0
G082.5682+00.4040A	1.4	2787			✗	3	1
G094.6028-01.7966	4.9	28459			✓	4	0
G095.0531+03.9724	8.7	12374			✗	4	0
G096.4353+01.3233A	7.0	9659			✗	2	0
G100.1685+02.0266	5.9	8374			✗	3	0
G100.2124+01.8829	5.9	8303			✗	5	4
G101.2490+02.5764	6.1	4319			✗	3	3
G151.6120-00.4575	6.4	60777			✗	0	0
G168.0627+00.8221	2.0	10667			✗	3	1

Table 5.1: Continued.

RMS ID	d_{RMS} (kpc)	L_{bol} ($L_\odot$)	RV?	InF?	PMa?	IR?	Gaia?
G173.4839+02.4317	2.0	2932			✗	2	0
G174.1974-00.0763	2.0	5892			✗	3	1
G207.2654-01.8080A	1.0	9106	✗			2	
G212.0641-00.7395	4.7	16183	✗			1	
G217.0441-00.0584	5.3	8634				4	1
G231.7986-01.9682	3.2	5608	✗	✓	✓		1
G268.3957-00.4842	0.7	3011	✗		✗		0
G282.2988-00.7769	3.7	4050		✓	✓		1
G287.3716+00.6444	4.5	17887		✗			1
G296.2654-00.3901	8.1	4850			✗	1	4
G298.2620+00.7394	4.0	15320	✓			1	
G300.3412-00.2190	4.2	5970			✗	1	2
G301.1726+01.0034	4.3	20545			✗	0	1
G301.8147+00.7808A	4.4	21580	✗	✗		3	
G304.3674-00.3359A	11.8	94462			✗	3	1
G305.2017+00.2072A	4.0	48512	✗			1	
G305.6327+01.6467	4.9	15684			✓	1	0
G309.9206+00.4790B	5.4	11049	✗			2	
G309.9796+00.5496	3.5	7565	✗			1	
G310.0135+00.3892	3.2	67075	✗			1	
G320.2437-00.5619	9.5	31326	✗			0	
G320.2878-00.3069A	8.7	12242			✗	0	0
G330.8768-00.3836	3.9	7613	✗			1	
G332.0939-00.4206	3.6	92768	✗			0	
G332.8256-00.5498A	3.6	130093	✗			0	
G336.4917-01.4741B	2.0	12285	✗			3	
G338.9196+00.5495	4.2	32030	✗			0	
G339.7602+00.0530A	12.0	7442			✗	1	2
G347.0775-00.3927	1.7	2961	✗			1	

To conclude, multiplicity is an intrinsic factor of the formation of MYSOs and massive stars in general. Large fractions of MYSOs are found to form in multiple systems, and it is possible that observational bias is hindering the true phenomenon that all MYSOs are in binary systems. In addition, a significant amount of these multiple systems could be in triple systems, meaning that the order of multiplicity of massive stars may be larger than originally anticipated. Therefore, a comprehensive star formation theory should seriously consider including triplicity or higher-order multiplicity. The separations and mass ratios of the detected companions have generally suggested that disc fragmentation is the most likely formation scenario for massive multiple systems, with capture being a more unlikely explanation.

5.2 Future work

5.2.1 Infrared imaging of binary companions

The data presented in Chapter 2 currently comprises the largest study of MYSO binarity to date, focusing on the wider separations (10,000s of au). To improve this technique, additional observations using higher-resolution instruments should be performed, such as imaging instruments on the VLT (ERIS/VISIR) as opposed to the lower-resolution WFCAM used in the UKIDSS survey. Higher-resolution observations will allow for better resolving power of close-in objects and less source confusion, improving the ability to detect close companions. Chance projections/non-MYSOs can be more effectively identified and removed through additional analysis of infrared colours. Additionally, determinations of the mass ratios of companions can be improved through follow-up spectroscopic observations to further constrain their fluxes and extinctions.

The new ERIS imager and spectrograph at the VLT will be important in observing and characterising MYSO companions at infrared wavelengths. Its adaptive optics will allow for some of the sharpest images of MYSO companions, and will replace the NaCo and SINFONI instruments previously used for studying MYSO binarity. Also the recent VVV eXtended Survey (VVVX, Minniti, 2018) covers more of the sky than VVV, and will allow for more MYSOs in the southern sky to be studied for companions via this method.

5.2.2 Radial velocity variations

Chapter 3 shows that RV variability is a key tool in detecting close companions that are not able to be resolved through direct imaging. However, a relatively low number of epochs were used in this chapter; an effective RV analysis requires a much larger number of epochs and/or a larger sample size. Further MYSO observations are currently being performed using X-shooter to increase the number of objects that have been observed more than once, improving the sample size. Dedicated analysis of a few objects would also provide a more complete view of MYSO multiplicity by observing them much more frequently, allowing for any RV variations to be determined to a higher level of accuracy.

5.2.3 Optically visible MYSO binaries

In Chapter 4 the first large-scale analysis of MYSOs at optical wavelengths was performed. To improve this method of determining companions, more rigorous criteria should be used to classify whether an object is a true companion. Additional Gaia data such as radial velocities could be used to further assess the companion status of nearby objects, and Gaia magnitudes and $BP - RP$ colours can provide additional data for mass ratios in optical wavelengths, instead of infrared data as used in this chapter. In addition, the proper motion anomaly technique of Dodd et al. (in prep) is currently being used to assess the binarity of MYSOs and Herbig Ae/Be stars. Further data releases of Gaia will help improve companion detection via improved parallaxes/proper motions, and longer baselines for PMa detection.

5.3 Closing remarks

In conclusion, this thesis has presented a multi-scale, multi-waveband analysis of the multiplicity of MYSOs. These massive star precursors were studied to determine the primordial multiplicity properties of massive stars. A $K-$band imaging survey found that more than half of a sample of hundreds of MYSOs had at least one companion, and simulations of the separation distribution found that the majority of these companions lie at very large distances. An RV analysis found that a number of MYSOs exhibit signs of a close-in companion at ≤ 20 au from a small number of observed epochs. A study of MYSOs in optical wavelengths showed that 20% of MYSOs are bright enough to be observed in Gaia, and that many of them again were found to have companions. Together these studies suggest that MYSOs commonly form in binary systems and sometimes triple systems: one companion lying at very close separations, and another at wide separations which maintains stability. Further studies of MYSO multiplicity with higher resolution and using larger sample sizes can supply more complete data to help inform simulations. More complex radiative hydrodynamical models, which include turbulence, magnetic fields and other effects, will be crucial in providing a complete understanding of the formation of massive stars and the role of multiplicity in it.

References

Adams, Fred C., Ruden, Steven P., and Shu, Frank H. (Dec. 1989). "Eccentric Gravitational Instabilities in Nearly Keplerian Disks". In: The Astrophysical Journal 347, p. 959. DOI: 10.1086/168187.

André, Ph., Arzoumanian, D., Könyves, V., Shimajiri, Y., and Palmeirim, P. (Sept. 2019). "The role of molecular filaments in the origin of the prestellar core mass function and stellar initial mass function". In: Astronomy and Astrophysics 629, L4, p. L4. DOI: 10.1051/0004-6361/201935915. arXiv: 1907.13448 [astro-ph.GA].

André, Ph. et al. (July 2010). "From filamentary clouds to prestellar cores to the stellar IMF: Initial highlights from the Herschel Gould Belt Survey". In: Astronomy and Astrophysics 518, L102, p. L102. DOI: 10.1051/0004-6361/201014666. arXiv: 1005.2618 [astro-ph.GA].

Apai, Dániel, Bik, Arjan, Kaper, Lex, Henning, Thomas, and Zinnecker, Hans (Jan. 2007). "Massive Binaries in High-Mass Star-forming Regions: A Multiepoch Radial Velocity Survey of Embedded O Stars". In: The Astrophysical Journal 655.1, pp. 484–491. DOI: 10.1086/509705. arXiv: astro-ph/0610085 [astro-ph].

Astropy Collaboration et al. (Oct. 2013). "Astropy: A community Python package for astronomy". In: Astronomy and Astrophysics 558, A33, A33. DOI: 10.1051/0004-6361/201322068. arXiv: 1307.6212 [astro-ph.IM].

Bailer-Jones, C. A. L., Rybizki, J., Fouesneau, M., Demleitner, M., and Andrae, R. (Mar. 2021). "Estimating Distances from Parallaxes. V. Geometric and Photogeometric Distances to 1.47 Billion Stars in Gaia Early Data Release 3". In: Astronomical Journal 161.3, 147, p. 147. DOI: 10.3847/1538-3881/abd806. arXiv: 2012.05220 [astro-ph.SR].

Baines, Deborah, Oudmaijer, René D., Porter, John M., and Pozzo, Monica (Apr. 2006). "On the binarity of Herbig Ae/Be stars". In: Monthy Notices of the Royal Astronomical Society 367.2, pp. 737–753. DOI: 10.1111/j.1365-2966.2006.10006.x. arXiv: astro-ph/0512534 [astro-ph].

Banyard, G., Sana, H., Mahy, L., Bodensteiner, J., Villaseñor, J. I., and Evans, C. J. (Aug. 2021). "The observed multiplicity properties of B-type stars in the Galactic young open cluster NGC 6231". In: *arXiv e-prints*, arXiv:2108.07814, arXiv:2108.07814. arXiv: 2108.07814 [astro-ph.SR].

Barsony, M. (Jan. 1994). "Class 0 Protostars". In: *Clouds, Cores, and Low Mass Stars.* Ed. by Dan P. Clemens and Richard Barvainis. Vol. 65. Astronomical Society of the Pacific Conference Series, p. 197.

Bate, Matthew R. (Feb. 2012). "Stellar, brown dwarf and multiple star properties from a radiation hydrodynamical simulation of star cluster formation". In: Monthy Notices of the Royal Astronomical Society 419.4, pp. 3115–3146. DOI: 10.1111/j.1365-2966.2011.19955.x. arXiv: 1110.1092 [astro-ph.SR].

– (Apr. 2018). "On the diversity and statistical properties of protostellar discs". In: Monthy Notices of the Royal Astronomical Society 475.4, pp. 5618–5658. DOI: 10.1093/mnras/sty169. arXiv: 1801.07721 [astro-ph.SR].

Bate, Matthew R. and Bonnell, Ian A. (Feb. 1997). "Accretion during binary star formation - II. Gaseous accretion and disc formation". In: Monthy Notices of the Royal Astronomical Society 285.1, pp. 33–48. DOI: 10.1093/mnras/285.1.33.

Bessel, F. W. (Dec. 1844). "On the variations of the proper motions of Procyon and Sirius". In: Monthy Notices of the Royal Astronomical Society 6, pp. 136–141. DOI: 10.1093/mnras/6.11.136.

Beuther, H., Ahmadi, A., Mottram, J. C., Linz, H., Maud, L. T., Henning, Th., Kuiper, R., Walsh, A. J., Johnston, K. G., and Longmore, S. N. (Jan. 2019). "High-mass star formation at sub-50 au scales". In: Astronomy and Astrophysics 621, A122, A122. DOI: 10.1051/0004-6361/201834064. arXiv: 1811.10245 [astro-ph.SR].

Beuther, H., Schilke, P., Menten, K. M., Motte, F., Sridharan, T. K., and Wyrowski, F. (Feb. 2002). "High-Mass Protostellar Candidates. II. Density Structure from Dust Continuum and CS Emission". In: The Astrophysical Journal 566.2, pp. 945–965. DOI: 10.1086/338334. arXiv: astro-ph/0110370 [astro-ph].

Blandford, R. D. and Payne, D. G. (June 1982). "Hydromagnetic flows from accretion disks and the production of radio jets." In: Monthy Notices of the Royal Astronomical Society 199, pp. 883–903. DOI: 10.1093/mnras/199.4.883.

Bonnarel, F., Fernique, P., Bienaymé, O., Egret, D., Genova, F., Louys, M., Ochsenbein, F., Wenger, M., and Bartlett, J. G. (Apr. 2000). "The ALADIN interactive sky atlas. A reference tool for identification of astronomical sources". In: Astronomy and Astrophysics Supplement 143, pp. 33–40. DOI: 10.1051/aas:2000331.

Bonnell, I. A., Bate, M. R., Clarke, C. J., and Pringle, J. E. (Feb. 1997). "Accretion and the stellar mass spectrum in small clusters". In: Monthy Notices of the Royal Astronomical Society 285.1, pp. 201–208. DOI: 10.1093/mnras/285.1.201.

– (May 2001). "Competitive accretion in embedded stellar clusters". In: Monthy Notices of the Royal Astronomical Society 323.4, pp. 785–794. DOI: 10.1046/j.1365-8711.2001.04270.x. arXiv: astro-ph/0102074 [astro-ph].

Bonnell, Ian A. and Bate, Matthew R. (July 2006). "Star formation through gravitational collapse and competitive accretion". In: Monthy Notices of the Royal Astronomical Society 370.1, pp. 488–494. DOI: 10.1111/j.1365-2966.2006.10495.x. arXiv: astro-ph/0604615 [astro-ph].

Bonnell, Ian A., Bate, Matthew R., and Zinnecker, Hans (July 1998). "On the formation of massive stars". In: Monthy Notices of the Royal Astronomical Society 298.1, pp. 93–102. DOI: 10.1046/j.1365-8711.1998.01590.x. arXiv: astro-ph/9802332 [astro-ph].

Bordier, E., Frost, A. J., Sana, H., Reggiani, M., Mérand, A., Rainot, A., Ramıérez-Tannus, M. C., and de Wit, W. J. (July 2022). "The origin of close massive binaries in the M17 star-forming region". In: Astronomy and Astrophysics 663, A26, A26. DOI: 10.1051/0004-6361/202141849. arXiv: 2203.05036 [astro-ph.SR].

Busfield, A. L., Purcell, C. R., Hoare, M. G., Lumsden, S. L., Moore, T. J. T., and Oudmaijer, R. D. (Mar. 2006). "Resolving the kinematic distance ambiguity of southern massive young stellar object candidates". In: Monthy Notices of the Royal Astronomical Society 366.3, pp. 1096–1117. DOI: 10.1111/j.1365-2966.2005.09909.x. arXiv: astro-ph/0511712 [astro-ph].

Campbell, Bel, Persson, S. E., and Matthews, K. (Aug. 1989). "Identifications of New Young Stellar Objects Associated with IRAS Point Sources. III. The Northern Galactic Plane". In: Astronomical Journal 98, p. 643. DOI: 10.1086/115164.

Capitanio, L., Lallement, R., Vergely, J. L., Elyajouri, M., and Monreal-Ibero, A. (Oct. 2017). "Three-dimensional mapping of the local interstellar medium with composite data". In: Astronomy and Astrophysics 606, A65, A65. DOI: 10.1051/0004-6361/201730831. arXiv: 1706.07711 [astro-ph.GA].

Caratti o Garatti, A., Stecklum, B., Linz, H., Garcia Lopez, R., and Sanna, A. (Jan. 2015). "A near-infrared spectroscopic survey of massive jets towards extended green objects". In: Astronomy and Astrophysics 573, A82, A82. DOI: 10.1051/0004-6361/201423992. arXiv: 1410.4041 [astro-ph.SR].

Chini, R., Hoffmeister, V. H., Nasseri, A., Stahl, O., and Zinnecker, H. (Aug. 2012). "A spectroscopic survey on the multiplicity of high-mass stars". In: Monthy Notices of the Royal Astronomical Society 424.3, pp. 1925–1929. DOI: 10.1111/j.1365-2966.2012.21317.x. arXiv: 1205.5238 [astro-ph.SR].

Churchwell, E., Povich, M. S., Allen, D., Taylor, M. G., Meade, M. R., Babler, B. L., Indebetouw, R., Watson, C., Whitney, B. A., Wolfire, M. G., Bania, T. M., Benjamin, R. A., Clemens, D. P., Cohen, M., Cyganowski, C. J., Jackson, J. M., Kobulnicky, H. A., Mathis, J. S., Mercer, E. P., Stolovy, S. R., Uzpen, B., Watson, D. F., and Wolff, M. J. (Oct. 2006). "The Bubbling Galactic Disk". In: The Astrophysical Journal 649.2, pp. 759–778. DOI: 10.1086/507015.

Churchwell, E., Watson, D. F., Povich, M. S., Taylor, M. G., Babler, B. L., Meade, M. R., Benjamin, R. A., Indebetouw, R., and Whitney, B. A. (Nov. 2007). "The Bubbling Galactic Disk. II. The Inner 20°". In: The Astrophysical Journal 670.1, pp. 428–441. DOI: 10.1086/521646.

Churchwell, Ed (Jan. 2002). "Ultra-Compact HII Regions and Massive Star Formation". In: Annual Review of Astronomy and Astrophysics 40, pp. 27–62. DOI: 10.1146/annurev.astro.40.060401.093845.

Clarke, A. J., Lumsden, S. L., Oudmaijer, R. D., Busfield, A. L., Hoare, M. G., Moore, T. J. T., Sheret, T. L., and Urquhart, J. S. (Oct. 2006). "Evidence for variable outflows in the young stellar object V645 Cygni". In: Astronomy and Astrophysics 457.1, pp. 183–188. DOI: 10.1051/0004-6361:20064839. arXiv: astro-ph/0606652 [astro-ph].

Comerón, F., Schneider, N., Djupvik, A. A., and Schnugg, C. (July 2018). "The ionizing source of the bipolar HII region S106: A close massive binary". In: Astronomy and Astrophysics 615, A2, A2. DOI: 10.1051/0004-6361/20173197910.48550/arXiv.1801.08958. arXiv: 1801.08958 [astro-ph.SR].

Connelley, Michael S., Reipurth, Bo, and Tokunaga, Alan T. (June 2008). "The Evolution of the Multiplicity of Embedded Protostars. II. Binary Separation Distribution and Analysis". In: Astronomical Journal 135.6, pp. 2526–2536. DOI: 10.1088/0004-6256/135/6/2526. arXiv: 0803.1172 [astro-ph].

Cooper, H. D. B., Lumsden, S. L., Oudmaijer, R. D., Hoare, M. G., Clarke, A. J., Urquhart, J. S., Mottram, J. C., Moore, T. J. T., and Davies, B. (Apr. 2013). "The RMS survey: near-IR spectroscopy of massive young stellar objects". In: Monthy Notices of the Royal Astronomical Society 430.2, pp. 1125–1157. DOI: 10.1093/mnras/sts681. arXiv: 1301.4109 [astro-ph.GA].

Cooper, Heather Danielle Blythe (2013). "Observational studies of regions of massive star formation". Thesis. URL: https://ui.adsabs.harvard.edu/abs/2013PhDT.......441C.

Correia, S., Zinnecker, H., Ratzka, Th., and Sterzik, M. F. (Dec. 2006). "A VLT/NACO survey for triple and quadruple systems among visual pre-main sequence binaries". In: Astronomy and Astrophysics 459.3, pp. 909–926. DOI: 10.1051/0004-6361:20065545. arXiv: astro-ph/0608674 [astro-ph].

Crowther, Paul A., Caballero-Nieves, S. M., Bostroem, K. A., Maıéz Apellániz, J., Schneider, F. R. N., Walborn, N. R., Angus, C. R., Brott, I., Bonanos, A., de Koter, A., de Mink, S. E., Evans, C. J., Gräfener, G., Herrero, A., Howarth, I. D., Langer, N., Lennon, D. J., Puls, J., Sana, H., and Vink, J. S. (May 2016). "The R136 star cluster dissected with Hubble Space Telescope/STIS. I. Far-ultraviolet spectroscopic census and the origin of He II λ1640 in young star clusters". In: Monthy Notices of the Royal Astronomical Society 458.1, pp. 624–659. DOI: 10.1093/mnras/stw273. arXiv: 1603.04994 [astro-ph.SR].

Davies, Ben, Hoare, Melvin G., Lumsden, Stuart L., Hosokawa, Takashi, Oudmaijer, René D., Urquhart, James S., Mottram, Joseph C., and Stead, Joseph (Sept. 2011). "The Red MSX Source survey: critical tests of accretion models for the formation of massive stars". In: Monthy Notices of the Royal Astronomical Society 416.2, pp. 972–990. DOI: 10.1111/j.1365-2966.2011.19095.x. arXiv: 1105.3984 [astro-ph.GA].

De Rosa, R. J., Patience, J., Wilson, P. A., Schneider, A., Wiktorowicz, S. J., Vigan, A., Marois, C., Song, I., Macintosh, B., Graham, J. R., Doyon, R., Bessell, M. S., Thomas, S., and Lai, O. (Jan. 2014). "The VAST Survey - III. The multiplicity of A-type stars within 75 pc". In: Monthy Notices of the Royal Astronomical Society 437.2, pp. 1216–1240. DOI: 10.1093/mnras/stt1932. arXiv: 1311.7141 [astro-ph.SR].

Dempsey, Adam M., Muñoz, Diego J., and Lithwick, Yoram (Sept. 2021). "Outward Migration of Super-Jupiters". In: The Astrophysical Journal Letters 918.2, L36, p. L36. DOI: 10.3847/2041-8213/ac22af. arXiv: 2105.05277 [astro-ph.EP].

Derkink, A. R., Ramıérez-Tannus, M. C., Kaper, L., de Koter, A., Backs, F., Poorta, J., and van Gelder, M. L. (Oct. 2023). "Spectroscopic variability of massive pre-main-sequence stars in M17". In: *arXiv e-prints*, arXiv:2310.04287, arXiv:2310.04287. DOI: 10.48550/arXiv.2310.04287. arXiv: 2310.04287 [astro-ph.SR].

Derkink, Annelotte, Kaper, Lex, de Koter, Alex, Ramıérez-Tannus, Maria, Backs, Frank, and Poorta, Hanneke (Oct. 2021). "Variability as a diagnostic tool in massive young stellar objects". In: *MOBSTER-1 virtual conference: Stellar Variability as a Probe of Magnetic Fields in Massive Stars*, 51, p. 51. DOI: 10.5281/zenodo.5576537.

Duchêne, Gaspard and Kraus, Adam (Aug. 2013). "Stellar Multiplicity". In: Annual Review of Astronomy and Astrophysics 51.1, pp. 269–310. DOI: 10.1146/annurev-astro-081710-102602. arXiv: 1303.3028 [astro-ph.SR].

Duquennoy, A. and Mayor, M. (Aug. 1991). "Multiplicity among Solar Type Stars in the Solar Neighbourhood - Part Two - Distribution of the Orbital Elements in an Unbiased Sample". In: Astronomy and Astrophysics 248, p. 485.

Earl, Nicholas, Tollerud, Erik, Jones, Craig, O'Steen, Ricky, Kerzendorf, Wolfgang, Busko, Ivo, shaileshahuja, D'Avella, Dan, Robitaille, Thomas, Ginsburg, Adam, Homeier, Derek, Sipőcz, Brigitta, Averbukh, Jesse, Tocknell, James, Cherinka, Brian, Ogaz, Sara, Geda, Robel, Lim, P. L., Davies, James, Günther, Hans Moritz, Barbary, Kyle, Foster, Jonathan, Conroy, Kyle, Droettboom, Michael, Torres, Simon, Bray, E. M., Casey, Andy, Teuben, Peter, Crawford, Steve, and Ferguson, Henry (Feb. 2022). *astropy/specutils: V1.7.0*. Version v1.7.0. DOI: 10.5281/zenodo.6207491. URL: https://doi.org/10.5281/zenodo.6207491.

Egan, M. P., Price, S. D., Kraemer, K. E., Mizuno, D. R., Carey, S. J., Wright, C. O., Engelke, C. W., Cohen, M., and Gugliotti, M. G. (Jan. 2003). "VizieR Online Data Catalog: MSX6C Infrared Point Source Catalog. The Midcourse Space Experiment Point Source Catalog Version 2.3 (October 2003)". In: *VizieR Online Data Catalog*, V/114, pp. V/114.

Fabrycky, Daniel and Tremaine, Scott (Nov. 2007). "Shrinking Binary and Planetary Orbits by Kozai Cycles with Tidal Friction". In: The Astrophysical Journal 669.2, pp. 1298–1315. DOI: 10.1086/521702. arXiv: 0705.4285 [astro-ph].

Frost, A. J., Oudmaijer, R. D., de Wit, W. J., and Lumsden, S. L. (May 2019). "A multi-scale exploration of a massive young stellar object. A transition disk around G305.20+0.21?" In: Astronomy and Astrophysics 625, A44, A44. DOI: 10.1051/0004-6361/201834583. arXiv: 1903.04393 [astro-ph.SR].

– (Apr. 2021). "Unveiling the traits of massive young stellar objects through a multi-scale survey". In: Astronomy and Astrophysics 648, A62, A62. DOI: 10.1051/0004-6361/202039748. arXiv: 2102.05087 [astro-ph.SR].

Gaia Collaboration et al. (May 2021). "Gaia Early Data Release 3. Summary of the contents and survey properties". In: Astronomy and Astrophysics 649, A1, A1. DOI: 10.1051/0004-6361/202039657. arXiv: 2012.01533 [astro-ph.GA].

Gaia Collaboration et al. (July 2022). "Gaia Data Release 3: Summary of the content and survey properties". In: *arXiv e-prints*, arXiv:2208.00211, arXiv:2208.00211. DOI: 10.48550/arXiv.2208.00211. arXiv: 2208.00211 [astro-ph.GA].

Gammie, Charles F. (May 2001). "Nonlinear Outcome of Gravitational Instability in Cooling, Gaseous Disks". In: The Astrophysical Journal 553.1, pp. 174–183. DOI: 10.1086/320631. arXiv: astro-ph/0101501 [astro-ph].

Goodwin, S. P., Whitworth, A. P., and Ward-Thompson, D. (Aug. 2004). "Simulating star formation in molecular cores. II. The effects of different levels of turbulence". In: Astronomy and Astrophysics 423, pp. 169–182. DOI: 10.1051/0004-6361:20040285. arXiv: astro-ph/0405117 [astro-ph].

GRAVITY Collaboration et al. (Mar. 2020). “The GRAVITY young stellar object survey. II. First spatially resolved observations of the CO bandhead emission in a high-mass YSO”. In: Astronomy and Astrophysics 635, L12, p. L12. DOI: 10.1051/0004-6361/202037583. arXiv: 2003.05404 [astro-ph.SR].

Gravity Collaboration et al. (Dec. 2018). “Multiple star systems in the Orion nebula”. In: Astronomy and Astrophysics 620, A116, A116. DOI: 10.1051/0004-6361/201833575. arXiv: 1809.10376 [astro-ph.SR].

Green, Gregory M., Schlafly, Edward, Zucker, Catherine, Speagle, Joshua S., and Finkbeiner, Douglas (Dec. 2019). “A 3D Dust Map Based on Gaia, Pan-STARRS 1, and 2MASS”. In: The Astrophysical Journal 887.1, 93, p. 93. DOI: 10.3847/1538-4357/ab5362. arXiv: 1905.02734 [astro-ph.GA].

Griffiths, Daniel W., Goodwin, Simon P., and Caballero-Nieves, Saida M. (May 2018). “Massive, wide binaries as tracers of massive star formation”. In: Monthy Notices of the Royal Astronomical Society 476.2, pp. 2493–2500. DOI: 10.1093/mnras/sty412. arXiv: 1802.04560 [astro-ph.GA].

Guszejnov, Dávid, Grudić, Michael Y., Hopkins, Philip F., Offner, Stella S. R., and Faucher-Giguère, Claude-André (Apr. 2021). “STARFORGE: the effects of protostellar outflows on the IMF”. In: Monthy Notices of the Royal Astronomical Society 502.3, pp. 3646–3663. DOI: 10.1093/mnras/stab278. arXiv: 2010.11249 [astro-ph.GA].

Halbwachs, J. -L. (Mar. 1988). “Statistical Studies on Wide Pairs”. In: Ap&SS 142.1-2, pp. 237–244. DOI: 10.1007/BF00656216.

Hillier, D. J. (June 2008). “The Enigmatic Eta Carinae: Current Status”. In: *Mass Loss from Stars and the Evolution of Stellar Clusters*. Ed. by A. de Koter, L. J.

Smith, and Laurens B. F. M. Waters. Vol. 388. Astronomical Society of the Pacific Conference Series, p. 119.

Hosokawa, Takashi, Yorke, Harold W., and Omukai, Kazuyuki (Sept. 2010). "Evolution of Massive Protostars Via Disk Accretion". In: The Astrophysical Journal 721.1, pp. 478–492. DOI: 10.1088/0004-637X/721/1/478. arXiv: 1005.2827 [astro-ph.SR].

Hosokawa, Takashi. and Omukai, Kazuyuki (Jan. 2009). "Evolution of Massive Protostars with High Accretion Rates". In: The Astrophysical Journal 691.1, pp. 823–846. DOI: 10.1088/0004-637X/691/1/823. arXiv: astro-ph/0806.4122 [astro-ph].

Houghton, Rebecca (Oct. 2023). "Investigating the formation and properties of multiple star systems using Monte Carlo models". Thesis. University of Sheffield. URL: https://etheses.whiterose.ac.uk/33693/.

Ilee, J. D., Cyganowski, C. J., Brogan, C. L., Hunter, T. R., Forgan, D. H., Haworth, T. J., Clarke, C. J., and Harries, T. J. (Dec. 2018a). "G11.92-0.61 MM 1: A Fragmented Keplerian Disk Surrounding a Proto-O Star". In: The Astrophysical Journal Letters 869.2, L24, p. L24. DOI: 10.3847/2041-8213/aaeffc. arXiv: 1811.05267 [astro-ph.SR].

Ilee, J. D., Oudmaijer, R. D., Wheelwright, H. E., and Pomohaci, R. (July 2018b). "Blinded by the light: on the relationship between CO first overtone emission and mass accretion rate in massive young stellar objects". In: Monthy Notices of the Royal Astronomical Society 477.3, pp. 3360–3368. DOI: 10.1093/mnras/sty863. arXiv: 1804.01934 [astro-ph.SR].

Ilee, J. D., Wheelwright, H. E., Oudmaijer, R. D., de Wit, W. J., Maud, L. T., Hoare, M. G., Lumsden, S. L., Moore, T. J. T., Urquhart, J. S., and Mottram, J. C. (Mar. 2013). "CO bandhead emission of massive young stellar objects: determining disc properties". In: Monthy Notices of the Royal Astronomical Society 429.4, pp. 2960–2973. DOI: 10.1093/mnras/sts537. arXiv: 1212.0554 [astro-ph.SR].

Jeans, J. H. (Jan. 1902). "The Stability of a Spherical Nebula". In: *Philosophical Transactions of the Royal Society of London Series A* 199, pp. 1–53. DOI: 10.1098/rsta.1902.0012.

Johnston, Katharine G., Robitaille, Thomas P., Beuther, Henrik, Linz, Hendrik, Boley, Paul, Kuiper, Rolf, Keto, Eric, Hoare, Melvin G., and van Boekel, Roy (Nov. 2015). "A Keplerian-like Disk around the Forming O-type Star AFGL 4176". In: The Astrophysical Journal Letters 813.1, L19, p. L19. DOI: 10.1088/2041-8205/813/1/L19. arXiv: 1509.08469 [astro-ph.SR].

Kahn, F. D. (Dec. 1974). "Cocoons around early-type stars." In: Astronomy and Astrophysics 37, pp. 149–162.

Kennicutt, Robert C. (Jan. 2005). "The role of massive stars in astrophysics". In: *Massive Star Birth: A Crossroads of Astrophysics*. Ed. by R. Cesaroni, M. Felli, E. Churchwell, and M. Walmsley. Vol. 227. IAU Symposium, pp. 3–11. DOI: 10.1017/S1743921305004308.

Kervella, Pierre, Arenou, Frédéric, and Thévenin, Frédéric (Jan. 2022). "Stellar and substellar companions from Gaia EDR3. Proper-motion anomaly and resolved common proper-motion pairs". In: Astronomy and Astrophysics 657, A7, A7. DOI: 10.1051/0004-6361/202142146. arXiv: 2109.10912 [astro-ph.SR].

King, Robert R., Parker, Richard J., Patience, Jenny, and Goodwin, Simon P. (Apr. 2012). "Testing the universality of star formation - I. Multiplicity in nearby star-forming regions". In: Monthy Notices of the Royal Astronomical Society 421.3, pp. 2025–2042. DOI: 10.1111/j.1365-2966.2012.20437.x. arXiv: 1201.1311 [astro-ph.SR].

Kirk, H., Dunham, M. M., Di Francesco, J., Johnstone, D., Offner, S. S. R., Sadavoy, S. I., Tobin, J. J., Arce, H. G., Bourke, T. L., Mairs, S., Myers, P. C., Pineda, J. E., Schnee, S., and Shirley, Y. L. (Apr. 2017). "ALMA Observations of Starless Core Substructure in Ophiuchus". In: The Astrophysical Journal 838.2, 114, p. 114. DOI: 10.3847/1538-4357/aa63f8. arXiv: 1703.00506 [astro-ph.SR].

Könyves, V., André, Ph., Men'shchikov, A., Palmeirim, P., Arzoumanian, D., Schneider, N., Roy, A., Didelon, P., Maury, A., Shimajiri, Y., Di Francesco, J., Bontemps, S., Peretto, N., Benedettini, M., Bernard, J. -Ph., Elia, D., Griffin, M. J., Hill, T., Kirk, J., Ladjelate, B., Marsh, K., Martin, P. G., Motte, F., Nguyên Luong, Q., Pezzuto, S., Roussel, H., Rygl, K. L. J., Sadavoy, S. I., Schisano, E., Spinoglio, L., Ward-Thompson, D., and White, G. J. (Dec. 2015). "A census of dense cores in the Aquila cloud complex: SPIRE/PACS observations from the Herschel Gould Belt survey". In: Astronomy and Astrophysics 584, A91, A91. DOI: 10.1051/0004-6361/201525861. arXiv: 1507.05926 [astro-ph.GA].

Koumpia, E., Ababakr, K. M., de Wit, W. J., Oudmaijer, R. D., Caratti o Garatti, A., Boley, P., Linz, H., Kraus, S., Vink, J. S., and Le Bouquin, J. -B. (Mar. 2019). "Resolving the MYSO binaries PDS 27 and PDS 37 with VLTI/PIONIER". In: Astronomy and Astrophysics 623, L5, p. L5. DOI: 10.1051/0004-6361/201834624. arXiv: 1903.02667 [astro-ph.SR].

Koumpia, E., de Wit, W. -J., Oudmaijer, R. D., Frost, A. J., Lumsden, S., Caratti o Garatti, A., Goodwin, S. P., Stecklum, B., Mendigutıéa, I., Ilee, J. D., and Vioque, M. (Oct. 2021). "The first interferometric survey of massive YSOs in the K-band. Hot dust, ionised gas, and binarity at au scales". In: Astronomy and Astrophysics 654, A109, A109. DOI: 10.1051/0004-6361/202141373. arXiv: 2108.02868 [astro-ph.SR].

Koumpia, Evgenia, Koutoulaki, M., de Wit, W. -J., Oudmaijer, R. D., Frost, A. J., Lumsden, S. L., and Pittard, J. M. (Feb. 2023). "First spatially resolved Na I and He I transitions towards a massive young stellar object. Finding new tracers for the gaseous star/disc interface". In: Monthy Notices of the Royal Astronomical Society 519.1, pp. L51–L56. DOI: 10.1093/mnrasl/slac151. arXiv: 2211.13085 [astro-ph.SR].

Kratter, K. M. (Sept. 2011). "The Formation of Close Binaries". In: *Evolution of Compact Binaries*. Ed. by L. Schmidtobreick, M. R. Schreiber, and C. Tappert. Vol. 447. Astronomical Society of the Pacific Conference Series, p. 47. arXiv: 1109.3740 [astro-ph.SR].

Kratter, Kaitlin and Lodato, Giuseppe (Sept. 2016). "Gravitational Instabilities in Circumstellar Disks". In: Annual Review of Astronomy and Astrophysics 54, pp. 271–311. DOI: 10.1146/annurev-astro-081915-023307. arXiv: 1603.01280 [astro-ph.SR].

Kratter, Kaitlin M., Matzner, Christopher D., and Krumholz, Mark R. (July 2008). "Global Models for the Evolution of Embedded, Accreting Protostellar Disks". In: The Astrophysical Journal 681.1, pp. 375–390. DOI: 10.1086/587543. arXiv: 0709.4252 [astro-ph].

Kratter, Kaitlin M., Matzner, Christopher D., Krumholz, Mark R., and Klein, Richard I. (Jan. 2010). "On the Role of Disks in the Formation of Stellar Systems: A Numerical Parameter Study of Rapid Accretion". In: The Astrophysical Journal 708.2, pp. 1585–1597. DOI: 10.1088/0004-637X/708/2/1585. arXiv: 0907.3476 [astro-ph.SR].

Kraus, Adam L., Ireland, Michael J., Martinache, Frantz, and Hillenbrand, Lynne A. (Apr. 2011). "Mapping the Shores of the Brown Dwarf Desert. II. Multiple Star

Formation in Taurus-Auriga". In: The Astrophysical Journal 731.1, 8, p. 8. DOI: 10.1088/0004-637X/731/1/8. arXiv: 1101.4016 [astro-ph.SR].

Kraus, S., Kluska, J., Kreplin, A., Bate, M., Harries, T. J., Hofmann, K. -H., Hone, E., Monnier, J. D., Weigelt, G., Anugu, A., Wit, W. J. de, and Wittkowski, M. (2017). "A High-mass Protobinary System with Spatially Resolved Circumstellar Accretion Disks and Circumbinary Disk". In: The Astrophysical Journal 835. URL: https://ui.adsabs.harvard.edu/abs/2017ApJ...835L...5K.

Kraus, Stefan, Hofmann, Karl-Heinz, Menten, Karl M., Schertl, Dieter, Weigelt, Gerd, Wyrowski, Friedrich, Meilland, Anthony, Perraut, Karine, Petrov, Romain, Robbe-Dubois, Sylvie, Schilke, Peter, and Testi, Leonardo (July 2010). "A hot compact dust disk around a massive young stellar object". In: Nature 466.7304, pp. 339–342. DOI: 10.1038/nature09174. arXiv: 1007.5062 [astro-ph.SR].

Krumholz, Mark R., Klein, Richard I., and McKee, Christopher F. (July 2012). "Radiation-hydrodynamic Simulations of the Formation of Orion-like Star Clusters. II. The Initial Mass Function from Winds, Turbulence, and Radiation". In: The Astrophysical Journal 754.1, 71, p. 71. DOI: 10.1088/0004-637X/754/1/71. arXiv: 1203.2620 [astro-ph.SR].

Krumholz, Mark R., Klein, Richard I., McKee, Christopher F., Offner, Stella S. R., and Cunningham, Andrew J. (Feb. 2009). "The Formation of Massive Star Systems by Accretion". In: Science 323.5915, p. 754. DOI: 10.1126/science.1165857. arXiv: 0901.3157 [astro-ph.SR].

Kuiper, R. and Hosokawa, T. (Aug. 2018). "First hydrodynamics simulations of radiation forces and photoionization feedback in massive star formation". In: Astronomy and Astrophysics 616, A101, A101. DOI: 10.1051/0004-6361/201832638. arXiv: 1804.10211 [astro-ph.GA].

Lakeland, Ben S. and Naylor, Tim (Aug. 2022). "Towards an understanding of YSO variability: a multiwavelength analysis of bursting, dipping, and symmetrically varying light curves of disc-bearing YSOs". In: Monthy Notices of the Royal Astronomical Society 514.2, pp. 2736–2755. DOI: 10.1093/mnras/stac1477. arXiv: 2205.13334 [astro-ph.SR].

Larson, Richard B. (Oct. 2003). "The physics of star formation". In: *Reports on Progress in Physics* 66.10, pp. 1651–1697. DOI: 10.1088/0034-4885/66/10/R03. arXiv: astro-ph/0306595 [astro-ph].

Lau, Y. Y. and Bertin, G. (Dec. 1978). "Discrete spiral modes, spiral waves, and the local dispersion relationship." In: The Astrophysical Journal 226, pp. 508–520. DOI: 10.1086/156635.

Lee, Aaron T., Offner, Stella S. R., Kratter, Kaitlin M., Smullen, Rachel A., and Li, Pak Shing (Dec. 2019). "The Formation and Evolution of Wide-orbit Stellar Multiples In Magnetized Clouds". In: The Astrophysical Journal 887.2, 232, p. 232. DOI: 10.3847/1538-4357/ab584b. arXiv: 1911.07863 [astro-ph.GA].

Lee, Aaron T. and Stahler, Steven W. (Oct. 2011). "Dynamical friction in a gas: the subsonic case". In: Monthy Notices of the Royal Astronomical Society 416.4, pp. 3177–3186. DOI: 10.1111/j.1365-2966.2011.19273.x. arXiv: 1106.4820 [astro-ph.GA].

Lucas, P. W., Hoare, M. G., Longmore, A., Schröder, A. C., Davis, C. J., Adamson, A., Bandyopadhyay, R. M., de Grijs, R., Smith, M., Gosling, A., Mitchison, S., Gáspár, A., Coe, M., Tamura, M., Parker, Q., Irwin, M., Hambly, N., Bryant, J., Collins, R. S., Cross, N., Evans, D. W., Gonzalez-Solares, E., Hodgkin, S., Lewis, J., Read, M., Riello, M., Sutorius, E. T. W., Lawrence, A., Drew, J. E., Dye, S., and Thompson, M. A. (Nov. 2008). "The UKIDSS Galactic Plane Survey". In: Monthy

Notices of the Royal Astronomical Society 391.1, pp. 136–163. DOI: 10.1111/j.1365-2966.2008.13924.x. arXiv: 0712.0100 [astro-ph].

Lumsden, S. L., Hoare, M. G., Oudmaijer, R. D., and Richards, D. (Oct. 2002). "The population of the Galactic plane as seen by MSX". In: *Monthly Notices of the Royal Astronomical Society* 336.2, pp. 621–636. DOI: 10.1046/j.1365-8711.2002.05785.x. arXiv: astro-ph/0206391 [astro-ph].

Lumsden, S. L., Hoare, M. G., Urquhart, J. S., Oudmaijer, R. D., Davies, B., Mottram, J. C., Cooper, H. D. B., and Moore, T. J. T. (Sept. 2013). "The Red MSX Source Survey: The Massive Young Stellar Population of Our Galaxy". In: The Astrophysical Journal Supplement 208.1, 11, p. 11. DOI: 10.1088/0067-0049/208/1/11. arXiv: 1308.0134 [astro-ph.GA].

Lumsden, S. L., Wheelwright, H. E., Hoare, M. G., Oudmaijer, R. D., and Drew, J. E. (Aug. 2012). "Tracers of discs and winds around intermediate- and high-mass young stellar objects". In: Monthy Notices of the Royal Astronomical Society 424.2, pp. 1088–1104. DOI: 10.1111/j.1365-2966.2012.21280.x. arXiv: 1205.2296 [astro-ph.SR].

Lund, Kristin and Bonnell, Ian A. (Sept. 2018). "The formation of high-mass binary star systems". In: Monthy Notices of the Royal Astronomical Society 479.2, pp. 2235–2242. DOI: 10.1093/mnras/sty1584. arXiv: 1806.07394 [astro-ph.SR].

Machida, Masahiro, Inutsuka, Shu-ichiro, and Matsumoto, Tomoaki (July 2009). "Protostellar Jet and Outflow in the Collapsing Cloud Core". In: DOI: 10.1007/978-3-642-00576-3_48.

Machida, Masahiro N. (Nov. 2017). "Protostellar Jets and Outflows in low-mass star formation". In: *arXiv e-prints*, arXiv:1711.00384, arXiv:1711.00384. DOI: 10.48550/arXiv.1711.00384. arXiv: 1711.00384 [astro-ph.GA].

Marks, M. and Kroupa, P. (July 2012). "Inverse dynamical population synthesis. Constraining the initial conditions of young stellar clusters by studying their binary populations". In: Astronomy and Astrophysics 543, A8, A8. DOI: 10.1051/0004-6361/201118231. arXiv: 1205.1508 [astro-ph.GA].

Mathieu, Robert D. (Jan. 1994). "Pre-Main-Sequence Binary Stars". In: Annual Review of Astronomy and Astrophysics 32, pp. 465–530. DOI: 10.1146/annurev.aa.32.090194.002341.

McKee, Christopher F. and Tan, Jonathan C. (Mar. 2003). "The Formation of Massive Stars from Turbulent Cores". In: The Astrophysical Journal 585.2, pp. 850–871. DOI: 10.1086/346149. arXiv: astro-ph/0206037 [astro-ph].

Mendigutıéa, I., de Wit, W. J., Oudmaijer, R. D., Fairlamb, J. R., Carciofi, A. C., Ilee, J. D., and Vieira, R. G. (Oct. 2015). "High-resolution Br γ spectro-interferometry of the transitional Herbig Ae/Be star HD 100546: a Keplerian gaseous disc inside the inner rim". In: Monthy Notices of the Royal Astronomical Society 453.2, pp. 2126–2132. DOI: 10.1093/mnras/stv1777. arXiv: 1509.05411 [astro-ph.SR].

Meyer, D. M. -A., Kreplin, A., Kraus, S., Vorobyov, E. I., Haemmerle, L., and Eislöffel, J. (Aug. 2019). "On the ALMA observability of nascent massive multiple systems formed by gravitational instability". In: Monthy Notices of the Royal Astronomical Society 487.4, pp. 4473–4491. DOI: 10.1093/mnras/stz1585. arXiv: 1906.02015 [astro-ph.SR].

Meyer, D. M. -A., Kuiper, R., Kley, W., Johnston, K. G., and Vorobyov, E. (Jan. 2018). "Forming spectroscopic massive protobinaries by disc fragmentation". In: Monthy Notices of the Royal Astronomical Society 473.3, pp. 3615–3637. DOI: 10.1093/mnras/stx2551. arXiv: 1710.01162 [astro-ph.SR].

Minniti, Dante (Jan. 2018). “Mapping the Milky Way in the Near-IR: The Future of the VVV Survey”. In: *The Vatican Observatory, Castel Gandolfo: 80th Anniversary Celebration*. Ed. by Gabriele Gionti and Jean-Baptiste Kikwaya Eluo. Vol. 51. Astrophysics and Space Science Proceedings, p. 63. DOI: 10.1007/978-3-319-67205-2_4.

Modigliani, Andrea, Goldoni, Paolo, Royer, Frédéric, Haigron, Regis, Guglielmi, Laurent, François, Patrick, Horrobin, Matthew, Bristow, Paul, Vernet, Joel, Moehler, Sabine, Kerber, Florian, Ballester, Pascal, Mason, Elena, and Christensen, Lise (July 2010). “The X-shooter pipeline”. In: *Observatory Operations: Strategies, Processes, and Systems III*. Ed. by David R. Silva, Alison B. Peck, and B. Thomas Soifer. Vol. 7737. Society of Photo-Optical Instrumentation Engineers (SPIE) Conference Series, 773728, p. 773728. DOI: 10.1117/12.857211.

Moe, Maxwell and Di Stefano, Rosanne (June 2017). “Mind Your Ps and Qs: The Interrelation between Period (P) and Mass-ratio (Q) Distributions of Binary Stars”. In: The Astrophysical Journal Supplement 230.2, 15, p. 15. DOI: 10.3847/1538-4365/aa6fb6. arXiv: 1606.05347 [astro-ph.SR].

Moe, Maxwell and Kratter, Kaitlin M. (Feb. 2018). “Dynamical Formation of Close Binaries during the Pre-main-sequence Phase”. In: The Astrophysical Journal 854.1, 44, p. 44. DOI: 10.3847/1538-4357/aaa6d2. arXiv: 1706.09894 [astro-ph.SR].

Moeckel, Nickolas and Bally, John (Feb. 2007). “Capture-formed Binaries via Encounters with Massive Protostars”. In: The Astrophysical Journal 656.1, pp. 275–286. DOI: 10.1086/510343. arXiv: astro-ph/0610633 [astro-ph].

Molinari, S., Brand, J., Cesaroni, R., and Palla, F. (Apr. 1996). “A search for precursors of ultracompact HII regions in a sample of luminous IRAS sources. I. Association with ammonia cores.” In: Astronomy and Astrophysics 308, pp. 573–587.

Molinari, S., Brand, J., Cesaroni, R., Palla, F., and Palumbo, G. G. C. (Aug. 1998). "A search for precursors of ultracompact H II regions in a sample of luminous IRAS sources. II. VLA observations". In: Astronomy and Astrophysics 336, pp. 339–351.

Mottram, J. C., Hoare, M. G., Urquhart, J. S., Lumsden, S. L., Oudmaijer, R. D., Robitaille, T. P., Moore, T. J. T., Davies, B., and Stead, J. (Jan. 2011). "The Red MSX Source survey: the bolometric fluxes and luminosity distributions of young massive stars". In: Astronomy and Astrophysics 525, A149, A149. DOI: 10.1051/0004-6361/201014479. arXiv: 1009.1774 [astro-ph.GA].

Muñoz, D. J., Kratter, K., Vogelsberger, M., Hernquist, L., and Springel, V. (Jan. 2015). "Stellar orbit evolution in close circumstellar disc encounters". In: Monthy Notices of the Royal Astronomical Society 446.2, pp. 2010–2029. DOI: 10.1093/mnras/stu2220. arXiv: 1410.4561 [astro-ph.EP].

Muñoz, Diego J., Miranda, Ryan, and Lai, Dong (Jan. 2019). "Hydrodynamics of Circumbinary Accretion: Angular Momentum Transfer and Binary Orbital Evolution". In: The Astrophysical Journal 871.1, 84, p. 84. DOI: 10.3847/1538-4357/aaf867. arXiv: 1810.04676 [astro-ph.HE].

Myers, Andrew T., McKee, Christopher F., Cunningham, Andrew J., Klein, Richard I., and Krumholz, Mark R. (Apr. 2013). "The Fragmentation of Magnetized, Massive Star-forming Cores with Radiative Feedback". In: The Astrophysical Journal 766.2, 97, p. 97. DOI: 10.1088/0004-637X/766/2/97. arXiv: 1211.3467 [astro-ph.SR].

Neugebauer, G., Beichman, C. A., Soifer, B. T., Aumann, H. H., Chester, T. J., Gautier, T. N., Gillett, F. C., Hauser, M. G., Houck, J. R., Lonsdale, C. J., Low, F. J., and Young, E. T. (Apr. 1984). "Early Results from the Infrared Astronomical Satellite". In: *Science* 224.4644, pp. 14–21. DOI: 10.1126/science.224.4644.14.

Offner, Stella S. R., Dunham, Michael M., Lee, Katherine I., Arce, Héctor G., and Fielding, Drummond B. (Aug. 2016). “The Turbulent Origin of Outflow and Spin Misalignment in Multiple Star Systems”. In: The Astrophysical Journal Letters 827.1, L11, p. L11. DOI: 10.3847/2041-8205/827/1/L11. arXiv: 1606.08445 [astro-ph.SR].

Offner, Stella S. R., Kratter, Kaitlin M., Matzner, Christopher D., Krumholz, Mark R., and Klein, Richard I. (Dec. 2010). “The Formation of Low-mass Binary Star Systems Via Turbulent Fragmentation”. In: The Astrophysical Journal 725.2, pp. 1485–1494. DOI: 10.1088/0004-637X/725/2/1485. arXiv: 1010.3702 [astro-ph.SR].

Offner, Stella S. R., Moe, Maxwell, Kratter, Kaitlin M., Sadavoy, Sarah I., Jensen, Eric L. N., and Tobin, John J. (Mar. 2022). “The Origin and Evolution of Multiple Star Systems”. In: *arXiv e-prints*, arXiv:2203.10066, arXiv:2203.10066. DOI: 10.48550/arXiv.2203.10066. arXiv: 2203.10066 [astro-ph.SR].

Öpik, E. (Jan. 1924). “Statistical Studies of Double Stars: On the Distribution of Relative Luminosities and Distances of Double Stars in the Harvard Revised Photometry North of Declination -31°”. In: *Publications of the Tartu Astrofizica Observatory* 25, p. 1.

Oudmaijer, R. D. and de Wit, W. -J. (Sept. 2014). “Star Formation at milli-arcsecond resolution”. In: *EAS Publications Series*. Vol. 69-70. EAS Publications Series, pp. 319–331. DOI: 10.1051/eas/1569019. arXiv: 1511.06130 [astro-ph.SR].

Oudmaijer, René D. and Parr, Andrew M. (July 2010). “The binary fraction and mass ratio of Be and B stars: a comparative Very Large Telescope/NACO study”. In: Monthy Notices of the Royal Astronomical Society 405.4, pp. 2439–2446. DOI: 10.1111/j.1365-2966.2010.16609.x. arXiv: 1003.0618 [astro-ph.SR].

Park, Chan, Jaffe, Daniel T., Yuk, In-Soo, Chun, Moo-Young, Pak, Soojong, Kim, Kang-Min, Pavel, Michael, Lee, Hanshin, Oh, Heeyoung, Jeong, Ueejeong, Sim, Chae Kyung, Lee, Hye-In, Nguyen Le, Huynh Anh, Strubhar, Joseph, Gully-Santiago, Michael, Oh, Jae Sok, Cha, Sang-Mok, Moon, Bongkon, Park, Kwijong, Brooks, Cynthia, Ko, Kyeongyeon, Han, Jeong-Yeol, Nah, Jakyoung, Hill, Peter C., Lee, Sungho, Barnes, Stuart, Yu, Young Sam, Kaplan, Kyle, Mace, Gregory, Kim, Hwihyun, Lee, Jae-Joon, Hwang, Narae, and Park, Byeong-Gon (July 2014). "Design and early performance of IGRINS (Immersion Grating Infrared Spectrometer)". In: *Ground-based and Airborne Instrumentation for Astronomy V*. Ed. by Suzanne K. Ramsay, Ian S. McLean, and Hideki Takami. Vol. 9147. Society of Photo-Optical Instrumentation Engineers (SPIE) Conference Series, 91471D, p. 91471D. DOI: 10.1117/12.2056431.

Pineda, Jaime E., Offner, Stella S. R., Parker, Richard J., Arce, Héctor G., Goodman, Alyssa A., Caselli, Paola, Fuller, Gary A., Bourke, Tyler L., and Corder, Stuartt A. (Feb. 2015). "The formation of a quadruple star system with wide separation". In: Nature 518.7538, pp. 213–215. DOI: 10.1038/nature14166.

Pomohaci, R., Oudmaijer, R. D., Lumsden, S. L., Hoare, M. G., and Mendigutıéa, I. (Dec. 2017). "Medium-resolution near-infrared spectroscopy of massive young stellar objects". In: Monthy Notices of the Royal Astronomical Society 472.3, pp. 3624–3636. DOI: 10.1093/mnras/stx2196. arXiv: 1709.03994 [astro-ph.SR].

Pomohaci, Robert, Oudmaijer, René D., and Goodwin, Simon P. (Mar. 2019). "A pilot survey of the binarity of Massive Young Stellar Objects with K-band adaptive optics". In: Monthy Notices of the Royal Astronomical Society 484.1, pp. 226–238. DOI: 10.1093/mnras/stz014. arXiv: 1901.04716 [astro-ph.SR].

Price-Whelan, A. M. et al. (Sept. 2018). "The Astropy Project: Building an Open-science Project and Status of the v2.0 Core Package". In: Astronomical Journal 156, 123, p. 123. DOI: 10.3847/1538-3881/aabc4f.

Pudritz, R. E. and Norman, C. A. (Feb. 1986). "Bipolar Hydromagnetic Winds from Disks around Protostellar Objects". In: The Astrophysical Journal 301, p. 571. DOI: 10.1086/163924.

Purcell, C. R., Hoare, M. G., Cotton, W. D., Lumsden, S. L., Urquhart, J. S., Chandler, C., Churchwell, E. B., Diamond, P., Dougherty, S. M., Fender, R. P., Fuller, G., Garrington, S. T., Gledhill, T. M., Goldsmith, P. F., Hindson, L., Jackson, J. M., Kurtz, S. E., Martıé, J., Moore, T. J. T., Mundy, L. G., Muxlow, T. W. B., Oudmaijer, R. D., Pandian, J. D., Paredes, J. M., Shepherd, D. S., Smethurst, S., Spencer, R. E., Thompson, M. A., Umana, G., and Zijlstra, A. A. (Mar. 2013). "The Coordinated Radio and Infrared Survey for High-mass Star Formation. II. Source Catalog". In: *The Astrophysical Journal Supplement Series* 205.1, 1, p. 1. DOI: 10.1088/0067-0049/205/1/1. arXiv: 1211.7116 [astro-ph.GA].

Raghavan, Deepak, McAlister, Harold A., Henry, Todd J., Latham, David W., Marcy, Geoffrey W., Mason, Brian D., Gies, Douglas R., White, Russel J., and ten Brummelaar, Theo A. (Sept. 2010). "A Survey of Stellar Families: Multiplicity of Solar-type Stars". In: The Astrophysical Journal Supplement 190.1, pp. 1–42. DOI: 10.1088/0067-0049/190/1/1. arXiv: 1007.0414 [astro-ph.SR].

Ramírez-Tannus, M. C., Backs, F., de Koter, A., Sana, H., Beuther, H., Bik, A., Brandner, W., Kaper, L., Linz, H., Henning, Th., and Poorta, J. (Jan. 2021). "A relation between the radial velocity dispersion of young clusters and their age. Evidence for hardening as the formation scenario of massive close binaries". In: Astronomy and Astrophysics 645, L10, p. L10. DOI: 10.1051/0004-6361/202039673. arXiv: 2101.01604 [astro-ph.SR].

Reynolds, Nickalas K., Tobin, John J., Sheehan, Patrick, Sadavoy, Sarah I., Kratter, Kaitlin M., Li, Zhi-Yun, Chandler, Claire J., Segura-Cox, Dominique, Looney, Leslie W., and Dunham, Michael M. (Jan. 2021). "Kinematic Analysis of a Protostellar

Multiple System: Measuring the Protostar Masses and Assessing Gravitational Instability in the Disks of L1448 IRS3B and L1448 IRS3A". In: The Astrophysical Journal Letters 907.1, L10, p. L10. DOI: 10.3847/2041-8213/abcc02. arXiv: 2011.08293 [astro-ph.GA].

Robitaille, Thomas P., Meade, Marilyn R., Babler, Brian L., Whitney, Barbara A., Johnston, Katharine G., Indebetouw, Rémy, Cohen, Martin, Povich, Matthew S., Sewilo, Marta, Benjamin, Robert A., and Churchwell, Edward (Dec. 2008). "Intrinsically Red Sources Observed by Spitzer in the Galactic Midplane". In: Astronomical Journal 136.6, pp. 2413–2440. DOI: 10.1088/0004-6256/136/6/2413. arXiv: 0809.1654 [astro-ph].

Rodriguez, Joseph E., Loomis, Ryan, Cabrit, Sylvie, Haworth, Thomas J., Facchini, Stefano, Dougados, Catherine, Booth, Richard A., Jensen, Eric L. N., Clarke, Cathie J., Stassun, Keivan G., Dent, William R. F., and Pety, Jérôme (June 2018). "Multiple Stellar Flybys Sculpting the Circumstellar Architecture in RW Aurigae". In: The Astrophysical Journal 859.2, 150, p. 150. DOI: 10.3847/1538-4357/aac08f. arXiv: 1804.09190 [astro-ph.SR].

Rosen, Anna L. (Dec. 2022). "A Massive Star Is Born: How Feedback from Stellar Winds, Radiation Pressure, and Collimated Outflows Limits Accretion onto Massive Stars". In: The Astrophysical Journal 941.2, 202, p. 202. DOI: 10.3847/1538-4357/ac9f3d. arXiv: 2204.09700 [astro-ph.SR].

Rosen, Anna L., Krumholz, Mark R., McKee, Christopher F., and Klein, Richard I. (Dec. 2016). "An unstable truth: how massive stars get their mass". In: Monthy Notices of the Royal Astronomical Society 463.3, pp. 2553–2573. DOI: 10.1093/mnras/stw2153. arXiv: 1607.03117 [astro-ph.SR].

Rosen, Anna L., Li, Pak Shing, Zhang, Qizhou, and Burkhart, Blakesley (Dec. 2019). "Massive-star Formation via the Collapse of Subvirial and Virialized Turbulent Massive Cores". In: The Astrophysical Journal 887.2, 108, p. 108. DOI: 10.3847/1538-4357/ab54c6. arXiv: 1902.10153 [astro-ph.SR].

Rozner, Mor, Generozov, Aleksey, and Perets, Hagai B. (May 2023). "Binary formation through gas-assisted capture and the implications for stellar, planetary, and compact object evolution". In: Monthy Notices of the Royal Astronomical Society 521.1, pp. 866–880. DOI: 10.1093/mnras/stad603. arXiv: 2212.00807 [astro-ph.GA].

Saito, R. K. et al. (Jan. 2012). "VVV DR1: The first data release of the Milky Way bulge and southern plane from the near-infrared ESO public survey VISTA variables in the Víéa Láctea". In: Astronomy and Astrophysics 537, A107, A107. DOI: 10.1051/0004-6361/201118407. arXiv: 1111.5511 [astro-ph.GA].

Salpeter, Edwin E. (Jan. 1955). "The Luminosity Function and Stellar Evolution." In: The Astrophysical Journal 121, p. 161. DOI: 10.1086/145971.

Sana, H., de Mink, S. E., de Koter, A., Langer, N., Evans, C. J., Gieles, M., Gosset, E., Izzard, R. G., Le Bouquin, J. -B., and Schneider, F. R. N. (July 2012). "Binary Interaction Dominates the Evolution of Massive Stars". In: *Science* 337.6093, p. 444. DOI: 10.1126/science.1223344. arXiv: 1207.6397 [astro-ph.SR].

Sana, H., Le Bouquin, J. -B., Lacour, S., Berger, J. -P., Duvert, G., Gauchet, L., Norris, B., Olofsson, J., Pickel, D., Zins, G., Absil, O., de Koter, A., Kratter, K., Schnurr, O., and Zinnecker, H. (Nov. 2014). "Southern Massive Stars at High Angular Resolution: Observational Campaign and Companion Detection". In: The Astrophysical Journal Supplement 215.1, 15, p. 15. DOI: 10.1088/0067-0049/215/1/15. arXiv: 1409.6304 [astro-ph.SR].

Sana, Hugues (Mar. 2022). "The interplay between mass-loss and binarity". In: *arXiv e-prints*, arXiv:2203.16332, arXiv:2203.16332. arXiv: 2203.16332 [astro-ph.SR].

Sana, Hugues and Evans, Christopher J. (July 2011). "The multiplicity of massive stars". In: *Active OB Stars: Structure, Evolution, Mass Loss, and Critical Limits.* Ed. by Coralie Neiner, Gregg Wade, Georges Meynet, and Geraldine Peters. Vol. 272. IAU Symposium, pp. 474–485. DOI: 10.1017/S1743921311011124. arXiv: 1009.4197 [astro-ph.SR].

Shu, F. H. (June 1977). "Self-similar collapse of isothermal spheres and star formation." In: The Astrophysical Journal 214, pp. 488–497. DOI: 10.1086/155274.

Shu, Frank H., Adams, Fred C., and Lizano, Susana (Jan. 1987). "Star formation in molecular clouds: observation and theory." In: Annual Review of Astronomy and Astrophysics 25, pp. 23–81. DOI: 10.1146/annurev.aa.25.090187.000323.

Shu, Frank H., Tremaine, Scott, Adams, Fred C., and Ruden, Steven P. (Aug. 1990). "SLING Amplification and Eccentric Gravitational Instabilities in Gaseous Disks". In: The Astrophysical Journal 358, p. 495. DOI: 10.1086/169003.

Simon, M., Righini-Cohen, G., Fischer, J., and Cassar, L. (Dec. 1981). "Velocity resolved spectroscopy of the brackett gamma line emission ofCRL 490 and M 17 IRS 1." In: The Astrophysical Journal 251, pp. 552–556. DOI: 10.1086/159497.

Sivkova, E. E., Wiebe, D. S., and Shustov, B. M. (May 2021). "The Sweeping-out of Dust by Radiation Pressure of Stars and Chemical Composition Peculiarities of Disc Galaxies". In: *Astronomy Reports* 65.5, pp. 370–384. DOI: 10.1134/S1063772921050061.

Skrutskie, M. F., Cutri, R. M., Stiening, R., Weinberg, M. D., Schneider, S., Carpenter, J. M., Beichman, C., Capps, R., Chester, T., Elias, J., Huchra, J., Liebert, J., Lonsdale, C., Monet, D. G., Price, S., Seitzer, P., Jarrett, T., Kirkpatrick, J. D., Gizis, J. E., Howard, E., Evans, T., Fowler, J., Fullmer, L., Hurt, R., Light, R., Kopan, E. L., Marsh, K. A., McCallon, H. L., Tam, R., Van Dyk, S., and Wheelock, S. (Feb. 2006). "The Two Micron All Sky Survey (2MASS)". In: Astronomical Journal 131.2, pp. 1163–1183. DOI: 10.1086/498708.

Sridharan, T. K., Beuther, H., Schilke, P., Menten, K. M., and Wyrowski, F. (Feb. 2002). "High-Mass Protostellar Candidates. I. The Sample and Initial Results". In: The Astrophysical Journal 566.2, pp. 931–944. DOI: 10.1086/338332. arXiv: astro-ph/0110363 [astro-ph].

Stetson, Peter B. (Mar. 1987). "DAOPHOT: A Computer Program for Crowded-Field Stellar Photometry". In: PASP 99, p. 191. DOI: 10.1086/131977.

Sugitani, K., Fukui, Y., Mizuni, A., and Ohashi, N. (July 1989). "Star Formation in Bright-rimmed Globules: Evidence for Radiation-driven Implosion". In: The Astrophysical Journal Letters 342, p. L87. DOI: 10.1086/185491.

Takahashi, S. Z., Tsukamoto, Y., and Inutsuka, S. (June 2016). "A revised condition for self-gravitational fragmentation of protoplanetary discs". In: Monthy Notices of the Royal Astronomical Society 458.4, pp. 3597–3612. DOI: 10.1093/mnras/stw557. arXiv: 1603.01402 [astro-ph.SR].

Tan, J. C., Beltrán, M. T., Caselli, P., Fontani, F., Fuente, A., Krumholz, M. R., McKee, C. F., and Stolte, A. (Jan. 2014). "Massive Star Formation". In: *Protostars and Planets VI*. Ed. by Henrik Beuther, Ralf S. Klessen, Cornelis P. Dullemond, and Thomas Henning, pp. 149–172. DOI: 10.2458/azu_uapress_9780816531240-ch007. arXiv: 1402.0919 [astro-ph.GA].

Tokovinin, Andrei and Moe, Maxwell (Feb. 2020). "Formation of close binaries by disc fragmentation and migration, and its statistical modelling". In: Monthy Notices of the Royal Astronomical Society 491.4, pp. 5158–5171. DOI: 10.1093/mnras/stz3299. arXiv: 1910.01522 [astro-ph.SR].

Toomre, A. (May 1964). “On the gravitational stability of a disk of stars.” In: The Astrophysical Journal 139, pp. 1217–1238. DOI: 10.1086/147861.

Urquhart, J. S., Busfield, A. L., Hoare, M. G., Lumsden, S. L., Oudmaijer, R. D., Moore, T. J. T., Gibb, A. G., Purcell, C. R., Burton, M. G., Maréchal, L. J. L., Jiang, Z., and Wang, M. (Aug. 2008). “The RMS survey. ^{13}CO observations of candidate massive YSOs in the northern Galactic plane”. In: Astronomy and Astrophysics 487.1, pp. 253–264. DOI: 10.1051/0004-6361:200809415. arXiv: 0806.0953 [astro-ph].

Urquhart, J. S., Hoare, M. G., Purcell, C. R., Lumsden, S. L., Oudmaijer, R. D., Moore, T. J. T., Busfield, A. L., Mottram, J. C., and Davies, B. (July 2009). “The RMS survey. 6 cm continuum VLA observations towards candidate massive YSOs in the northern hemisphere”. In: *Astronomy & Astrophysics* 501.2, pp. 539–551. DOI: 10.1051/0004-6361/200912108. arXiv: 0905.1174 [astro-ph.GA].

Urquhart, J. S., Moore, T. J. T., Hoare, M. G., Lumsden, S. L., Oudmaijer, R. D., Rathborne, J. M., Mottram, J. C., Davies, B., and Stead, J. J. (Jan. 2011). “The Red MSX Source survey: distribution and properties of a sample of massive young stars”. In: Monthy Notices of the Royal Astronomical Society 410.2, pp. 1237–1250. DOI: 10.1111/j.1365-2966.2010.17514.x. arXiv: 1008.3149 [astro-ph.GA].

van Albada, T. S. (Aug. 1968). “Statistical properties of early-type double and multiple stars”. In: Bull. Astron. Inst. Netherlands 20, p. 47.

Ward-Thompson, Derek and Whitworth, Anthony P. (2015). *An Introduction to Star Formation.*

Wheelwright, H. E., Oudmaijer, R. D., and Goodwin, S. P. (Jan. 2010). "The mass ratio and formation mechanisms of Herbig Ae/Be star binary systems". In: Monthy Notices of the Royal Astronomical Society 401.2, pp. 1199–1218. DOI: 10.1111/j.1365-2966.2009.15708.x. arXiv: 0910.1774 [astro-ph.SR].

Wheelwright, H. E., Vink, J. S., Oudmaijer, R. D., and Drew, J. E. (Aug. 2011). "On the alignment between the circumstellar disks and orbital planes of Herbig Ae/Be binary systems". In: *Astronomy & Astrophysics* 532, A28, A28. DOI: 10.1051/0004-6361/201116996. arXiv: 1106.3949 [astro-ph.SR].

Yorke, Harold W. and Sonnhalter, Cordula (Apr. 2002). "On the Formation of Massive Stars". In: The Astrophysical Journal 569.2, pp. 846–862. DOI: 10.1086/339264. arXiv: astro-ph/0201041 [astro-ph].

Young, M. D. and Clarke, C. J. (Sept. 2015). "Binary accretion rates: dependence on temperature and mass ratio". In: Monthy Notices of the Royal Astronomical Society 452.3, pp. 3085–3091. DOI: 10.1093/mnras/stv1512. arXiv: 1507.01850 [astro-ph.SR].

Yuk, In-Soo, Jaffe, Daniel T., Barnes, Stuart, Chun, Moo-Young, Park, Chan, Lee, Sungho, Lee, Hanshin, Wang, Weisong, Park, Kwi-Jong, Pak, Soojong, Strubhar, Joseph, Deen, Casey, Oh, Heeyoung, Seo, Haingja, Pyo, Tae-Soo, Park, Won-Kee, Lacy, John, Goertz, John, Rand, Jared, and Gully-Santiago, Michael (July 2010). "Preliminary design of IGRINS (Immersion GRating INfrared Spectrograph)". In: *Ground-based and Airborne Instrumentation for Astronomy III*. Ed. by Ian S. McLean, Suzanne K. Ramsay, and Hideki Takami. Vol. 7735. Society of Photo-Optical Instrumentation Engineers (SPIE) Conference Series, 77351M, p. 77351M. DOI: 10.1117/12.856864.

Zhu, Zhaohuan, Hartmann, Lee, Nelson, Richard P., and Gammie, Charles F. (Feb. 2012). “Challenges in Forming Planets by Gravitational Instability: Disk Irradiation and Clump Migration, Accretion, and Tidal Destruction”. In: The Astrophysical Journal 746.1, 110, p. 110. DOI: 10.1088/0004-637X/746/1/110. arXiv: 1111.6943 [astro-ph.SR].

Zinnecker, Hans and Yorke, Harold W. (Sept. 2007). “Toward Understanding Massive Star Formation”. In: Annual Review of Astronomy and Astrophysics 45.1, pp. 481–563. DOI: 10.1146/annurev.astro.44.051905.092549. arXiv: 0707.1279 [astro-ph].

Appendix A

YSO primaries in UKIDSS and VVV

RMS ID	RA (deg)	Dec (deg)	Distance (kpc)	L_{bol} ($L_\odot$)	Survey	J	H	K
G010.3208-00.1570B	272.2562	-20.0856	3.5	41620	UKIDSS	16.7	17.2	13.6
G010.3844+02.2128	270.0944	-18.8694	1.1	1180	UKIDSS	16.5	14.0	10.5
G010.5067+02.2285	270.1439	-18.755	2.9	1660	UKIDSS		16.7	14.1
G010.8856+00.1221	272.2833	-19.4567	2.7	3560	UKIDSS	18.6	13.2	9.6
G011.4201-01.6815	274.2362	-19.8522	1.5	7040	UKIDSS	18.9	14.5	11.7
G011.5001-01.4857	274.094	-19.69	1.7	6420	UKIDSS	13.6	11.4	10.3
G011.9019+00.7265	272.2449	-18.275	2.9	1840	UKIDSS	16.5	13.9	11.3
G011.9920-00.2731	273.2134	-18.6777	11.5	13140	UKIDSS	18.2		13.6
G012.0260-00.0317	273.0079	-18.5322	11.1	24640	UKIDSS	16.0	14.8	13.2
G012.1993-00.0342B	273.0976	-18.3808	12.0	34720	UKIDSS		18.0	15.1
G012.6814+00.0072A	273.3026	-17.9387	11.1	9260	UKIDSS	16.9	16.7	13.1
G012.7879-00.1786	273.5276	-17.9351	2.4	5250	UKIDSS	12.7	11.5	10.8
G012.8909+00.4938A	272.963	-17.5225	2.4	790	UKIDSS	17.5	15.1	13.1
G012.8909+00.4938C	272.9643	-17.525	2.4	790	UKIDSS		18.0	16.8
G012.9090-00.2607	273.6648	-17.8673	2.4	21740	UKIDSS	15.3	13.2	9.2
G013.1840-00.1069A	273.6624	-17.5521	11.9	13520	UKIDSS	18.2	17.8	12.1
G013.3310-00.0407	273.6742	-17.391	4.5	3240	UKIDSS	16.0	12.2	9.8
G013.6562-00.5997	274.3516	-17.3708	4.1	9870	UKIDSS	16.2	15.6	10.9
G014.0329-00.5155	274.461	-16.9993	1.1	580	UKIDSS	18.3	14.6	10.8
G014.2166-00.6344	274.661	-16.8936	1.1	180	UKIDSS	14.7	11.7	9.5
G014.4335-00.6969	274.8259	-16.7322	1.1	1280	UKIDSS	15.6	11.5	8.4

RMS ID	RA (deg)	Dec (deg)	Distance (kpc)	L_{bol} ($L_\odot$)	Survey	J	H	K
G014.6087+00.0127	274.2613	-16.2411	2.6	3890	UKIDSS	14.7	16.1	13.3
G014.9958-00.6732	275.0811	-16.225	2.0	12500	UKIDSS	12.7	9.8	7.3
G015.0939+00.1913	274.3369	-15.7294	2.9	1000	UKIDSS	16.3	14.4	11.1
G015.1288-00.6717	275.1442	-16.1079	2.0	11380	UKIDSS	12.8	11.8	12.2
G016.7122+01.3119	274.1099	-13.7734	2.1	1810	UKIDSS	13.9	10.7	8.7
G016.7981+00.1264	275.2304	-14.2586	1.7	1910	UKIDSS	16.7	13.4	9.7
G016.8055+00.8149	274.6081	-13.9272	2.1	540	UKIDSS	18.1	16.9	14.6
G016.8689-02.1552	277.351	-15.2634	2.0	6640	UKIDSS			15.9
G016.9261+00.2854	275.1477	-14.0705	2.4	3360	UKIDSS	17.9	13.6	9.9
G016.9270+00.9599	274.536	-13.752	2.1	5910	UKIDSS	17.8	13.0	9.4
G016.9512+00.7806	274.7096	-13.815	2.4	1630	UKIDSS	13.6	14.3	12.3
G017.0217+00.8442	274.6875	-13.7221	2.1	400	UKIDSS	12.9	11.1	9.8
G017.0332+00.7476A	274.7806	-13.7566	2.4	2310	UKIDSS			14.8
G017.0666+00.6826	274.8556	-13.7599	2.2	420	UKIDSS	17.0	14.6	11.1
G017.3765+02.2512	273.5877	-12.7426	1.3	1030	UKIDSS	14.7	11.3	9.2
G017.4507+00.8118A	274.9245	-13.3598	2.1	1290	UKIDSS	19.5	17.2	14.8
G017.4507+00.8118B	274.9268	-13.36	2.1	1270	UKIDSS	19.4	15.8	12.9
G017.6380+00.1566	275.6099	-13.5033	2.2	53190	UKIDSS	15.0	14.4	7.3
G017.9642+00.0798A	275.8372	-13.2515	2.2	760	UKIDSS	16.1	13.9	13.3
G017.9642+00.0798B	275.8363	-13.251	2.2	760	UKIDSS			15.4
G017.9642+00.0798C	275.8377	-13.253	2.2	760	UKIDSS			14.9
G017.9789+00.2335A	275.7047	-13.1671	14.4	31370	UKIDSS		17.9	15.2
G017.9868-00.1098	276.0188	-13.3195	4.3	3300	UKIDSS	10.9	8.7	7.6
G018.1968-00.1709	276.1767	-13.1622	10.6	16150	UKIDSS	13.8	12.6	11.9
G018.3412+01.7681	274.4921	-12.1236	2.8	21810	UKIDSS	16.6	13.9	9.3
G018.3706-00.3818	276.4515	-13.1081	3.5	3430	UKIDSS	15.0	11.7	9.3
G018.6608+00.0372A	276.2094	-12.6562	11.0	16230	UKIDSS			13.1
G018.8319-00.4788	276.7597	-12.744	4.5	3940	UKIDSS	17.8	14.9	11.4
G019.8817-00.5347	277.3112	-11.8399	3.3	7810	UKIDSS			
G019.8922+00.1023	276.7391	-11.536	3.4	6040	UKIDSS	14.2	12.8	10.7
G019.9224-00.2577	277.079	-11.6769	4.3	2740	UKIDSS	18.5	15.8	13.0
G019.9386-00.2079	277.0418	-11.6394	4.2	1990	UKIDSS	15.5	16.2	11.3
G020.5143+00.4936	276.6812	-10.8052	2.2	350	UKIDSS		17.5	15.1
G020.5703-00.8017	277.8774	-11.3554	3.2	2110	UKIDSS	11.6	9.6	8.1
G020.7617-00.0638B	277.3004	-10.8434	11.8	20820	UKIDSS	13.2	12.3	10.8
G020.7617-00.0638C	277.3011	-10.8428	11.8	17560	UKIDSS	12.4	10.8	9.8
G021.3570-00.1795B	277.6873	-10.3702	10.5	14750	UKIDSS			
G021.5624-00.0329	277.6503	-10.1198	9.7	23760	UKIDSS			10.9
G022.3554+00.0655	277.9337	-9.3718	4.9	14970	UKIDSS			13.7
G023.3891+00.1851	278.3097	-8.3993	4.5	41950	UKIDSS	14.4	11.6	8.4
G023.6566-00.1273	278.7149	-8.306	3.2	6160	UKIDSS	13.6	15.7	9.9
G023.8176+00.3841	278.3314	-7.9272	4.5	3780	UKIDSS	15.1	13.7	13.1
G024.0946+00.4565B	278.3945	-7.6469	5.2	1170	UKIDSS	15.7	12.7	10.7
G024.4916+00.1802	278.8278	-7.4219	7.6	5810	UKIDSS	16.8	13.3	11.1
G024.5206-00.2258	279.2044	-7.5824			UKIDSS	15.3	13.7	12.3

RMS ID	RA (deg)	Dec (deg)	Distance (kpc)	L_{bol} ($L_\odot$)	Survey	J	H	K
G024.6343-00.3233	279.3445	-7.5282	3.0	4800	UKIDSS	15.8	13.3	10.0
G024.7320+00.1530	278.9621	-7.2242	7.7	13190	UKIDSS			15.5
G024.7891+00.0846	279.052	-7.2028	7.7	12300	UKIDSS			
G025.3953+00.0336B	279.3763	-6.6883	2.7	4520	UKIDSS			16.5
G025.4118+00.1052A	279.3205	-6.6416	5.2	7140	UKIDSS	17.2	15.7	12.9
G025.4948-00.2990A	279.7202	-6.7522			UKIDSS	18.3	16.7	12.1
G025.6498+01.0491	278.5871	-5.9952	3.0	18590	UKIDSS	17.7	15.8	13.1
G026.2020+00.2262	279.5771	-5.8826	7.5	30530	UKIDSS	14.8	10.6	8.3
G026.3819+01.4057A	278.607	-5.1806	2.9	17500	UKIDSS	14.8	10.8	9.1
G026.4207+01.6858	278.3773	-5.0172	2.9	19340	UKIDSS	16.9	13.8	10.0
G026.4958+00.7105A	279.2804	-5.3995	11.8	14860	UKIDSS			16.3
G026.4958+00.7105B	279.2803	-5.4003	11.8	7320	UKIDSS			15.1
G026.5107+00.2824C	279.6697	-5.5846	5.4	4150	UKIDSS	17.9	16.2	15.4
G026.5254-00.2667A	280.1677	-5.8203	7.5	9800	UKIDSS	17.6	16.1	13.9
G027.1852-00.0812A	280.3049	-5.1503	13.0	94310	UKIDSS			
G027.7571+00.0500	280.4499	-4.5814	5.4	10090	UKIDSS	16.7	13.3	9.3
G027.7954-00.2772	280.7594	-4.6969	3.1	1980	UKIDSS	16.6	16.9	10.7
G028.1467-00.0040A	280.6774	-4.2598	5.4	2680	UKIDSS			
G028.2325+00.0394	280.6771	-4.1628	7.4	4660	UKIDSS	17.4	16.7	12.3
G028.3046-00.3871A	281.0916	-4.2943	10.0	38500	UKIDSS	16.9	14.5	11.0
G028.3199+01.2440	279.6443	-3.5341			UKIDSS		16.3	15.0
G028.3271+00.1617	280.612	-4.0245	4.6	7930	UKIDSS			16.1
G028.3373+00.1189	280.6546	-4.0339	4.6	11490	UKIDSS	17.3	15.8	12.9
G028.5483+03.7649	277.5057	-2.1738	0.7	120	UKIDSS	17.0	15.7	11.9
G028.6477+03.8174	277.5055	-2.062	0.7	50	UKIDSS	18.3	16.4	11.2
G028.7903+03.5450	277.8117	-2.0638			UKIDSS	8.3	7.5	7.1
G028.7987+03.5103	277.8498	-2.0697	0.7	610	UKIDSS	8.9	8.0	7.5
G028.8615+01.8526	279.3508	-2.774	0.9	140	UKIDSS	18.0	14.9	11.3
G028.8621+00.0657	280.9427	-3.5915	7.4	146200	UKIDSS	19.9	17.7	14.6
G029.4375-00.1741	281.4192	-3.1892	4.9	1770	UKIDSS	18.7	15.3	10.7
G029.5904-00.6144	281.8819	-3.2538	4.4	3510	UKIDSS	18.1	16.9	13.9
G029.8129+02.2195	279.4606	-1.7604	3.0	1180	UKIDSS			15.2
G029.8390-00.0980	281.5352	-2.7959	7.3	16190	UKIDSS	19.3	16.9	11.8
G029.8620-00.0444	281.4981	-2.7518	7.3	56100	UKIDSS	17.0	12.5	9.8
G030.1981-00.1691	281.7628	-2.51	7.3	33260	UKIDSS	17.9	13.1	9.3
G030.4117-00.2277	281.9123	-2.3478	4.9	2070	UKIDSS	16.1	13.9	10.4
G030.5942-00.1273	281.9064	-2.1388	4.9	4430	UKIDSS	13.2	10.6	8.8
G030.8185+00.2729	281.6525	-1.7562	4.9	7850	UKIDSS		14.7	11.5
G030.8715-00.1018	282.0105	-1.8826	4.9	2810	UKIDSS	16.3	13.5	11.1
G030.8786+00.0566	281.8702	-1.802	4.9	1780	UKIDSS	19.6	15.7	13.5
G030.9585+00.0862B	281.8826	-1.7166	11.7	50480	UKIDSS			15.7
G030.9726-00.1410	282.0918	-1.8084	4.9	2040	UKIDSS	18.4	14.9	13.3
G030.9727+00.5620	281.4654	-1.4869	12.6	22900	UKIDSS	17.6	16.1	12.7
G030.9959-00.0771	282.0444	-1.757	4.9	4370	UKIDSS	17.4	16.7	13.9
G031.2803+00.0615A	282.0516	-1.4418	4.9	16450	UKIDSS	14.6	17.8	12.6

RMS ID	RA (deg)	Dec (deg)	Distance (kpc)	L_{bol} ($L_\odot$)	Survey	J	H	K
G032.0451+00.0589	282.4023	-0.7626	4.9	20430	UKIDSS			15.3
G032.0518-00.0902	282.5385	-0.8248	4.2	3430	UKIDSS	16.0	13.6	12.7
G032.8205-00.3300	283.1025	-0.2494	4.7	11850	UKIDSS	19.0	17.2	11.8
G032.9957+00.0415A	282.8519	0.0761	9.2	22520	UKIDSS	17.2	16.0	10.3
G033.3891+00.1989	282.891	0.4975	5.0	10170	UKIDSS	13.2	9.6	7.2
G033.3933+00.0100	283.0609	0.4146	7.0	15650	UKIDSS			15.3
G033.5237+00.0198	283.1114	0.5358	7.0	10040	UKIDSS	17.1	12.0	8.9
G034.0126-00.2832	283.6044	0.8324	12.9	33890	UKIDSS	11.5	9.6	7.7
G034.0500-00.2977	283.6346	0.8591	12.9	22570	UKIDSS	11.0	9.6	8.4
G034.4035+00.2282A	283.3265	1.4151	1.6	480	UKIDSS		17.4	13.7
G034.4035+00.2282C	283.3278	1.4136	1.6	240	UKIDSS		18.0	14.7
G034.5964-01.0292	284.5352	1.0116	1.1	320	UKIDSS	15.7	14.0	11.0
G034.6849+00.0670	283.5992	1.5905			UKIDSS	14.0	10.3	8.2
G034.7123-00.5946	284.2011	1.3131	2.9	8510	UKIDSS	18.4	13.9	9.2
G034.7569+00.0247	283.6697	1.6353	4.6	8000	UKIDSS			15.7
G034.8211+00.3519	283.4079	1.8418	3.5	8540	UKIDSS	13.3	9.3	6.6
G035.1979-00.7427	284.5542	1.6753	2.2	30940	UKIDSS			15.5
G035.3449+00.3474	283.6506	2.3056	6.8	9250	UKIDSS	16.4	17.8	13.8
G035.3778-01.6405	285.4356	1.4277	3.3	5500	UKIDSS	12.4	9.5	7.5
G035.8546+00.2663	283.9553	2.7223	2.0	1400	UKIDSS	12.5	10.1	8.3
G036.8780-00.4728	285.0826	3.2952	3.8	5550	UKIDSS	18.2	18.0	13.3
G036.9194+00.4825A	284.2491	3.7678	15.8	15580	UKIDSS	18.2	17.8	14.3
G037.2657+00.0825A	284.7638	3.8938	6.7	1060	UKIDSS	18.8	16.7	15.0
G037.3412-00.0600A	284.9262	3.897	9.8	15830	UKIDSS			16.7
G037.4974+00.5301	284.4724	4.3049	0.9	330	UKIDSS			15.4
G037.5536+00.2008	284.7915	4.2044	6.7	38060	UKIDSS	18.4	18.7	12.7
G038.1208-00.2262B	285.434	4.5105	6.6	1400	UKIDSS	16.9	16.5	13.0
G038.2577-00.0733	285.3592	4.7049	1.0	70	UKIDSS			14.8
G038.3543-00.9519	286.1869	4.3885	1.3	300	UKIDSS	17.2	15.5	12.3
G038.9365-00.4592	286.0153	5.1314	2.8	990	UKIDSS			
G039.2731-00.0440	285.8001	5.621	11.4	11800	UKIDSS	18.3	17.0	14.7
G039.3880-00.1421B	285.9381	5.679	4.3	2150	UKIDSS			15.4
G039.4943-00.9933	286.7487	5.3815	3.5	7570	UKIDSS	15.6	14.1	10.5
G039.5328-00.1969	286.0564	5.7819	3.4	830	UKIDSS	17.9	17.4	11.6
G039.9284-00.3741A	286.397	6.0504	9.0	1370	UKIDSS	19.7	16.0	13.6
G040.0809+01.5117	284.7797	7.0505	2.0	770	UKIDSS			11.5
G040.2816-00.2190	286.4221	6.4368	6.4	9460	UKIDSS	17.6	14.0	11.4
G040.2849-00.2378	286.4403	6.4312	6.4	5330	UKIDSS	15.0	13.3	11.9
G040.5451+02.5961B	284.019	7.9581	2.3	19100	UKIDSS	16.9	13.4	10.6
G040.5967-00.7188	287.0142	6.4867	4.3	4160	UKIDSS		16.0	13.2
G041.0780-00.6365	287.1635	6.9522	6.3	3090	UKIDSS	17.4	13.4	10.4
G042.0341+00.1905A	286.8675	8.1815	11.1	29400	UKIDSS	17.8	14.5	10.6
G042.0977+00.3521A	286.7521	8.3122	10.9	31370	UKIDSS	16.0	16.6	13.6
G042.0977+00.3521B	286.7522	8.3127	10.9	31370	UKIDSS	19.2	16.9	13.8
G042.1099-00.4466	287.4732	7.954	8.7	43440	UKIDSS	19.7	15.5	12.5

RMS ID	RA (deg)	Dec (deg)	Distance (kpc)	L_{bol} ($L_\odot$)	Survey	J	H	K
G043.0786+00.0033A	287.5209	9.021	11.1	6570	UKIDSS	18.3	16.6	12.7
G043.0884-00.0109	287.5398	9.0241	11.1	32920	UKIDSS		17.8	14.2
G043.1635-00.0697A	287.6262	9.0626	11.1	9870	UKIDSS	15.4	13.6	12.5
G043.5216-00.6476	288.3144	9.1136	8.1	3710	UKIDSS	16.4	13.7	11.5
G043.8152-00.1172	287.9758	9.6202	3.3	1360	UKIDSS	17.8	14.2	11.5
G043.9956-00.0111	287.9652	9.8279	6.0	16440	UKIDSS	16.8	13.6	9.9
G044.2836-00.5249	288.5622	9.8454	6.0	7380	UKIDSS	17.5	15.2	12.8
G045.1894-00.4387	288.9125	10.6873	5.9	7070	UKIDSS	18.4	14.8	10.8
G045.4543+00.0600B	288.5886	11.1543	7.3	34990	UKIDSS			12.8
G045.4543+00.0600C	288.5885	11.1556	7.3	34990	UKIDSS			
G045.4641+00.0284	288.6213	11.1472	7.4	12570	UKIDSS	17.6	15.9	14.5
G045.8164-03.8310	292.2536	9.6453			UKIDSS	11.2	10.5	9.8
G046.0345-01.5825	290.3443	10.8991	0.8	70	UKIDSS	15.6	12.2	10.3
G047.9002+00.0671	289.7492	13.3205	5.6	3650	UKIDSS	13.6	11.9	10.2
G048.9897-00.2992A	290.6111	14.1128	5.4	10540	UKIDSS	13.2	12.0	12.1
G049.0431-01.0787	291.3427	13.7888	3.0	4340	UKIDSS	17.1	14.3	12.2
G049.2015-00.1876	290.6106	14.3498	5.4	4780	UKIDSS	17.4	15.1	13.4
G049.2077+02.8863	287.7968	15.7877			UKIDSS	7.0	6.6	6.0
G049.2982-00.0582	290.5393	14.4964	5.4	4340	UKIDSS	16.1	12.2	9.9
G049.4606-00.4334A	290.9601	14.4632	5.4	930	UKIDSS	17.8	18.0	13.8
G049.4883-00.3545B	290.9033	14.5212	5.4	5620	UKIDSS	18.0	17.5	14.6
G049.5993-00.2488	290.8609	14.6714	5.4	4160	UKIDSS	16.3	15.1	13.4
G050.0721+00.5591	290.3534	15.4679	10.8	16800	UKIDSS	17.6	15.3	12.8
G050.2213-00.6063	291.4908	15.0499	3.3	4450	UKIDSS	13.7	11.4	9.8
G050.2844-00.3925A	291.3241	15.2068	9.3	18820	UKIDSS	18.6	14.6	11.3
G050.7796+00.1520	291.0726	15.9005	5.3	5890	UKIDSS	18.2	16.3	13.0
G051.3617-00.0132	291.5126	16.3344	5.2	5060	UKIDSS	10.9	9.5	8.9
G051.4006-00.8893A	292.3321	15.9516	5.2	4980	UKIDSS	15.7	12.7	9.8
G052.2025+00.7217A	291.2493	17.4217	10.0	14940	UKIDSS	16.1	13.1	10.1
G052.2078+00.6890	291.2856	17.4132	9.8	17490	UKIDSS	17.2	16.1	12.7
G052.5405-00.9272	292.9376	16.9331	5.1	14700	UKIDSS	17.0	16.6	11.8
G052.9217+00.4142	291.8958	17.9106	5.1	2560	UKIDSS	19.3	16.4	13.5
G053.0366+00.1110A	292.2319	17.8665	9.5	3630	UKIDSS		18.9	15.5
G053.0366+00.1110B	292.2321	17.8676	9.5	8390	UKIDSS			18.1
G053.1417+00.0705	292.3233	17.9397	1.9	4500	UKIDSS	17.5	14.5	12.1
G053.5343-00.7943	293.3183	17.868	5.0	7070	UKIDSS	14.5	10.7	8.3
G053.5671-00.8653	293.4003	17.8624	7.8	8320	UKIDSS	13.1	11.9	10.9
G053.6185+00.0376	292.596	18.3407	7.9	20010	UKIDSS		17.9	14.3
G055.1581-00.2991A	293.6916	19.5272	4.8	9230	UKIDSS	18.8	15.2	12.4
G056.3694-00.6333	294.6318	20.4219	5.9	5480	UKIDSS			
G056.4120-00.0277	294.0898	20.755	9.3	14590	UKIDSS	12.5	9.9	8.1
G056.9657-00.2340	294.5713	21.1348	3.4	1120	UKIDSS			
G057.5474-00.2717A	294.915	21.6255	8.3	5190	UKIDSS	16.6	13.6	10.8
G058.4670+00.4360A	294.7366	22.7755	4.4	900	UKIDSS	17.3	17.7	14.2
G058.7087+00.6607	294.6535	23.0954	4.4	4240	UKIDSS	17.1	16.0	12.5

RMS ID	RA (deg)	Dec (deg)	Distance (kpc)	L_{bol} ($L_\odot$)	Survey	J	H	K
G059.3614-00.2068	295.8249	23.2338	2.2	940	UKIDSS	14.2	11.5	9.6
G059.4657-00.0457	295.7291	23.4041	2.2	850	UKIDSS	10.5	9.6	8.6
G059.4982-00.2365	295.927	23.3372	2.2	690	UKIDSS		19.5	15.8
G059.6403-00.1812	295.9522	23.4883	2.2	1510	UKIDSS	14.8	13.0	11.2
G059.7831+00.0648	295.7968	23.7344	2.2	8360	UKIDSS	17.3	16.9	10.8
G059.8329+00.6729	295.2472	24.0789	2.2	490	UKIDSS			
G059.9997+00.1167	295.8658	23.9481	9.3	7320	UKIDSS	19.4	16.6	12.3
G060.5750-00.1861	296.4688	24.2952	7.5	30160	UKIDSS		15.0	12.3
G060.8828-00.1295B	296.5839	24.5915	2.2	21800	UKIDSS			
G061.4736+00.0908A	296.6983	25.2126	2.2	8110	UKIDSS	16.3	12.1	9.3
G062.5748+02.3875	295.0897	27.3121	13.4	96190	UKIDSS	14.6	14.4	11.9
G063.1140+00.3416	297.3838	26.7542	4.7	4220	UKIDSS	18.9	13.3	9.7
G063.1538+00.4375A	297.3104	26.8369			UKIDSS	17.8	14.9	11.9
G064.8131+00.1743	298.5244	28.1279	8.2	184400	UKIDSS	9.3	7.3	5.7
G065.7798-02.6121	301.7777	27.4799	1.1	610	UKIDSS	15.0	11.0	8.7
G068.2040+00.2387	300.4998	31.0529	9.0	10690	UKIDSS	17.9	14.2	11.5
G071.5219-00.3854	303.2412	33.5074	1.4	1420	UKIDSS	14.4	11.4	9.0
G071.8944+01.3107	301.77	34.7452	1.4	2370	UKIDSS	18.2	16.1	13.6
G072.2479+00.2617B	303.0725	34.4701	11.3	8010	UKIDSS	18.1	15.6	13.4
G072.5056-01.1708	304.6841	33.8858	7.2	6100	UKIDSS	15.3	13.7	13.9
G073.0633+01.7958	302.042	35.99	1.4	1600	UKIDSS	19.4	16.8	14.0
G073.6525+00.1944	304.0915	35.6018	11.2	259200	UKIDSS	14.2	11.5	9.6
G073.6952-00.9996	305.3287	34.9641	7.4	16550	UKIDSS	12.9	10.6	8.0
G074.0364-01.7133	306.2802	34.8348	1.4	510	UKIDSS	14.7	11.2	9.7
G075.6014+01.6394	303.9506	38.0254	11.2	28600	UKIDSS	16.3	14.4	13.2
G075.7666+00.3424A	305.4202	37.4267	1.4	4910	UKIDSS		14.9	12.1
G075.7666+00.3424B	305.4232	37.4351	1.4	4910	UKIDSS	14.9	12.4	10.0
G075.7666+00.3424C	305.4142	37.4208	1.4	1640	UKIDSS	13.2	15.2	11.3
G075.8404+00.3682	305.4498	37.5049	1.4	260	UKIDSS			15.9
G076.0902+00.1412	305.8637	37.5817	1.4	690	UKIDSS	17.0	16.8	12.4
G076.1807+00.0619	306.0118	37.6103	1.4	220	UKIDSS	19.4	14.9	11.5
G076.3829-00.6210	306.8615	37.3799	1.4	39720	UKIDSS	10.4	7.7	5.9
G076.8322+02.1876	304.2464	39.3509	1.4	310	UKIDSS			17.5
G076.8356+02.2494	304.1822	39.3889	1.4	190	UKIDSS		18.9	13.1
G077.4052-01.2136	308.2254	37.8582	1.4	440	UKIDSS	17.1	16.3	12.8
G077.4622+01.7600A	305.1636	39.6329	1.4	2790	UKIDSS		13.0	10.5
G077.5671+01.2336	305.8023	39.4176	1.4	180	UKIDSS		14.0	
G077.5671+03.6911	303.1405	40.7946	5.7	4530	UKIDSS	13.4	12.1	11.2
G077.8999+01.7678	305.4792	39.996	1.4	740	UKIDSS	16.7	13.6	9.8
G078.1224+03.6320	303.6078	41.2268	1.4	3970	UKIDSS	14.6	13.2	10.3
G078.3762+01.0191	306.6347	39.9558	1.4	310	UKIDSS	17.3	15.0	14.7
G078.4373+02.6584B	304.9104	40.9427	1.4	7030	UKIDSS	13.6	12.0	10.1
G078.4754+01.0421	306.6852	40.0494	1.4	1840	UKIDSS	17.2	12.9	8.7
G078.7641+01.6862	306.2153	40.657	10.5	42390	UKIDSS	18.5	17.2	14.2
G078.8699+02.7602	305.1275	41.3574	1.4	6510	UKIDSS	11.7	12.2	10.0

RMS ID	RA (deg)	Dec (deg)	Distance (kpc)	L_{bol} ($L_{\odot}$)	Survey	J	H	K
G078.8867+00.7087	307.3536	40.1887	3.3	185380	UKIDSS	16.2	10.8	6.6
G078.9761+00.3567A	307.7969	40.0521	1.4	2100	UKIDSS	11.4	9.4	8.0
G078.9761+00.3567B	307.793	40.0546	1.4	3890	UKIDSS	14.1	10.7	8.3
G079.1272+02.2782	305.8493	41.2942	1.4	1850	UKIDSS	16.1	11.9	9.6
G079.3398+00.3417	308.092	40.3381	1.4	280	UKIDSS	18.8	18.0	11.6
G079.3439+00.3191	308.119	40.3282	1.4	280	UKIDSS	15.8	11.4	8.9
G079.8538-01.5042	310.417	39.6327	1.4	210	UKIDSS	18.6	15.2	15.2
G079.8855+02.5517A	306.1271	42.0693	1.4	120	UKIDSS	17.8	13.5	10.4
G079.8855+02.5517B	306.132	42.0729	1.4	2160	UKIDSS			
G079.8855+02.5517C	306.1314	42.0704	1.4	120	UKIDSS			
G080.0251+02.6933	306.0834	42.2672	1.4	750	UKIDSS			15.0
G080.0467+00.3101	308.6802	40.8871	1.4	870	UKIDSS	15.1	11.4	9.3
G080.1710+02.7450	306.1393	42.4162	1.4	1290	UKIDSS	16.5	13.9	11.4
G080.1909+00.5353	308.5552	41.1373	1.4	1700	UKIDSS	14.3	10.8	8.4
G080.8282+00.5670A	309.0314	41.6692	1.4	4310	UKIDSS	15.8	12.0	8.9
G080.8624+00.3827	309.2539	41.5822	1.4	1250	UKIDSS			14.2
G080.9340-00.1880	309.9177	41.2928			UKIDSS	10.3	9.1	8.3
G081.3039+01.0520	308.8948	42.3381	1.4	240	UKIDSS	14.3	12.1	9.9
G081.4650+00.5892	309.5224	42.1873	1.4	300	UKIDSS	10.0	9.1	8.7
G081.5168+00.1926	309.9907	41.9874	1.4	490	UKIDSS	18.3	16.2	12.3
G081.6632+00.4651	309.8197	42.2692	1.4	230	UKIDSS	17.6	16.0	11.0
G081.7131+00.5792	309.7383	42.3781	1.4	4600	UKIDSS	13.4	10.3	8.2
G081.7522+00.5906	309.7583	42.4164	1.4	1680	UKIDSS			15.0
G081.7624+00.5916	309.7655	42.4249	1.4	690	UKIDSS	17.7	18.1	11.8
G081.8375+00.9134	309.4807	42.6797	1.4	230	UKIDSS	19.2	15.2	11.7
G081.8652+00.7800	309.6474	42.6205	1.4	3410	UKIDSS	16.9	13.1	9.5
G082.1735+00.0792	310.6553	42.4361	1.4	1070	UKIDSS	13.4	12.0	11.1
G082.5682+00.4040A	310.6407	42.9476	1.4	4190	UKIDSS	10.9	8.7	7.1
G082.5687+00.1917	310.8677	42.8167	1.1	210	UKIDSS	16.2	14.9	11.1
G082.5828+00.2014	310.8687	42.8339	1.4	1500	UKIDSS	17.8	16.0	11.8
G083.6748+00.3053	311.6902	43.7532			UKIDSS	10.6	10.2	9.8
G083.7071+03.2817	308.4021	45.5956	1.4	3860	UKIDSS	12.2	10.0	8.0
G083.8536+00.1434	312.02	43.7905			UKIDSS	9.5	8.9	8.2
G084.1940+01.4388	310.9029	44.8651	1.4	3200	UKIDSS	16.9	14.7	11.2
G084.3065+01.8933	310.4938	45.2334	10.5	7750	UKIDSS	15.5	12.2	10.0
G084.4678-00.1344	312.8592	44.0899	1.4	270	UKIDSS	19.4	16.6	13.2
G084.5978+00.1408	312.6784	44.3654	1.4	280	UKIDSS	12.3	10.6	9.5
G084.9505-00.6910	313.8854	44.1028	5.5	12610	UKIDSS	15.2	12.2	9.8
G085.0331+00.3629A	312.8304	44.8412	1.4	230	UKIDSS	16.8	14.9	
G085.0331+00.3629B	312.8258	44.843	1.4	230	UKIDSS	16.3	13.1	11.8
G085.4102+00.0032A	313.5598	44.9013	5.5	20470	UKIDSS	17.9	15.5	11.3
G085.4597-01.0466	314.7239	44.2579			UKIDSS	8.0	7.0	6.2
G089.6368+00.1732	317.4407	48.1828	6.5	15780	UKIDSS	18.4	14.2	10.3
G090.2095+02.0405	315.924	49.8631	7.4	29730	UKIDSS	15.0	12.2	10.1
G090.7764+02.8281	315.591	50.8097	1.7	780	UKIDSS	14.8	13.1	11.7

RMS ID	RA (deg)	Dec (deg)	Distance (kpc)	L_{bol} ($L_{\odot}$)	Survey	J	H	K
G092.6781+03.0767	317.3407	52.3863	0.6	280	UKIDSS	11.5	10.2	9.6
G093.1610+01.8687	319.3091	51.9064	6.8	9810	UKIDSS	20.1	18.4	14.6
G093.4126-00.3576	322.0912	50.4998	5.3	3240	UKIDSS	17.0	16.7	13.0
G093.7587-04.6377	326.8361	47.5343	-1.0	110	UKIDSS	9.9	8.1	7.0
G094.2615-00.4116	323.1275	51.0378	5.2	9030	UKIDSS	18.0	16.1	11.5
G094.3228-00.1671	322.938	51.2598	4.4	5650	UKIDSS	16.9	12.0	9.8
G094.4637-00.8043	323.788	50.886	4.9	20800	UKIDSS	17.7	14.0	11.1
G094.6028-01.7966	324.9927	50.2391	4.9	43260	UKIDSS	10.9	9.2	6.8
G095.0026-01.5779A	325.239	50.6663	4.5	4500	UKIDSS	15.2	13.7	13.1
G095.0531+03.9724	318.9818	54.7253	8.7	12370	UKIDSS	18.0	16.6	14.3
G096.3597+01.2982	323.7709	53.7168	7.3	13740	UKIDSS	18.2	15.6	13.7
G096.4353+01.3233A	323.8385	53.7867	7.0	11760	UKIDSS	14.4	12.1	9.9
G096.5438+01.3592	323.9326	53.8859	7.0	22690	UKIDSS	16.9	14.5	13.7
G097.5268+03.1837B	323.0471	55.8944	6.9	30600	UKIDSS	16.2	18.1	13.5
G097.5268+03.1837C	323.0446	55.8932	6.9	21760	UKIDSS	15.9	13.0	10.5
G097.9978+01.4688	325.68	54.9311	6.5	4350	UKIDSS	14.5	11.7	9.7
G098.8555+02.9344	325.1208	56.5988	-1.0	240	UKIDSS	18.2	17.2	14.2
G099.9881+03.0733	326.5297	57.4422	-1.0	130	UKIDSS	15.4	12.0	10.1
G100.0141+02.3591	327.4094	56.9102	5.9	2510	UKIDSS	14.0	13.3	12.3
G100.1620+01.6647A	328.4121	56.4638	6.0	4350	UKIDSS	17.7	15.4	13.2
G100.1685+02.0266	328.0115	56.7499	5.9	14390	UKIDSS	15.2	13.9	11.1
G100.2124+01.8829	328.2381	56.6651	5.9	10720	UKIDSS	13.6	13.4	11.1
G100.3779-03.5784	334.0431	52.3596	3.7	17250	UKIDSS	16.8	13.8	10.5
G101.2490+02.5764	328.9398	57.8516	6.1	4710	UKIDSS	12.9	10.9	9.3
G101.3193+02.6785	328.9244	57.9752	6.2	2880	UKIDSS	16.1	14.1	12.6
G101.7639+02.8100A	329.4405	58.3539	7.8	1600	UKIDSS	19.6	17.3	15.6
G101.7639+02.8100B	329.4321	58.3538	7.8	2670	UKIDSS	17.8	15.3	13.0
G102.8051-00.7184A	334.7902	56.0845	4.0	2310	UKIDSS			11.4
G102.8051-00.7184B	334.788	56.0834	4.0	2310	UKIDSS	17.4	12.6	11.1
G102.8051-00.7184C	334.7846	56.0864	4.0	1320	UKIDSS	12.0	11.2	10.5
G103.8034+00.4062	335.1924	57.5715	5.7	4380	UKIDSS	19.0	16.3	12.9
G103.8744+01.8558	333.7879	58.8188	1.6	4630	UKIDSS	17.4	13.8	13.0
G105.5072+00.2294	338.0994	58.3166	4.6	9630	UKIDSS	15.5	14.7	10.6
G141.0732-01.5795	47.0765	56.3934	2.3	380	UKIDSS	16.9	13.9	10.7
G143.8118-01.5699	51.2123	54.9591	2.4	9240	UKIDSS	16.0	12.3	10.1
G144.6678-00.7136	53.2918	55.1819	2.0	370	UKIDSS	13.4	11.6	10.3
G145.1975+02.9870	58.1139	57.8088	6.4	4490	UKIDSS	16.3	14.9	13.9
G148.1201+00.2928	59.064	53.8703	3.2	3870	UKIDSS	17.5	14.5	10.5
G150.6862-00.6887	61.2068	51.4492	1.9	190	UKIDSS	11.7	10.3	9.1
G151.6120-00.4575	62.5494	50.9985	6.4	21590	UKIDSS	10.9	8.9	7.1
G152.3371-00.2899	63.5649	50.6252	3.3	1250	UKIDSS	12.4	11.9	12.0
G160.1452+03.1559	75.4162	47.1227	1.9	2070	UKIDSS			11.2
G167.6904-00.6315	77.5091	38.8217	1.7	390	UKIDSS	11.5	11.3	11.1
G168.0627+00.8221	79.307	39.3721	2.0	1220	UKIDSS	13.6	12.1	10.2
G169.1895-00.9011	78.3584	37.4526	0.9	770	UKIDSS	15.6	13.2	10.2

RMS ID	RA (deg)	Dec (deg)	Distance (kpc)	L_{bol} ($L_{\odot}$)	Survey	J	H	K
G169.6459-00.0687	79.545	37.5662	2.0	1030	UKIDSS	13.6	12.7	11.8
G172.8742+02.2687	84.2186	36.1829	2.0	310	UKIDSS	19.1	14.4	10.2
G173.4815+02.4459	84.8042	35.7642	2.0	7560	UKIDSS			
G173.4839+02.4317	84.7913	35.7548	2.0	2740	UKIDSS	12.4	10.6	9.3
G173.5826+02.4452	84.8695	35.6772	2.0	410	UKIDSS	17.9	15.9	13.9
G173.6243+02.8734	85.3446	35.869	2.0	680	UKIDSS	18.3	18.8	16.2
G173.6328+02.8064	85.2793	35.8263	2.0	2940	UKIDSS	12.4	10.1	8.0
G173.6339+02.8218	85.2959	35.8338	2.0	5060	UKIDSS	12.2	8.9	6.6
G173.7215+02.6924	85.2182	35.6915	2.0	4920	UKIDSS	10.7	9.5	8.5
G174.1974-00.0763	82.6919	33.7984	2.0	5890	UKIDSS	12.5	11.3	10.4
G177.7291-00.3358	84.6965	30.6884	2.0	3740	UKIDSS	11.3	9.2	7.7
G178.7540+01.1609	86.8011	30.6034	2.0	1060	UKIDSS	12.5	11.0	10.8
G178.8454+04.2936	90.0208	32.1088	1.1	2190	UKIDSS	14.0	10.0	7.6
G179.0380+04.3003	90.1392	31.9457	1.1	480	UKIDSS	16.2	11.8	9.7
G182.4185-04.0399	83.9936	24.7484			UKIDSS	7.9	7.1	6.2
G183.3485-00.5751	87.7965	25.7712	2.0	4150	UKIDSS	16.8	14.9	14.8
G183.4530-01.7774	86.7147	25.0632	2.0	630	UKIDSS	15.1	13.0	10.1
G183.7203-03.6647	85.1009	23.8485	2.0	1090	UKIDSS	11.3	12.9	10.0
G184.8704-01.7329	87.5579	23.8716	2.0	1980	UKIDSS	10.2	8.9	7.7
G185.0090-03.9329	85.5885	22.6131	1.1	250	UKIDSS	8.9	7.8	7.0
G188.8120+01.0686	92.3246	21.8472	2.0	1040	UKIDSS	16.6	14.2	12.6
G188.9479+00.8871	92.2225	21.6411	1.8	7300	UKIDSS	15.2	12.2	9.7
G188.9696-01.9380	89.6018	20.2327	2.0	1890	UKIDSS	16.7	14.4	11.1
G189.0307+00.7821	92.1688	21.5168	2.0	19910	UKIDSS	16.2	12.2	8.6
G189.0323+00.8092	92.1948	21.5289	2.0	7760	UKIDSS	15.2	10.7	7.6
G189.8557+00.5011B	92.3325	20.6588	2.0	1130	UKIDSS	14.7	11.9	10.6
G192.6005-00.0479	93.225	17.9898	2.0	35600	UKIDSS			10.9
G192.6240-03.0385	90.5	16.5158	0.2	10	UKIDSS	8.5	7.5	6.6
G192.9089-00.6259	92.8489	17.4413	2.0	3820	UKIDSS	15.9	16.1	14.1
G194.9349-01.2224	93.3172	15.3787	2.0	2620	UKIDSS	16.5	13.2	9.8
G196.1620-01.2546	93.8946	14.2842	1.5	1070	UKIDSS	16.7	17.2	12.0
G196.4542-01.6777	93.6544	13.8268	5.3	94030	UKIDSS	14.6	14.8	10.3
G197.1387-03.0996	92.7081	12.5459	3.4	1010	UKIDSS	15.1	13.1	10.8
G201.3419+00.2914	97.7788	10.4347	-1.0	1870	UKIDSS	8.1	6.7	5.5
G202.6270+02.3747	100.261	10.2507	0.6	180	UKIDSS	16.0	16.9	14.3
G202.9943+02.1040	100.186	9.8006	0.3	20	UKIDSS	11.4	10.4	9.3
G203.3166+02.0564	100.2923	9.4927	0.6	1080	UKIDSS	11.5	7.6	4.9
G203.7637+01.2705	99.7915	8.736	0.8	480	UKIDSS	9.7	8.0	6.4
G206.7804-01.9395A	98.3144	4.5833	1.2	230	UKIDSS	15.2	11.7	9.9
G207.2654-01.8080A	98.6572	4.2123	1.0	2240	UKIDSS	16.1	11.5	7.7
G207.2654-01.8080B	98.6559	4.2118	1.0	560	UKIDSS	12.1	9.6	7.6
G211.5350+01.0053	103.1177	1.7018	4.8	6870	UKIDSS	16.9	15.5	14.0
G211.8957-01.2025	101.3167	0.3736	4.8	5320	UKIDSS	14.6	15.7	12.9
G212.0641-00.7395	101.8057	0.4352	4.7	13840	UKIDSS	15.0	12.0	10.0
G212.2344-03.5038	99.4233	-0.9771	4.9	2470	UKIDSS	12.7	10.6	8.9

RMS ID	RA (deg)	Dec (deg)	Distance (kpc)	L_{bol} ($L_\odot$)	Survey	J	H	K
G212.9626+01.2954	104.0263	0.5633	4.2	1310	UKIDSS	13.9	12.0	10.3
G213.9180+00.3786	103.6464	-0.7049	3.9	1160	UKIDSS	15.2	12.3	10.0
G214.4934-01.8103A	101.9595	-2.2142	2.1	400	UKIDSS			15.8
G214.4934-01.8103B	101.959	-2.2153	2.1	270	UKIDSS	15.6	17.2	13.8
G214.6353+00.7704	104.3222	-1.164	4.9	2640	UKIDSS	16.6	14.1	11.0
G215.8902-02.0094	102.4177	-3.5479	6.1	2690	UKIDSS	15.7	12.9	10.7
G217.0441-00.0584	104.6848	-3.6861	5.3	27950	UKIDSS	11.5	10.8	9.9
G217.3020-00.0567	104.8047	-3.9148	1.3	460	UKIDSS	14.4	13.2	10.5
G217.6047-02.6170	102.6559	-5.3502	6.8	4220	UKIDSS	16.6	14.8	12.5
G218.0230-00.3139A	104.9062	-4.6732	1.9	620	UKIDSS	13.5	10.5	8.4
G218.0230-00.3139B	104.9047	-4.6734	1.9	310	UKIDSS	16.4	11.9	9.7
G218.1025-00.3638	104.899	-4.7674	1.9	340	UKIDSS	15.0	12.9	11.1
G220.4587-00.6081	105.7628	-6.9739	2.2	770	UKIDSS	11.0	9.4	8.0
G220.7565-02.1557	104.5111	-7.9455			UKIDSS	9.5	8.3	7.5
G220.7899-01.7148	104.9233	-7.7745	0.8	1840	UKIDSS	10.5	9.9	9.3
G221.0108-02.5073	104.3116	-8.3305	0.8	120	UKIDSS	14.9	13.0	10.7
G221.9605-01.9926	105.2122	-8.9417	3.2	5690	UKIDSS	15.2	11.4	9.2
G222.4278-03.1357	104.3964	-9.8779	0.6	150	UKIDSS	10.9	9.5	8.0
G224.3494-02.0143	106.3029	-11.075	1.0	210	UKIDSS	16.8	14.1	10.3
G224.6065-02.5563	105.9299	-11.5518	0.8	1180	UKIDSS	6.5	5.2	3.8
G224.6075-01.0063	107.3356	-10.8412	0.9	570	UKIDSS	16.4	14.4	11.3
G225.3266-00.5318	108.102	-11.2593	1.0	280	UKIDSS	16.0	13.9	9.9
G229.5711+00.1525	110.7575	-14.6923	4.1	7180	UKIDSS	18.4	15.6	12.8
G295.2090-00.7434A	175.8865	-62.5904	9.8	13040	VVV	17.0	15.3	13.8
G295.5570-01.3787A	176.2697	-63.2962	10.0	5980	VVV	14.6	12.9	11.1
G296.1773+00.0179	178.3052	-62.0892			VVV	10.0	9.6	9.3
G296.2654-00.3901	178.2956	-62.5056	8.1	3630	VVV	13.3	10.9	8.9
G296.4036-01.0185A	178.2843	-63.1491	9.4	13050	VVV	15.0	15.4	13.0
G296.7256-01.0382	178.9721	-63.2395	9.1	8170	VVV	17.5	15.6	13.4
G297.1390-01.3510	179.7292	-63.6299	8.9	10790	VVV	16.9	14.4	12.4
G297.2535-00.7557	180.2418	-63.0678			VVV	16.4	14.4	13.9
G297.4048-00.6224	180.6268	-62.9678	9.5	15730	VVV	17.0	16.7	14.4
G297.4585-00.7636B	180.6812	-63.1159	9.7	3220	VVV	16.4	13.6	11.1
G297.4701-00.7343	180.7211	-63.0907	9.7	9680	VVV	17.4	14.8	12.1
G297.4709-00.7297	180.7267	-63.0843	9.7	3360	VVV			15.5
G298.2620+00.7394	182.9487	-61.7719	4.0	15570	VVV	20.0	16.0	11.1
G298.3323-00.2200	182.7812	-62.7321	10.0	11520	VVV	13.0	12.2	12.0
G298.8418-00.3390A	183.8375	-62.9228	4.1	2400	VVV	16.4	13.6	10.8
G299.0142+00.1277B	184.3556	-62.4868	9.6	1590	VVV	9.7	7.9	6.8
G299.5265+00.1478	185.461	-62.5284	7.5	34760	VVV	17.5	14.2	10.2
G300.1615-00.0877	186.7869	-62.8289	4.2	4950	VVV	15.2	12.1	9.3
G300.3412-00.2190	187.1489	-62.9765	4.2	5970	VVV	13.3	10.7	8.7
G300.3770-00.2857A	187.2218	-63.0462	10.7	2640	VVV	15.6	15.7	12.5
G300.5047-00.1745A	187.515	-62.9468	8.9	42800	VVV	17.7	14.2	13.9
G300.7221+01.2007	188.209	-61.5908	4.3	1550	VVV	16.3	17.7	14.3

RMS ID	RA (deg)	Dec (deg)	Distance (kpc)	L_{bol} ($L_\odot$)	Survey	J	H	K
G301.0130+01.1153	188.8103	-61.6964	4.3	3580	VVV	16.6	15.8	15.6
G301.1726+01.0034	189.1333	-61.8175	4.3	13570	VVV	12.7	10.2	7.9
G301.8147+00.7808A	190.4745	-62.0707	4.4	22030	VVV	12.0	9.3	6.8
G302.4546-00.7401	191.7859	-63.6084	11.5	19480	VVV	16.5	14.0	12.2
G302.6604-00.7908	192.2473	-63.6611	10.8	11620	VVV	16.4	13.7	10.0
G303.9973+00.2800	195.1734	-62.5724	11.4	20420	VVV		16.2	12.9
G304.3674-00.3359A	196.0411	-63.1723	11.8	88210	VVV	14.9	13.7	13.2
G304.6668-00.9654	196.7849	-63.7841	11.4	24890	VVV			14.6
G304.7592-00.6299	196.9476	-63.4436	11.2	3790	VVV	15.3	12.2	10.0
G304.7700-00.5193	196.9556	-63.3327	11.1	19860	VVV	16.2	14.7	13.6
G304.7738+01.3522	196.715	-61.4644	2.6	640	VVV			
G304.8872+00.6356	197.0506	-62.1729	3.8	2430	VVV	15.6	13.6	14.6
G305.1940-00.0051	197.8102	-62.7904	4.0	2760	VVV	14.8	14.9	14.2
G305.2017+00.2072A	197.7936	-62.5774	4.0	30320	VVV	14.3	11.7	9.4
G305.3676+00.2095	198.152	-62.559	4.0	28200	VVV	16.8	13.6	10.4
G305.4748-00.0961	198.4408	-62.8577	4.0	6420	VVV	16.5	16.4	13.3
G305.4840+00.2248	198.4	-62.5372	4.0	5220	VVV	14.8	12.8	10.0
G305.5393+00.3394	198.4982	-62.4188	4.0	5120	VVV	17.4	16.3	14.8
G305.5610+00.0124	198.6099	-62.7418	4.0	42050	VVV	17.0	13.0	9.7
G305.6327+01.6467	198.452	-61.108	4.9	14650	VVV	8.6	7.5	7.2
G305.8871+00.0179A	199.3142	-62.7066	4.0	890	VVV	18.2	15.8	14.3
G305.9402-00.1634	199.4707	-62.8808	4.0	8400	VVV	17.4	14.7	11.0
G306.1160+00.1386A	199.7868	-62.5613	4.0	3330	VVV	14.7	12.7	10.8
G306.1160+00.1386B	199.7817	-62.5615	4.0	1640	VVV	11.5	9.8	8.4
G307.3950-00.5838	202.766	-63.1119	12.5	10960	VVV	16.0	14.0	13.7
G307.6138-00.2559B	203.1302	-62.7547	7.0	7040	VVV	15.9	13.5	11.2
G308.0049-00.3868	204.0205	-62.8182	7.1	8450	VVV	14.5	11.6	9.5
G308.0108+02.0146	203.1948	-60.4486	2.0	1370	VVV	17.5	15.4	14.0
G308.6480+00.6469A	204.9832	-61.683	4.0	1040	VVV	17.5	13.4	10.6
G308.6876+00.5241	205.1109	-61.7989	4.0	2290	VVV	18.2	16.2	14.1
G308.7008+00.5312	205.136	-61.7889	4.0	1860	VVV	14.2	13.1	12.2
G308.9176+00.1231A	205.7571	-62.1476	5.3	186810	VVV	15.6	9.8	6.4
G309.2203-00.4619	206.655	-62.6577	3.5	3530	VVV	14.5	12.5	10.9
G309.4230-00.6208	207.162	-62.7693	3.5	3140	VVV	18.0	16.0	14.5
G309.5356-00.7388A	207.4595	-62.8591	3.5	1550	VVV			15.4
G309.5356-00.7388B	207.46	-62.8602	3.5	1550	VVV		17.8	15.5
G309.5356-00.7388C	207.4576	-62.8606	3.5	1550	VVV			17.2
G309.9206+00.4790B	207.6764	-61.5855	5.4	26620	VVV	14.5	12.2	10.6
G309.9796+00.5496	207.7614	-61.5039	3.5	13790	VVV	16.3	13.1	9.7
G310.0135+00.3892	207.9078	-61.6521	3.2	54680	VVV	11.8	7.6	4.9
G310.1420+00.7583A	207.9928	-61.2616	5.4	4730	VVV			15.0
G310.9438+00.4411	209.7742	-61.3741	2.9	100	VVV		18.0	15.8
G311.0341+00.3791	209.99	-61.4102	2.9	1050	VVV	17.7	13.8	10.9
G311.0593-00.3349	210.4413	-62.0917	5.5	3360	VVV	16.7	13.2	10.3
G311.2292-00.0315	210.6144	-61.7539	5.5	4070	VVV			14.9

RMS ID	RA (deg)	Dec (deg)	Distance (kpc)	L_{bol} ($L_\odot$)	Survey	J	H	K
G311.4402+00.4243	210.7793	-61.2578	3.6	7540	VVV	13.7	10.3	7.8
G311.4925+00.4021	210.895	-61.2645	5.6	4220	VVV			16.1
G311.5131-00.4532	211.441	-62.0803	4.2	4700	VVV	15.5	13.1	13.4
G311.5671+00.3189	211.0925	-61.3243	3.8	680	VVV			13.4
G311.5955-00.3981	211.5764	-62.0041			VVV	18.4	16.1	15.1
G311.6050-00.6369A	211.7423	-62.2303	13.6	7670	VVV	17.4	16.3	13.3
G311.6380+00.3009A	211.2456	-61.3213	7.3	2530	VVV	16.8	13.6	11.1
G311.9799-00.9527	212.7144	-62.4211	3.2	1460	VVV			12.2
G312.0963-00.2356	212.4929	-61.7021	7.7	14600	VVV	16.3	15.8	15.3
G313.3153-00.4640A	215.0765	-61.5294	8.4	2160	VVV		14.6	11.6
G313.5769+00.3267A	215.0375	-60.7	3.5	2510	VVV			16.4
G313.5769+00.3267B	215.0355	-60.7003	3.5	2510	VVV	17.9	15.5	14.2
G313.7051-00.1895	215.6447	-61.1406	8.5	19460	VVV			16.7
G313.7654-00.8620	216.2564	-61.7494	7.8	16980	VVV		16.6	14.3
G314.3197+00.1125	216.6095	-60.6421	3.6	12870	VVV	16.4	16.3	10.6
G315.3273-00.2270	218.773	-60.5819	12.5	17780	VVV	15.7	14.5	15.4
G316.1386-00.5009B	220.5078	-60.5026	7.7	4340	VVV	14.8	13.6	11.6
G316.5871-00.8086	221.5968	-60.5964	3.2	2820	VVV	17.0	13.8	10.7
G316.6412-00.0867	221.0763	-59.9197	1.4	1450	VVV			15.8
G317.0298+00.3601A	221.4012	-59.3494	3.5	750	VVV			
G317.7477+00.0112A	222.9666	-59.3512	13.8	15660	VVV	18.5	17.0	15.2
G318.0489+00.0854B	223.4264	-59.1479	3.4	6810	VVV	18.9	15.5	12.7
G318.9480-00.1969A	225.2305	-58.9813	2.4	9420	VVV	18.7	15.4	10.9
G319.3993-00.0135C	225.8237	-58.6041	11.7	109820	VVV	18.5	15.4	13.4
G319.8366-00.1963	226.727	-58.5497	11.7	38940	VVV			17.3
G320.1239-00.5045A	227.5007	-58.6712	12.1	9860	VVV	19.8	17.8	16.3
G320.1542+00.7976	226.322	-57.5278	2.5	5060	VVV	11.2	10.3	9.8
G320.2046+00.8626B	226.341	-57.447	2.8	660	VVV	14.9	11.7	9.7
G320.2437-00.5619	227.7566	-58.6603	9.5	18380	VVV	17.7	13.0	9.4
G320.2878-00.3069A	227.5781	-58.4191	8.7	16760	VVV	12.7	11.6	11.1
G320.3767-01.9727	229.4125	-59.7967	2.8	690	VVV	18.3	15.6	13.7
G321.0523-00.5070	229.0254	-58.1949	9.1	74440	VVV			12.9
G321.3803-00.3016B	229.3475	-57.8508	9.4	9210	VVV	18.6	15.2	13.1
G321.3824-00.2861	229.3342	-57.8334	9.4	24650	VVV	17.2	13.1	9.3
G322.1729+00.6442	229.6596	-56.6252	3.6	9290	VVV			15.2
G322.9343+01.3922	230.0924	-55.5862	2.7	6070	VVV			
G323.4468+00.0968B	232.1307	-56.3868	4.1	1300	VVV	16.2	15.0	11.9
G323.7399-00.2617A	232.9392	-56.5138	3.2	7280	VVV			14.4
G323.7399-00.2617B	232.941	-56.5141	3.2	7280	VVV	17.4	14.4	10.9
G323.7986+00.0173	232.7382	-56.2504	9.9	19110	VVV	16.4	14.8	12.7
G324.1581+00.2359	233.0435	-55.8666	6.8	12100	VVV	14.6	13.2	12.4
G324.1594+00.2622	233.0162	-55.8432	6.8	12970	VVV	14.7	12.0	9.3
G326.4477-00.7485B	237.3277	-55.2816	4.0	8480	VVV	17.6	16.2	11.3
G326.4755+00.6947	235.8289	-54.1265	1.8	3750	VVV	16.0	13.1	9.3
G326.5437+00.1684	236.4719	-54.5004	4.4	2140	VVV	15.5	14.0	11.2

RMS ID	RA (deg)	Dec (deg)	Distance (kpc)	L_{bol} ($L_{\odot}$)	Survey	J	H	K
G326.6618+00.5207	236.2618	-54.1508	1.8	15380	VVV	16.7	14.5	11.8
G326.7249+00.6159B	236.2476	-54.0382	1.8	4250	VVV	11.7	9.5	7.6
G326.7796-00.2405	237.23	-54.6772	3.9	9170	VVV	17.0	14.0	11.0
G327.1192+00.5103	236.8867	-53.8776	4.9	41660	VVV	16.5	14.6	12.2
G327.3941+00.1970	237.5836	-53.952	5.2	8080	VVV	17.4	14.2	10.5
G327.6184-00.1109	238.2093	-54.05	9.1	5580	VVV	15.5	14.0	13.8
G327.8097-00.6339A	239.0328	-54.3308	3.0	1580	VVV	13.4	10.7	8.6
G327.8097-00.6339B	239.0319	-54.3328	3.0	1610	VVV	14.3	13.2	10.3
G327.8097-00.6339C	239.0288	-54.3322	3.0	1290	VVV		15.6	12.5
G327.8097-00.6339D	239.0302	-54.3326	3.0	780	VVV	16.6	13.1	9.9
G327.9455-00.1149	238.6442	-53.8451	3.1	2780	VVV	16.5	13.1	10.0
G328.2523-00.5320A	239.4993	-53.9668	2.9	40510	VVV			15.7
G328.2523-00.5320B	239.4974	-53.9659	2.9	21300	VVV	17.9	16.8	15.6
G328.2658+00.5316	238.3667	-53.1427	2.7	1550	VVV	12.5	9.8	7.8
G328.3442-00.4629	239.5401	-53.8551	2.9	3530	VVV	10.1	8.9	7.7
G328.5487+00.2717	239.0063	-53.1622	3.7	1950	VVV	16.0	15.5	12.4
G328.5657+00.4233	238.8676	-53.0348	5.1	1640	VVV			16.2
G328.6558+00.0568	239.3742	-53.2577			VVV	16.6	15.7	14.6
G328.8230-00.0794B	239.73	-53.2531			VVV	18.8	17.4	16.1
G328.9842-00.4361	240.3297	-53.4178	4.7	1460	VVV	13.6	12.8	12.0
G329.0663-00.3081	240.2914	-53.2673	11.6	65610	VVV	16.9	16.9	14.8
G329.2713+00.1147	240.0907	-52.8131	4.5	9170	VVV	15.5	16.5	12.7
G329.3402-00.6436	241.007	-53.3391	10.1	7930	VVV	15.3	14.8	12.8
G329.4579+00.1724A	240.2698	-52.6481	7.2	7740	VVV	16.3	12.2	9.2
G329.6098+00.1139	240.5129	-52.5926	3.9	6460	VVV	15.3	14.1	14.5
G330.0699+01.0639	240.065	-51.5735	3.2	4840	VVV	17.8	16.9	14.5
G330.2923+00.0010A	241.4738	-52.2254	3.9	1210	VVV	17.1	15.8	12.9
G330.8768-00.3836	242.5991	-52.1154	3.9	19950	VVV	11.4	10.6	10.2
G331.0890+00.0163A	242.412	-51.6788	5.3	3080	VVV	18.2	15.6	13.9
G331.2759-00.1891B	242.8583	-51.6992	4.9	35070	VVV		17.9	14.7
G331.3402-00.3444	243.1102	-51.7713	4.0	17730	VVV			13.5
G331.3486+01.0442	241.6146	-50.7433			VVV	11.4	10.5	10.1
G331.3576+01.0626	241.6074	-50.7228	4.5	22290	VVV	12.6	12.8	11.0
G331.5131-00.1020	243.0415	-51.477	5.0	69390	VVV	14.7	18.2	14.8
G331.5180-00.0947A	243.0373	-51.4673	5.0	32200	VVV	17.4	14.7	10.5
G331.5651+00.2883	242.6766	-51.1555	3.6	1040	VVV	18.9	15.4	11.3
G331.6191-00.0442A	243.1025	-51.3618	4.4	3310	VVV			16.4
G331.7953-00.0979	243.3668	-51.2797	14.5	105380	VVV	16.9	14.6	9.8
G332.0939-00.4206	244.0686	-51.307	3.6	76190	VVV	15.4	9.6	5.9
G332.4683-00.5228A	244.6105	-51.12	3.6	3340	VVV	16.4	16.4	14.4
G332.4683-00.5228B	244.6121	-51.1191	3.6	2050	VVV			15.3
G332.7013-00.5874A	244.9478	-51.0019	3.6	4360	VVV	14.6	15.7	13.3
G332.8256-00.5498A	245.0461	-50.8878	3.6	207710	VVV	19.5	13.2	8.9
G332.9565+01.8035B	242.6622	-49.0993	1.8	500	VVV	15.3	16.4	12.7
G332.9636-00.6800	245.3456	-50.8829	3.2	3300	VVV	19.4	18.5	

RMS ID	RA (deg)	Dec (deg)	Distance (kpc)	L_{bol} ($L_{\odot}$)	Survey	J	H	K
G332.9868-00.4871	245.1576	-50.7305	3.6	26710	VVV	17.6	14.2	9.3
G333.0058+00.7707	243.8075	-49.8145	3.2	1880	VVV	15.8	15.0	11.0
G333.0494+00.0324B	244.6528	-50.3168	3.6	2140	VVV	15.9	11.8	9.2
G333.0682-00.4461	245.204	-50.6445	3.6	12260	VVV			16.8
G333.1075-00.5020	245.3092	-50.6535	3.6	3020	VVV	17.6	14.8	12.9
G333.1153+00.0950	244.659	-50.2258	3.6	4510	VVV	12.7	9.8	7.7
G333.1256-00.4367	245.2611	-50.5987	3.6	85010	VVV	14.4	13.1	11.7
G333.3151+00.1053	244.8708	-50.078	3.6	5670	VVV	18.5	15.3	13.5
G333.3752-00.2015B	245.2753	-50.254	3.6	2260	VVV	15.6	15.5	11.9
G333.4747-00.2366	245.4229	-50.2089	3.6	3210	VVV	16.5	12.0	9.6
G333.7608-00.2253	245.7261	-49.9983	3.6	960	VVV	15.2	13.2	10.9
G333.9305-00.1319	245.8079	-49.8119	3.6	4110	VVV	17.7	14.8	11.2
G334.1602-00.0604	245.9788	-49.5972	4.1	1790	VVV			14.8
G334.7302+00.0052	246.5194	-49.1449	2.5	2830	VVV	17.8	12.9	9.6
G334.8438+00.2095A	246.4188	-48.9212	10.6	25480	VVV	16.4	17.6	14.6
G335.0611-00.4261A	247.3458	-49.2075	2.8	1240	VVV	14.3	14.2	14.0
G335.7288-00.0966	247.6801	-48.4949	11.2	19180	VVV	16.9	14.1	13.9
G335.9960-00.8532	248.795	-48.8139	3.3	1610	VVV			13.4
G336.3684-00.0033B	248.2328	-47.9627	7.7	15990	VVV	18.5	15.8	13.9
G336.4102-00.2545A	248.555	-48.1043	10.5	8590	VVV			16.4
G336.4917-01.4741B	250.0048	-48.8646	2.0	11470	VVV	11.7	10.3	8.8
G336.5299-01.7344	250.3353	-49.0048	1.8	2130	VVV	13.1	10.4	8.4
G336.6568-01.4099	250.0939	-48.6959			VVV			15.7
G336.8308-00.3752	249.109	-47.8752	13.5	50920	VVV	15.5	14.7	13.6
G336.9033-00.1521B	248.9319	-47.6743	4.4	1550	VVV	10.2	8.5	7.4
G337.0963-00.9291	249.9908	-48.0468	3.1	3140	VVV	12.9	15.7	13.0
G337.1555-00.3951	249.4566	-47.6473	3.1	3080	VVV	18.0	15.8	12.1
G337.3071-00.1521A	249.3438	-47.3683	4.3	2420	VVV	15.3	14.8	11.9
G337.4050-00.4071A	249.7092	-47.4718	3.1	10370	VVV	18.7	15.9	13.9
G337.9715+00.0908	249.726	-46.7158			VVV	17.1	15.1	11.2
G337.9955-00.0963	249.9518	-46.8225	11.4	11590	VVV	16.3	15.4	15.0
G338.0008-00.1498A	250.0168	-46.855	11.4	50400	VVV	16.3	15.4	13.8
G338.0715+00.0126B	249.9082	-46.696	3.0	420	VVV	16.0	15.1	14.8
G338.0715+00.0126C	249.9087	-46.6913	3.0	1550	VVV		17.9	16.9
G338.1127-00.1905A	250.1702	-46.7986	12.1	6840	VVV			14.9
G338.1260+00.1719	249.7878	-46.5468			VVV			13.9
G338.2253-00.5094	250.6291	-46.9229	13.7	103020	VVV	16.5	13.6	9.9
G338.2717+00.5211A	249.5525	-46.2046	4.1	3060	VVV			13.2
G338.2717+00.5211B	249.5515	-46.2046	4.1	3050	VVV			13.2
G338.2801+00.5419A	249.538	-46.1844	4.1	1160	VVV			14.4
G338.2801+00.5419B	249.5368	-46.1859	4.1	1160	VVV		17.7	14.4
G338.3597+00.1430A	250.0495	-46.3909	12.8	30190	VVV		16.7	14.2
G338.4387+00.1907	250.068	-46.3019	12.8	380	VVV			12.1
G338.4712+00.2871	249.9954	-46.2101	13.1	86140	VVV			
G338.4763+00.0418A	250.2686	-46.3719	12.6	28300	VVV			15.9

RMS ID	RA (deg)	Dec (deg)	Distance (kpc)	L_{bol} ($L_\odot$)	Survey	*J*	*H*	*K*
G338.5459+02.1175	248.1341	-44.9252	0.5	50	VVV	10.2	8.6	7.2
G338.5821+02.0080	248.2822	-44.9735	0.6	60	VVV	17.5	15.9	12.8
G338.8872+00.5963	250.0599	-45.6954	4.0	4170	VVV			15.4
G338.9196+00.5495	250.1419	-45.7022	4.2	32030	VVV	18.2	13.6	9.6
G338.9289+00.3880A	250.3214	-45.8011	2.2	450	VVV			17.4
G338.9341-00.0623	250.8168	-46.0946	3.3	3420	VVV	15.9	12.2	9.5
G338.9377-00.4890A	251.2843	-46.3718	2.9	880	VVV	13.9	11.0	9.1
G338.9377-00.4890B	251.2895	-46.3728	2.9	880	VVV	17.0	14.2	10.9
G339.3316+00.0964	251.0183	-45.6909	13.1	39620	VVV	12.4	11.2	12.4
G339.3940-00.4084	251.6265	-45.9724	3.0	900	VVV	17.7	13.8	10.1
G339.5836-00.1265	251.4937	-45.6449	2.8	1450	VVV	13.8	10.8	9.1
G339.6221-00.1209	251.525	-45.6122	2.8	23860	VVV	15.5	12.6	10.1
G339.6816-01.2058	252.7748	-46.2646	2.4	2040	VVV	13.3	10.4	8.5
G339.7602+00.0530A	251.4649	-45.3926	12.0	14730	VVV	13.4	12.4	11.8
G339.8838-01.2588	253.0194	-46.1427	2.7	63920	VVV			
G339.9267-00.0837	251.7664	-45.3557	3.8	2910	VVV	15.8	14.8	14.2
G339.9489-00.5401	252.2831	-45.633	10.5	20830	VVV			15.5
G340.0543-00.2437A	252.057	-45.3618	3.8	5380	VVV			15.4
G340.0543-00.2437B	252.0547	-45.3612	3.8	2690	VVV	16.7	15.1	13.1
G340.0543-00.2437D	252.0577	-45.3627	3.8	2690	VVV			
G340.1537+00.5116	251.3338	-44.7972	3.8	1280	VVV	11.5	9.4	7.9
G340.4287-00.3711	252.5381	-45.1568	3.5	1530	VVV	18.1	15.6	13.9
G340.7455-01.0021	253.5169	-45.3139	2.6	4760	VVV	16.9	17.9	14.6
G341.1281-00.3466A	253.1389	-44.6029	3.3	5390	VVV			13.9
G341.2105-00.2325	253.0912	-44.4655	3.4	14990	VVV			13.1
G341.2182-00.2136	253.0747	-44.4481	3.4	3450	VVV	17.1	15.8	11.0
G342.3693+00.4234	253.4032	-43.1542			VVV	14.6	13.4	13.1
G342.7057+00.1260B	254.0117	-43.0809	3.4	4640	VVV	17.3	15.2	13.9
G342.9583-00.3180	254.7023	-43.159	12.7	62270	VVV	17.9	16.3	11.3
G343.1261-00.0623	254.5717	-42.8686	2.8	66190	VVV	18.0	15.6	14.0
G343.1880-00.0803	254.6417	-42.8321	2.8	910	VVV	17.0	12.2	10.4
G343.4702-00.0595	254.8586	-42.5965	2.8	3530	VVV	14.1	11.2	9.6
G343.4867-00.0584A	254.8738	-42.5846	2.7	370	VVV		16.6	15.0
G343.5213-00.5171	255.3918	-42.8388	3.2	14160	VVV	17.9	14.5	12.7
G343.6489-00.1842	255.1402	-42.5338	3.0	2580	VVV	18.2	16.6	13.7
G343.8354-00.1058	255.212	-42.3382	2.5	1040	VVV	15.4	12.8	10.5
G343.9033-00.6713	255.8755	-42.6302	2.8	1860	VVV	17.2	16.2	11.2
G344.4257+00.0451B	255.5367	-41.783	4.7	17250	VVV	14.5	11.6	9.6
G344.4257+00.0451C	255.5359	-41.7862	4.7	23190	VVV	18.4	14.8	11.3
G344.5818-00.0232	255.7407	-41.6983	0.3	30	VVV			16.6
G344.6608+00.3401	255.4209	-41.4134	12.7	20320	VVV	15.8	11.9	9.5
G344.8746+01.4347	254.455	-40.5688	2.4	1210	VVV	16.3	13.3	11.1
G344.8889+01.4349	254.4666	-40.5574	2.4	1970	VVV	14.2	10.2	7.4
G344.9816+01.8252A	254.1417	-40.242	2.4	1210	VVV	12.1	10.8	9.8
G344.9816+01.8252B	254.1464	-40.2392	2.4	510	VVV	15.0	13.3	10.8

RMS ID	RA (deg)	Dec (deg)	Distance (kpc)	L_{bol} ($L_\odot$)	Survey	J	H	K
G345.0034-00.2240B	256.2958	-41.4872	2.8	6430	VVV	18.1	16.8	14.0
G345.0061+01.7944A	254.1932	-40.2408	2.4	4230	VVV	14.3	12.0	10.6
G345.1876+01.0308	255.1272	-40.5732	2.4	2750	VVV		15.1	13.1
G345.2012+01.0562	255.1124	-40.5459	2.4	2630	VVV	16.0	10.5	7.4
G345.2619-00.4188A	256.7106	-41.3962	2.7	1400	VVV	13.9	10.5	8.6
G345.2619-00.4188B	256.7125	-41.3979	2.7	1080	VVV	17.8	13.4	10.2
G345.3974+01.5091A	254.8058	-40.1117	2.4	880	VVV	9.9	9.5	9.2
G345.4938+01.4677	254.9234	-40.0621	2.4	154430	VVV			12.4
G345.5043+00.3480	256.0953	-40.7399	2.0	23730	VVV	17.7	16.5	13.9
G345.6985-00.0894	256.711	-40.8499	1.0	410	VVV	15.5	14.5	11.2
G345.7172+00.8166A	255.7767	-40.2858	1.6	1080	VVV			17.8
G345.7172+00.8166B	255.7716	-40.286	1.6	530	VVV			
G345.9561+00.6123	256.1792	-40.2204	2.5	9890	VVV	14.6	10.9	8.3
G346.3273+00.1251	256.9812	-40.2182	13.3	11130	VVV	17.7	16.5	12.4
G346.4809+00.1320	257.0946	-40.0906	15.0	19520	VVV			
G346.9409-00.3142	257.9203	-39.9863	1.5	2090	VVV	15.5	14.5	10.7
G347.0775-00.3927	258.1075	-39.9222	1.7	2240	VVV	13.9	10.8	8.5
G347.6236+00.1251	257.9815	-39.1762	5.8	8590	VVV	17.6	15.4	13.9
G347.6316+00.2126A	257.8999	-39.1195	5.8	2630	VVV	19.2	16.6	14.7
G347.8944-00.1713	258.4973	-39.13			VVV	12.3	12.9	11.4
G347.9023+00.0481A	258.2714	-38.993	3.3	4950	VVV	17.0	15.8	13.3
G348.5477+00.3721A	258.4217	-38.2817	1.5	40	VVV	12.2	9.5	8.0
G348.6491+00.0225B	258.8606	-38.4046	11.1	6320	VVV			
G348.6491+00.0225C	258.8636	-38.4059	11.1	1260	VVV			16.3
G348.7342-01.0359B	260.033	-38.9541	2.8	7180	VVV			
G349.1469-00.9765	260.2704	-38.5735	2.8	790	VVV	17.2		
G349.5786-00.6798A	260.2728	-38.0485	13.4	4800	VVV			
G349.5786-00.6798B	260.2713	-38.0472	13.4	6400	VVV	15.2	13.3	11.7
G349.6433-01.0957A	260.7549	-38.2311	2.8	3960	VVV			16.9
G349.7215+00.1203A	259.5467	-37.4735	11.3	65960	VVV	17.2	15.2	13.5

Appendix B

Companions found in UKIDSS and VVV

Table B.1: Table of all companions detected using infrared imaging surveys. Companions detected around primaries up to G229.5711+00.1525 were detected in UKIDSS; objects afterwards were detected in VVV. The J,H and K magnitudes are from the corresponding IR survey unless they are brighter than that survey's saturation limit; in these cases 2MASS magnitudes were used instead. $q_{fg,X}$ represents a mass ratio derived using foreground extinction, and $q_{tot,X}$ represents a mass ratio derived using total extinction, labelled with the waveband X.

Survey ID	Primary RMS ID	RA (deg)	Dec (deg)	J	H	K	Sep. (arcsec)	$\mathrm{Sep_{phys}}$ (au)	$\mathrm{P_{chance}}$ (%)	$q_{fg,K}$	$q_{fg,J}$	$q_{tot,K}$	$q_{tot,J}$
438306049182	G010.5067+02.2285	270.1444	-18.7559	18.2	14.9	12.3	3.7	10646	5.0	0.9	0.2	3.0	3.6
438306049183	G010.5067+02.2285	270.1453	-18.7547	15.9	14.5	13.1	4.7	13593	13.9	0.6	0.4	0.9	1.0
438466784310	G010.8856+00.1221	272.2851	-19.4582	16.4	12.6	10.8	8.8	23887	13.5	1.0	0.2	5.2	9.0
438466784296	G010.8856+00.1221	272.2841	-19.4546	14.1	12.0	10.9	7.7	20861	11.8	1.0	0.4	2.3	3.0
438466784158	G010.8856+00.1221	272.2837	-19.4573	15.9	13.9	12.8	3.2	8681	13.0	0.5	0.2	1.0	1.4
438402984624	G011.4201-01.6815	274.2375	-19.8513	12.8	12.5	12.4	5.3	7922	3.4	0.2	0.3	0.3	0.3
438144312770	G011.5001-01.4857	274.0929	-19.69	17.4	14.0	11.1	3.9	6557	0.9	0.5	0.1	2.0	2.2
438144312771	G011.5001-01.4857	274.0932	-19.6907	16.6	14.2	12.4	3.9	6707	5.6	0.3	0.1	0.8	0.9
438635465594	G011.9019+00.7265	272.2454	-18.2747	17.0	14.9	13.6	2.1	5957	7.2	0.4	0.2	1.0	1.4
438635497754	G011.9019+00.7265	272.2449	-18.2743		16.1	14.5	2.4	6886	18.3	0.3		0.8	
438244412673	G012.7879-00.1786	273.5257	-17.9358	11.1	11.5	10.4	7.1	17143	0.6	0.9	0.8	0.7	0.4
438244412680	G012.7879-00.1786	273.5275	-17.9335	12.1	11.8	11.7	5.7	13562	8.3	0.5	0.5	0.6	0.7
438943343966	G012.9090-00.2607	273.6656	-17.865	11.5	11.6	10.6	7.6	18311	1.4	0.5	0.5	0.5	0.3
438585642545	G014.9958-00.6732	275.0802	-16.2241		13.9	12.2	4.3	8580	7.9	0.3		0.8	
438585622897	G014.9958-00.6732	275.0801	-16.2238	16.7	14.0	12.6	5.5	10977	15.7	0.2	0.1	0.7	1.2
438483074375	G015.0939+00.1913	274.3357	-15.7299		12.1	11.2	4.6	13360	17.4	1.3		2.3	
438585625951	G015.1288-00.6717	275.1451	-16.1073	13.3	11.6	10.4	3.8	7656	0.2	0.6	0.2	1.2	1.4
438585625950	G015.1288-00.6717	275.1438	-16.1065	15.4	12.8	10.7	4.9	9801	3.2	0.5	0.1	1.7	1.9
438811195612	G016.7122+01.3119	274.1092	-13.7726		15.9	13.8	4.0	8448	16.5	0.4		1.1	
439019514717	G016.9270+00.9599	274.5358	-13.7503	19.6	15.9	13.8	5.6	11657	14.8	0.2	0.0	1.0	1.8
439019532589	G016.9270+00.9599	274.5361	-13.7501		16.1	13.8	6.5	13583	19.9	0.2		0.9	
439019532585	G016.9270+00.9599	274.5353	-13.7508		16.6	14.2	4.3	9056	13.1	0.2		0.8	
438953753188	G017.0332+00.7476A	274.7799	-13.7566	15.7	14.6	13.6	2.5	6083	8.1	0.3	0.2	0.5	0.6

Survey ID	Primary RMS ID	RA (deg)	Dec (deg)	J	H	K	Sep. (arcsec)	$\mathrm{Sep_{phys}}$ (au)	$\mathrm{P_{chance}}$ (%)	$q_{fg,K}$	$q_{fg,J}$	$q_{tot,K}$	$q_{tot,J}$
438867004636	G017.3765+02.2512	273.5886	-12.7422	16.1	14.6	13.1	3.1	4047	4.8	0.3	0.1	0.5	0.6
439019685363	G017.4507+00.8118A	274.9249	-13.3602			15.3	1.7	3477	16.7	0.2			
439019633173	G017.4507+00.8118B	274.928	-13.3598	15.2	13.7	12.9	4.2	8804	17.0	0.5	0.4	0.8	1.2
439019685364	G017.4507+00.8118B	274.9269	-13.3603			14.2	1.7	3616	8.8	0.3			
438312899805	G017.6380+00.1566	275.612	-13.503	16.1	13.1	10.7	7.4	16204	3.3	0.3	0.0	1.2	1.3
438312940844	G017.6380+00.1566	275.6107	-13.5042			10.7	4.3	9533	1.4	0.3			
438643551175	G017.9642+00.0798A	275.8375	-13.2516	16.5	14.9	13.6	1.3	2789	3.5	0.4	0.2	0.8	1.0
438643550983	G017.9642+00.0798B	275.8368	-13.2508	17.0	14.8	13.4	2.0	4462	6.9	0.5	0.2	1.1	1.6
438643550983	G017.9642+00.0798B	275.8368	-13.2508	17.0	14.8	13.4	2.8	6114	12.4	0.5	0.2	1.1	1.6
438146144520	G018.1968-00.1709	276.177	-13.1617	15.1	13.4	12.6	2.7	28246	11.4	1.1	0.5	2.0	2.4
438777897220	G018.3412+01.7681	274.4915	-12.1233	18.1	15.5	12.6	2.8	7933	3.4	0.3	0.0	0.8	0.7
438777897225	G018.3412+01.7681	274.4904	-12.1232	14.3	13.3	12.8	6.4	17794	18.5	0.3	0.2	0.4	0.4
438777918784	G018.3412+01.7681	274.4932	-12.1235		16.4	13.7	3.9	11021	13.7	0.2		1.0	
438413879626	G018.3706-00.3818	276.4505	-13.1087	14.5	12.2	10.5	4.1	14180	0.8	1.5	0.4	3.9	4.2
438460493467	G018.8319-00.4788	276.7585	-12.7436	19.8	16.0	13.5	4.1	18599	16.8	0.5	0.1	2.5	3.7
438460547437	G018.8319-00.4788	276.759	-12.7441			14.3	2.5	11160	12.4	0.4			
438444233670	G020.5143+00.4936	276.6802	-10.8051	13.6	12.3	11.4	3.0	6548	5.1	1.3	0.7	2.2	2.6
438925651973	G020.7617-00.0638B	277.3005	-10.8434	13.2	12.3	10.8	2.3	27017	1.7	2.7	1.5	2.9	2.0
438925651948	G020.7617-00.0638C	277.3009	-10.8428	12.6	11.8	10.6	2.3	27017	0.6	3.0	2.0	3.1	2.3
438925799859	G021.3570-00.1795B	277.6884	-10.3708	13.1	13.9	10.8	4.5	47313	2.2	2.3	1.2	1.4	0.3
438423490560	G021.5624-00.0329	277.6494	-10.1192	13.8	12.1	10.8	3.6	34728	0.9	1.9	0.8	3.3	3.3
438423490562	G021.5624-00.0329	277.65	-10.1203	17.2	14.5	13.2	2.3	22050	8.2	0.7	0.2	1.9	2.8
438669382020	G022.3554+00.0655	277.9316	-9.3727	11.6	11.8	11.3	7.8	38368	18.5	0.9	0.9	0.7	0.6
438669382019	G022.3554+00.0655	277.9328	-9.3716	16.2	14.3	13.1	3.0	14594	13.5	0.4	0.2	0.9	1.1
438419669167	G023.6566-00.1273	278.7151	-8.3048	12.4	12.1	11.2	4.6	14806	5.9	0.8	0.6	0.8	0.7
438514647106	G025.3953+00.0336B	279.3757	-6.6885	16.0	14.7	14.0	2.2	6008	14.5	0.3	0.2	0.4	0.5
438354202483	G025.4118+00.1052A	279.3208	-6.64	19.2	12.2	11.1	6.7	35055	9.1	1.3	0.1	29.3	181.0
438351893987	G025.6498+01.0491	278.5872	-5.9961			13.6	3.3	9797	4.8	0.2			
438473589720	G026.3819+01.4057A	278.6078	-5.1815	16.8	14.4	12.2	4.5	13173	6.4	0.3	0.1	1.0	1.0

Survey ID	Primary RMS ID	RA (deg)	Dec (deg)	J	H	K	Sep. (arcsec)	$\mathrm{Sep}_{\mathrm{phys}}$ (au)	$\mathrm{P}_{\mathrm{chance}}$ (%)	$q_{fg,K}$	$q_{fg,J}$	$q_{tot,K}$	$q_{tot,J}$
438473589721	G026.3819+01.4057A	278.6068	-5.1797	16.3		12.8	3.4	9915	6.2	0.3	0.1		
438657966451	G026.4207+01.6858	278.3781	-5.018	16.2		11.5	3.8	10934	3.1	0.5	0.1		
438657966455	G026.4207+01.6858	278.3774	-5.0158	15.8	14.2	13.1	5.2	14939	13.4	0.2	0.1	0.5	0.6
438111334181	G026.5107+00.2824C	279.6717	-5.5854	15.9	12.8	11.3	6.3	34231	9.4	1.5	0.3	5.5	8.4
438889218639	G026.5254-00.2667A	280.168	-5.8199	16.1	15.1	14.4	1.8	13703	19.8	0.4	0.3	0.6	0.7
438582223122	G027.1852-00.0812A	280.3045	-5.1502	18.8	16.4	14.8	1.5	19925	14.5	0.3	0.1	0.7	0.9
438493110978	G028.2325+00.0394	280.678	-4.165		14.5	10.5	8.6	63913	5.4	2.6		40.0	
438493090641	G028.2325+00.0394	280.6779	-4.161	12.8	12.3	12.0	6.9	51289	17.8	1.4	1.2	1.6	1.7
438493024296	G028.3046-00.3871A	281.0911	-4.2935	13.8	13.6	13.3	3.3	32512	12.5	0.6	0.6	0.5	0.5
438705454047	G028.3199+01.2440	279.644	-3.5333	11.1	11.2	10.8	3.6		2.5				
439041605442	G028.3271+00.1617	280.6128	-4.0249	15.4	14.5	14.1	2.6	11995	14.6	0.3	0.3	0.4	0.6
439041632313	G028.3271+00.1617	280.6129	-4.0246		15.6	14.5	2.6	11923	19.3	0.3		0.5	
438367285384	G028.6477+03.8174	277.5065	-2.0612		18.9	16.9	4.6	3204	17.4	0.1		0.3	
438799668256	G028.8621+00.0657	280.943	-3.5919			14.7	2.1	15455	13.3	0.1			
439066919445	G029.4375-00.1741	281.4188	-3.1889	19.6	17.0	14.5	2.2	10854	15.7	0.5	0.1	1.3	1.4
438209360439	G029.8129+02.2195	279.4605	-1.7623	12.6	11.7	10.8	6.9	20701	3.5	1.6	1.0	2.2	2.2
439053129880	G029.8390-00.0980	281.5356	-2.7944	11.3	11.3	10.7	5.9	42777	5.0	1.6	1.4	1.4	1.1
438933895382	G030.1981-00.1691	281.7611	-2.5122	16.8	13.3	10.6	10.0	48998	3.6				4.3
438702718670	G030.4117-00.2277	281.9133	-2.3482	16.0	14.2	13.0	3.1	15325	8.9	0.9	0.4	1.6	2.0
438834477083	G030.8185+00.2729	281.6511	-1.7576	17.9	13.7	11.5	7.5	36505	15.7	1.0	0.1	6.1	10.5
438834509008	G030.8185+00.2729	281.6518	-1.7562			14.1	2.8	13828	16.5	0.3			
438702893162	G030.8715-00.1018	282.01	-1.8828	17.0	15.7	14.8	2.2	10666	11.6	0.4	0.3	0.6	0.8
438702916017	G030.9585+00.0862B	281.8839	-1.7143	16.6	12.3	10.4	9.2	107712	4.1	1.9	0.2	11.5	20.0
438585260814	G030.9727+00.5620	281.4658	-1.4852	15.3	12.5	11.2	6.6	83323	9.3	2.0	0.5	5.9	7.8
438568181920	G031.2803+00.0615A	282.0522	-1.4433	11.2		10.3	6.0	29384	1.3	1.3	1.2		
438498011544	G033.3891+00.1989	282.8897	0.4977		15.3	12.8	4.7	23434	19.3	0.6		2.8	
438360724606	G033.5237+00.0198	283.1098	0.537	14.7	12.5	11.5	7.2	50636	11.6	1.4	0.6	3.1	4.2
438208737466	G034.0500-00.2977	283.6347	0.8593	11.3	12.4	10.6	0.8	10543	0.0	3.2	3.8	1.4	0.4
438208737469	G034.0500-00.2977	283.6329	0.8591	16.9	14.3	12.2	6.1	78780	18.3	1.7	0.5	3.7	3.5

Survey ID	Primary RMS ID	RA (deg)	Dec (deg)	J	H	K	Sep. (arcsec)	$\mathrm{Sep_{phys}}$ (au)	$\mathrm{P_{chance}}$ (%)	$q_{fg,K}$	$q_{fg,J}$	$q_{tot,K}$	$q_{tot,J}$
438887587087	G034.4035+00.2282A	283.3271	1.4144	15.6	13.7	12.6	4.0	6436	3.0	0.6	0.3	1.2	1.7
438887587087	G034.4035+00.2282A	283.3271	1.4144	15.6	13.7	12.6	3.4	5369	1.9	0.6	0.3	1.2	1.7
438887620699	G034.4035+00.2282C	283.327	1.4138			14.7	2.6	4238	9.0	0.3			
438887606718	G034.4035+00.2282C	283.3273	1.413		18.0	15.2	2.2	3483	8.8	0.2		1.5	
438315600949	G034.5964-01.0292	284.5356	1.0123	16.9	15.7	14.2	2.8	3031	9.7	0.2	0.2	0.4	0.4
438172741373	G034.7123-00.5946	284.2005	1.3121			14.1	4.2	12040	13.7	0.2			
438172820631	G034.7569+00.0247	283.6692	1.6345	18.5	15.6	14.0	3.1	14405	13.9	0.4	0.1	1.2	1.9
438887635187	G034.8211+00.3519	283.4059	1.8406	11.7	11.9	11.1	8.1	28204	7.0	0.9	0.9	0.7	0.5
438887635192	G034.8211+00.3519	283.4066	1.8403	13.7	13.3	13.0	7.1	24988	14.0	0.4	0.4	0.4	0.5
438887635190	G034.8211+00.3519	283.4075	1.8433	17.9	15.6	13.8	5.4	19025	17.6	0.3	0.1	0.7	0.8
438461552989	G035.1979-00.7427	284.5546	1.6777	19.4		12.0	9.0	19734	6.7	0.3	0.0		
438316031336	G035.1979-00.7427	284.5546	1.6778	19.2	15.0	12.0	9.3	20455	8.2	0.3	0.0	1.5	2.2
438316047941	G035.1979-00.7427	284.5536	1.6749		18.3	14.4	1.9	4218	3.7	0.1		1.4	
438316047938	G035.1979-00.7427	284.5532	1.6754		18.2	15.0	2.4	5201	8.7	0.1		0.6	
438316061752	G035.1979-00.7427	284.5537	1.6758			15.7	1.8	4020	9.7	0.1			
438140124617	G035.3449+00.3474	283.6516	2.3048	15.6	13.7	12.8	4.5	30614	11.1	1.0	0.7	1.5	2.0
438140148542	G035.3449+00.3474	283.6506	2.3061		17.0	14.7	1.7	11691	7.2	0.5		1.5	
439038130441	G035.3778-01.6405	285.4347	1.4286	17.5	15.6	13.8	4.7	15429	19.0	0.4	0.3	0.7	0.7
438723090073	G037.2657+00.0825A	284.7633	3.8951	11.3	11.9	10.5	5.3	35711	1.0	5.1	6.6	2.5	1.1
438641869336	G037.4974+00.5301	284.4733	4.3069	14.5	12.6	11.6	8.0	7186	10.4	0.7	0.5	1.2	1.8
438364116885	G038.2577-00.0733	285.3613	4.7057	13.7	12.6	11.9	7.7	7733	13.7	0.8	0.7	1.2	1.6
438364117062	G038.2577-00.0733	285.3591	4.7035	14.7	13.2	12.3	4.8	4815	8.5	0.7	0.5	1.3	1.9
438759022761	G038.9365-00.4592	286.0145	5.1322		16.3	13.7	4.1	11558	9.6	0.5		2.7	
438759001179	G038.9365-00.4592	286.0151	5.1317	17.7	15.6	14.1	1.6	4401	2.2	0.4	0.2	0.9	1.3
438759001275	G038.9365-00.4592	286.0162	5.131	18.0	15.8	14.2	3.5	9910	11.5	0.4	0.1	1.0	1.4
438999591287	G039.4943-00.9933	286.7496	5.3832	19.7	15.2	11.5	7.0	24448	5.3	0.8	0.1	5.4	6.2
438999591132	G039.4943-00.9933	286.7495	5.3818	17.8	15.6	13.6	3.0	10594	6.1	0.4	0.1	0.8	0.9
438999591150	G039.4943-00.9933	286.7485	5.3823	16.2	15.4	14.9	3.0	10412	14.5	0.2	0.2	0.2	0.3
439046220955	G039.9284-00.3741A	286.3978	6.0508		16.8	14.1	3.6	31974	19.5	1.2		6.2	

Survey ID	Primary RMS ID	RA (deg)	Dec (deg)	J	H	K	Sep. (arcsec)	$\mathrm{Sep_{phys}}$ (au)	$\mathrm{P_{chance}}$ (%)	$q_{fg,K}$	$q_{fg,J}$	$q_{tot,K}$	$q_{tot,J}$
438581030494	G040.0809+01.5117	284.7796	7.0498	16.8	14.5	13.1	2.5	4956	1.4	0.5	0.2	1.2	1.8
438217163182	G040.2849-00.2378	286.4402	6.4318			15.5	2.1	13735	18.7	0.3			
438926607560	G040.5451+02.5961B	284.0197	7.958			12.0	2.1	4780	0.5	0.4			
438926582960	G040.5451+02.5961B	284.019	7.9572	18.6	14.9	12.1	3.2	7365	1.6	0.4	0.1	1.4	1.8
438926582958	G040.5451+02.5961B	284.0186	7.9583	19.2	15.4	12.9	1.8	4170	1.2	0.3	0.0	1.1	1.7
438926598363	G040.5451+02.5961B	284.0198	7.9565		16.3	13.2	6.2	14197	14.0	0.2		1.6	
439083143595	G042.0977+00.3521A	286.7521	8.3123		16.6	13.6	1.5	15826	1.9	0.7		3.9	
439083115214	G042.0977+00.3521A	286.7531	8.3119	16.5	14.8	14.0	3.6	38834	15.7	0.6	0.5	0.9	1.2
439083115298	G042.0977+00.3521B	286.7522	8.3127	19.2	16.9	13.8	1.5	15826	2.4	0.7	0.2	1.2	0.8
438608324006	G042.1099-00.4466	287.4732	7.9555	18.7		13.7	5.0	43368	18.1	0.4	0.1		
438437708537	G043.0884-00.0109	287.5387	9.0243	14.7	14.1	13.8	3.5	39212	16.4	0.7	1.1	0.6	0.7
438999948727	G043.1635-00.0697A	287.6251	9.0628	16.2	14.1	13.1	3.7	41012	8.4	1.5	1.0	2.3	3.0
439030620787	G043.5216-00.6476	288.3157	9.1135	15.5	13.8	12.8	4.8	38517	7.8	1.6	1.2	2.3	2.8
439030620829	G043.5216-00.6476	288.314	9.1131	16.0	15.2	14.5	2.2	18214	8.2	0.8	1.0	0.8	0.8
439059123072	G045.4543+00.0600B	288.5914	11.1542	10.9	12.0	10.5	10.0	72899	4.8	1.4	1.5	0.7	0.3
439059141524	G045.4543+00.0600B	288.5885	11.1529		13.6	11.6	5.0	36774	4.0	0.9		3.1	
439059141521	G045.4543+00.0600B	288.5867	11.1556		12.7	11.9	8.0	58051	15.8	0.8		1.2	
439059141532	G045.4543+00.0600B	288.5879	11.1533		14.5	12.4	4.5	33118	8.3	0.6		2.4	
439059141529	G045.4543+00.0600B	288.5897	11.1545		15.6	13.6	4.1	29656	14.0	0.4		1.4	
438940958115	G047.9002+00.0671	289.7492	13.3202	13.6	12.3	11.1	1.5	8564	0.2	1.9	1.0	2.8	2.8
438940958117	G047.9002+00.0671	289.7486	13.3196	16.2	13.9	12.0	4.1	23155	2.1	1.3	0.4	3.1	3.3
438450121486	G048.9897-00.2992A	290.6092	14.1131	11.6	12.0	10.7	6.4	34645	2.0	1.5	1.4	1.0	0.5
438450121525	G048.9897-00.2992A	290.6108	14.1139	13.5	12.5	11.8	4.4	23882	4.7	1.0	0.7	1.2	1.3
438450121503	G048.9897-00.2992A	290.6108	14.1128	16.6		13.2	0.9	5061	0.7	0.5	0.2		
438450121490	G048.9897-00.2992A	290.6112	14.1116	16.9	15.2	13.4	3.8	20679	12.9	0.5	0.2	0.9	0.9
438450121498	G048.9897-00.2992A	290.6114	14.1123	16.7	15.6	14.9	2.0	10579	11.6	0.3	0.2	0.4	0.5
438434708641	G049.0431-01.0787	291.3423	13.7891		16.0	13.2	1.6	4755	1.9	0.4		2.6	
438114073298	G049.2015-00.1876	290.6102	14.3491	17.4	13.4	11.3	3.0	16157	1.2	1.5	0.2	7.6	12.2
438114073050	G049.2015-00.1876	290.6103	14.3509	16.3	15.7	14.7	3.9	21251	17.9	0.4	0.3	0.4	0.4

Survey ID	Primary RMS ID	RA (deg)	Dec (deg)	J	H	K	Sep. (arcsec)	$\mathrm{Sep_{phys}}$ (au)	$\mathrm{P_{chance}}$ (%)	$q_{fg,K}$	$q_{fg,J}$	$q_{tot,K}$	$q_{tot,J}$
438356356275	G049.2077+02.8863	287.7953	15.7885	12.3	12.0	11.6	6.3		7.6				
438114056593	G049.2982-00.0582	290.5407	14.4983	12.0	12.6	10.9	8.6	46241	4.4	1.9	1.7	1.1	0.5
438114056601	G049.2982-00.0582	290.5403	14.4976	17.1	14.2	12.0	5.6	30151	6.7	1.2	0.3	3.8	4.2
438719466455	G049.4606-00.4334A	290.9607	14.4632	17.8	16.8	16.2	2.0	10992	16.4	0.3	0.3	0.4	0.6
438712669154	G049.5993-00.2488	290.8607	14.6719	15.8	14.5	13.9	2.2	11795	3.3	0.5	0.4	0.8	1.0
438781961918	G050.2213-00.6063	291.4917	15.0489	15.6	14.0	12.6	4.5	14968	4.0	0.5	0.2	1.0	1.1
438781961916	G050.2213-00.6063	291.4896	15.0497	15.4	13.9	12.7	4.6	15067	4.8	0.5	0.3	0.9	1.0
438781961919	G050.2213-00.6063	291.4919	15.0502	15.5	14.0	13.0	3.6	11837	3.6	0.5	0.2	0.8	1.0
438781961917	G050.2213-00.6063	291.4927	15.0497	16.5	14.9	13.9	6.2	20305	19.7	0.3	0.2	0.6	0.8
438580241689	G050.2844-00.3925A	291.3249	15.2042	13.9	12.4	11.6	9.8	91539	5.8	1.3	0.6	2.2	2.5
438580262665	G050.2844-00.3925A	291.3246	15.2065		16.4	13.6	2.1	19979	2.6	0.6		3.5	
438580241808	G050.2844-00.3925A	291.3231	15.2059	16.5	14.8	13.8	4.8	44770	13.8	0.5	0.2	1.0	1.2
438580241807	G050.2844-00.3925A	291.3233	15.2068	17.7	16.4	15.4	2.9	27368	19.5	0.3	0.2	0.4	0.5
438802631683	G050.7796+00.1520	291.0723	15.9001	17.9	16.6	15.6	2.2	11508	13.5	0.2	0.1	0.4	0.5
438220052243	G051.4006-00.8893A	292.3329	15.9518	15.5	13.9	12.9	3.2	16653	4.0	0.7	0.4	1.3	1.6
438586694621	G052.2078+00.6890	291.2864	17.4133	15.8	14.6	14.0	2.6	25374	7.6	0.6	0.5	0.8	0.9
438938172669	G052.9217+00.4142	291.8952	17.9101	15.9	14.9	14.2	2.8	14163	8.2	0.5	0.4	0.7	0.9
438938172553	G052.9217+00.4142	291.8964	17.9098	16.6	15.7	14.6	3.3	16741	14.5	0.4	0.3	0.6	0.6
438938245644	G053.1417+00.0705	292.3219	17.9381			12.6	7.7	14646	8.4	0.4			
438938245645	G053.1417+00.0705	292.3231	17.9394			13.2	1.6	2969	0.8	0.3			
438938245643	G053.1417+00.0705	292.3241	17.9396			14.8	2.6	5032	7.7	0.1			
438522240555	G055.1581-00.2991A	293.6916	19.5288	17.1	14.5	13.0	6.0	28867	13.7	0.5	0.1	1.5	2.1
438185312261	G056.3694-00.6333	294.6329	20.422	17.6	14.9	12.6	4.0	23421	4.9	0.9	0.2	2.6	2.8
438185312079	G056.3694-00.6333	294.6311	20.4216	19.6	15.9	13.2	2.4	14446	3.1	0.7	0.1	3.2	4.2
438185312447	G056.3694-00.6333	294.6311	20.4228	15.3	14.3	13.5	3.7	21987	9.2	0.6	0.5	0.9	1.0
438553305633	G057.5474-00.2717A	294.9139	21.6258	15.9	14.3	12.8	4.2	34457	7.0	1.3	0.6	1.9	1.8
438553305649	G057.5474-00.2717A	294.9163	21.6256	15.7	14.8	14.3	4.3	35603	18.5	0.7	0.7	0.8	0.9
438777063585	G058.7087+00.6607	294.6545	23.0971	16.7	14.0	12.2	7.0	30719	8.6	0.8	0.2	2.6	3.4
438556751148	G059.3614-00.2068	295.8253	23.2316	18.2	14.7	12.1	8.0	17502	3.8	0.7	0.1	3.3	4.3

Survey ID	Primary RMS ID	RA (deg)	Dec (deg)	J	H	K	Sep. (arcsec)	$\mathrm{Sep}_{\mathrm{phys}}$ (au)	$\mathrm{P}_{\mathrm{chance}}$ (%)	$q_{fg,K}$	$q_{fg,J}$	$q_{tot,K}$	$q_{tot,J}$
438556765053	G059.3614-00.2068	295.8229	23.2333		14.7	12.8	6.6	14417	7.6	0.5		2.0	
438386038701	G059.6403-00.1812	295.9521	23.4894		17.1	14.2	4.4	9576	13.3	0.3		1.9	
438556904062	G059.7831+00.0648	295.7966	23.7366		14.9	11.6	7.9	17393	8.8	0.4		4.2	
438556892245	G059.7831+00.0648	295.7951	23.7347	15.2	14.0	12.2	5.4	11822	8.2	0.4	0.1	0.6	0.5
438556908030	G059.7831+00.0648	295.7974	23.7347			13.4	2.6	5630	4.2	0.2			
438753034432	G060.5750-00.1861	296.4699	24.2955	16.4	15.0	13.7	4.2	31526	15.6	0.4	0.2	0.6	0.7
438604516474	G060.8828-00.1295B	296.5838	24.5898		15.3	12.5	6.4	14122	15.0	0.2		1.5	
438604504775	G060.8828-00.1295B	296.5823	24.5923	14.9	13.7	12.9	6.0	13172	19.8	0.2	0.2	0.3	0.4
438604504774	G060.8828-00.1295B	296.5849	24.5902	16.7	14.3	12.9	5.6	12348	18.3	0.2	0.1	0.5	0.8
438662272884	G061.4736+00.0908A	296.6971	25.2127	13.3	12.0	10.9	3.8	8298	1.0	0.7	0.4	1.0	1.1
438662272909	G061.4736+00.0908A	296.696	25.2127	14.2	13.1	12.3	7.5	16423	9.8	0.4	0.3	0.5	0.6
438662272906	G061.4736+00.0908A	296.6982	25.2115	16.2	14.3	13.0	4.1	9039	7.0	0.3	0.1	0.6	0.8
438494373830	G062.5748+02.3875	295.0896	27.3117		15.9	14.3	1.8	24225	3.0	0.3		0.9	
438535566887	G063.1140+00.3416	297.3846	26.7563	14.1	13.4	13.1	7.9	37109	18.1	0.6	0.5	0.8	1.0
438535576223	G063.1538+00.4375A	297.311	26.8392	13.4	12.6	12.0	8.5		19.3				
438209924735	G063.1538+00.4375A	297.3109	26.8366	16.2	14.5	13.3	2.0		2.8				
438996156676	G065.7798-02.6121	301.7774	27.4814	16.2	13.1	10.9	5.2	5668	1.9	0.7	0.1	2.7	3.7
438996156677	G065.7798-02.6121	301.7766	27.4825	17.0	14.4	12.2	9.4	10371	17.0	0.4	0.1	1.3	1.6
438996156440	G065.7798-02.6121	301.7754	27.479	17.0	14.0	12.2	7.9	8657	12.9	0.4	0.1	1.5	2.6
438996156469	G065.7798-02.6121	301.7762	27.4801	18.5	15.5	13.7	4.5	4956	12.4	0.2	0.1	0.8	1.3
438139551561	G071.5219-00.3854	303.2411	33.5068		15.5	12.4	2.5	3566	2.0	0.3		3.1	
438139538491	G071.5219-00.3854	303.2427	33.5072	17.8	15.7	14.3	4.7	6585	16.0	0.2	0.1	0.4	0.6
438868062049	G071.8944+01.3107	301.7686	34.7448		17.9	14.4	3.8	5376	9.2	0.1		1.5	
438283415330	G072.2479+00.2617B	303.072	34.4697	17.7	15.5	13.8	1.9	21396	1.7	0.9	0.3	2.0	2.2
438824348383	G072.5056-01.1708	304.6839	33.8844	19.2	16.6	14.2	5.2	37565	17.4	0.5	0.1	1.5	1.6
438824348379	G072.5056-01.1708	304.6841	33.8869	16.5	15.2	14.3	3.8	27435	10.2	0.5	0.3	0.8	1.0
438511620840	G073.0633+01.7958	302.0405	35.9905	14.2	12.3	11.1	5.3	7436	2.7	0.6	0.2	1.4	1.8
438511620839	G073.0633+01.7958	302.0413	35.9896	17.2	16.3	14.5	2.9	4016	7.4	0.1	0.1	0.2	0.2
438503853507	G073.6525+00.1944	304.0917	35.6028		16.1	14.4	4.0	44652	9.2	0.2		0.5	

Survey ID	Primary RMS ID	RA (deg)	Dec (deg)	J	H	K	Sep. (arcsec)	Sep$_{\mathrm{phys}}$ (au)	P$_{\mathrm{chance}}$ (%)	q$_{fg,K}$	q$_{fg,J}$	q$_{tot,K}$	q$_{tot,J}$
439037646370	G074.0364-01.7133	306.281	34.8362	18.5	17.3	15.1	5.6	7801	16.8	0.2	0.1	0.3	0.2
439037658218	G074.0364-01.7133	306.2793	34.8337		16.9	15.1	4.7	6519	12.5	0.2		0.6	
439037658217	G074.0364-01.7133	306.2787	34.8338		17.1	15.2	5.8	8058	19.5	0.2		0.6	
438849751014	G075.7666+00.3424A	305.4193	37.4282	14.6	12.9	12.0	6.1	8553	7.1	0.3	0.2	0.6	0.9
438849750997	G075.7666+00.3424A	305.4186	37.4268	13.0		12.6	4.5	6346	5.2	0.2	0.3		
438849751020	G075.7666+00.3424A	305.4196	37.4259	16.1	14.6	13.0	3.3	4663	4.4	0.2	0.1	0.4	0.4
438849751022	G075.7666+00.3424A	305.4193	37.4263	17.0	14.7	13.2	2.8	3930	3.5	0.2	0.1	0.5	0.7
438849767592	G075.7666+00.3424A	305.4209	37.4272			14.5	2.6	3694	9.1	0.1			
438849750970	G075.7666+00.3424B	305.4221	37.4349	14.2	12.3	11.0	3.2	4548	0.3	0.5	0.2	1.0	1.3
438849750960	G075.7666+00.3424B	305.4256	37.4347	13.4	12.9	12.7	6.8	9472	14.6	0.2	0.2	0.3	0.3
438849750999	G075.7666+00.3424B	305.4247	37.4343	17.2	15.2	13.9	5.1	7128	18.0	0.1	0.1	0.3	0.5
438849751580	G075.7666+00.3424C	305.4154	37.4182			11.9	10.0	13930	19.7	0.5			
438849767761	G075.7666+00.3424C	305.4146	37.4216			14.6	2.7	3847	11.7	0.1			
438920867949	G076.1807+00.0619	306.0136	37.61		16.9	14.4	5.5	7631	18.0	0.3		1.5	
438933683292	G076.3829-00.6210	306.8623	37.3783			11.4	6.1	8537	4.5	0.2			
438933672662	G076.3829-00.6210	306.8613	37.3819	16.8	14.2	12.3	7.4	10335	19.9	0.1	0.0	0.4	0.5
438933672681	G076.3829-00.6210	306.8604	37.3809	15.9	14.0	12.4	4.8	6761	9.8	0.1	0.0	0.3	0.3
438933672682	G076.3829-00.6210	306.8633	37.3803	16.1	14.3	12.5	5.2	7321	13.5	0.1	0.0	0.2	0.3
438795495783	G077.4052-01.2136	308.2238	37.8577	16.1	15.3	14.8	5.1	7104	16.6	0.2	0.2	0.3	0.4
438795504608	G077.4052-01.2136	308.2252	37.8595		17.8	14.9	4.6	6492	14.3	0.2		1.4	
438795495784	G077.4052-01.2136	308.2237	37.8583	18.8	16.6	15.2	5.1	7082	19.3	0.2	0.1	0.4	0.7
438795504607	G077.4052-01.2136	308.2263	37.8584		17.6	15.7	2.4	3429	7.6	0.1		0.5	
438795506946	G077.4052-01.2136	308.2242	37.8583			15.7	3.6	5072	16.2	0.1			
438795506945	G077.4052-01.2136	308.2247	37.8579			15.9	2.5	3508	9.5	0.1			
438736953845	G077.4622+01.7600A	305.1627	39.633	13.6	11.9	10.4	3.6	4993	0.2	0.7	0.2	1.4	1.4
438736953851	G077.4622+01.7600A	305.1624	39.6315	14.0	12.4	11.3	5.8	8136	1.7	0.5	0.2	0.9	1.2
438736953852	G077.4622+01.7600A	305.164	39.632	14.3	12.8	11.4	2.2	3023	0.3	0.4	0.2	0.9	1.0
438736953853	G077.4622+01.7600A	305.1634	39.6319	14.9	13.2	11.8	2.9	4088	0.6	0.4	0.1	0.8	1.0
438736953847	G077.4622+01.7600A	305.1616	39.6338	17.7	14.7	12.7	7.9	11004	6.6	0.3	0.1	0.9	1.4

Survey ID	Primary RMS ID	RA (deg)	Dec (deg)	J	H	K	Sep. (arcsec)	$\mathrm{Sep_{phys}}$ (au)	$\mathrm{P_{chance}}$ (%)	$q_{fg,K}$	$q_{fg,J}$	$q_{tot,K}$	$q_{tot,J}$
438736962757	G077.4622+01.7600A	305.1617	39.6319		15.6	13.5	6.6	9215	5.7	0.2		0.9	
438736962755	G077.4622+01.7600A	305.1643	39.634		17.5	14.2	5.2	7244	6.7	0.1		1.4	
438736964348	G077.4622+01.7600A	305.1645	39.6342			14.2	5.9	8273	9.0	0.1			
438999102200	G077.5671+03.6911	303.14	40.7942			13.6	1.8	10390	0.9	0.6			
438999095447	G077.5671+03.6911	303.1388	40.7942	15.0	14.4	13.8	4.7	26616	7.3	0.5	0.4	0.6	0.7
438999095443	G077.5671+03.6911	303.1407	40.7927	16.5	15.1	14.1	7.0	39831	17.0	0.5	0.3	0.8	1.0
438999095446	G077.5671+03.6911	303.1416	40.7942	17.1	16.3	15.7	3.7	20974	17.2	0.2	0.2	0.3	0.4
438999102199	G077.5671+03.6911	303.1395	40.7954			15.8	3.7	21133	19.9	0.2			
438891516394	G077.8999+01.7678	305.4809	39.9984	17.3	15.0	13.4	9.9	13840	15.5	0.3	0.1	0.8	1.1
438891523779	G077.8999+01.7678	305.4768	39.9952		16.2	13.8	7.3	10287	12.5	0.3		1.4	
438891516451	G077.8999+01.7678	305.4802	39.9956	18.0	15.6	14.1	3.1	4343	3.6	0.2	0.1	0.6	0.9
438891516447	G077.8999+01.7678	305.4774	39.9952	19.8	16.9	14.9	5.7	8000	16.6	0.2	0.0	0.5	0.8
438814851948	G078.1224+03.6320	303.6083	41.2262	17.7	15.0	12.5	2.9	4012	1.6	0.3	0.0	0.8	0.9
438814851949	G078.1224+03.6320	303.6061	41.2269	18.3	16.8	13.9	4.7	6604	10.2	0.1	0.0	0.3	0.2
438187132281	G078.3762+01.0191	306.6358	39.9549	16.6		14.2	4.0	5607	7.1	0.3	0.2		
438187132179	G078.3762+01.0191	306.635	39.9568	18.4		15.4	4.0	5593	16.7	0.2	0.1		
438690127801	G078.4373+02.6584B	304.9112	40.9424	13.9	12.9	12.3	3.5	4843	3.1	0.3	0.2	0.3	0.4
438650712116	G078.4373+02.6584B	304.9108	40.9422	16.2	14.6	13.4	3.0	4206	5.6	0.2	0.1	0.3	0.4
438187129406	G078.4754+01.0421	306.6857	40.0488	19.8		13.0	2.6	3591	1.1	0.3	0.0		
438468044028	G078.7641+01.6862	306.2141	40.657	18.6	17.0	16.2	3.0	31737	18.3	0.2	0.2	0.3	0.4
438690158426	G078.8699+02.7602	305.1274	41.3587	12.1	12.7	12.9	5.0	6992	12.7	0.2	0.6	0.1	0.1
438690158422	G078.8699+02.7602	305.1286	41.3567	16.8	15.2	14.2	3.9	5455	10.3	0.1	0.1	0.2	0.3
438394844675	G078.8867+00.7087	307.3515	40.1878	15.0	12.8	11.0	6.6	21821	2.1	0.3	0.1	0.6	0.7
438394853587	G078.8867+00.7087	307.3526	40.1879		13.7	11.3	4.1	13640	1.0	0.3		1.1	
438394844667	G078.8867+00.7087	307.3521	40.1889	16.7	14.1	11.8	3.9	12904	1.9	0.2	0.0	0.6	0.6
438832592407	G078.9761+00.3567A	307.7966	40.0528	12.5	11.7	10.6	2.7	3830	0.2	0.9	0.7	0.9	0.9
438832602546	G078.9761+00.3567A	307.7966	40.0533			12.5	4.5	6317	2.5	0.4			
438832602545	G078.9761+00.3567A	307.7972	40.053			12.7	3.7	5186	2.3	0.4			
438517704834	G079.1272+02.2782	305.8495	41.2959	15.3	13.3	12.1	6.0	8417	3.1	0.4	0.2	0.9	1.3

Survey ID	Primary RMS ID	RA (deg)	Dec (deg)	J	H	K	Sep. (arcsec)	$\mathrm{Sep_{phys}}$ (au)	$\mathrm{P_{chance}}$ (%)	$q_{fg,K}$	$q_{fg,J}$	$q_{tot,K}$	$q_{tot,J}$
438210415755	G079.3439+00.3191	308.116	40.3284	19.2	15.5	12.9	8.4	11730	5.9	0.6	0.1	2.5	3.8
438585862801	G079.8538-01.5042	310.4181	39.6337		17.6	14.3	4.4	6110	3.9	0.3		2.8	
438585862707	G079.8538-01.5042	310.4159	39.6349		19.0	14.7	7.6	10678	16.4	0.3		4.8	
438622086418	G080.0251+02.6933	306.082	42.2669		19.0	16.1	3.7	5174	12.3	0.1		0.7	
438620534923	G080.1710+02.7450	306.1404	42.4156	18.0	17.0	16.4	3.5	4876	16.5	0.1	0.1	0.1	0.2
438288950545	G080.8282+00.5670A	309.0298	41.6701	17.7	16.0	14.7	5.4	7492	16.8	0.1	0.1	0.2	0.3
438377729692	G080.8624+00.3827	309.2522	41.5805	13.2	12.8	12.7	7.5	10466	7.9	0.4	0.7	0.4	0.5
438629181049	G080.8624+00.3827	309.2568	41.5835	16.7	14.5	13.1	9.3	12962	17.3	0.4	0.2	0.7	1.1
438629181109	G080.8624+00.3827	309.2549	41.5819	17.2	15.7	14.7	3.1	4326	7.8	0.2	0.2	0.3	0.4
438377737790	G080.8624+00.3827	309.2548	41.5813		17.6	14.9	4.0	5620	15.7	0.2		0.9	
438894300547	G080.9340-00.1880	309.9143	41.292	15.1	13.3	12.1	9.1		19.4				
438774307609	G081.4650+00.5892	309.5206	42.1874	15.8	14.3	13.5	4.8	6737	10.6	0.4	0.3	0.7	1.0
438774307608	G081.4650+00.5892	309.5211	42.1885	16.0	14.8	14.0	5.6	7785	19.6	0.3	0.2	0.5	0.7
439007659375	G081.5168+00.1926	309.9908	41.9886		17.2	14.3	4.5	6269	9.0	0.2		1.7	
439007655412	G081.5168+00.1926	309.9906	41.9861	17.8	15.6	14.3	4.6	6484	9.8	0.2	0.1	0.6	1.0
439007663251	G081.5168+00.1926	309.9908	41.9866			15.0	2.8	3956	4.9	0.2			
439023354853	G081.7131+00.5792	309.7368	42.3801	14.5	12.7	11.9	8.3	11619	3.3	0.3	0.2	0.7	1.0
439023354801	G081.7131+00.5792	309.7403	42.3801	15.5	13.6	12.4	9.1	12777	6.0	0.3	0.1	0.6	0.8
439023354857	G081.7131+00.5792	309.736	42.3762	16.9	14.6	13.0	9.1	12672	8.7	0.2	0.1	0.5	0.8
439023354602	G081.7522+00.5906	309.7583	42.4169	17.6	15.1	13.7	1.8	2529	1.0	0.2	0.1	0.6	1.0
439023354526	G081.7624+00.5916	309.7684	42.4263	12.1	12.0	11.8	9.1	12765	6.9	0.6	0.7	0.6	0.7
439023365382	G081.7624+00.5916	309.7642	42.4254			15.9	4.0	5540	17.3	0.1			
438265589664	G081.8375+00.9134	309.4794	42.68		17.8	16.0	3.5	4925	16.4	0.1		0.5	
438948007203	G081.8652+00.7800	309.6442	42.6191	18.2	14.9	12.7	9.9	13791	12.3	0.3	0.1	1.1	1.6
438682214296	G082.1735+00.0792	310.6535	42.4337	15.6	13.5	12.0	9.9	13928	5.9				1.5
438682214295	G082.1735+00.0792	310.6544	42.434	15.5	13.6	12.2	8.0	11154	4.6	0.5	0.2	1.0	1.3
438682214294	G082.1735+00.0792	310.6561	42.4351	15.9	13.9	12.7	4.1	5772	3.5	0.4	0.2	0.8	1.2
438682214289	G082.1735+00.0792	310.6528	42.436	18.7	15.7	13.8	6.7	9348	18.4	0.2	0.1	0.8	1.3
438682247199	G082.5682+00.4040A	310.638	42.9469			12.1	7.3	10160	6.3	0.3			

Survey ID	Primary RMS ID	RA (deg)	Dec (deg)	J	H	K	Sep. (arcsec)	$\mathrm{Sep_{phys}}$ (au)	$\mathrm{P_{chance}}$ (%)	$q_{fg,K}$	$q_{fg,J}$	$q_{tot,K}$	$q_{tot,J}$
438682236546	G082.5682+00.4040A	310.641	42.9491	14.9	13.6	12.8	5.6	7903	6.8	0.2	0.2	0.4	0.6
438682244992	G082.5682+00.4040A	310.6387	42.9482		14.9	12.9	5.7	7933	9.8	0.2		0.8	
438453407938	G082.5687+00.1917	310.8679	42.8186	16.3	14.7	13.6	7.1	7844	13.4	0.3	0.2	0.6	0.8
438453408424	G082.5828+00.2014	310.8667	42.8327	15.1	13.6	12.6	6.8	9520	9.2	0.3	0.2	0.6	0.8
438674195123	G083.7071+03.2817	308.4058	45.5953	11.6	11.9	10.7	8.9	12435	5.7	0.5	0.4	0.4	0.3
438674195134	G083.7071+03.2817	308.4015	45.5948	15.0	12.8	11.2	3.2	4435	0.9	0.4	0.1	1.1	1.4
438674195127	G083.7071+03.2817	308.401	45.5935	15.3	13.7	12.9	8.0	11237	14.0	0.2	0.1	0.4	0.6
438674195129	G083.7071+03.2817	308.4023	45.597	16.3	14.9	13.7	5.5	7694	12.9	0.1	0.1	0.3	0.4
438674195131	G083.7071+03.2817	308.404	45.5945	16.9	15.3	13.8	5.7	7928	15.3	0.1	0.1	0.3	0.3
438674195132	G083.7071+03.2817	308.4042	45.5958	17.6	15.7	14.0	5.0	6995	13.5	0.1	0.0	0.3	0.4
438338644341	G083.8536+00.1434	312.0185	43.7902	15.6	14.9	14.6	3.9		9.4				
438338644342	G083.8536+00.1434	312.0205	43.7913	16.1	15.4	14.8	3.3		7.9				
439022803259	G084.1940+01.4388	310.9027	44.8647		14.9	10.8	1.4	1928	0.0	0.6		10.4	
439022793463	G084.1940+01.4388	310.901	44.8645	17.1	15.8	14.0	5.4	7526	9.5	0.1	0.1	0.3	0.3
439022793480	G084.1940+01.4388	310.902	44.8652	17.2	15.9	14.7	2.4	3342	4.3	0.1	0.1	0.2	0.2
438534368372	G084.5978+00.1408	312.678	44.3647	14.5	13.0	11.9	2.8	3961	0.7	0.8	0.5	1.3	1.7
438615307601	G084.9505-00.6910	313.8856	44.1028		14.8	11.7	1.0	5613	0.1	1.0		7.4	
438615300606	G084.9505-00.6910	313.8878	44.1032	13.4	12.9	12.9	6.7	36935	9.5	0.6	0.7	0.6	0.7
438534457720	G085.0331+00.3629A	312.8306	44.8408			13.1	1.4	2023	0.3	0.6			
438534457717	G085.0331+00.3629A	312.8316	44.8403			16.3	4.5	6313	18.6	0.2			
439041888069	G089.6368+00.1732	317.4419	48.1834	16.5	13.8	10.7	3.7	24166	0.2	1.5	0.2	4.6	3.4
438719909382	G090.2095+02.0405	315.9254	49.8629	16.7	15.5	14.6	3.4	24806	7.9	0.3	0.2	0.4	0.5
438719909380	G090.2095+02.0405	315.9248	49.8622	16.3	15.6	15.0	3.9	28991	15.2	0.2	0.2	0.3	0.3
438163852562	G090.7764+02.8281	315.5917	50.8096	17.5	15.0	13.4	1.7	2893	0.5	0.4	0.1	1.0	1.4
438163852561	G090.7764+02.8281	315.5904	50.8105	16.6	14.9	13.8	3.2	5477	3.0	0.3	0.1	0.6	0.8
438163852559	G090.7764+02.8281	315.5924	50.8103	17.7	15.8	14.4	3.9	6677	6.6	0.2	0.1	0.5	0.7
438163852554	G090.7764+02.8281	315.5911	50.8083	17.2	16.0	15.3	4.8	8123	18.4	0.2	0.1	0.3	0.4
438163868935	G090.7764+02.8281	315.5895	50.81			16.2	3.5	6018	19.8	0.1			
438878812533	G092.6781+03.0767	317.3421	52.3864	17.3	15.8	14.6	3.2	1914	7.3	0.1	0.1	0.2	0.3

Survey ID	Primary RMS ID	RA (deg)	Dec (deg)	J	H	K	Sep. (arcsec)	$\mathrm{Sep_{phys}}$ (au)	$\mathrm{P_{chance}}$ (%)	$q_{fg,K}$	$q_{fg,J}$	$q_{tot,K}$	$q_{tot,J}$
438362456437	G093.4126-00.3576	322.0924	50.5012	17.3	15.3	13.3	6.0	31627	6.0	0.7	0.2	1.5	1.4
438362470271	G093.4126-00.3576	322.0897	50.4993			14.5	3.6	19339	6.7	0.4			
438362456539	G093.4126-00.3576	322.0897	50.4984	15.7	15.1	14.8	5.7	29968	17.9	0.4	0.4	0.4	0.5
438362456436	G093.4126-00.3576	322.0927	50.5005	18.9	16.6	15.1	4.5	23707	14.6	0.3	0.1	0.8	1.2
438840840615	G094.2615-00.4116	323.1264	51.0376	20.1	17.0	14.9	2.6	13666	4.0	0.3	0.1	0.9	1.3
438840846822	G094.2615-00.4116	323.1267	51.0386		17.2	15.7	3.3	17186	14.4	0.2		0.4	
438881502828	G094.3228-00.1671	322.9336	51.2601	14.8	13.6	12.7	9.2	40646	10.0	0.6	0.4	1.0	1.1
438881502794	G094.3228-00.1671	322.9373	51.2614	18.0	15.6	13.8	4.5	19854	7.0	0.4	0.1	1.1	1.3
438881502807	G094.3228-00.1671	322.9367	51.2593	17.2	15.3	14.0	4.0	17387	6.9	0.4	0.1	0.8	1.0
438310990824	G094.4637-00.8043	323.7867	50.8854	17.6	15.6	14.2	3.7	18208	6.6	0.2	0.1	0.5	0.7
438310990825	G094.4637-00.8043	323.7871	50.8843	17.5	15.5	14.2	5.9	29085	16.7	0.2	0.1	0.5	0.7
438177834948	G094.6028-01.7966	324.9919	50.24	13.8	12.7	11.2	3.6	17743	0.6	0.6	0.2	1.0	0.8
439007166934	G094.6028-01.7966	324.9901	50.2395			12.1	6.2	30545	5.6	0.4			
438177837835	G094.6028-01.7966	324.9941	50.2408			13.2	6.6	32207	17.9	0.3			
439007166930	G094.6028-01.7966	324.9912	50.2393			13.9	3.5	16971	7.5	0.2			
438443600565	G095.0026-01.5779A	325.2384	50.6665			12.9	1.9	8376	0.5	0.6			
438443582397	G095.0026-01.5779A	325.2377	50.6656	16.1	14.5	13.5	3.9	17404	4.9	0.5	0.2	0.9	1.1
438443582398	G095.0026-01.5779A	325.241	50.6652	15.8	14.6	13.9	5.7	25603	13.7	0.4	0.3	0.6	0.8
439007265698	G095.0531+03.9724	318.9788	54.7243	13.5	13.2	13.1	7.4	63954	9.5	0.7	0.7	0.8	0.8
439007265696	G095.0531+03.9724	318.9803	54.725	16.6	15.5	15.0	3.4	29855	8.1	0.3	0.2	0.5	0.7
439007265570	G095.0531+03.9724	318.9825	54.726	18.3	16.5	15.5	2.9	25309	7.6	0.3	0.1	0.6	0.8
439007272492	G095.0531+03.9724	318.9811	54.7258			16.3	2.3	20118	9.6	0.2			
438883868652	G096.3597+01.2982	323.7711	53.716		16.9	15.5	3.0	21906	11.7	0.2		0.5	
438883853222	G096.3597+01.2982	323.7693	53.7168	18.7	17.0	15.8	3.4	25034	18.5	0.2	0.1	0.4	0.5
438641385943	G096.4353+01.3233A	323.8383	53.7863			11.6	2.0	13861	0.2	1.1			
438641382998	G096.4353+01.3233A	323.8366	53.7866	12.8		11.8	4.3	30414	1.6	1.1	0.8		
438641376111	G096.5438+01.3592	323.9353	53.8867	14.7		14.0	6.1	42558	12.0	0.3	0.3		
438641376283	G096.5438+01.3592	323.9328	53.884	18.0		14.1	7.2	50560	17.6	0.3	0.1		
438641385462	G096.5438+01.3592	323.9334	53.8854			16.0	2.7	18997	11.6	0.1			

Survey ID	Primary RMS ID	RA (deg)	Dec (deg)	J	H	K	Sep. (arcsec)	$\mathrm{Sep_{phys}}$ (au)	$\mathrm{P_{chance}}$ (%)	$q_{fg,K}$	$q_{fg,J}$	$q_{tot,K}$	$q_{tot,J}$
438641385463	G096.5438+01.3592	323.9321	53.8853			16.0	2.7	18665	11.6	0.1			
438557868516	G097.5268+03.1837B	323.049	55.8948	19.0	17.0	14.9	4.5	30948	12.3	0.2	0.1	0.5	0.5
438557868614	G097.5268+03.1837B	323.0464	55.8936	19.3	17.4	15.0	3.3	22738	7.6	0.2	0.1	0.4	0.4
438557868697	G097.5268+03.1837B	323.0458	55.8948	18.8	16.9	15.5	2.5	17218	6.0	0.2	0.1	0.4	0.4
438557877521	G097.5268+03.1837B	323.0469	55.8944		18.1	13.5	6.6	45567	8.3	0.4		9.2	
438557868614	G097.5268+03.1837B	323.0464	55.8936	19.3	17.4	15.0	4.1	27946	11.3	0.2	0.1	0.4	0.4
438557868701	G097.5268+03.1837C	323.0445	55.8932	15.9	13.0	10.8	6.6	45567	0.5	1.3	0.2	4.3	4.7
438557868620	G097.5268+03.1837C	323.0462	55.8929	18.4	16.6	15.4	3.6	24565	10.8	0.2	0.1	0.4	0.5
439034186288	G097.9978+01.4688	325.6798	54.9322	15.5	14.8	14.4	4.0	26308	6.8	0.5	0.5	0.6	0.7
439034186289	G097.9978+01.4688	325.6807	54.9328	16.7	15.4	14.8	6.3	40635	19.1	0.4	0.3	0.7	0.9
438667614629	G100.0141+02.3591	327.4067	56.9096	14.4	13.2	12.0	5.9	34701	1.7	1.4	0.7	2.1	2.0
438667614630	G100.0141+02.3591	327.4101	56.909	17.7	16.2	15.0	4.2	24949	10.8	0.4	0.2	0.7	0.9
438667614631	G100.0141+02.3591	327.4085	56.9092	17.7	16.4	15.1	3.8	22539	9.1	0.4	0.2	0.6	0.7
438667614632	G100.0141+02.3591	327.4104	56.9095	17.4	16.2	15.4	3.0	17880	7.5	0.3	0.2	0.5	0.7
438667585665	G100.1620+01.6647A	328.4113	56.4641	16.7	15.9	13.6	1.9	11156	0.7	0.6	0.2	0.8	0.5
438667585661	G100.1620+01.6647A	328.4128	56.4656	16.9		14.5	6.8	41096	18.3	0.4	0.2		
438667592140	G100.1620+01.6647A	328.4134	56.4652			14.6	5.8	34699	14.9	0.4			
438667585669	G100.1620+01.6647A	328.4141	56.464	17.9	16.3	14.8	4.2	25368	8.9	0.4	0.2	0.7	0.7
438667585663	G100.1620+01.6647A	328.4121	56.4627	18.6	16.6	15.2	4.1	24563	10.8	0.3	0.1	0.7	0.9
438667590984	G100.1620+01.6647A	328.4136	56.4635		17.2	15.6	3.3	19893	10.7	0.3		0.7	
438969573921	G100.1685+02.0266	328.0119	56.7494		14.9	11.8	1.8	10371	0.2	0.9		7.2	
438969561108	G100.1685+02.0266	328.0113	56.7502	15.8	14.1	12.6	1.6	9237	0.4	0.6	0.2	1.2	1.3
438969561106	G100.1685+02.0266	328.013	56.7505	17.7	16.1	15.0	3.6	21319	13.9	0.2	0.1	0.4	0.6
438126671357	G100.2124+01.8829	328.2357	56.663	14.0	13.2	12.9	8.6	50711	10.4	0.6	0.5	0.8	0.9
438126671367	G100.2124+01.8829	328.2388	56.6646	16.7	14.9	13.0	2.0	12071	0.7	0.6	0.2	1.2	1.1
438126671361	G100.2124+01.8829	328.2361	56.6662	14.6	13.6	13.0	5.8	34075	6.0	0.6	0.4	0.8	1.0
438126671363	G100.2124+01.8829	328.2403	56.6644	18.5	16.0	13.5	4.9	28776	6.0	0.5	0.1	1.3	1.3
438126677148	G100.2124+01.8829	328.237	56.6657			14.3	3.1	18554	4.4	0.3			
439027837174	G100.3779-03.5784	334.0399	52.3581	15.5	14.4	13.6	9.1	33658	8.8	0.2	0.1	0.4	0.5

Survey ID	Primary RMS ID	RA (deg)	Dec (deg)	J	H	K	Sep. (arcsec)	$\mathrm{Sep_{phys}}$ (au)	$\mathrm{P_{chance}}$ (%)	$q_{fg,K}$	$q_{fg,J}$	$q_{tot,K}$	$q_{tot,J}$
439027837189	G100.3779-03.5784	334.0456	52.3588	17.3	15.3	13.8	6.0	22143	4.7	0.2	0.1	0.5	0.7
439027837057	G100.3779-03.5784	334.0457	52.3604	15.5	14.6	14.2	6.2	23092	7.8	0.2	0.1	0.3	0.4
439027837088	G100.3779-03.5784	334.0409	52.3596	17.3	15.7	14.8	5.0	18357	8.7	0.1	0.1	0.3	0.4
439027837159	G100.3779-03.5784	334.044	52.3583	16.4	15.4	14.9	4.9	17980	9.2	0.1	0.1	0.2	0.3
439027837030	G100.3779-03.5784	334.0434	52.3608	19.0	16.7	14.9	4.2	15591	7.8	0.1	0.0	0.4	0.5
439058937439	G101.2490+02.5764	328.9358	57.8522	14.7	14.2	14.1	7.9	48109	12.9	0.5	0.5	0.6	0.7
439058937440	G101.2490+02.5764	328.938	57.8533	16.1	15.1	14.4	7.3	44626	15.8	0.4	0.3	0.6	0.8
439058937446	G101.2490+02.5764	328.9381	57.8521	17.8		15.2	3.9	23791	9.8	0.3	0.2		
438371948127	G101.3193+02.6785	328.9255	57.9749		16.7	15.3	2.4	14850	4.4	0.4		0.9	
438371948126	G101.3193+02.6785	328.9232	57.976		17.4	16.3	3.6	22468	16.5	0.2		0.5	
438270869481	G101.7639+02.8100A	329.4382	58.3518	14.0	13.5	13.2	8.6	67019	11.2	1.3	1.2	1.4	1.5
438270869373	G101.7639+02.8100A	329.4393	58.3536	19.6	18.4	16.3	2.3	18202	7.9	0.3	0.1	0.5	0.5
438270876127	G101.7639+02.8100B	329.4318	58.353		17.8	15.6	2.7	20992	6.6	0.4		1.6	
438270869601	G101.7639+02.8100B	329.4324	58.3528	18.7	17.1	15.9	3.6	28227	14.0	0.3	0.2	0.6	0.8
438493554728	G102.8051-00.7184A	334.7902	56.0845			11.4	5.8	23170	2.5	1.2			
438493552606	G102.8051-00.7184A	334.7893	56.0868		15.6	13.4	8.6	34216	15.0	0.5		2.5	
438493538926	G102.8051-00.7184A	334.7902	56.0852	17.0	15.3	13.8	2.6	10214	2.5	0.5	0.2	0.9	1.0
438493538959	G102.8051-00.7184B	334.7895	56.0834	16.4		11.5	2.8	11077	0.8	1.2	0.2		
438493552610	G102.8051-00.7184B	334.7873	56.0835		14.7	13.7	1.8	7106	1.2	0.5		0.9	
438493552608	G102.8051-00.7184B	334.7875	56.0827		16.4	14.9	2.8	11038	7.4	0.3		0.8	
438493538957	G102.8051-00.7184B	334.7869	56.0831	16.8		15.2	2.6	10486	7.7	0.3	0.2		
438493538959	G102.8051-00.7184B	334.7895	56.0834	16.4		11.5	3.9	15774	1.3	1.2	0.2		
438493552610	G102.8051-00.7184B	334.7873	56.0835		14.7	13.7	6.8	27222	15.3	0.5		0.9	
438493538961	G102.8051-00.7184C	334.7833	56.0872	14.6	13.6	13.2	3.5	14167	2.3	0.7	0.5	1.0	1.3
438493538909	G102.8051-00.7184C	334.7834	56.0891	14.5	13.6	13.3	9.8	39200	18.3	0.7	0.5	0.9	1.2
438493538921	G102.8051-00.7184C	334.788	56.0873	16.0	16.4	13.6	7.9	31404	18.6	0.6	0.3	0.4	0.2
438493538946	G102.8051-00.7184C	334.7818	56.0855	15.2	14.3	14.0	6.3	25248	18.3	0.5	0.4	0.7	1.0
438493538953	G102.8051-00.7184C	334.784	56.0851	16.2	15.2	14.5	4.8	19201	15.9	0.4	0.3	0.6	0.8
438493552609	G102.8051-00.7184C	334.783	56.0866		15.5	14.9	3.1	12472	9.8	0.3		0.5	

Survey ID	Primary RMS ID	RA (deg)	Dec (deg)	J	H	K	Sep. (arcsec)	$\mathrm{Sep_{phys}}$ (au)	$\mathrm{P_{chance}}$ (%)	$q_{fg,K}$	$q_{fg,J}$	$q_{tot,K}$	$q_{tot,J}$
438313867087	G103.8034+00.4062	335.1904	57.5706	17.7	16.2	15.3	4.8	27528	19.2	0.3	0.2	0.5	0.7
438313873355	G103.8034+00.4062	335.1913	57.5713			15.7	2.1	11941	5.9	0.2			
438425130271	G103.8744+01.8558	333.7864	58.8211	15.9	13.8	12.2	9.1	14508	11.5	0.3	0.1	0.8	1.0
438923822639	G103.8744+01.8558	333.7861	58.8174		15.7	13.1	5.7	9068	9.1	0.2		1.3	
438236528179	G105.5072+00.2294	338.0991	58.3188	13.9	13.3	13.0	8.0	36666	8.3	0.5	0.4	0.6	0.7
438236528171	G105.5072+00.2294	338.0985	58.3171	17.6	16.0	13.8	2.3	10717	1.9	0.3	0.1	0.6	0.5
438236528163	G105.5072+00.2294	338.1021	58.3154	15.7	14.8	14.3	7.0	32103	19.9	0.3	0.2	0.4	0.5
438920414567	G141.0732-01.5795	47.0773	56.3928	15.0	13.6	12.9	3.0	6943	0.4	0.7	0.5	1.2	1.7
438920414561	G141.0732-01.5795	47.0765	56.3915	17.4	15.8	14.9	7.3	16712	15.6	0.3	0.2	0.6	1.0
438920414590	G141.0732-01.5795	47.0745	56.3935	17.8	16.2	15.2	3.7	8518	6.1	0.3	0.2	0.5	0.8
438677521629	G143.8118-01.5699	51.2151	54.9595	12.9	12.3	11.8	6.0	14404	2.2	0.4	0.4	0.5	0.6
438677521626	G143.8118-01.5699	51.2108	54.9588	15.7	14.4	13.5	3.3	7995	4.3	0.2	0.1	0.4	0.5
438796983635	G144.6678-00.7136	53.2942	55.183	15.5	14.7	14.2	6.3	12520	9.2	0.4	0.3	0.5	0.7
438796983636	G144.6678-00.7136	53.2929	55.1831	17.6	15.7	14.4	4.7	9366	6.3	0.3	0.2	0.7	1.0
438796983633	G144.6678-00.7136	53.2902	55.1826	17.7	16.8	16.3	3.9	7895	17.8	0.2	0.1	0.2	0.3
439011550532	G145.1975+02.9870	58.1168	57.8083	15.3	13.5	12.0	6.0	38402	1.3	1.2	0.4	2.5	2.7
439011550531	G145.1975+02.9870	58.1157	57.8108	14.4	14.1	14.0	7.8	49725	10.6	0.5	0.5	0.6	0.6
439011551047	G145.1975+02.9870	58.115	57.8082			15.2	3.3	21307	6.0	0.3			
439011551048	G145.1975+02.9870	58.1151	57.8092			15.3	2.8	17709	4.6	0.3			
438697417458	G145.1975+02.9870	58.115	57.8097		17.0	15.9	3.8	24488	13.8	0.2		0.5	
439011551045	G145.1975+02.9870	58.1127	57.8079			16.0	4.0	25600	15.5	0.2			
439036205344	G148.1201+00.2928	59.0663	53.868	16.8	14.6	13.1	9.6	30633	8.7	0.5	0.2	1.1	1.4
439036205288	G148.1201+00.2928	59.0673	53.8697	19.7	15.7	13.4	7.2	23175	9.8	0.4	0.1	2.2	3.8
439036205313	G148.1201+00.2928	59.0634	53.8696	18.0	15.4	13.5	2.9	9327	2.2	0.4	0.1	1.1	1.5
439036205335	G148.1201+00.2928	59.063	53.8681	16.5	14.9	13.6	8.3	26568	19.2	0.4	0.2	0.7	0.9
439036205311	G148.1201+00.2928	59.0633	53.8691	17.0	15.5	14.2	4.6	14839	12.2	0.3	0.2	0.5	0.6
439036205308	G148.1201+00.2928	59.0654	53.8711	18.2	16.4	14.8	4.1	13041	13.5	0.2	0.1	0.5	0.6
438670598297	G150.6862-00.6887	61.2067	51.4503	15.1	13.9	12.9	3.7	7066	0.7	0.7	0.4	1.1	1.3
438670598214	G150.6862-00.6887	61.2033	51.45	15.0	14.5	14.3	8.1	15466	13.7	0.4	0.4	0.5	0.6

Survey ID	Primary RMS ID	RA (deg)	Dec (deg)	J	H	K	Sep. (arcsec)	$\mathrm{Sep_{phys}}$ (au)	$\mathrm{P_{chance}}$ (%)	$q_{fg,K}$	$q_{fg,J}$	$q_{tot,K}$	$q_{tot,J}$
438792634468	G152.3371-00.2899	63.5664	50.6256	14.3	13.8	13.5	3.8	12532	1.2	0.5	0.5	0.6	0.7
438792634464	G152.3371-00.2899	63.5631	50.6267	14.2	13.7	13.6	6.7	22182	4.4	0.5	0.5	0.6	0.8
438792634459	G152.3371-00.2899	63.5678	50.6236	15.0	14.5	14.1	8.6	28436	16.8	0.4	0.4	0.5	0.6
438792634469	G152.3371-00.2899	63.5645	50.6258	15.2	14.8	14.5	2.4	7804	1.8	0.4	0.4	0.4	0.5
438792634466	G152.3371-00.2899	63.563	50.6259	16.1	15.1	14.7	5.0	16660	10.1	0.3	0.3	0.5	0.7
438792634465	G152.3371-00.2899	63.5648	50.6266	17.1	16.0	15.2	5.3	17348	13.6	0.3	0.2	0.4	0.5
438645852799	G160.1452+03.1559	75.4167	47.1219	17.9	15.6	14.1	3.0	5613	1.3	0.2	0.1	0.6	0.8
438645852803	G160.1452+03.1559	75.4174	47.1226	17.4	15.4	14.2	2.8	5356	1.3	0.2	0.1	0.5	0.7
438645856139	G160.1452+03.1559	75.4128	47.1222		16.3	14.3	8.7	16493	13.8	0.2		0.7	
438645852806	G160.1452+03.1559	75.4151	47.1234	17.5	15.9	14.7	3.7	7011	3.1	0.2	0.1	0.3	0.4
438645852800	G160.1452+03.1559	75.4183	47.1221	15.8	15.0	14.7	5.6	10559	7.3	0.2	0.1	0.2	0.3
438645856595	G160.1452+03.1559	75.4174	47.122			15.0	3.8	7219	4.5	0.1			
438645852805	G160.1452+03.1559	75.4145	47.1223	17.8	16.3	15.2	4.5	8538	8.6	0.1	0.1	0.2	0.3
438645856136	G160.1452+03.1559	75.4154	47.1217		17.8	16.3	4.1	7784	14.0	0.1		0.2	
438645856135	G160.1452+03.1559	75.4174	47.1236		18.2	16.4	4.4	8409	17.6	0.1		0.3	
438855143473	G167.6904-00.6315	77.5068	38.8224	13.7	13.5	13.4	7.1	12018	6.6	0.4	0.4	0.4	0.5
438855143475	G167.6904-00.6315	77.5089	38.8227	17.5	16.7	16.2	4.0	6796	13.8	0.1	0.1	0.2	0.3
438651106179	G168.0627+00.8221	79.3035	39.3719	11.5	11.7	11.2	9.9	19714	1.2	0.8	0.8	0.7	0.6
438651106184	G168.0627+00.8221	79.3083	39.3715	18.7	17.2	15.0	4.2	8346	7.6	0.2	0.1	0.3	0.3
438651106191	G168.0627+00.8221	79.3062	39.3732	17.4	16.0	15.1	4.8	9545	10.9	0.2	0.1	0.3	0.5
438233708299	G169.1895-00.9011	78.3573	37.4529	14.0	12.8	11.9	3.3	3015	0.8	0.3	0.2	0.6	0.7
438233708315	G169.1895-00.9011	78.3568	37.4533	15.5	14.5	13.8	5.3	4745	9.5	0.2	0.1	0.2	0.4
438233708306	G169.1895-00.9011	78.358	37.4515	15.5	14.4	14.0	4.1	3647	6.1	0.1	0.1	0.2	0.4
438233708312	G169.1895-00.9011	78.3572	37.4519	15.8	14.7	14.0	4.3	3892	7.1	0.1	0.1	0.2	0.3
438233708307	G169.1895-00.9011	78.3591	37.4517	15.7	14.6	14.1	3.5	3171	5.2	0.1	0.1	0.2	0.4
438233708308	G169.1895-00.9011	78.3599	37.4521	16.4	15.3	14.8	4.4	3936	13.6	0.1	0.1	0.2	0.3
438796143788	G169.6459-00.0687	79.5469	37.5663	17.1	15.3	13.5	5.6	11172	5.3	0.3	0.1	0.8	0.9
438796143789	G169.6459-00.0687	79.5461	37.5647	15.9	14.8	13.8	6.0	11983	7.3	0.3	0.2	0.5	0.6
438796143784	G169.6459-00.0687	79.5467	37.567	16.6	15.5	14.9	5.6	11147	16.8	0.2	0.1	0.3	0.4

Survey ID	Primary RMS ID	RA (deg)	Dec (deg)	J	H	K	Sep. (arcsec)	Sep_{phys} (au)	P_{chance} (%)	$q_{fg,K}$	$q_{fg,J}$	$q_{tot,K}$	$q_{tot,J}$
438796143791	G169.6459-00.0687	79.545	37.5652	16.8	15.7	15.1	3.4	6750	8.0	0.2	0.1	0.3	0.4
438993759628	G169.6459-00.0687	79.5452	37.5668			16.2	2.5	5082	9.8	0.1			
438796143790	G169.6459-00.0687	79.5456	37.5654	17.7	16.8	16.3	3.3	6635	17.3	0.1	0.1	0.2	0.2
438742637411	G172.8742+02.2687	84.2198	36.1825	19.9	17.2	15.3	3.7	7440	5.3	0.3	0.1	0.7	1.1
438501857539	G173.4839+02.4317	84.7932	35.7536	17.3	15.3	13.8	6.9	13843	14.3	0.2	0.1	0.5	0.7
438501857538	G173.4839+02.4317	84.7912	35.7528	17.1	15.3	14.0	7.3	14652	19.6	0.2	0.1	0.5	0.6
438395509441	G173.5826+02.4452	84.8664	35.6782	13.4	13.0	12.9	9.5	19069	8.6	0.6	0.8	0.7	0.8
438395513228	G173.5826+02.4452	84.8681	35.6789		18.3	14.3	7.2	14465	8.6	0.4		5.5	
438395509469	G173.5826+02.4452	84.8692	35.6764	18.3	16.5	14.7	2.9	5827	2.4	0.3	0.1	0.6	0.7
438395509456	G173.5826+02.4452	84.8682	35.6775	17.0	15.7	14.9	3.9	7717	4.3	0.3	0.2	0.4	0.6
438942746040	G173.6243+02.8734	85.3446	35.8706		16.7	14.4	5.5	11011	13.6	0.3		1.4	
438891628041	G173.6328+02.8064	85.2787	35.8247	13.3	12.0	10.8	6.6	13100	3.1	0.9	0.5	1.4	1.5
438891628047	G173.6328+02.8064	85.2778	35.8269	14.3	13.0	12.0	4.6	9255	2.9	0.5	0.3	0.8	1.0
438891628036	G173.6328+02.8064	85.2813	35.8271	16.3	15.0	14.0	6.1	12287	17.8	0.2	0.2	0.3	0.4
438891631760	G173.6339+02.8218	85.2943	35.833			14.3	5.6	11130	17.7	0.2			
438216875816	G174.1974-00.0763	82.6916	33.7977	16.8	15.0	13.9	2.7	5308	1.6	0.2	0.1	0.4	0.5
438216875815	G174.1974-00.0763	82.6908	33.7977	16.2	14.9	14.2	4.3	8543	4.8	0.1	0.1	0.3	0.4
438216877964	G174.1974-00.0763	82.6923	33.7975		16.5	15.0	3.5	7044	7.4	0.1		0.3	
438917360338	G177.7291-00.3358	84.6974	30.6877		15.3	13.6	3.8	7550	2.3	0.3		0.7	
438917355716	G177.7291-00.3358	84.6951	30.6877	17.4	15.2	13.6	4.8	9635	3.9	0.3	0.1	0.6	0.8
438917355719	G177.7291-00.3358	84.6952	30.6889	15.9	14.9	13.9	4.3	8697	4.6	0.2	0.2	0.3	0.4
438917360336	G177.7291-00.3358	84.6948	30.6882		15.7	14.4	5.3	10532	9.5	0.2		0.4	
438314204063	G178.7540+01.1609	86.8022	30.6037	12.3	12.2	10.9	3.5	7047	0.2	1.1	0.8	1.0	0.7
438314204069	G178.7540+01.1609	86.8029	30.605	16.0	14.8	14.2	7.9	15709	19.2	0.3	0.2	0.4	0.6
438357078245	G178.8454+04.2936	90.0185	32.1076	18.5	15.2	12.0	8.4	9263	3.4	0.3	0.0	1.3	1.4
438357078837	G178.8454+04.2936	90.0205	32.1073		14.2	12.3	5.8	6366	2.4	0.3		1.0	
438357078248	G178.8454+04.2936	90.0214	32.1072	13.5	13.0	12.8	6.4	7034	4.9	0.2	0.2	0.3	0.4
438406978538	G179.0380+04.3003	90.1382	31.9478	16.3	14.5	13.3	8.3	9130	9.7	0.3	0.1	0.6	0.9
438406978548	G179.0380+04.3003	90.1373	31.9455	17.8	15.4	13.7	5.8	6360	6.0	0.2	0.1	0.7	1.0

Survey ID	Primary RMS ID	RA (deg)	Dec (deg)	J	H	K	Sep. (arcsec)	Sep_{phys} (au)	P_{chance} (%)	$q_{fg,K}$	$q_{fg,J}$	$q_{tot,K}$	$q_{tot,J}$
438406978547	G179.0380+04.3003	90.1383	31.9465	16.3	14.9	14.1	4.1	4498	4.2	0.2	0.1	0.3	0.5
438357043334	G183.3485-00.5751	87.7981	25.7717	14.3	13.8	13.5	6.0	11936	5.6	0.2	0.2	0.3	0.4
438357043411	G183.3485-00.5751	87.7947	25.7733	17.6	15.4	13.5	9.2	18470	15.5	0.2	0.1	0.6	0.7
438357043333	G183.3485-00.5751	87.7991	25.7715	17.1	15.1	13.8	9.1	18125	18.4	0.2	0.1	0.5	0.7
438357046705	G183.3485-00.5751	87.7955	25.7713			16.1	2.8	5506	10.8	0.1			
438357046706	G183.3485-00.5751	87.7955	25.771			16.5	2.7	5437	12.0	0.1			
438357046699	G183.3485-00.5751	87.7956	25.7706			17.1	3.1	6183	18.6	0.1			
438289384455	G183.4530-01.7774	86.7129	25.0629	15.4	14.5	13.9	5.8	11647	6.9	0.3	0.2	0.5	0.6
438289384389	G183.4530-01.7774	86.7136	25.0646	17.6	15.7	14.5	6.1	12178	12.4	0.3	0.1	0.6	0.9
438289384458	G183.4530-01.7774	86.7147	25.0617	17.0	15.5	14.6	5.6	11258	11.4	0.2	0.1	0.5	0.7
438289384461	G183.4530-01.7774	86.7162	25.0628	17.0	16.1	15.7	5.4	10749	19.6	0.2	0.1	0.2	0.4
439021868167	G183.7203-03.6647	85.103	23.8495	18.7	15.8	13.7	7.5	15000	5.4	0.3	0.1	1.1	1.7
438278518945	G184.8704-01.7329	87.5575	23.8723	14.4	13.5	13.0	2.5	5044	0.8	0.3	0.3	0.5	0.6
438278518946	G184.8704-01.7329	87.5572	23.872	14.5		13.0	2.6	5293	0.9	0.3	0.2		
438278518942	G184.8704-01.7329	87.5556	23.8704	15.5	14.3	13.7	8.8	17556	15.7	0.3	0.2	0.4	0.6
438278518936	G184.8704-01.7329	87.559	23.8725	17.1	16.2	15.6	4.9	9849	16.2	0.1	0.1	0.2	0.3
438271871199	G188.8120+01.0686	92.3265	21.8462	18.2	15.7	14.3	7.2	14485	16.6	0.2	0.1	0.8	1.2
438271871213	G188.8120+01.0686	92.3236	21.8474	17.5	15.7	14.4	3.3	6687	4.6	0.2	0.1	0.5	0.7
438271873684	G188.8120+01.0686	92.3233	21.8477			14.8	4.5	9092	10.6	0.2			
438271873682	G188.8120+01.0686	92.3236	21.8464			15.5	4.4	8877	16.5	0.1			
438426229867	G188.9479+00.8871	92.2239	21.6414	16.5	14.6	13.2	5.0	9008	6.6	0.2	0.1	0.4	0.6
438426229866	G188.9479+00.8871	92.2236	21.6406	17.5	15.6	13.9	4.3	7829	9.3	0.1	0.0	0.3	0.4
439057418146	G188.9696-01.9380	89.6002	20.2324		16.9	13.5	5.5	11072	4.8	0.3		2.9	
439057416565	G188.9696-01.9380	89.6	20.2334	16.5	14.9	13.9	6.4	12823	8.7	0.3	0.1	0.5	0.7
439057416571	G188.9696-01.9380	89.5997	20.2324	17.3	15.7	14.3	7.2	14411	15.4	0.2	0.1	0.4	0.5
439057416564	G188.9696-01.9380	89.6008	20.2336	16.9	15.3	14.4	4.6	9186	7.5	0.2	0.1	0.4	0.6
438920477909	G189.0307+00.7821	92.1682	21.5149			12.7	7.2	14415	7.4	0.2			
438920476621	G189.0307+00.7821	92.1677	21.5181	16.1	14.5	13.1	6.1	12272	8.9	0.2	0.1	0.3	0.4
438920476528	G189.0307+00.7821	92.1705	21.5183	15.9	14.5	13.4	7.6	15229	18.2	0.1	0.1	0.3	0.3

Survey ID	Primary RMS ID	RA (deg)	Dec (deg)	J	H	K	Sep. (arcsec)	$\mathrm{Sep_{phys}}$ (au)	$\mathrm{P_{chance}}$ (%)	$q_{fg,K}$	$q_{fg,J}$	$q_{tot,K}$	$q_{tot,J}$
438920477160	G189.0323+00.8092	92.1942	21.5279	17.3	14.6	12.7	4.0	8059	1.4	0.3	0.1	0.9	1.1
438920477006	G189.0323+00.8092	92.1921	21.5293	18.6	15.3	12.7	8.6	17259	7.1	0.2	0.0	1.1	1.4
438920477007	G189.0323+00.8092	92.1934	21.5293	17.6	14.8	12.8	4.6	9194	2.3	0.2	0.1	0.8	1.1
438532265764	G189.8557+00.5011B	92.3318	20.6614	12.0	12.1	11.1	9.6	19273	4.5	0.9	0.8	0.9	0.7
438532265895	G189.8557+00.5011B	92.3335	20.6587	17.4	15.5	14.0	3.4	6753	8.5	0.3	0.1	0.7	0.9
438661217822	G192.6005-00.0479	93.2244	17.9899	18.7	15.1	11.4	2.4	4803	0.6	0.3	0.0	1.3	1.1
438661217848	G192.6005-00.0479	93.2265	17.9903	16.7	14.3	12.4	5.3	10603	8.0	0.2	0.0	0.5	0.6
438661223764	G192.6005-00.0479	93.2242	17.9891			12.7	3.8	7563	5.7	0.2			
438557780598	G192.9089-00.6259	92.8484	17.4418	17.7	15.8	14.4	3.1	6274	2.4	0.2	0.1	0.4	0.5
438557780600	G192.9089-00.6259	92.847	17.442	18.0	16.1	14.6	7.6	15165	16.3	0.2	0.1	0.3	0.5
438557780599	G192.9089-00.6259	92.8482	17.4411	18.5	16.7	15.2	2.9	5737	3.6	0.1	0.1	0.3	0.3
439072384102	G194.9349-01.2224	93.3175	15.3794		16.5	14.1	2.5	5030	1.9	0.2		1.0	
439072384095	G194.9349-01.2224	93.3168	15.3798		17.7	15.0	4.2	8480	11.9	0.1		0.9	
439072384099	G194.9349-01.2224	93.3181	15.379		17.2	15.2	3.1	6238	7.7	0.1		0.5	
438243575983	G196.1620-01.2546	93.8941	14.2853		16.8	13.7	4.2	6366	3.7	0.2		2.0	
438243576492	G196.1620-01.2546	93.8954	14.2847			14.2	3.5	5287	4.1	0.2			
438243573547	G196.1620-01.2546	93.8942	14.2827	19.1	16.9	15.3	5.4	8142	19.0	0.1	0.0	0.3	0.5
438243575980	G196.1620-01.2546	93.8934	14.2841		18.6	16.1	3.8	5704	17.5	0.1		0.5	
438400814197	G196.4542-01.6777	93.6555	13.8267	16.7	14.5	12.4	4.4	23530	2.2	0.3	0.1	0.8	0.7
438400814140	G196.4542-01.6777	93.6534	13.825	12.9	12.6	12.6	7.3	38581	6.3	0.3	0.3	0.3	0.3
438400814178	G196.4542-01.6777	93.6563	13.8277	15.8	14.6	13.5	8.1	42912	16.3	0.2	0.1	0.3	0.3
438400814163	G196.4542-01.6777	93.6533	13.8267	16.7	15.2	14.0	3.1	16628	4.2	0.2	0.1	0.3	0.3
438400816331	G196.4542-01.6777	93.6536	13.8275			14.9	3.1	16630	9.2	0.1			
438400714552	G197.1387-03.0996	92.7068	12.5457	16.6	15.5	14.7	4.1	13898	5.4	0.4	0.2	0.5	0.7
438400714543	G197.1387-03.0996	92.7069	12.5445	18.3	16.4	15.0	6.0	20518	13.4	0.3	0.1	0.7	1.0
438400714553	G197.1387-03.0996	92.709	12.5469	17.3	16.5	15.8	5.2	17832	17.0	0.2	0.2	0.3	0.4
438484337597	G202.6270+02.3747	100.2609	10.251			14.7	1.5	913	0.2	0.1			
438484329344	G202.9943+02.1040	100.1874	9.8004	17.3	16.4	16.0	5.0	1501	14.1	0.1	0.1	0.1	0.2
438235293153	G203.3166+02.0564	100.292	9.4913			12.2	5.1	3081	4.8	0.2			

Survey ID	Primary RMS ID	RA (deg)	Dec (deg)	J	H	K	Sep. (arcsec)	$\mathrm{Sep}_{\mathrm{phys}}$ (au)	$\mathrm{P}_{\mathrm{chance}}$ (%)	$q_{fg,K}$	$q_{fg,J}$	$q_{tot,K}$	$q_{tot,J}$
438357030882	G206.7804-01.9395A	98.3149	4.5845		14.9	12.8	5.1	6102	1.6	0.4		1.9	
438357030881	G206.7804-01.9395A	98.3131	4.5833		16.3	14.5	4.6	5567	5.9	0.2		0.7	
438609050025	G207.2654-01.8080A	98.6572	4.2122	16.1	11.7	11.2	5.1	5123	0.6	0.4	0.1	2.7	10.4
438609049985	G207.2654-01.8080A	98.6588	4.2131	18.1	15.2	13.6	6.3	6289	9.3	0.1	0.0	0.5	0.9
438609051865	G207.2654-01.8080B	98.6541	4.2129		15.6	13.6	7.5	7538	14.3	0.2		0.8	
438609049966	G207.2654-01.8080B	98.654	4.2119	19.0	15.6	13.7	6.8	6783	13.2	0.2	0.0	0.9	1.7
438609050019	G207.2654-01.8080B	98.6559	4.2118	12.2	11.2	11.6	5.1	5123	0.6	0.5	0.4	0.7	1.4
438454650871	G211.5350+01.0053	103.1177	1.7035	18.1	16.1	14.4	6.6	31505	9.1	0.3	0.1	0.7	0.8
438454657768	G211.5350+01.0053	103.1175	1.7023			15.5	2.5	11950	3.1	0.2			
438578161678	G211.8957-01.2025	101.3174	0.3733	14.9	13.8	13.1	3.0	14544	0.7	0.6	0.3	0.9	1.0
438578161577	G211.8957-01.2025	101.3166	0.3711	17.5	15.4	13.9	9.3	44657	14.8	0.4	0.1	1.0	1.3
438578160761	G212.0641-00.7395	101.8069	0.435			14.7	4.5	21306	8.7	0.2			
438129687750	G212.2344-03.5038	99.4225	-0.9761	15.5	13.9	12.5	4.6	22640	1.8	0.9	0.3	1.8	1.8
438799696380	G212.9626+01.2954	104.0268	0.5616	16.8	15.6	14.8	6.1	25637	17.2	0.4	0.2	0.6	0.8
438799696448	G212.9626+01.2954	104.0253	0.5633	16.7	15.6	14.9	3.7	15449	7.1	0.3	0.2	0.6	0.7
438916256737	G213.9180+00.3786	103.6468	-0.7062	16.5	15.4	14.7	4.7	18365	5.8	0.4	0.2	0.6	0.7
438916256736	G213.9180+00.3786	103.6473	-0.7055	17.2	16.6	16.1	3.9	15174	11.9	0.2	0.2	0.3	0.3
438888088958	G214.4934-01.8103A	101.9604	-2.2149	16.0	14.4	13.5	5.5	11474	3.6	0.4	0.2	0.9	1.3
438888094768	G214.4934-01.8103A	101.9607	-2.2145		16.4	14.7	6.9	14438	15.1	0.3		0.9	
438888088853	G214.4934-01.8103A	101.9582	-2.2143	16.5	15.6	15.0	4.4	9338	8.0	0.2	0.2	0.4	0.5
438888095479	G214.4934-01.8103A	101.9594	-2.2143			15.8	4.1	8692	13.6	0.2			
438888088958	G214.4934-01.8103A	101.9604	-2.2149	16.0	14.4	13.5	4.0	8454	2.0	0.4	0.2	0.9	1.3
438888094768	G214.4934-01.8103A	101.9607	-2.2145		16.4	14.7	4.6	9581	7.2	0.3		0.9	
438888088853	G214.4934-01.8103A	101.9582	-2.2143	16.5	15.6	15.0	4.4	9157	8.3	0.2	0.2	0.4	0.5
438888088956	G214.4934-01.8103B	101.9579	-2.2158	16.3	15.1	14.7	4.1	8696	6.2	0.3	0.2	0.5	0.8
438888088957	G214.4934-01.8103B	101.9592	-2.2167	17.1	16.1	15.4	5.2	10879	16.1	0.2	0.2	0.4	0.5
438888094767	G214.4934-01.8103B	101.9589	-2.2153		17.2	13.8	4.1	8692	3.1	0.4		4.8	
438261005576	G214.6353+00.7704	104.3202	-1.1651	16.4	15.1	14.2	8.0	39292	16.0	0.5	0.3	0.8	1.0
438261005583	G214.6353+00.7704	104.323	-1.1632	19.2	16.9	14.2	4.0	19359	4.9	0.5	0.1	1.1	1.0

Survey ID	Primary RMS ID	RA (deg)	Dec (deg)	J	H	K	Sep. (arcsec)	$\mathrm{Sep_{phys}}$ (au)	$\mathrm{P_{chance}}$ (%)	$q_{fg,K}$	$q_{fg,J}$	$q_{tot,K}$	$q_{tot,J}$
438261005586	G214.6353+00.7704	104.3237	-1.1645	19.3	16.9	14.7	5.7	28009	12.8	0.4	0.1	1.0	1.0
438261007241	G214.6353+00.7704	104.3214	-1.1631			15.0	4.4	21494	9.9	0.3			
439061930352	G215.8902-02.0094	102.4191	-3.5468		12.3	11.9	6.4	39119	1.5	1.4		1.7	
438543678552	G217.0441-00.0584	104.686	-3.6874	15.8	15.4	15.0	6.3	33453	13.3	0.2	0.2	0.2	0.2
438543678553	G217.0441-00.0584	104.6862	-3.6859	16.3	15.6	15.2	5.2	27396	9.4	0.1	0.1	0.2	0.2
438543681916	G217.0441-00.0584	104.6832	-3.6862		16.4	15.3	5.7	30443	12.6	0.1		0.3	
438543678551	G217.0441-00.0584	104.6835	-3.6849	17.3	16.3	15.5	6.3	33141	17.6	0.1	0.1	0.2	0.2
438969717928	G217.3020-00.0567	104.8031	-3.915		12.5	11.2	6.0	7746	0.4	0.7		1.9	
438969717934	G217.3020-00.0567	104.8052	-3.9129		14.1	13.9	6.9	8991	14.2	0.2		0.3	
438399336249	G217.6047-02.6170	102.6555	-5.3512			15.8	3.8	26050	7.8	0.3			
438399335821	G217.6047-02.6170	102.6565	-5.3489		16.4	16.1	4.9	33429	16.9	0.2		0.3	
438399336248	G217.6047-02.6170	102.657	-5.3508			16.1	4.4	29812	14.3	0.2			
438399335015	G217.6047-02.6170	102.6548	-5.3509	18.0	16.9	16.3	4.7	31964	17.8	0.2	0.2	0.3	0.4
438317064802	G218.0230-00.3139A	104.9065	-4.6742	16.6	14.8	13.4	3.7	7064	2.0	0.4	0.1	0.9	1.2
438317064798	G218.0230-00.3139A	104.9078	-4.6723	15.7	14.5	13.6	6.9	13123	9.0	0.3	0.2	0.6	0.8
438317064803	G218.0230-00.3139A	104.9076	-4.6729	16.6	14.9	13.8	5.4	10337	7.4	0.3	0.1	0.7	0.9
438317064799	G218.0230-00.3139A	104.9053	-4.6721	17.1	15.4	14.2	5.1	9641	8.8	0.3	0.1	0.6	0.8
438317064796	G218.0230-00.3139A	104.9061	-4.6732	13.5	11.0	9.3	5.3	10146	0.4	2.0	0.4	6.8	8.4
438317064802	G218.0230-00.3139A	104.9065	-4.6742	16.6	14.8	13.4	7.1	13441	8.3	0.4	0.1	0.9	1.2
438317064799	G218.0230-00.3139A	104.9053	-4.6721	17.1	15.4	14.2	5.3	10116	9.7	0.3	0.1	0.6	0.8
438317064805	G218.0230-00.3139B	104.9047	-4.6733	15.5	12.5	9.8	5.1	9707	0.3	2.0	0.2	8.1	8.1
438317064795	G218.0230-00.3139B	104.9039	-4.6751	16.0	14.6	13.7	6.5	12430	9.6	0.4	0.2	0.8	1.1
438317068830	G218.0230-00.3139B	104.9032	-4.6744		16.5	14.6	6.2	11839	17.4	0.3		1.1	
439082244258	G218.1025-00.3638	104.8988	-4.768			12.1	2.6	4938	0.2	0.7			
438824275534	G220.4587-00.6081	105.7632	-6.9752	13.7	12.9	12.2	5.0	10953	0.6	0.7	0.5	1.0	1.1
438824275535	G220.4587-00.6081	105.7623	-6.9752	13.7	13.3	13.1	5.2	11345	2.3	0.5	0.5	0.5	0.7
438824276732	G220.4587-00.6081	105.7628	-6.9749			13.2	3.7	8194	1.5	0.5			
438775327507	G220.7899-01.7148	104.9238	-7.7727	13.4	12.1	11.2	6.8	5463	3.4	0.3	0.2	0.6	0.7
438775327515	G220.7899-01.7148	104.9235	-7.7754	15.0	13.7	12.7	3.1	2516	2.9	0.2	0.1	0.3	0.4

Survey ID	Primary RMS ID	RA (deg)	Dec (deg)	J	H	K	Sep. (arcsec)	Sep_{phys} (au)	P_{chance} (%)	$q_{fg,K}$	$q_{fg,J}$	$q_{tot,K}$	$q_{tot,J}$
438775328587	G220.7899-01.7148	104.9228	-7.7734			14.3	4.4	3503	17.3	0.1			
438221324128	G221.0108-02.5073	104.3096	-8.3291	13.8	11.8	10.3	8.3	6627	0.8	1.0	0.3	2.5	3.2
438221324109	G221.0108-02.5073	104.3107	-8.3321	12.2	11.8	11.0	7.2	5754	1.3	0.7	0.5	0.9	0.9
438221324135	G221.0108-02.5073	104.3135	-8.3316	12.4	11.9	11.2	8.3	6677	2.5	0.7	0.5	0.9	1.0
438221324139	G221.0108-02.5073	104.312	-8.3309	15.0	13.0	11.6	2.4	1917	0.4	0.6	0.2	1.4	1.9
438221324134	G221.0108-02.5073	104.3129	-8.3303	14.7	13.2	12.1	4.9	3893	2.6	0.5	0.2	0.9	1.3
438221324125	G221.0108-02.5073	104.3138	-8.329	16.6	14.8	12.6	9.4	7554	16.1	0.4	0.1	0.9	0.9
438221330026	G221.0108-02.5073	104.3125	-8.329		15.3	13.1	5.9	4715	9.0	0.3		1.4	
438221324132	G221.0108-02.5073	104.3124	-8.3294	17.3	15.2	13.4	4.7	3757	6.6	0.3	0.1	0.7	0.9
438221330600	G221.0108-02.5073	104.313	-8.3314			13.6	6.5	5213	15.0	0.2			
438221324131	G221.0108-02.5073	104.3107	-8.3293	16.0	14.7	13.8	4.7	3789	9.7	0.2	0.1	0.4	0.6
438995625451	G222.4278-03.1357	104.3976	-9.8777	11.1	12.2	10.8	4.0	2424	0.8	0.6	0.6	0.4	0.2
438995625455	G222.4278-03.1357	104.3964	-9.8797	15.1	14.1	13.3	6.8	4094	8.8	0.2	0.1	0.3	0.5
438995629538	G222.4278-03.1357	104.3961	-9.8761			14.2	6.3	3793	11.2	0.1			
438101217965	G224.3494-02.0143	106.303	-11.0747	17.3	14.8	13.2	2.4	2385	1.3	0.3	0.1	1.0	1.5
438409717355	G224.6065-02.5563	105.9305	-11.5542	14.1	13.3	12.8	9.1	7308	11.6	0.2	0.1	0.3	0.4
438409717357	G224.6065-02.5563	105.9293	-11.5537	14.5	13.7	13.0	7.4	5935	9.1	0.2	0.1	0.3	0.3
438810118229	G224.6075-01.0063	107.3335	-10.8421	15.4	13.7	12.4	8.5	7685	5.3	0.3	0.1	0.7	0.9
438810118238	G224.6075-01.0063	107.3347	-10.8419	16.0	14.4	12.9	4.4	3973	2.8	0.2	0.1	0.5	0.7
438810118228	G224.6075-01.0063	107.3369	-10.8433	14.8	13.6	13.0	8.8	7940	11.7	0.2	0.1	0.4	0.6
438810118237	G224.6075-01.0063	107.3338	-10.8427	15.7	14.4	13.6	8.8	7931	19.8	0.2	0.1	0.3	0.5
438810118270	G224.6075-01.0063	107.3351	-10.8392	14.8	14.0	13.6	7.2	6489	14.3	0.2	0.1	0.3	0.4
438810123634	G224.6075-01.0063	107.3342	-10.8409			15.2	5.3	4812	14.7	0.1			
438999721872	G225.3266-00.5318	108.1005	-11.2603		15.8	14.3	6.4	6351	9.9	0.2		0.5	
438999719207	G225.3266-00.5318	108.1024	-11.2584	17.3	16.0	15.0	3.7	3674	5.5	0.1	0.1	0.3	0.4
438975902354	G229.5711+00.1525	110.7579	-14.6939	13.3	12.1	10.9	6.2	25233	0.9	1.0	0.4	1.7	1.5
438975902358	G229.5711+00.1525	110.7582	-14.6933	16.6	14.7	13.1	4.4	17910	2.1	0.4	0.1	0.9	1.0
438975904549	G229.5711+00.1525	110.7567	-14.6917		18.3	16.2	3.5	14502	16.5	0.1		0.5	
515435907971	G295.2090-00.7434A	175.8888	-62.5921	14.8	13.7	13.1	7.7	75307	17.9	0.7	0.4	1.1	1.2

Survey ID	Primary RMS ID	RA (deg)	Dec (deg)	J	H	K	Sep. (arcsec)	$\mathrm{Sep_{phys}}$ (au)	$\mathrm{P_{chance}}$ (%)	$q_{fg,K}$	$q_{fg,J}$	$q_{tot,K}$	$q_{tot,J}$
515413713143	G295.5570-01.3787A	176.2687	-63.2968	15.9	15.2	14.6	2.7	26512	8.2	0.5	0.3	0.7	0.7
515430634437	G296.2654-00.3901	178.2939	-62.5073	11.7	12.2	10.4	7.1	57329	0.6	2.9	1.6	2.4	1.0
515430719771	G296.4036-01.0185A	178.2819	-63.1492	15.6	14.3	13.4	4.3	40658	11.1	0.6	0.3	1.0	1.1
515411060609	G297.1390-01.3510	179.7304	-63.6299	17.3	15.1	13.1	2.2	19987	2.0	0.7	0.2	1.8	1.5
515410670676	G297.1390-01.3510	179.729	-63.6284	14.4	13.6	13.1	5.5	49086	12.6	0.7	0.4	1.0	1.0
515431396402	G297.4701-00.7343	180.7224	-63.0915	13.0	12.6	11.7	3.9	38012	1.1	1.5	0.8	1.8	1.3
515431392932	G297.4709-00.7297	180.7249	-63.0846	16.3	15.6	15.1	2.9	28032	17.7	0.5	0.3	0.7	0.7
515451898377	G298.2620+00.7394	182.9496	-61.7711			14.2	3.3	13332	11.7	0.2			
515427556339	G298.3323-00.2200	182.7785	-62.7326	14.0	13.2	12.3	4.9	48777	7.6	1.1	0.6	1.5	1.2
515427847335	G298.8418-00.3390A	183.8363	-62.9245	14.1	13.1	12.8	6.4	26051	12.6	0.7	0.4	1.0	1.2
515423409689	G300.1615-00.0877	186.7871	-62.8274		15.8	13.2	5.5	23015	15.4	0.5			
515422684953	G300.3412-00.2190	187.1503	-62.9784	14.7	13.1	11.9	7.4	31228	6.6	0.7	0.3	1.4	1.3
515422700965	G300.3770-00.2857A	187.2201	-63.046	15.3	14.1	13.3	2.8	29577	4.4	1.2	0.6	2.0	2.1
515422772343	G300.5047-00.1745A	187.5101	-62.9457	14.4	13.3	12.7	8.2	73112	16.7	0.5	0.3	0.8	0.8
515423496760	G300.5047-00.1745A	187.5153	-62.947			14.5	2.2	19821	6.5	0.3			
515468112054	G300.7221+01.2007	188.2068	-61.5908		16.6	14.3	3.7	15723	9.9	0.4			
515468223486	G300.7221+01.2007	188.2077	-61.5913			14.5	2.7	11477	6.7	0.4			
515441359357	G301.8147+00.7808A	190.4732	-62.0684	15.0	12.9	11.1	8.5	37508	5.2	0.7	0.2	1.6	1.4
515440763907	G301.8147+00.7808A	190.4741	-62.0689	12.3	12.1	11.3	6.5	28779	4.6	0.6	0.5	0.7	0.5
515440763916	G301.8147+00.7808A	190.4753	-62.0718	15.3	13.7	12.0	4.0	17648	2.9	0.5	0.2	0.9	0.8
515415092857	G302.4546-00.7401	191.7861	-63.6094	14.3	13.3	12.8	4.1	47392	6.7	0.9	0.5	1.3	1.3
515416024340	G302.4546-00.7401	191.7879	-63.6086	17.7	15.1	13.4	3.7	42917	10.7	0.7	0.2	1.9	1.9
515415227394	G302.6604-00.7908	192.2464	-63.6605	15.6	14.3	13.4	2.4	26026	5.7	0.8	0.4	1.2	1.2
515439017352	G303.9973+00.2800	195.1708	-62.5726	12.9	12.6	11.8	4.4	50420	4.0	1.3	0.9	1.4	1.1
515439017958	G303.9973+00.2800	195.1761	-62.5728	14.0	12.8	11.9	4.7	53425	5.3	1.2	0.6	1.9	1.8
515439017961	G303.9973+00.2800	195.1753	-62.5721	15.6	14.7	14.1	3.3	37906	11.3	0.5	0.3	0.7	0.7
515417091913	G304.3674-00.3359A	196.0428	-63.1735	13.3	12.5	11.5	5.1	60525	3.2	0.9	0.5	1.1	0.9
515417091912	G304.3674-00.3359A	196.0433	-63.1715	12.8	12.6	12.2	3.4	39948	3.5	0.6	0.5	0.7	0.6
515418102995	G304.3674-00.3359A	196.0429	-63.1725			14.4	2.1	25050	7.1	0.3			

Survey ID	Primary RMS ID	RA (deg)	Dec (deg)	J	H	K	Sep. (arcsec)	$\mathrm{Sep_{phys}}$ (au)	$\mathrm{P_{chance}}$ (%)	$q_{fg,K}$	$q_{fg,J}$	$q_{tot,K}$	$q_{tot,J}$
515417338013	G304.7592-00.6299	196.9441	-63.4445	12.3	13.0	11.1	6.4	71878	0.5	3.0	1.9	2.2	0.9
515417340714	G304.7592-00.6299	196.9526	-63.4445	12.5	12.6	11.2	8.7	97922	3.7	2.9	1.8	2.6	1.3
515417346057	G304.7700-00.5193	196.9538	-63.3317	15.1	13.8	13.0	4.4	48697	12.3	0.8	0.4	1.3	1.3
515417346219	G304.7700-00.5193	196.957	-63.3315	17.4	15.6	13.4	4.7	52315	18.6	0.7	0.2	1.3	1.0
515417346061	G304.7700-00.5193	196.9565	-63.3332	16.3	15.3	14.4	2.4	26757	11.4	0.4	0.2	0.6	0.6
515439392701	G304.8872+00.6356	197.0511	-62.1736	15.2	13.3	12.1	2.8	10780	1.5	0.9	0.3	1.8	1.9
515439575629	G304.8872+00.6356	197.0502	-62.1724	17.6	15.9	14.8	1.6	6073	3.3	0.3	0.1	0.5	0.6
515443769068	G305.1940-00.0051	197.8103	-62.792	14.1	13.2	12.7	5.7	22821	18.9	0.7	0.5	0.9	1.0
515443769881	G305.1940-00.0051	197.8114	-62.7905	16.4	15.4	14.3	1.5	6117	4.6	0.3	0.2	0.5	0.5
515445065969	G305.1940-00.0051	197.8119	-62.7901			14.4	2.8	11125	15.8	0.3			
515444525628	G305.2017+00.2072A	197.7915	-62.5779	17.5	14.8	12.5	3.8	15012	4.3	0.3	0.1	0.9	0.8
515421631601	G305.4748-00.0961	198.4415	-62.8576		16.1	13.2	2.1	8522	2.7	0.4			
515443895112	G305.4840+00.2248	198.398	-62.5352	13.9	13.2	12.5	7.8	31021	17.6	0.6	0.4	0.8	0.7
515470763672	G305.6327+01.6467	198.4509	-61.1063	15.4	13.4	12.2	6.4	31232	5.4	0.6	0.2	1.2	1.3
515445083255	G305.8871+00.0179A	199.3146	-62.7071			15.1	1.9	7576	19.3	0.3			
515420646984	G305.9402-00.1634	199.4672	-62.8817	12.1	12.7	10.9	6.7	26660	0.5	1.0	0.7	0.7	0.3
515444184798	G306.1160+00.1386A	199.7867	-62.5613	14.7	12.7	11.2	8.4	33575	13.0	1.2	0.3	2.5	2.4
515445006121	G306.1160+00.1386A	199.7867	-62.5621		15.9	14.3	3.0	12026	18.1	0.3			
515444184786	G306.1160+00.1386B	199.7817	-62.5615	11.7	12.6	11.0	8.4	33575	11.5	1.6	1.3	1.1	0.5
515425992703	G307.3950-00.5838	202.7695	-63.1132	13.6	12.6	11.5	7.4	93072	18.0	1.9	0.8	2.8	2.1
515426392456	G307.3950-00.5838	202.7657	-63.1122	16.7	14.5	12.6	1.7	21788	2.6	1.2	0.3	2.8	2.3
515426918537	G307.6138-00.2559B	203.1278	-62.7526		13.1	11.8	8.6	60123	18.9	1.2			
515428823692	G308.0049-00.3868	204.0178	-62.8189	14.6	13.2	12.4	4.9	34516	8.1	0.9	0.4	1.5	1.6
515479614914	G308.0108+02.0146	203.1919	-60.4493		16.2	12.8	5.9	11742	10.1	0.4			
515478306274	G308.0108+02.0146	203.1971	-60.448	16.1	14.8	14.0	4.4	8768	13.9	0.3	0.1	0.4	0.5
515479279175	G308.0108+02.0146	203.196	-60.4479	19.0	16.9	15.7	2.9	5783	18.8	0.1	0.0	0.3	0.4
515453289189	G308.9176+00.1231A	205.7576	-62.1452	18.6	15.0	11.5	8.7	46132	12.3	0.3	0.0	1.2	0.9
515433939916	G309.4230-00.6208	207.1561	-62.7699	12.9	12.3	11.1	9.6	33635	5.5	1.1	0.6	1.3	1.0
515434787271	G309.4230-00.6208	207.1582	-62.7689	18.1	15.1	13.3	6.3	22162	18.0	0.4	0.1	1.5	1.8

Survey ID	Primary RMS ID	RA (deg)	Dec (deg)	J	H	K	Sep. (arcsec)	$\mathrm{Sep}_{\mathrm{phys}}$ (au)	$\mathrm{P}_{\mathrm{chance}}$ (%)	$q_{fg,K}$	$q_{fg,J}$	$q_{tot,K}$	$q_{tot,J}$
515433940724	G309.4230-00.6208	207.162	-62.7702	18.9	17.5	15.0	2.6	8939	11.6	0.2	0.1	0.4	0.3
515433989608	G309.5356-00.7388A	207.46	-62.8587	13.8	13.6	13.4	5.8	20406	16.9	0.5	0.5	0.5	0.6
515433989608	G309.5356-00.7388A	207.46	-62.8587	13.8	13.6	13.4	2.2	7679	2.5	0.5	0.5	0.5	0.6
515460055405	G309.9206+00.4790B	207.6743	-61.5865		14.0	11.2	5.3	28738	0.3	0.8			
515459148809	G309.9206+00.4790B	207.673	-61.5849	17.0	15.5	13.5	6.3	33927	18.1	0.3	0.1	0.5	0.4
515460217188	G309.9796+00.5496	207.7628	-61.5037		16.2	13.6	2.8	9636	3.0	0.2			
515459184200	G310.0135+00.3892	207.9078	-61.655	16.0	14.4	12.7	10.0	31950	14.8	0.2	0.1	0.4	0.3
515460484243	G310.1420+00.7583A	207.9924	-61.262			15.4	1.9	10300	9.0	0.2			
515459232054	G310.1420+00.7583A	207.9937	-61.2622	17.7	16.9	15.7	2.6	13871	19.2	0.2	0.1	0.3	0.3
515468496688	G311.0341+00.3791	209.9896	-61.4082	15.0	12.9	11.4	7.7	22410	7.1	1.1	0.3	2.6	2.8
515468633092	G311.4402+00.4243	210.78	-61.2563	14.0	12.9	12.0	5.7	20505	7.3	0.6	0.3	0.9	0.9
515468632338	G311.4402+00.4243	210.7754	-61.2591	14.5	13.1	12.4	8.2	29587	18.8	0.5	0.3	0.8	0.9
515468650220	G311.4925+00.4021	210.8946	-61.264	16.7	16.0	15.7	2.1	11748	17.5	0.2	0.2	0.3	0.4
515445560311	G311.5131-00.4532	211.4435	-62.0813	14.6	12.8	11.2	5.3	22465	0.4	1.1	0.3	2.3	2.0
515468677192	G311.5671+00.3189	211.0919	-61.3249		12.5	11.4	2.3	8614	0.3	1.6			
515445772395	G311.9799-00.9527	212.7131	-62.4212	11.9	12.1	10.7	2.2	6955	0.1	1.5	1.0	1.4	0.8
515446326642	G312.0963-00.2356	212.4937	-61.7026	19.4	16.4	15.0	2.2	17225	14.1	0.3	0.1	0.9	1.2
515454343401	G313.3153-00.4640A	215.0759	-61.5287	12.5	12.3	10.9	3.1	26125	0.2	2.9	1.6	3.0	1.7
515454342410	G313.3153-00.4640A	215.0728	-61.5303	15.0	13.2	12.4	7.1	60025	16.7	1.6	0.6	3.2	3.6
515455186129	G313.3153-00.4640A	215.0751	-61.5305		15.8	13.4	4.4	36603	13.5	1.0			
515455186128	G313.3153-00.4640A	215.078	-61.5303		16.1	13.8	3.8	31897	13.6	0.9			
515481406509	G313.5769+00.3267A	215.0371	-60.6996			16.4	1.3	4687	11.3	0.1			
515483024267	G315.3273-00.2270	218.7723	-60.5818			15.5	1.6	19452	11.3	0.3			
515482173914	G316.5871-00.8086	221.5945	-60.5959	14.5	13.1	12.3	4.9	15750	14.9	0.6	0.3	1.1	1.2
515492626989	G316.6412-00.0867	221.0748	-59.9196	16.3	15.7	15.5	2.4	3369	17.3	0.1	0.1	0.1	0.2
515506521631	G320.1239-00.5045A	227.5027	-58.6691	12.6	13.3	11.6	8.6	104536	7.1	1.9	1.3	1.4	0.6
515517203115	G320.1542+00.7976	226.3185	-57.529	14.4	13.3	12.3	8.0	20011	17.3	0.4	0.2	0.6	0.6
515518203010	G320.1542+00.7976	226.3218	-57.5275		13.6	13.2	1.6	3877	1.5	0.3			
515498238548	G320.3767-01.9727	229.4114	-59.7988	12.2	13.1	11.2	8.7	24490	2.8	1.3	1.0	0.9	0.4

Survey ID	Primary RMS ID	RA (deg)	Dec (deg)	J	H	K	Sep. (arcsec)	$\mathrm{Sep}_{\mathrm{phys}}$ (au)	$\mathrm{P}_{\mathrm{chance}}$ (%)	$q_{fg,K}$	$q_{fg,J}$	$q_{tot,K}$	$q_{tot,J}$
515499248392	G320.3767-01.9727	229.412	-59.797		16.5	14.1	2.3	6546	6.4	0.4			
515515162146	G321.0523-00.5070A	229.0295	-58.1951	12.6	12.0	11.4	7.6	68800	13.2	0.8	0.5	1.0	0.9
515541604371	G322.9343+01.3922	230.091	-55.5846		16.1	13.5	6.0	16299	15.3	0.3			
515540272173	G322.9343+01.3922	230.0905	-55.5867	14.3	13.7	13.6	5.2	13951	12.6	0.2	0.2	0.3	0.4
515531365248	G323.4468+00.0968B	232.1296	-56.3858	15.9	13.9	12.7	4.7	19397	9.7	0.9	0.3	1.9	2.2
515523618706	G323.7399-00.2617B	232.9434	-56.5142		14.7	12.6	4.1	13202	6.5	0.4			
515522509023	G323.7399-00.2617B	232.9445	-56.5145	16.3	14.3	13.1	6.4	20337	19.3	0.3	0.1	0.7	0.8
515523763300	G323.7399-00.2617B	232.9424	-56.5136			13.7	3.2	10320	8.8	0.3			
515522799412	G323.7399-00.2617B	232.9416	-56.5149	17.9	16.0	14.7	2.4	7575	9.9	0.2	0.1	0.4	0.5
515523284413	G323.7399-00.2617B	232.9413	-56.5142	17.4	14.4	12.1	3.8	12124	2.8	0.5	0.1	1.7	1.7
515536557562	G324.1581+00.2359	233.045	-55.8683	13.7	12.4	11.3	7.1	48163	9.4	1.2	0.5	1.9	1.6
515536557279	G324.1581+00.2359	233.0402	-55.8666	13.4	12.9	12.6	5.8	39133	18.5	0.7	0.5	0.8	0.9
515536558826	G324.1594+00.2622	233.0186	-55.8426	12.5	12.7	10.7	5.3	35844	0.3	1.5	0.7	1.3	0.6
515537147966	G324.1594+00.2622	233.0164	-55.8446	16.0	13.6	12.2	4.8	32775	8.2	0.8	0.2	2.0	2.1
515535042518	G326.4477-00.7485B	237.3259	-55.282	13.4	13.1	12.5	3.9	15493	6.3	0.5	0.4	0.6	0.5
515542295499	G326.4755+00.6947	235.8246	-54.1271	12.0	12.7	10.8	9.7	17525	5.7	0.6	0.4	0.5	0.2
515542973521	G326.4755+00.6947	235.8288	-54.1272	17.2	14.4	12.5	2.2	3906	1.5	0.3	0.1	0.9	1.1
515542311226	G326.5437+00.1684	236.4713	-54.5011	13.6	13.2	12.9	2.9	12698	3.6	0.7	0.6	0.8	0.9
515542337595	G326.6618+00.5207	236.2607	-54.1509	18.0	15.8	13.5	2.5	4560	6.4	0.1	0.0	0.3	0.3
515542596047	G326.6618+00.5207	236.2632	-54.1501	17.6	15.0	13.6	3.8	6794	15.8	0.1	0.0	0.3	0.5
515535147370	G326.7796-00.2405	237.2322	-54.676	13.1	12.9	12.5	5.9	22889	13.1	0.5	0.4	0.5	0.5
515535147372	G326.7796-00.2405	237.2305	-54.6755	13.8	13.2	12.6	5.8	22724	15.1	0.5	0.3	0.6	0.6
515551077705	G327.3941+00.1970	237.5802	-53.9519	16.9	14.0	12.3	7.4	38683	17.4	0.7	0.1	2.3	2.6
515546009749	G327.6184-00.1109	238.2089	-54.0496	17.2	15.9	15.1	2.1	19042	18.3	0.4	0.2	0.7	0.8
515546029768	G327.8097-00.6339A	239.031	-54.3303	16.6	14.4	13.1	4.5	13464	9.5	0.5	0.2	1.2	1.4
515546029769	G327.8097-00.6339A	239.0342	-54.3315	17.0	15.0	13.8	3.6	10728	10.3	0.4	0.1	0.8	1.1
515545721408	G327.8097-00.6339A	239.0328	-54.3309	13.4	12.5	11.3	7.5	22446	5.4	1.1	0.5	1.6	1.3
515545721408	G327.8097-00.6339A	239.0328	-54.3309	13.4	12.5	11.3	9.7	28982	8.8	1.1	0.5	1.6	1.3
515545721408	G327.8097-00.6339A	239.0328	-54.3309	13.4	12.5	11.3	8.4	25188	5.9	1.1	0.5	1.6	1.3

Survey ID	Primary RMS ID	RA (deg)	Dec (deg)	J	H	K	Sep. (arcsec)	$\mathrm{Sep_{phys}}$ (au)	$\mathrm{P_{chance}}$ (%)	$q_{fg,K}$	$q_{fg,J}$	$q_{tot,K}$	$q_{tot,J}$
515545721406	G327.8097-00.6339B	239.0321	-54.333	14.3	13.2	12.3	7.5	22446	14.1	0.7	0.4	1.1	1.1
515545721406	G327.8097-00.6339B	239.0321	-54.333	14.3	13.2	12.3	7.2	21699	13.8	0.7	0.4	1.1	1.1
515545721406	G327.8097-00.6339B	239.0321	-54.333	14.3	13.2	12.3	4.1	12218	4.2	0.7	0.4	1.1	1.1
515546657622	G327.8097-00.6339C	239.0288	-54.3323		15.6	12.5	7.2	21699	14.9	0.7			
515545721150	G327.8097-00.6339C	239.0252	-54.3318	11.9	13.3	11.1	7.9	23584	3.7	1.3	1.0	0.7	0.2
515546657622	G327.8097-00.6339C	239.0288	-54.3323		15.6	12.5	3.2	9633	3.1	0.7			
515546334969	G327.8097-00.6339D	239.0302	-54.3327	16.6	13.1	11.0	8.4	25188	0.9	1.5	0.2	6.3	7.0
515546334969	G327.8097-00.6339D	239.0302	-54.3327	16.6	13.1	11.0	4.1	12218	0.2	1.5	0.2	6.3	7.0
515546334969	G327.8097-00.6339D	239.0302	-54.3327	16.6	13.1	11.0	3.2	9633	0.1	1.5	0.2	6.3	7.0
515545774780	G327.9455-00.1149	238.6402	-53.8447	12.1	11.9	10.4	9.0	27786	2.9	1.4	0.8	1.4	0.8
515546360227	G327.9455-00.1149	238.6413	-53.8458	17.5	14.0	11.5	6.9	21490	7.4	0.8	0.1	3.4	3.4
515552621953	G329.0663-00.3081	240.2924	-53.2655	13.0	12.5	11.9	7.2	83006	14.1	0.8	0.5	1.0	0.8
515557836531	G329.2713+00.1147	240.0904	-52.8144	14.4	13.5	13.1	4.2	19025	11.8	0.4	0.3	0.6	0.7
515552769903	G329.3402-00.6436	241.0062	-53.3395	15.2	14.8	14.3	2.4	24000	18.0	0.5	0.4	0.6	0.7
515557934316	G329.6098+00.1139	240.5102	-52.5933	12.2	12.1	11.0	6.3	24682	4.4	1.0	0.6	1.0	0.7
515557934317	G329.6098+00.1139	240.5134	-52.5921	16.5	15.1	14.3	2.1	8324	8.5	0.2	0.1	0.4	0.6
515557934319	G329.6098+00.1139	240.5121	-52.5927	16.0	15.3	14.8	1.9	7281	9.7	0.2	0.2	0.3	0.3
515560291348	G330.2923+00.0010A	241.4747	-52.225	17.3	14.4	12.5	2.9	11324	8.4	0.9	0.2	2.8	3.0
515559976827	G330.8768-00.3836	242.5979	-52.1167	13.0	12.7	12.5	5.2	20354	11.1	0.4	0.3	0.4	0.4
515566316492	G331.3402-00.3444	243.1128	-51.7713	14.5	13.3	12.3	5.4	21553	17.3	0.4	0.2	0.6	0.6
515572615966	G331.3486+01.0442	241.6154	-50.7432		13.2	12.3	2.1		5.0				
515571581630	G331.3576+01.0626	241.6064	-50.7219	14.8	13.3	12.3	4.2	18787	16.0	0.4	0.2	0.8	0.8
515567182394	G331.5131-00.1020	243.0371	-51.477	13.5	13.1	11.3	9.9	49608	12.5	0.5	0.2	0.5	0.3
515566411007	G331.5131-00.1020	243.0399	-51.477	14.2	13.9	13.7	3.8	18894	18.5	0.2	0.2	0.2	0.2
515566577682	G331.7953-00.0979	243.3663	-51.282	12.2	13.3	11.5	8.3	121022	12.9	0.9	0.7	0.6	0.2
515567664536	G331.7953-00.0979	243.3666	-51.2813		13.6	12.2	5.9	84847	17.7	0.7			
515568034642	G332.4683-00.5228A	244.6099	-51.1205			14.2	1.6	5918	6.4	0.3			
515573312688	G332.7013-00.5874A	244.9512	-51.001	11.8	12.7	11.0	8.5	30609	9.4	1.1	0.8	0.7	0.3
515573312738	G332.7013-00.5874A	244.9503	-51.0001	13.1	12.4	11.8	8.5	30598	19.3	0.7	0.5	1.0	1.0

Survey ID	Primary RMS ID	RA (deg)	Dec (deg)	J	H	K	Sep. (arcsec)	$\mathrm{Sep_{phys}}$ (au)	$\mathrm{P_{chance}}$ (%)	$q_{fg,K}$	$q_{fg,J}$	$q_{tot,K}$	$q_{tot,J}$
515574939899	G332.7013-00.5874A	244.9476	-51.0027			13.2	3.1	11053	8.7	0.4			
515573312734	G332.7013-00.5874A	244.9492	-51.0018	14.7	14.4	13.9	3.5	12459	19.5	0.3	0.3	0.3	0.4
515584292924	G332.9565+01.8035B	242.6647	-49.0999	15.7	14.1	13.0	6.1	10999	18.0	0.5	0.2	0.9	1.1
515573462162	G332.9868-00.4871	245.1561	-50.7329	12.5	12.3	11.5	9.5	34354	9.6	0.5	0.3	0.5	0.4
515579546653	G333.0494+00.0324B	244.6509	-50.3146	17.5	12.7	11.0	9.4	33707	3.2	1.3	0.1	9.4	16.9
515579822626	G333.0494+00.0324B	244.6541	-50.317		15.2	13.5	2.8	10215	13.3	0.5			
515573522467	G333.1075-00.5020	245.3104	-50.6532	15.7	14.9	13.8	2.2	7852	6.0	0.4	0.2	0.5	0.5
515579603638	G333.3151+00.1053	244.8694	-50.0778	18.3	15.3	13.3	3.2	11347	7.2	0.4	0.1	1.2	1.4
515573641559	G333.3752-00.2015B	245.2744	-50.2544	16.2	15.6	15.0	2.5	9141	18.0	0.2	0.2	0.3	0.3
515574367341	G333.4747-00.2366	245.4229	-50.2098	19.7	16.4	14.5	3.0	10911	15.5	0.3	0.0	1.0	1.3
515573816229	G333.7608-00.2253	245.7264	-49.9967	14.3	13.2	12.7	6.1	22065	15.8	0.8	0.5	1.3	1.6
515581883959	G334.1602-00.0604	245.9799	-49.5963		15.8	12.7	4.1	16882	18.5	0.8			
515580753362	G334.7302+00.0052	246.5165	-49.1444	12.4	13.3	11.5	7.1	17720	15.4	0.7	0.6	0.5	0.2
515586996399	G334.8438+00.2095A	246.4199	-48.9213	17.9	15.7	14.6	2.0	21057	17.9	0.3	0.1	0.8	1.0
515580897500	G335.0611-00.4261A	247.3477	-49.2062	13.0	13.0	12.5	6.4	18019	19.7	0.6	0.6	0.6	0.6
515588705665	G335.7288-00.0966	247.6819	-48.494	17.1	13.8	12.3	5.4	60791	13.9	1.0	0.2	3.8	4.6
515588705660	G335.7288-00.0966	247.6804	-48.4934	18.3	14.4	12.5	5.4	60727	15.4	1.0	0.1	4.7	6.0
515588466750	G335.7288-00.0966	247.68	-48.4961	16.1	13.6	12.6	4.4	48788	11.3	0.9	0.3	2.4	2.9
515589124634	G335.9960-00.8532	248.7955	-48.8136		17.8	15.8	1.8	6098	18.5	0.2			
515588120132	G336.4102-00.2545A	248.5542	-48.1035	14.6	14.0	13.8	2.2	22616	10.4	0.7	0.5	0.9	0.9
515583013712	G336.4917-01.4741B	250.0053	-48.8626	15.2	12.9	11.6	7.2	14433	6.8	0.3	0.1	0.9	1.0
515583013709	G336.4917-01.4741B	250.0065	-48.8634	14.3	12.7	11.7	5.7	11317	4.6	0.3	0.1	0.6	0.7
515583013719	G336.4917-01.4741B	250.0068	-48.8648	14.8	13.2	12.4	5.0	9911	7.3	0.3	0.1	0.5	0.6
515583027208	G336.5299-01.7344	250.3372	-49.0066	14.3	12.8	11.6	7.8	14123	10.1	0.5	0.2	1.0	1.0
515588352197	G336.9033-00.1521B	248.932	-47.6753	14.3	13.0	12.4	3.7	16335	8.5	1.0	0.5	1.6	1.9
515596638929	G337.0963-00.9291	249.9895	-48.0462			14.0	3.8	11720	15.6	0.3			
515595892351	G337.0963-00.9291	249.9916	-48.0469			14.0	2.1	6415	5.5	0.3			
515596283789	G337.0963-00.9291	249.9905	-48.0461			14.2	2.5	7764	9.7	0.3			
515595501603	G338.1127-00.1905A	250.1703	-46.7967	13.5	12.2	11.6	6.7	81586	16.4	2.1	1.0	3.3	3.3

Survey ID	Primary RMS ID	RA (deg)	Dec (deg)	J	H	K	Sep. (arcsec)	$\mathrm{Sep_{phys}}$ (au)	$\mathrm{P_{chance}}$ (%)	$q_{fg,K}$	$q_{fg,J}$	$q_{tot,K}$	$q_{tot,J}$
515595498800	G338.1127-00.1905A	250.1694	-46.7991	13.9	12.4	11.7	2.6	31869	3.1	2.0	0.9	3.6	3.8
515596745399	G338.1127-00.1905A	250.1693	-46.7986			14.2	1.9	22857	10.5	0.7			
515601275082	G338.1260+00.1719	249.7885	-46.5477	13.0	12.3	11.5	4.7		8.7				
515601275078	G338.1260+00.1719	249.7893	-46.5461	13.2	12.4	11.9	4.3		11.0				
515601736668	G338.1260+00.1719	249.788	-46.5471	15.6	14.1	13.5	2.0		8.7				
515595565950	G338.2253-00.5094	250.6316	-46.922	14.4	12.6	11.5	7.2	99009	11.0	0.9	0.3	1.9	1.8
515601377155	G338.2801+00.5419A	249.5386	-46.1851	15.1	14.8	14.6	1.8	7583	13.6	0.4	0.4	0.4	0.5
515601436294	G338.3597+00.1430A	250.0483	-46.3901	14.5	12.8	12.0	4.2	54269	16.1	1.1	0.4	2.2	2.3
515602099125	G338.4387+00.1907	250.0692	-46.3019	17.7	14.0	12.2	3.3	41855	5.9	4.1	0.5	18.5	23.1
515608330474	G338.8872+00.5963	250.0598	-45.6948	15.4	14.6	14.2	2.4	9575	9.3	0.3	0.2	0.4	0.5
515609374536	G338.9289+00.3880A	250.32	-45.8007	18.2	14.4	12.6	3.5	7689	6.7	0.7	0.1	3.2	4.6
515608622840	G339.3316+00.0964	251.019	-45.6898	12.4	13.5	11.3	4.6	60337	2.3	1.4	0.9	0.8	0.3
515609979732	G339.3316+00.0964	251.0184	-45.6904			12.8	2.0	26182	6.7	0.7			
515597620925	G339.6816-01.2058	252.7751	-46.2654	15.4	14.0	12.9	2.9	6967	2.6	0.4	0.2	0.7	0.8
515597620924	G339.6816-01.2058	252.7743	-46.2633	14.8	14.2	13.9	4.7	11301	16.5	0.3	0.3	0.3	0.4
515608889031	G339.7602+00.0530A	251.4638	-45.3922	12.8	12.2	11.3	2.9	34461	4.4	1.8	1.0	2.2	1.6
515603185630	G339.9267-00.0837	251.765	-45.3571	13.2	12.3	11.8	6.1	23027	18.5	0.9	0.6	1.2	1.3
515610121100	G339.9489-00.5401	252.2798	-45.6347	13.4	12.5	11.5	9.0	94157	19.6	1.3	0.6	1.9	1.5
515610121772	G339.9489-00.5401	252.2822	-45.633	16.9	15.7	15.0	2.2	23245	18.0	0.3	0.2	0.5	0.5
515610162496	G340.0543-00.2437B	252.0539	-45.359	13.5	12.9	11.8	7.4	28308	19.7	0.9	0.5	1.1	0.9
515610162124	G340.0543-00.2437B	252.0556	-45.3608	16.1	15.2	14.9	2.5	9610	19.1	0.3	0.2	0.4	0.5
515610162123	G340.0543-00.2437B	252.0544	-45.3616	17.9	17.0	15.2	2.0	7416	14.7	0.2	0.1	0.3	0.3
515610307153	G340.4287-00.3711	252.5395	-45.1559	13.1	13.4	12.5	4.5	15600	8.0	0.8	0.7	0.7	0.5
515610307155	G340.4287-00.3711	252.5389	-45.1563	15.0	14.4	14.2	2.3	8191	8.9	0.4	0.3	0.5	0.6
515610811233	G340.7455-01.0021	253.5154	-45.3148	17.8	15.2	13.8	4.8	12573	16.4	0.2	0.1	0.7	0.9
515611604332	G340.7455-01.0021	253.5173	-45.3127		16.7	14.0	4.3	11173	15.5	0.2			
515611237920	G341.1281-00.3466A	253.1404	-44.6028	18.5	14.2	11.4	4.1	13452	2.6	0.8	0.1	4.3	4.5
515610570051	G341.1281-00.3466A	253.1401	-44.6011	15.4	13.3	11.7	7.3	24138	10.6	0.7	0.2	1.5	1.6
515610570052	G341.1281-00.3466A	253.1407	-44.6015	14.4	12.9	12.0	7.0	23084	11.9	0.6	0.3	1.1	1.1

Survey ID	Primary RMS ID	RA (deg)	Dec (deg)	J	H	K	Sep. (arcsec)	Sep_{phys} (au)	P_{chance} (%)	$q_{fg,K}$	$q_{fg,J}$	$q_{tot,K}$	$q_{tot,J}$
515611706730	G341.1281-00.3466A	253.1394	-44.6026		15.4	12.3	1.9	6358	1.2	0.5			
515610604420	G341.2105-00.2325	253.0897	-44.4661	11.7	12.8	10.3	4.6	15703	0.8	0.9	0.5	0.6	0.2
515610859695	G341.2182-00.2136	253.0766	-44.4487	15.9	13.9	12.9	5.5	18822	17.5	0.5	0.2	1.1	1.4
515611729419	G341.2182-00.2136	253.0757	-44.4474		16.1	14.2	3.3	11337	18.7	0.3			
515623599739	G342.3693+00.4234	253.4034	-43.1545	14.3	13.6	13.1	1.6		2.7				
515624805906	G342.7057+00.1260B	254.0118	-43.0799		17.4	14.4	3.2	10849	14.0	0.2			
515630740918	G343.4702-00.0595	254.8584	-42.5971	14.4	12.8	12.0	2.8	7709	5.2	0.6	0.3	1.1	1.3
515630747797	G343.4867-00.0584A	254.874	-42.5852	14.9	14.4	14.1	2.2	5887	18.2	0.5	0.4	0.6	0.7
515626028054	G343.5213-00.5171	255.3909	-42.8397	18.8	15.8	14.0	3.8	12136	10.1	0.2	0.0	0.6	0.8
515626269480	G343.5213-00.5171	255.3902	-42.8387		16.2	14.7	3.2	10369	11.6	0.1			
515625474834	G343.9033-00.6713	255.8784	-42.6309	12.5	12.6	11.6	8.7	24231	10.5	0.9	0.7	0.8	0.5
515625473797	G343.9033-00.6713	255.8742	-42.6318	13.3	12.7	11.6	6.8	19178	8.3	0.9	0.5	1.1	0.9
515633467516	G344.4257+00.0451B	255.536	-41.784		12.7	11.3	4.1	19265	2.3	0.8			
515633467516	G344.4257+00.0451B	255.536	-41.784		12.7	11.3	7.7	36386	11.2	0.8			
515641572596	G344.6608+00.3401	255.42	-41.4127			12.9	3.3	41731	9.6	0.9			
515646756772	G344.8746+01.4347	254.4549	-40.5711	16.2	13.1	11.5	8.8	21092	2.8	0.9	0.2	3.1	3.9
515647533435	G344.8746+01.4347	254.4543	-40.5679		16.3	13.9	3.6	8612	9.1	0.3			
515646444047	G344.9816+01.8252A	254.1405	-40.2428	14.5	13.2	11.6	4.4	10503	0.2	0.8	0.3	1.4	1.1
515646444049	G344.9816+01.8252A	254.1399	-40.2424	15.6	14.0	13.0	5.0	12030	9.2	0.5	0.2	0.9	1.1
515647109439	G344.9816+01.8252A	254.1436	-40.2419	16.8	14.6	13.0	5.4	13059	11.7	0.5	0.1	1.1	1.3
515646444048	G344.9816+01.8252B	254.1476	-40.2385	14.5	13.3	12.1	4.2	10065	1.5	0.9	0.4	1.4	1.3
515646444037	G344.9816+01.8252B	254.1487	-40.2393	13.0	13.2	12.3	6.4	15309	6.3	0.8	0.7	0.7	0.6
515646444036	G344.9816+01.8252B	254.1464	-40.2374	15.5	13.8	12.9	6.6	15863	15.4	0.6	0.3	1.2	1.5
515646765877	G345.0061+01.7944A	254.1926	-40.2402	16.5	14.5	13.4	2.5	5893	3.0	0.3	0.1	0.6	0.7
515647114260	G345.0061+01.7944A	254.1913	-40.2402	17.4	15.1	13.6	5.4	13067	15.5	0.3	0.1	0.6	0.8
515640947981	G345.1876+01.0308	255.1274	-40.571	18.7	14.0	11.6	7.8	18649	14.5	0.7	0.1	4.3	6.0
515640255500	G345.1876+01.0308	255.1266	-40.5725	13.2	12.6	11.7	3.0	7154	2.6	0.6	0.4	0.8	0.7
515633756325	G345.2619-00.4188A	256.7105	-41.3962	13.9	12.9	11.4	8.0	21541	15.9	1.0	0.5	1.4	1.1
515634485770	G345.2619-00.4188B	256.7124	-41.3979	17.8	13.4	11.2	8.0	21541	3.1	1.2	0.1	6.6	9.3

Survey ID	Primary RMS ID	RA (deg)	Dec (deg)	J	H	K	Sep. (arcsec)	$\mathrm{Sep_{phys}}$ (au)	$\mathrm{P_{chance}}$ (%)	$q_{fg,K}$	$q_{fg,J}$	$q_{tot,K}$	$q_{tot,J}$
515646564826	G345.3974+01.5091A	254.8032	-40.1107	13.0	12.6	11.1	8.1	19448	4.7	1.1	0.6	1.3	0.9
515647269972	G345.4938+01.4677	254.9248	-40.0626	18.1	14.3	11.4	4.0	9604	1.6	0.2	0.0	0.7	0.7
515647269969	G345.4938+01.4677	254.9257	-40.0636	17.9	14.7	12.1	8.1	19349	9.9	0.1	0.0	0.5	0.4
515646810510	G345.4938+01.4677	254.9243	-40.0635	17.5	15.2	13.7	5.5	13189	18.5	0.1	0.0	0.2	0.2
515643998179	G346.9409-00.3142	257.9208	-39.9836	11.9	11.9	11.1	9.6	14384	14.7	0.6	0.5	0.6	0.5
515644623690	G347.0775-00.3927	258.1107	-39.9232	15.2	12.3	10.8	9.4	15971	1.1	0.7	0.2	2.2	2.9
515669321651	G347.9023+00.0481A	258.2717	-38.9924	13.9	12.7	12.1	2.6	8505	9.8	0.6	0.3	0.9	1.1
515669587487	G348.5477+00.3721A	258.4208	-38.2814	15.7	14.0	13.1	2.9	4387	11.4	0.8	0.4	1.5	1.9
515676021609	G349.1469-00.9765	260.2704	-38.5723	15.5	14.2	12.4	4.3	12127	8.8	0.8	0.3	1.3	1.0
515677327100	G349.1469-00.9765	260.2697	-38.5736		15.1	13.1	1.0	2883	0.9	0.6			

Appendix C

Gaia YSO Catalogue

Table C.1: Catalogue of all YSOs detected in the Gaia DR3 database. d_{RMS} is the RMS kinematic distance and L_{bol} is the RMS bolometric luminosity. The rest of the columns were part of data taken from the Gaia archive.

RMS ID	Gaia Source ID	d_{RMS} (kpc)	L_{bol} $L_{\odot}$	ϖ (mas)	μ_{α} (mas yr^{-1})	μ_{δ} (mas yr^{-1})	RV (kms^{-1})	G (mag)	BP-RP (mag)
G011.5001-01.4857	4094465750048582272	1.7	2217	0.216 ± 0.57	3.049 ± 0.566	0.07 ± 0.435		19.6	3.8
G012.7879-00.1786	4095715654253795712	2.4	5624	-0.042 ± 0.16	0.416 ± 0.184	-0.447 ± 0.147		18.1	4.6
G012.9090-00.2607	4095722874108019456	2.4	32072					18.7	2.1
G015.1288-00.6717	4098003634866306048	2.0	12191	0.539 ± 0.446	-0.243 ± 0.511	-1.986 ± 0.374		19.5	3.3
G017.0217+00.8442	4146613009566162432	2.1	540	0.061 ± 0.43	-0.204 ± 0.358	-1.553 ± 0.306		19.0	3.5
G018.1968-00.1709	4152546283548983808	10.6	5636	0.006 ± 0.287	-0.294 ± 0.307	0.091 ± 0.247		19.0	4.0
G020.5703-00.8017	4154666352463531264	3.2	2488	-0.048 ± 0.137	-0.032 ± 0.136	-2.02 ± 0.113		17.1	3.4
G020.7617-00.0638B	4154942501654989184	11.8	13395	0.208 ± 0.113	0.166 ± 0.12	0.887 ± 0.099		17.1	3.2
G020.7617-00.0638C	4154942501642616320	11.8	13103	0.258 ± 0.295	-3.714 ± 0.354	-5.996 ± 0.305		18.7	4.2
G023.8176+00.3841	4156713844937718528	4.5	3920	0.398 ± 1.706	-1.382 ± 1.684	-4.757 ± 1.411		20.6	2.3
G024.5206-00.2258	4252809653677424896							21.8	3.0
G028.7903+03.5450	4270236599432306560		564	1.542 ± 0.118	-0.177 ± 0.115	-8.211 ± 0.105		12.1	3.3
G028.7987+03.5103	4270235916532991104	0.7	345	2.037 ± 0.044	-0.106 ± 0.047	-6.154 ± 0.044		13.1	3.7
G030.4117-00.2277	4259104529532391936	4.9	2522	0.545 ± 0.677	-1.962 ± 0.604	-3.921 ± 0.583		19.9	2.8
G030.5942-00.1273	4259111637713229696	4.9	1989					20.8	3.2
G032.0518-00.0902	4266059696498164224	4.2	3402	0.626 ± 0.548	-2.344 ± 0.542	-4.347 ± 0.447		19.8	2.3
G034.0126-00.2832	4266888762623009536	12.9	31473	0.71 ± 0.124	2.32 ± 0.134	-6.68 ± 0.114		16.3	3.1
G034.0500-00.2977	4266890373232343168	12.9	22570	1.421 ± 0.077	1.489 ± 0.077	-7.03 ± 0.063		14.9	2.6
G034.5964-01.0292	4266811178332758528	1.1	229					20.6	2.5
G035.3778-01.6405	4268294694398321280	3.3	5891	0.424 ± 0.558	-0.518 ± 0.597	-2.439 ± 0.523		19.7	3.9
G035.8546+00.2663	4280693195531645824	2.0	1606	0.014 ± 0.239	-0.265 ± 0.245	-2.82 ± 0.235		18.8	3.9
G045.8164-03.8310	4308446999329032064							16.6	1.8
G049.2077+02.8863	4512807594894454912			0.679 ± 0.515	5.343 ± 0.031	-21.088 ± 0.029		19.5	0.1
G049.5993-00.2488	4319862060333767808	5.4	1806	-0.613 ± 1.237	-1.781 ± 1.378	-3.805 ± 1.098		20.7	3.0
G051.3617-00.0132	4322379396498886400	5.2	5415	-0.059 ± 0.1	-2.524 ± 0.087	-5.986 ± 0.088		16.2	4.9
G053.5343-00.7943	4323046868764065792	5.0	7348	-1.229 ± 1.121	0.082 ± 0.961	-4.834 ± 1.852		20.4	
G053.5671-00.8653	4323044120007789824	7.8	6926	0.786 ± 0.087	-1.409 ± 0.076	-5.354 ± 0.089		17.2	3.5
G056.4120-00.0277	1826022736244143104	9.3	22243	0.945 ± 0.568	-2.899 ± 0.506	-6.289 ± 0.666		20.0	3.6
G059.3614-00.2068	2020085606516364160	2.2	1019	-1.169 ± 1.478	-4.338 ± 1.046	-9.185 ± 1.419		20.6	3.0
G059.4657-00.0457	2020102721973255296	2.2	1032	0.411 ± 0.019	-1.583 ± 0.012	-5.173 ± 0.018		13.7	2.5
G064.8131+00.1743	2028373970018601088	8.2	89444	-0.501 ± 0.107	-2.258 ± 0.089	-3.7 ± 0.101		14.9	4.5
G073.6525+00.1944	2057378841908096384	11.2	101843	1.871 ± 1.743	-1.392 ± 1.53	-1.219 ± 2.284		20.7	3.2

RMS ID	Gaia Source ID	d_{RMS} (kpc)	L_{bol} $L_{\odot}$	ϖ (mas)	μ_{α} (mas yr^{-1})	μ_{δ} (mas yr^{-1})	RV (kms^{-1})	G (mag)	BP-RP (mag)
G073.6952-00.9996	2057078507727080576	7.4	16547					20.5	3.5
G074.0364-01.7133	2056390037354772992	1.4	510					21.4	3.1
G077.5671+03.6911	2062501741455086720	5.7	4533	0.109 ± 0.071	-3.929 ± 0.069	-4.518 ± 0.075		17.2	2.4
G078.1224+03.6320	2062619427869074560	1.4	3967	0.243 ± 0.236	-3.966 ± 0.273	-5.255 ± 0.3		19.2	3.2
G078.8699+02.7602	2068392276220214272	1.4	6505	1.462 ± 0.138	-1.093 ± 0.14	-6.774 ± 0.163		13.1	3.5
G080.1909+00.5353	2067766757181346560	1.4	2315					20.9	3.4
G080.9340-00.1880	2066325847192286720			0.65 ± 0.072	-1.951 ± 0.075	-4.394 ± 0.079		15.5	4.8
G081.4650+00.5892	2069414925111096192	1.4	364	0.496 ± 0.045	-2.176 ± 0.047	-4.237 ± 0.048		13.8	3.3
G082.1735+00.0792	2066481011474619392	1.4	527	0.7 ± 0.16	-2.287 ± 0.161	-2.726 ± 0.182		18.8	4.2
G082.5682+00.4040A	2066562310912751360	1.4	2787	0.191 ± 0.085	-2.762 ± 0.09	-4.772 ± 0.097		16.8	3.6
G082.5687+00.1917	2066557019513454080	1.1	431	1.265 ± 0.269	-4.787 ± 0.807	-2.296 ± 0.628		19.3	3.5
G083.6748+00.3053	2066940886514158848			1.384 ± 0.018	-1.68 ± 0.018	-2.098 ± 0.022		11.7	0.8
G083.8536+00.1434	2067031939819593600			1.173 ± 0.015	-1.375 ± 0.015	-2.073 ± 0.015		11.0	1.1
G084.4678-00.1344	2066869246454772224	1.4	2145	1.243 ± 0.039	-2.197 ± 0.048	-3.935 ± 0.052		16.0	2.2
G085.4597-01.0466	2162235662383047040			1.102 ± 0.023	-2.701 ± 0.026	-4.088 ± 0.027		11.5	2.4
G090.7764+02.8281	2169346856897877120	1.7	778	0.249 ± 1.026	-3.417 ± 0.906	-4.583 ± 1.256		20.7	2.6
G093.7587-04.6377	1977788979043015808	-1.0	113	1.448 ± 0.076	-4.202 ± 0.09	-2.81 ± 0.079		15.9	4.7
G094.6028-01.7966	1979222432974084480	4.9	28459	0.58 ± 0.112	-4.826 ± 0.132	-3.292 ± 0.127		12.2	2.5
G095.0531+03.9724	2176941419942083840	8.7	12374	-0.923 ± 0.654	-1.616 ± 1.056	-2.952 ± 0.938		20.6	1.6
G096.4353+01.3233A	2174213222354872576	7.0	9659	0.395 ± 0.304	-1.706 ± 0.317	-2.809 ± 0.312		19.2	2.3
G099.9881+03.0733	2178253687063658112	-1.0	131					19.6	2.8
G100.0141+02.3591	2175212888880239232	5.9	1348	0.193 ± 0.117	-1.948 ± 0.145	-2.716 ± 0.146		17.6	2.5
G100.1685+02.0266	2199165337365192960	5.9	8374	-0.182 ± 0.569	-2.077 ± 0.609	-3.016 ± 0.748		20.3	3.1
G100.2124+01.8829	2198977149085902208	5.9	8303	0.269 ± 0.414	-1.992 ± 0.623	-2.348 ± 0.414		19.7	
G101.2490+02.5764	2199376237451547008	6.1	4319	-0.22 ± 0.251	-2.222 ± 0.278	-3.091 ± 0.297		19.2	3.7
G102.3533+03.6360	2202523035433771776	8.4	107012	-0.761 ± 0.23	-6.994 ± 0.271	-1.857 ± 0.272		18.0	3.1
G107.6823-02.2423A	2010084796654091904	4.7	4144	1.003 ± 0.426	-4.138 ± 0.454	-3.522 ± 0.391		19.5	3.1
G110.0931-00.0641	2013653570870795136	4.3	16938					19.4	2.8
G111.2980-00.6606	2013835540048868480	3.5	3278	0.329 ± 0.02	-2.756 ± 0.022	-1.701 ± 0.021		13.9	2.6
G111.8904+00.9894	2014971399976660224	2.7	6629	2.402 ± 0.468	-0.71 ± 0.544	-0.239 ± 0.525		19.7	3.4
G114.5696+00.2899	2015551942114291968	2.5	860	1.554 ± 0.359	-6.863 ± 0.359	-0.443 ± 0.345		18.3	2.5
G117.7628-03.6445	422993981619055104	-1.0	1245					15.7	1.7
G117.7657-03.6355	422994084698268288	-1.0	1375	-4.25 ± 0.675	10.324 ± 0.596	-11.542 ± 0.623		17.3	2.4
G118.3717+03.1657	432259531738647296		1	-0.68 ± 0.461	-0.933 ± 0.517	-5.56 ± 0.473		16.2	2.8
G120.1483+03.3745	527470435475220608	5.6	20905	0.259 ± 0.191	-2.479 ± 0.197	0.16 ± 0.187		18.8	4.6
G121.2958+00.6563	430854115370063360	1.0	1018	0.997 ± 0.076	-0.766 ± 0.071	-0.761 ± 0.08		16.8	4.7

RMS ID	Gaia Source ID	d_{RMS} (kpc)	L_{bol} $L_{\odot}$	ϖ (mas)	μ_{α} (mas yr^{-1})	μ_{δ} (mas yr^{-1})	RV (kms^{-1})	G (mag)	BP-RP (mag)
G121.3479-03.3705	425522617840975488	3.0	1114	0.643 ± 0.391	-2.789 ± 0.485	-0.94 ± 0.296		18.6	
G123.2836+03.0307	526085531867871104	4.9	4280	0.259 ± 0.149	-0.839 ± 0.138	-0.123 ± 0.164		17.4	3.4
G123.8059-01.7805	426650029585407232	2.2	2376	0.354 ± 0.142	-2.38 ± 0.127	-1.207 ± 0.161		18.2	2.5
G125.7795+01.7285	524784289915687808	5.2	5427	0.172 ± 0.112	-1.708 ± 0.096	0.219 ± 0.121		17.9	3.9
G126.4274-01.2348	510895778733066112	0.6	33	1.862 ± 0.456	-7.743 ± 0.422	-1.946 ± 0.554		19.1	3.3
G126.8863-01.0516	510723666503329792	0.5	658	1.086 ± 0.184	-2.765 ± 0.147	-1.628 ± 0.167		18.5	4.5
G135.2774+02.7981	466047691568443904	6.0	28561					20.6	3.2
G136.3833+02.2666A	465748353819938944	3.2	6580					20.9	2.6
G136.5370+02.8934	467286433154722432	3.9	1222	0.271 ± 0.227	-0.548 ± 0.228	-0.031 ± 0.229		18.4	2.9
G136.9162+01.0849	464874035924528896							20.8	2.9
G139.9091+00.1969A	460477535597141632	3.2	11373					20.1	3.1
G141.9996+01.8202	450155767107967616	0.8	5542					18.8	4.6
G144.6678-00.7136	448158637380242304	2.0	365	0.104 ± 0.25	-0.367 ± 0.262	-2.598 ± 0.279		18.2	3.2
G150.6862-00.6887	250753320461058432	1.9	186	0.296 ± 0.026	-0.378 ± 0.03	-1.362 ± 0.023		14.7	2.4
G151.6120-00.4575	271698261059431424	6.4	60777	0.992 ± 0.112	-0.634 ± 0.128	0.639 ± 0.089		16.0	4.0
G167.6904-00.6315	188262538442656512	1.7	605	0.21 ± 0.027	-0.054 ± 0.033	-1.625 ± 0.022		12.8	0.8
G168.0627+00.8221	188633249953059328	2.0	10667	0.342 ± 0.169	0.714 ± 0.207	-0.35 ± 0.153		18.1	3.0
G173.4839+02.4317	3455765634510718464	2.0	2932	1.447 ± 0.213	0.292 ± 0.207	-2.111 ± 0.133		18.1	4.7
G174.1974-00.0763	3449181243491690112	2.0	5892	0.475 ± 0.132	0.054 ± 0.144	-1.939 ± 0.098		17.1	2.7
G177.7291-00.3358	3447561250543288192	2.0	2344	0.946 ± 0.222	0.424 ± 0.232	-2.869 ± 0.163		16.7	3.0
G182.4185-04.0399	3416747570320423552			6.695 ± 0.06	2.987 ± 0.061	-26.364 ± 0.042	31.4	10.2	1.2
G183.4530-01.7774	3428627900834658304	2.0	676					20.0	1.7
G183.7203-03.6647	3404437884812331904	2.0	1088	0.791 ± 0.253	0.165 ± 0.33	-2.195 ± 0.19		18.7	4.3
G184.8704-01.7329	3427704139268092544	2.0	1984	-3.051 ± 0.503	1.644 ± 0.643	-9.493 ± 0.379		14.0	1.5
G185.0090-03.9329	3403535563721314944	1.1	271	0.716 ± 0.024	0.114 ± 0.029	-1.999 ± 0.016		12.1	2.2
G192.6240-03.0385	3349288614945575680	0.2	13	1.315 ± 0.049	-0.328 ± 0.046	-5.296 ± 0.032		9.5	0.2
G201.3419+00.2914	3327886213092092800	-1.0	1107	3.171 ± 0.415	-1.105 ± 0.395	-5.038 ± 0.344		14.0	2.8
G202.9943+02.1040	3326715851681467904	0.3	20	1.414 ± 0.111	-1.076 ± 0.14	-3.826 ± 0.125		12.8	0.4
G203.3166+02.0564	3326686680263989376	0.6	1750					20.7	2.9
G203.7637+01.2705	3326498762563125376	0.8	483					13.8	1.4
G212.0641-00.7395	3113532435523229824	4.7	16183					20.9	3.1
G212.2344-03.5038	3118953027852550144	4.9	2475	0.277 ± 0.283	-0.293 ± 0.327	-1.788 ± 0.287		18.4	3.3
G212.9626+01.2954	3113711174889182976	4.2	1305	1.685 ± 0.182	-4.616 ± 0.203	1.791 ± 0.166		17.8	1.7
G213.9180+00.3786	3112486215855278464	3.9	1164					21.4	2.3
G217.0441-00.0584	3102590783007047296	5.3	8634	0.381 ± 0.201	-0.495 ± 0.221	1.257 ± 0.21		15.7	2.0
G220.4587-00.6081	3052559911559854208	2.2	2076	0.359 ± 0.1	-1.285 ± 0.115	1.102 ± 0.108		15.4	2.5

RMS ID	Gaia Source ID	d_{RMS} (kpc)	L_{bol} $L_{\odot}$	ϖ (mas)	μ_{α} (mas yr^{-1})	μ_{δ} (mas yr^{-1})	RV (kms^{-1})	G (mag)	BP-RP (mag)
G220.7565-02.1557	3051085844432140160			0.791 ± 0.028	-2.319 ± 0.026	1.094 ± 0.024		13.5	2.5
G221.0108-02.5073	3050858829639283328	0.8	132					20.6	
G222.4278-03.1357	3049851810127658496	0.6	147	0.928 ± 0.034	-2.788 ± 0.034	1.027 ± 0.036		14.9	2.4
G224.6065-02.5563	3046019775884203392	0.8	1180	2.035 ± 0.632	-4.839 ± 0.605	3.831 ± 0.526		9.0	1.7
G231.7986-01.9682	2931756259785199744	3.2	5608	0.387 ± 0.026	-1.485 ± 0.023	2.25 ± 0.023		12.8	2.3
G231.8652-02.0469	2931720182059980928	3.1	1376	1.927 ± 1.385	-0.41 ± 1.055	4.741 ± 0.914		19.9	2.9
G233.8306-00.1803	3026531890059168000	3.3	13121	1.702 ± 0.551	-2.933 ± 0.484	0.343 ± 0.566		19.5	3.1
G242.9402-00.4501	5601822769256910848	5.1	3196					19.3	2.5
G259.6695-01.3181	5526896927347784064	5.5	730					21.0	2.9
G259.7743-02.8799	5527205099835106688	0.9	263	1.676 ± 0.461	-5.824 ± 0.497	5.112 ± 0.489		16.0	1.1
G260.6877-01.3930	5526614249777593600	6.3	2956	0.221 ± 0.124	-3.173 ± 0.13	3.872 ± 0.147		18.2	3.5
G260.7658+00.6604	5525309404347345664			1.073 ± 0.04	-5.285 ± 0.044	3.324 ± 0.044		13.0	2.7
G260.7952+00.9182	5525337338813640192	0.7	264	0.435 ± 0.048	-6.394 ± 0.054	3.218 ± 0.055		15.6	2.4
G263.5846-03.9973	5522569524461191936	11.7	5939	0.179 ± 0.646	2.371 ± 0.757	2.198 ± 0.76		20.0	3.2
G263.5994-00.5236	5523960750257359232	0.7	199	0.349 ± 0.041	-4.596 ± 0.044	5.066 ± 0.045		15.9	3.4
G263.7521-00.3981	5523769916271763200			0.443 ± 0.011	-4.373 ± 0.012	7.338 ± 0.011		12.8	1.0
G264.5994-00.2460	5331549303478263680	0.7	227	1.704 ± 1.312	0.012 ± 1.261	2.549 ± 1.157		20.8	2.9
G265.1118-00.9300	5331492335031777536	3.2	434	1.207 ± 0.278	-1.459 ± 0.3	5.604 ± 0.213		19.3	2.5
G265.1438+01.4548	5331829305277838080	0.7	719	0.865 ± 0.163	-6.627 ± 0.175	3.973 ± 0.179		18.4	4.7
G265.3344+01.3916	5331811541293168640	0.7	49	2.086 ± 0.583	-7.387 ± 0.559	3.46 ± 0.669		20.3	2.7
G265.4642+01.4561	5331807555564175104	0.7	88	1.04 ± 0.159	-7.466 ± 0.161	3.715 ± 0.205		18.4	4.6
G267.7336-01.1058A	5330100769921829760	0.7	186	0.647 ± 0.15	-5.056 ± 0.16	4.348 ± 0.159		18.5	3.6
G267.9094+01.7816	5327717337954243328	0.7	162	0.834 ± 0.269	-8.049 ± 0.284	4.339 ± 0.272		18.9	4.3
G268.0288-01.0876	5330036242333302784			0.553 ± 0.016	-5.208 ± 0.019	4.883 ± 0.019		14.4	2.6
G268.3957-00.4842	5327053056831739264	0.7	3011	1.136 ± 0.216	-5.78 ± 0.203	0.95 ± 0.234		19.3	2.4
G269.1586-01.1383A	5326929155613298944	0.7	233	0.101 ± 0.184	-5.2 ± 0.218	3.342 ± 0.214		18.7	
G281.7578-02.0132	5259241123865464576	7.0	3559	0.829 ± 0.305	-5.331 ± 0.365	3.908 ± 0.326		19.5	3.3
G282.2988-00.7769	5258914706349974656	3.7	4049	0.614 ± 0.023	-5.244 ± 0.027	3.105 ± 0.024		12.7	2.4
G282.3764-01.8292	5258486657044928128							20.9	3.4
G282.6997-03.1668	5256807737168546048			0.443 ± 0.022	-6.362 ± 0.026	4.102 ± 0.024		10.4	1.3
G282.7848-01.2869	5258812043756451712	7.0	5604	0.172 ± 0.109	-5.137 ± 0.128	3.357 ± 0.118		17.7	4.9
G286.1626-00.1877A	5350681978349036288	2.3	187	0.383 ± 0.053	-6.82 ± 0.061	2.997 ± 0.066		15.7	2.6
G287.3716+00.6444	5350910367543366144	4.5	17887	-0.042 ± 0.051	-4.97 ± 0.057	2.687 ± 0.055		15.3	2.9
G287.6790-00.8669	5350302131442511360	2.5	1410	0.319 ± 0.095	-7.069 ± 0.115	1.779 ± 0.098		17.5	2.0
G287.8768-01.3618	5254210067899430016	6.1	18747	0.505 ± 0.351	-3.716 ± 0.412	0.059 ± 0.368		19.9	1.9
G288.9865+00.2533	5338737983510517632	5.7	958	0.149 ± 0.03	-5.833 ± 0.033	2.496 ± 0.03		15.9	2.4

RMS ID	Gaia Source ID	d_{RMS} (kpc)	L_{bol} $L_{\odot}$	ϖ (mas)	μ_{α} (mas yr^{-1})	μ_{δ} (mas yr^{-1})	RV (kms^{-1})	G (mag)	BP-RP (mag)
G289.1447-00.3454	5338323501993373184	7.6	3617	-0.549 ± 0.24	-5.8 ± 0.28	2.486 ± 0.263		18.5	
G290.0105-00.8668A	5337957222882584832	8.4	7134	0.15 ± 0.085	-5.795 ± 0.092	2.404 ± 0.092		17.6	2.1
G290.3745+01.6615	5339406246100051712	2.9	15078					20.4	
G294.5117-01.6205	5333595906936360576	2.6	9793	1.058 ± 0.349	-14.383 ± 0.37	-6.749 ± 0.345		19.9	2.0
G294.6168-02.3440	5333455448635878912	1.6	576	1.185 ± 1.867	-2.121 ± 1.696	4.451 ± 2.005		20.9	3.9
G296.2654-00.3901	5334625049823695744	8.1	4850	0.111 ± 0.46	-5.562 ± 0.532	1.674 ± 0.5		19.8	3.3
G300.3412-00.2190	6053804580395068928	4.2	5970	-0.158 ± 0.801	-6.343 ± 0.831	1.385 ± 0.965		20.6	3.5
G301.1726+01.0034	6054730055619549696	4.3	20545	-0.054 ± 0.206	-6.024 ± 0.189	-0.305 ± 0.207		17.9	4.6
G301.8147+00.7808A	6055404541600960512	4.4	21580					19.8	3.4
G304.3674-00.3359A	5862383385556063616	11.8	94462	-0.052 ± 0.451	-6.681 ± 0.385	-0.199 ± 0.455			
G305.6327+01.6467	5869598891938198656	4.9	15684	0.377 ± 0.024	-8.145 ± 0.019	-1.737 ± 0.024	-44.6	12.0	3.2
G306.1160+00.1386A	5868474160269012224	4.0	1731	-1.232 ± 1.236	-8.139 ± 1.006	-2.647 ± 1.558		20.6	2.5
G306.1160+00.1386B	5868474164593028864	4.0	1078	0.451 ± 0.061	-4.192 ± 0.051	-2.206 ± 0.058		15.7	1.9
G308.7008+00.5312	5865765208465714688	4.0	975	0.646 ± 0.512	-5.769 ± 0.389	-1.868 ± 0.424		19.7	3.1
G316.9003-03.9788	5874385551385330176	0.7	167	1.223 ± 0.038	-3.052 ± 0.035	-3.855 ± 0.035		15.2	2.9
G317.0902-04.1984	5873625204766490240	0.7	61	1.159 ± 0.02	-2.726 ± 0.018	-3.642 ± 0.021		12.5	1.9
G320.2878-00.3069A	5880048998358907264	8.7	12242	0.37 ± 0.077	-6.558 ± 0.076	-3.224 ± 0.079		16.9	3.6
G326.7249+00.6159B	5885649150368873600	1.8	1560	0.871 ± 0.324	-3.782 ± 0.351	-3.256 ± 0.308		19.0	4.6
G328.2658+00.5316	5981086244260691328	2.7	1812	0.507 ± 1.074	-11.057 ± 1.0	-1.702 ± 0.865		19.9	3.5
G328.3442-00.4629	5980805834434317184	2.9	2380	0.309 ± 0.07	-3.222 ± 0.069	-2.738 ± 0.062		12.7	1.6
G328.9842-00.4361	5980832944271979392	4.7	1777	0.324 ± 0.202	-2.77 ± 0.234	-2.189 ± 0.164		18.6	4.2
G332.9457+02.3855	5983883474877678976	2.0	909	0.638 ± 0.064	-2.095 ± 0.075	-2.318 ± 0.054		16.3	3.6
G336.4917-01.4741B	5940861268530185984	2.0	12285					16.3	3.1
G336.5299-01.7344	5937854649654626944	1.8	2133					20.5	2.8
G338.9377-00.4890B	5943066339056145792	2.9	885	0.461 ± 0.568	-0.246 ± 0.741	-0.834 ± 0.508		19.8	2.0
G339.6816-01.2058	5940114700099258496	2.4	6469					20.4	3.0
G339.7602+00.0530A	5943223912816728960	12.0	7442	0.29 ± 0.181	-4.039 ± 0.213	-3.43 ± 0.16		18.0	4.3
G340.1537+00.5116	5943270813887668480	3.8	1064	0.813 ± 0.302	-3.032 ± 0.34	-2.487 ± 0.272		17.9	3.8
G344.9816+01.8252B	5969717775072198400	2.4	542					20.2	4.1
G347.8944-00.1713	5972322896068646784			0.368 ± 0.054	-1.421 ± 0.06	-6.622 ± 0.038		15.8	2.8
G348.5477+00.3721A	5973485427780779136	1.5	71					20.3	3.7
G349.5786-00.6798B	5972788745407702272	13.4	3458						

Appendix D

Sky plots of Gaia YSOs

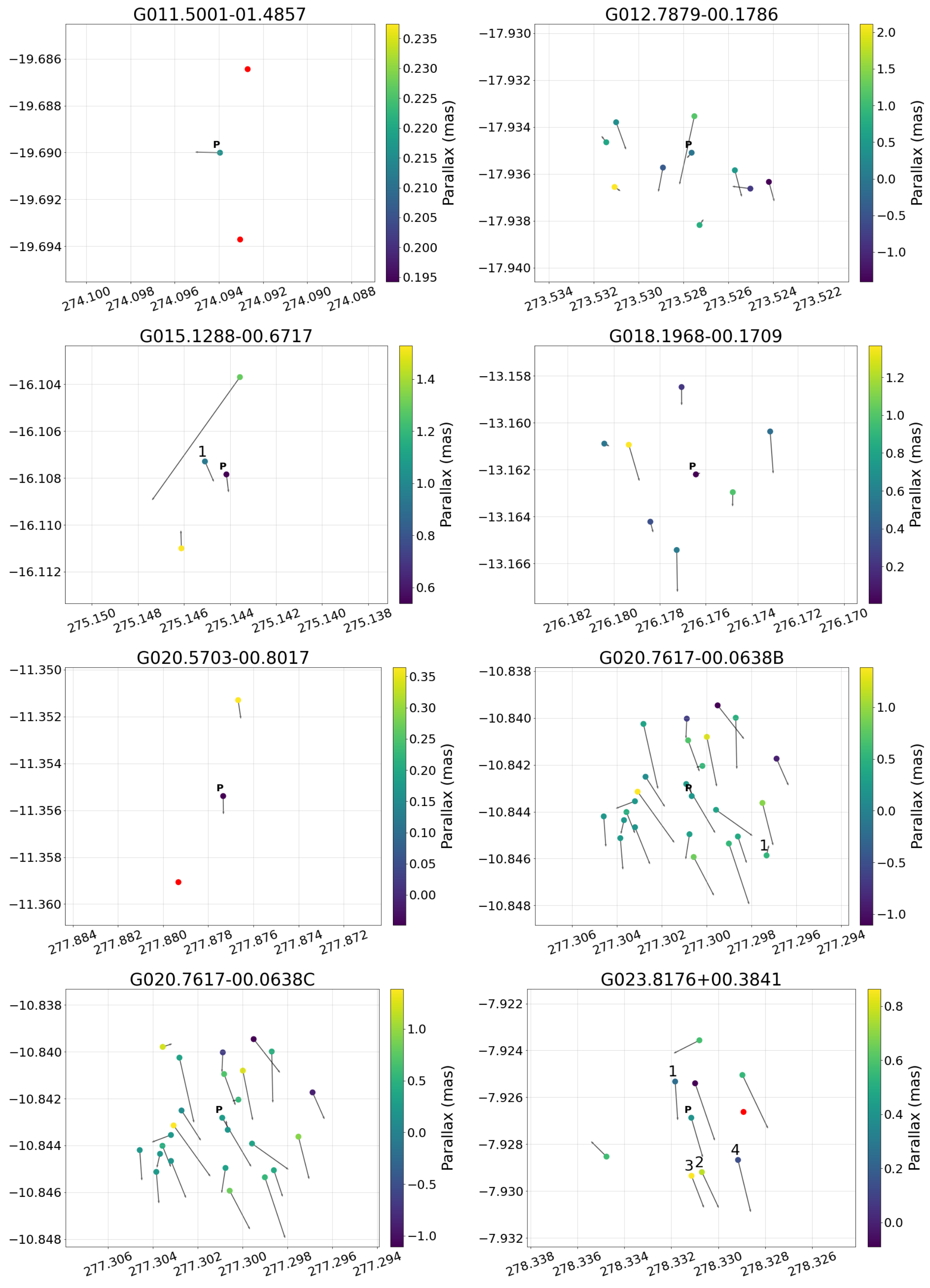

Figure D.1: Sky plots for YSOs observed in Gaia and their companions within a 15” radius. Primary YSO labelled as P. Companions labelled as numbers. RA is on the X-axis and Declination is on the Y-axis.

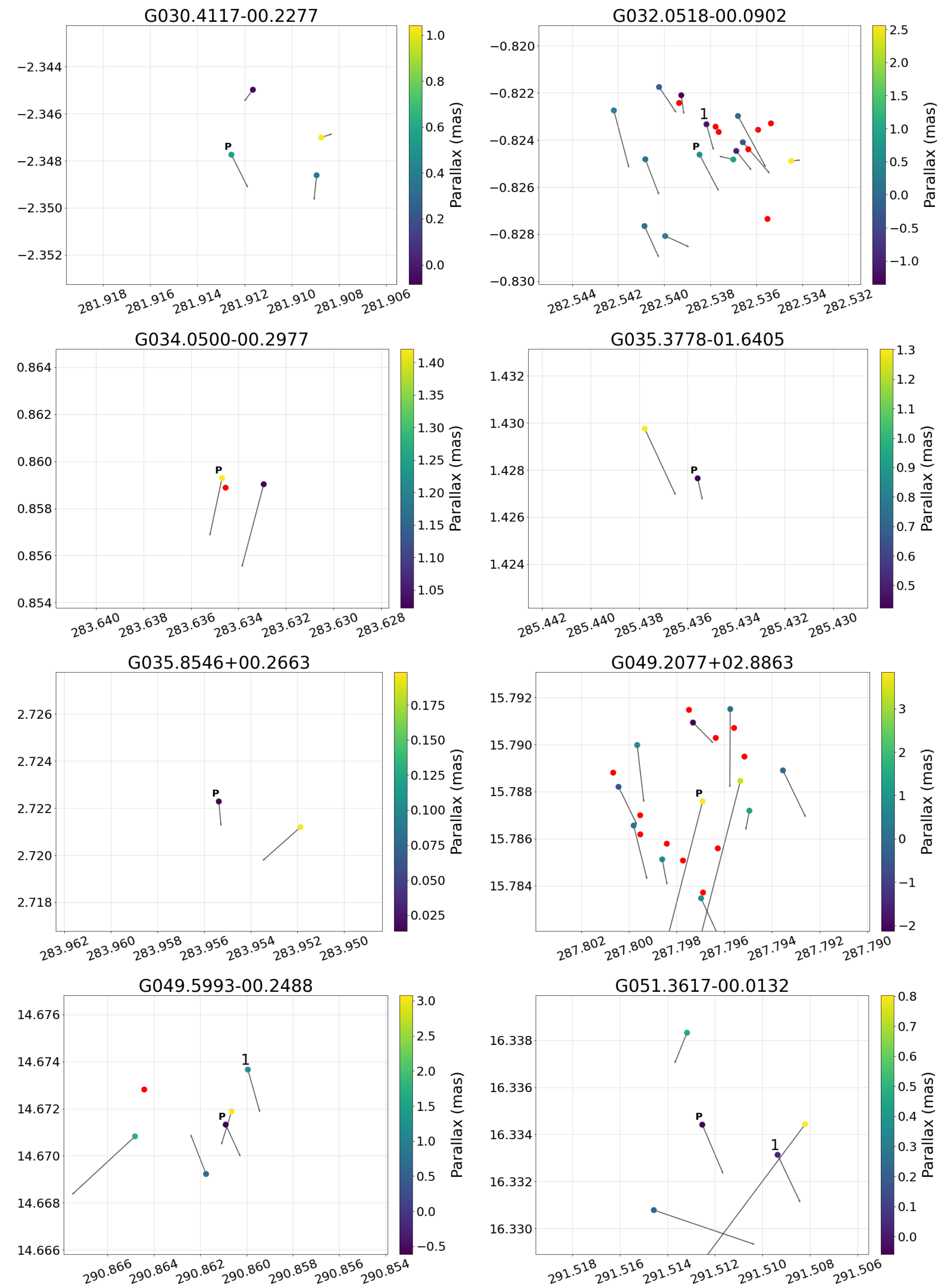

Figure D.2: Sky plots for YSOs observed in Gaia and their companions within a 15" radius. Primary YSO labelled as P. Companions labelled as numbers. RA is on the X-axis and Declination is on the Y-axis.

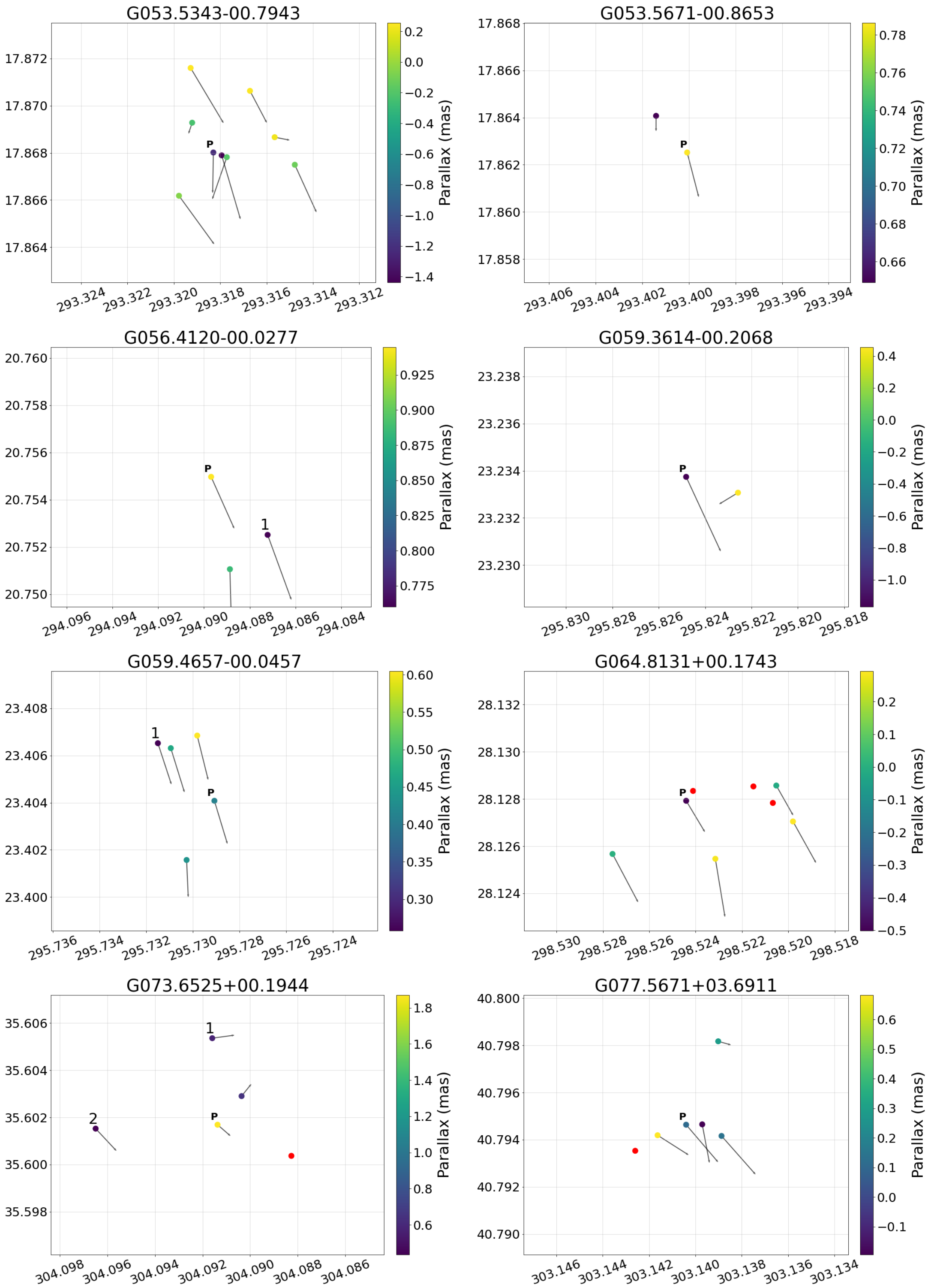

Figure D.3: Sky plots for YSOs observed in Gaia and their companions within a 15" radius. Primary YSO labelled as P. Companions labelled as numbers. RA is on the X-axis and Declination is on the Y-axis.

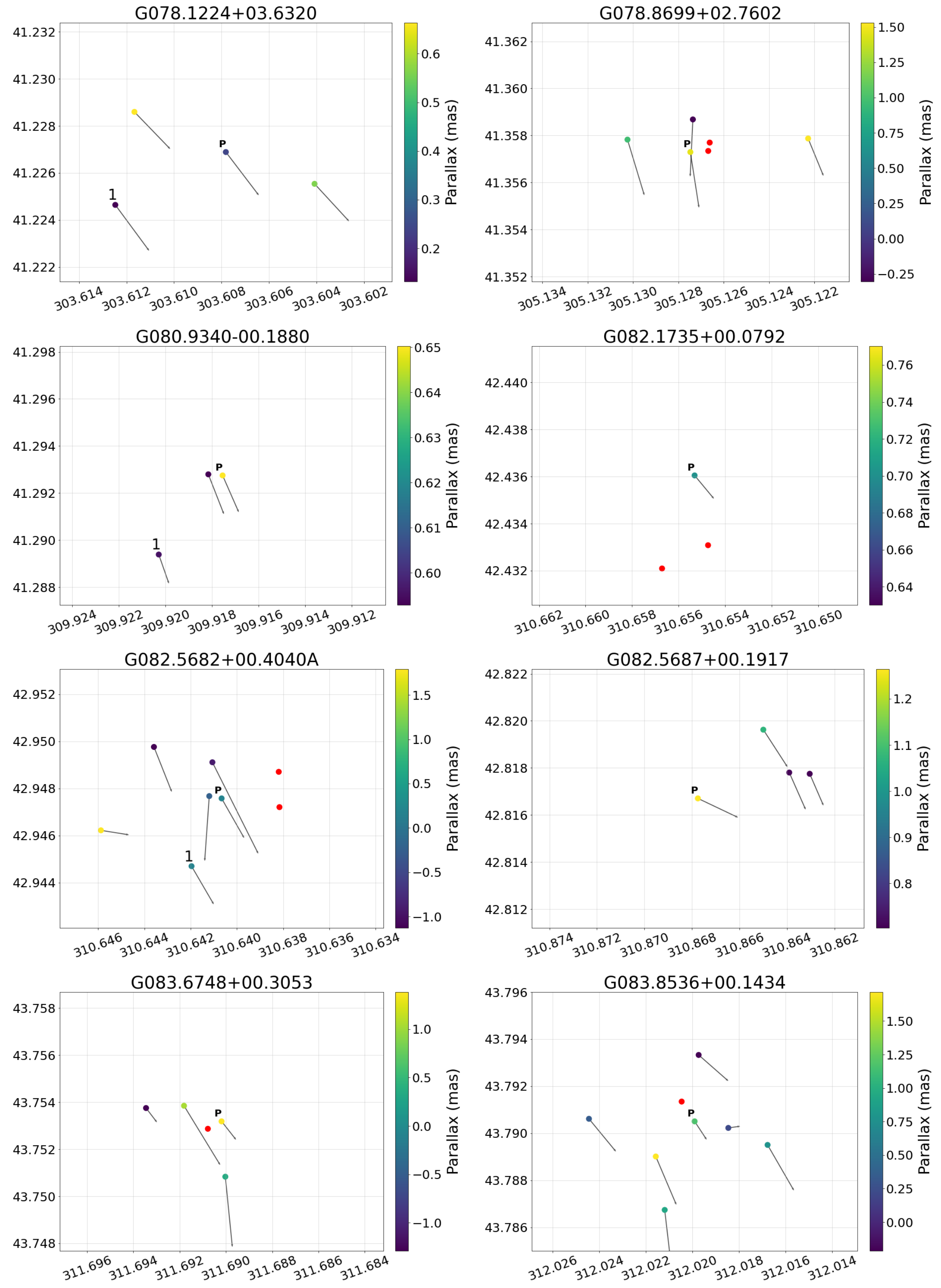

Figure D.4: Sky plots for YSOs observed in Gaia and their companions within a 15" radius. Primary YSO labelled as P. Companions labelled as numbers. RA is on the X-axis and Declination is on the Y-axis.

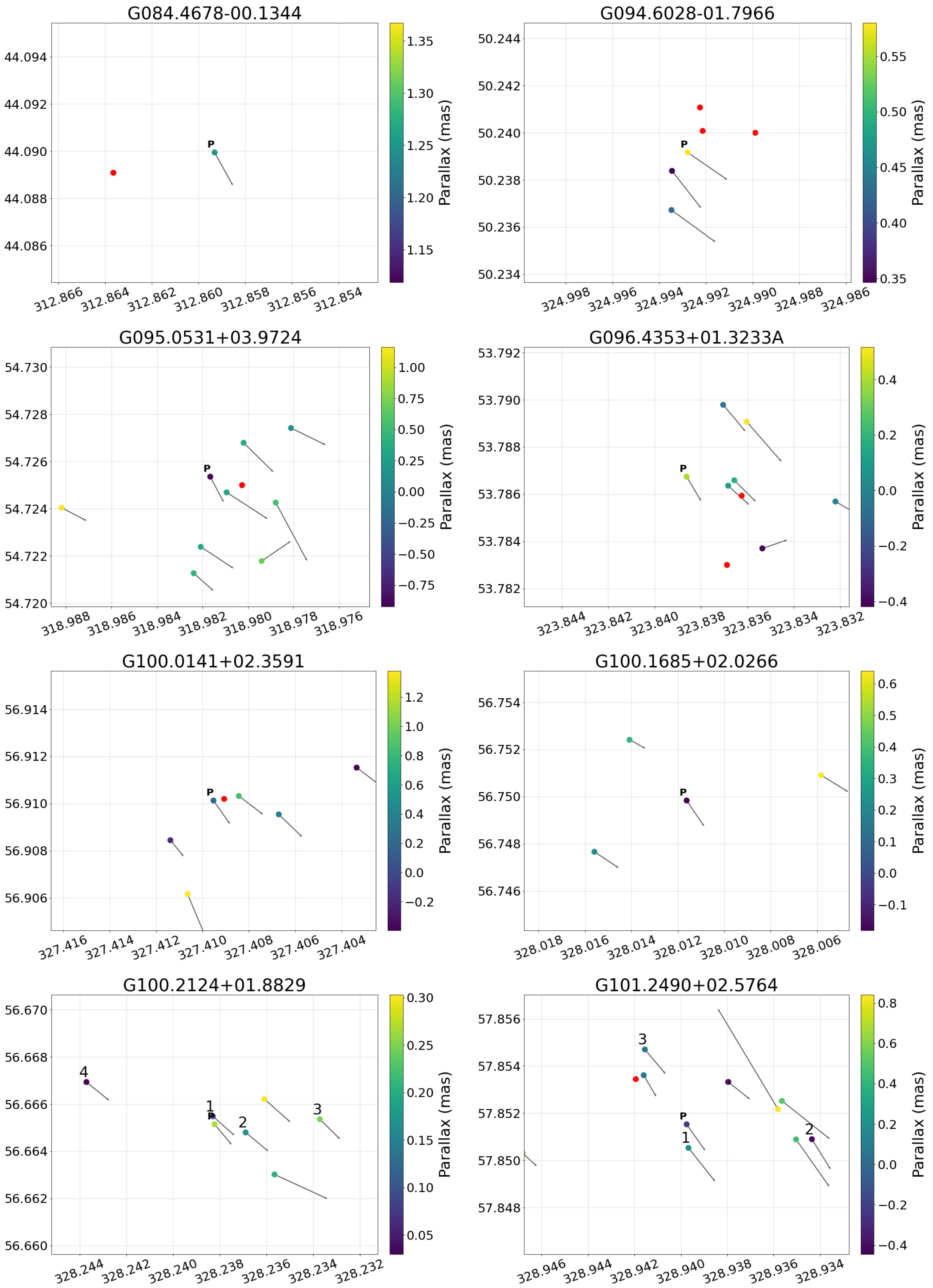

Figure D.5: Sky plots for YSOs observed in Gaia and their companions within a 15” radius. Primary YSO labelled as P. Companions labelled as numbers. RA is on the X-axis and Declination is on the Y-axis.

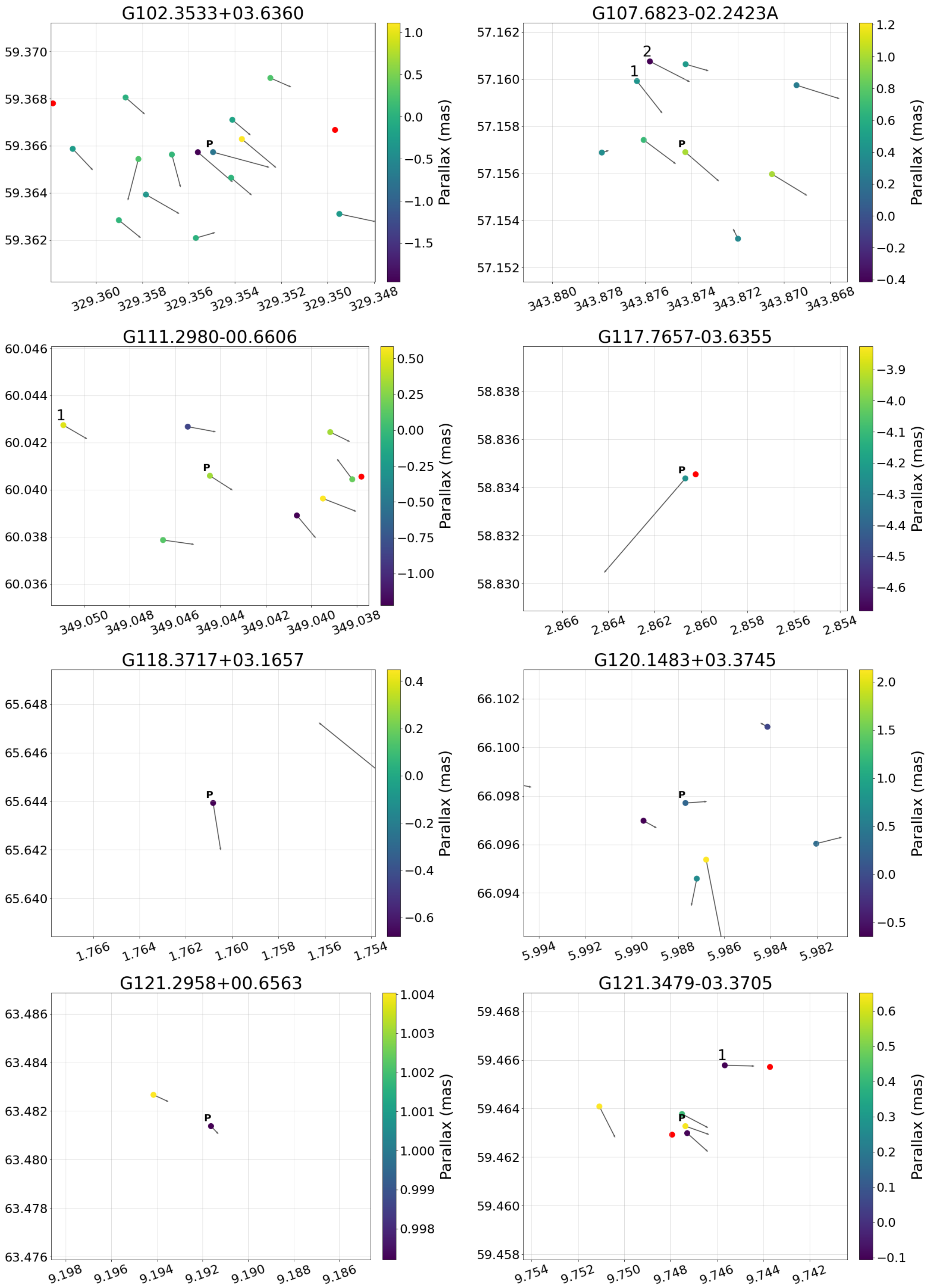

Figure D.6: Sky plots for YSOs observed in Gaia and their companions within a 15" radius. Primary YSO labelled as P. Companions labelled as numbers. RA is on the X-axis and Declination is on the Y-axis.

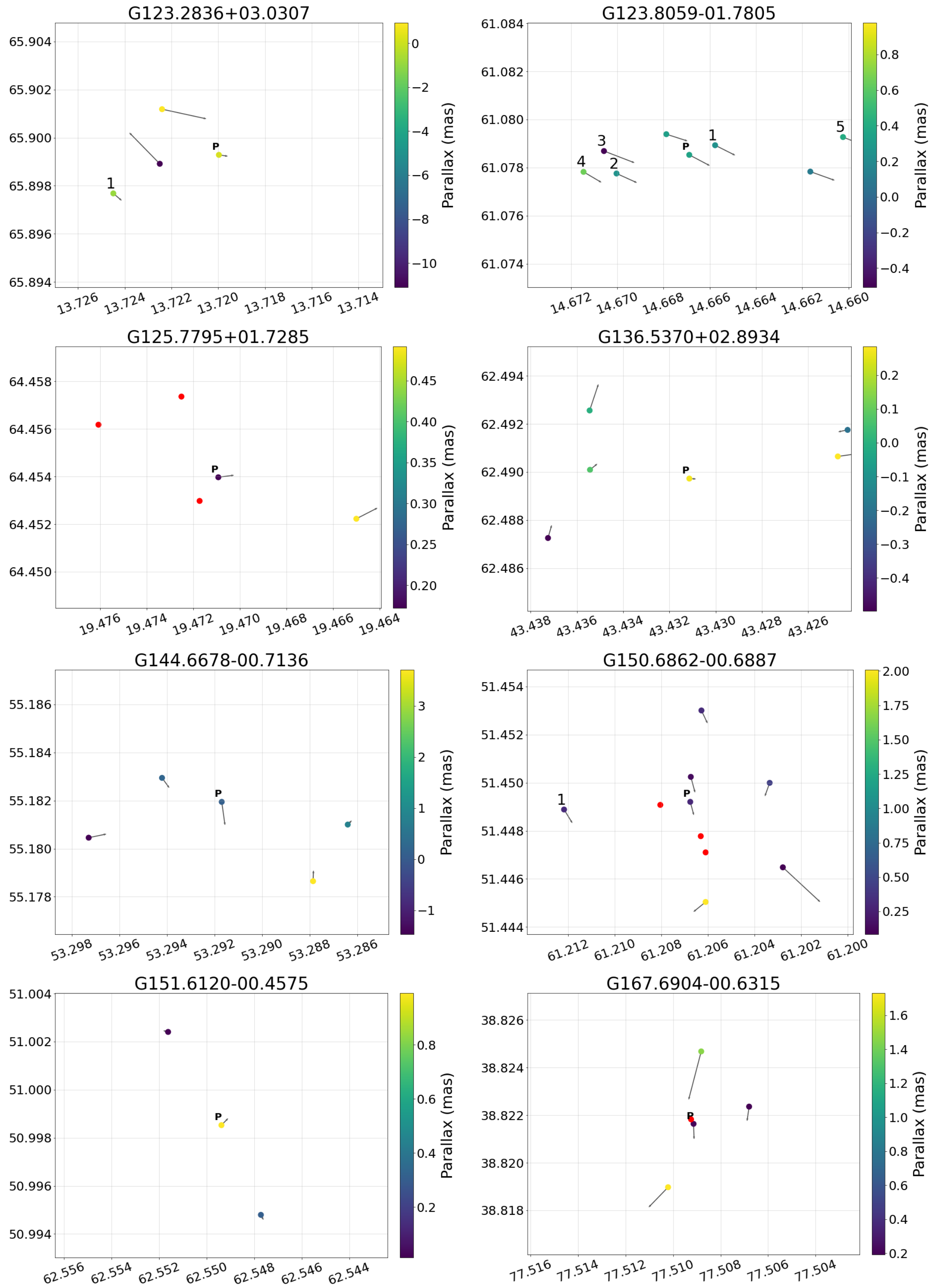

Figure D.7: Sky plots for YSOs observed in Gaia and their companions within a 15" radius. Primary YSO labelled as P. Companions labelled as numbers. RA is on the X-axis and Declination is on the Y-axis.

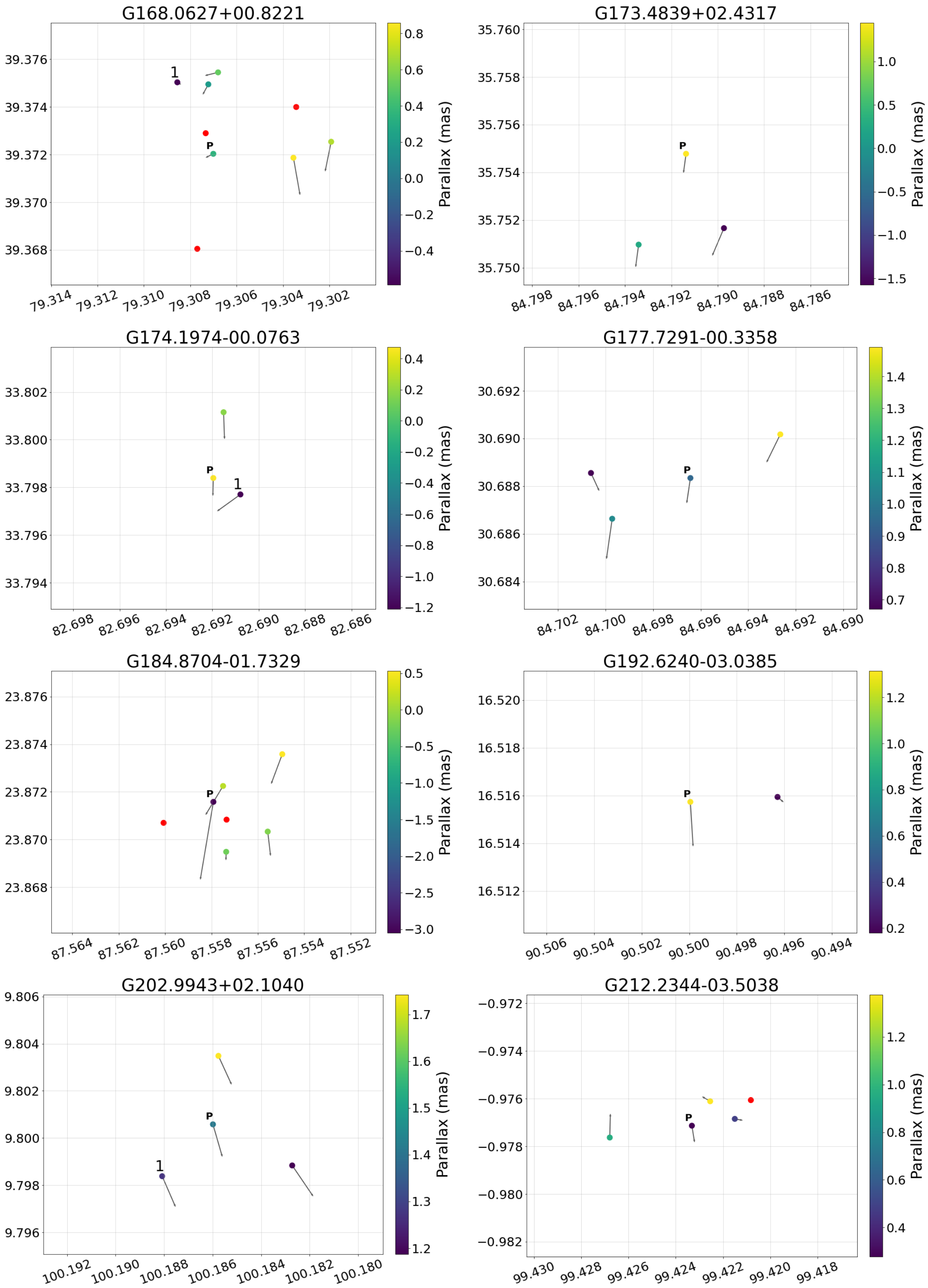

Figure D.8: Sky plots for YSOs observed in Gaia and their companions within a 15” radius. Primary YSO labelled as P. Companions labelled as numbers. RA is on the X-axis and Declination is on the Y-axis.

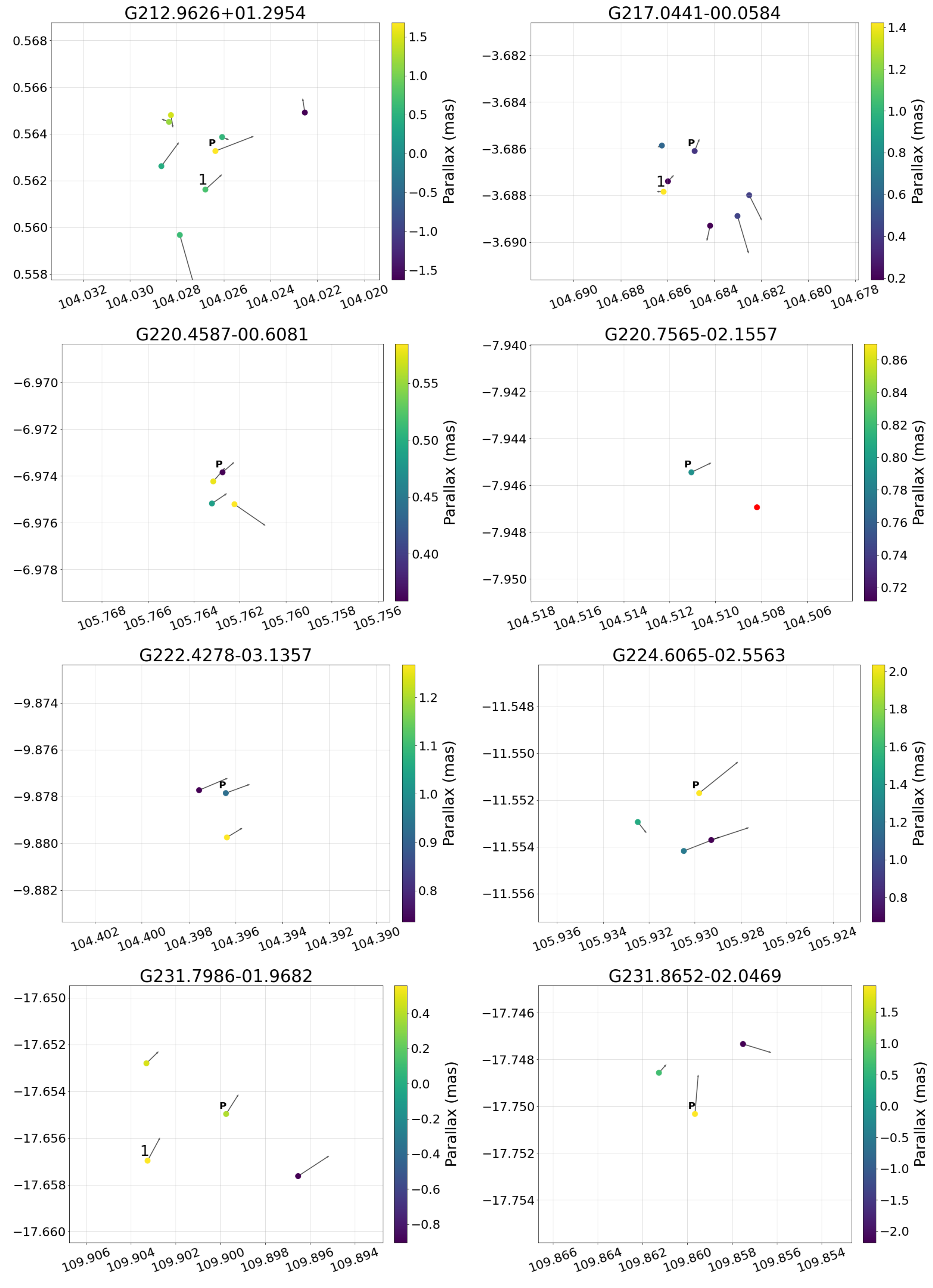

Figure D.9: Sky plots for YSOs observed in Gaia and their companions within a 15” radius. Primary YSO labelled as P. Companions labelled as numbers. RA is on the X-axis and Declination is on the Y-axis.

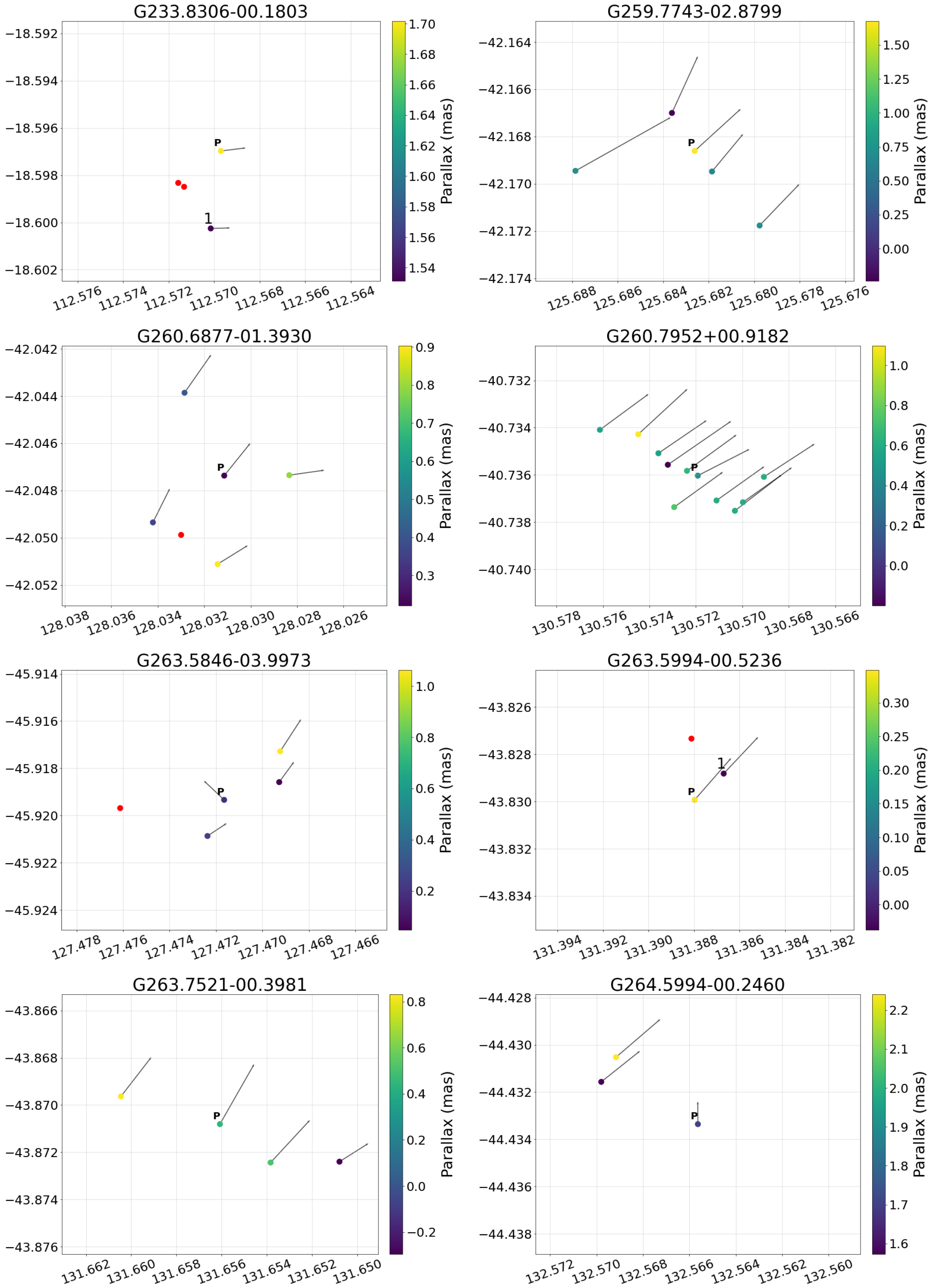

Figure D.10: Sky plots for YSOs observed in Gaia and their companions within a 15” radius. Primary YSO labelled as P. Companions labelled as numbers. RA is on the X-axis and Declination is on the Y-axis.

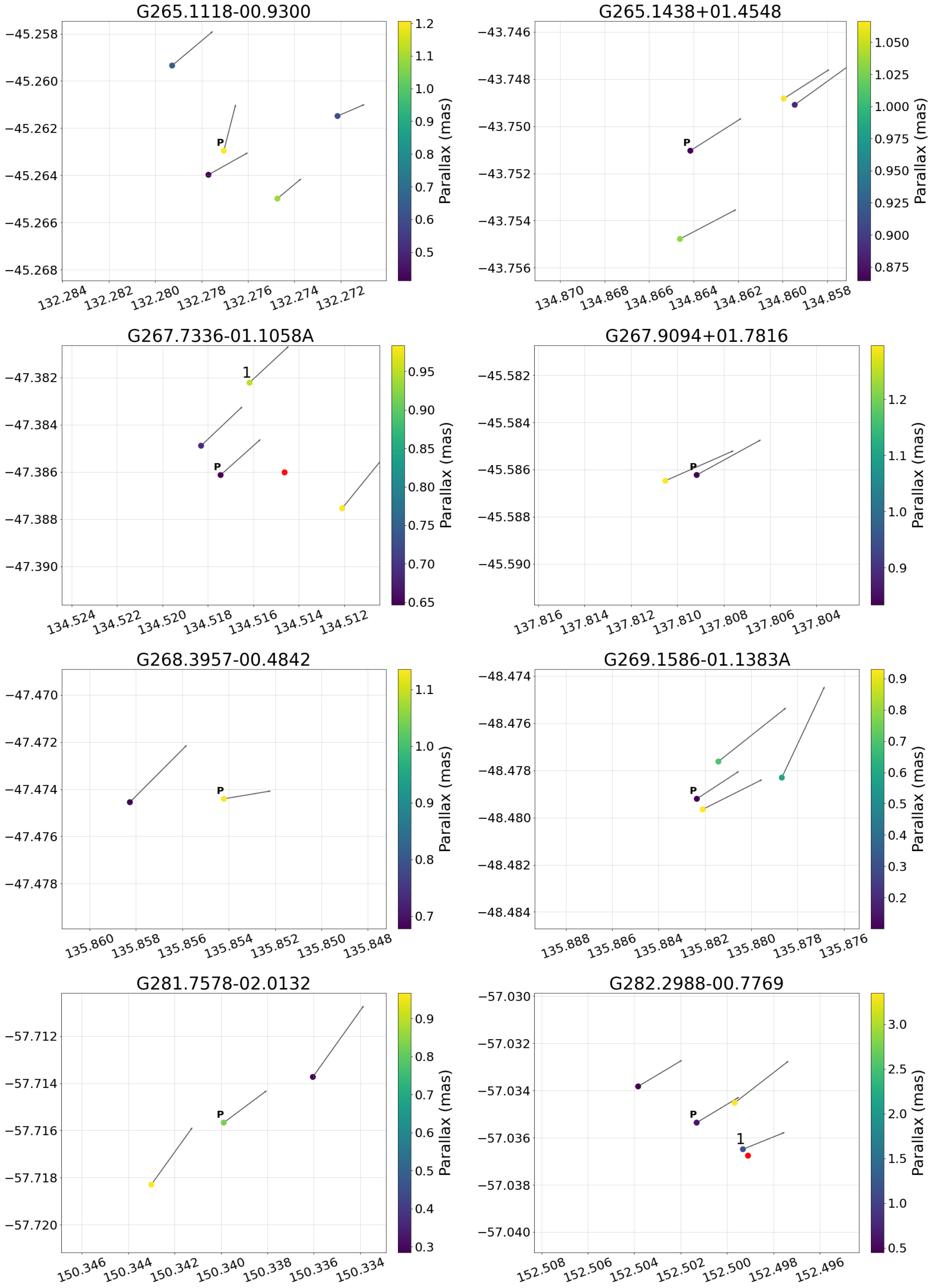

Figure D.11: Sky plots for YSOs observed in Gaia and their companions within a 15” radius. Primary YSO labelled as P. Companions labelled as numbers. RA is on the X-axis and Declination is on the Y-axis.

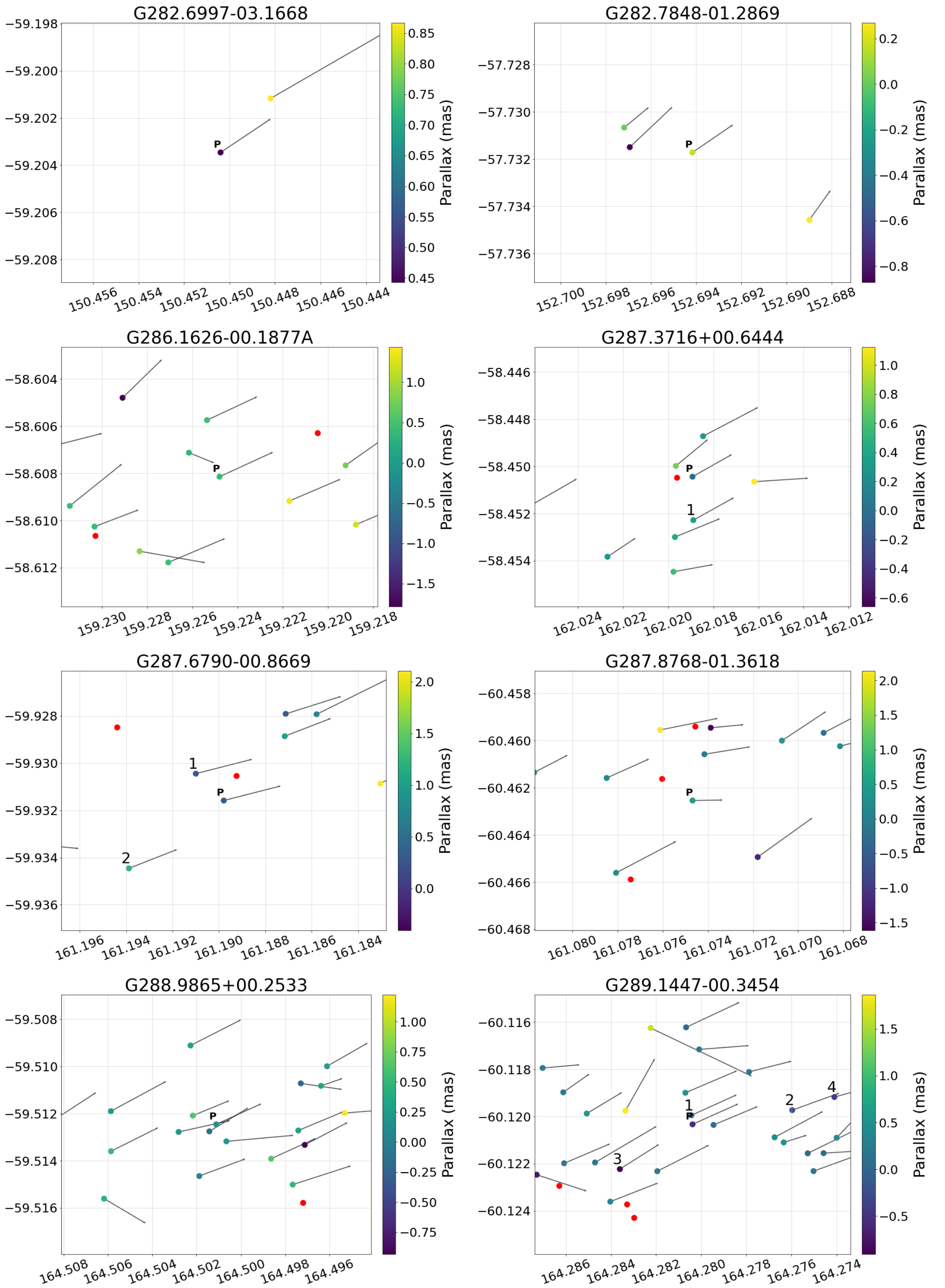

Figure D.12: Sky plots for YSOs observed in Gaia and their companions within a 15” radius. Primary YSO labelled as P. Companions labelled as numbers. RA is on the X-axis and Declination is on the Y-axis.

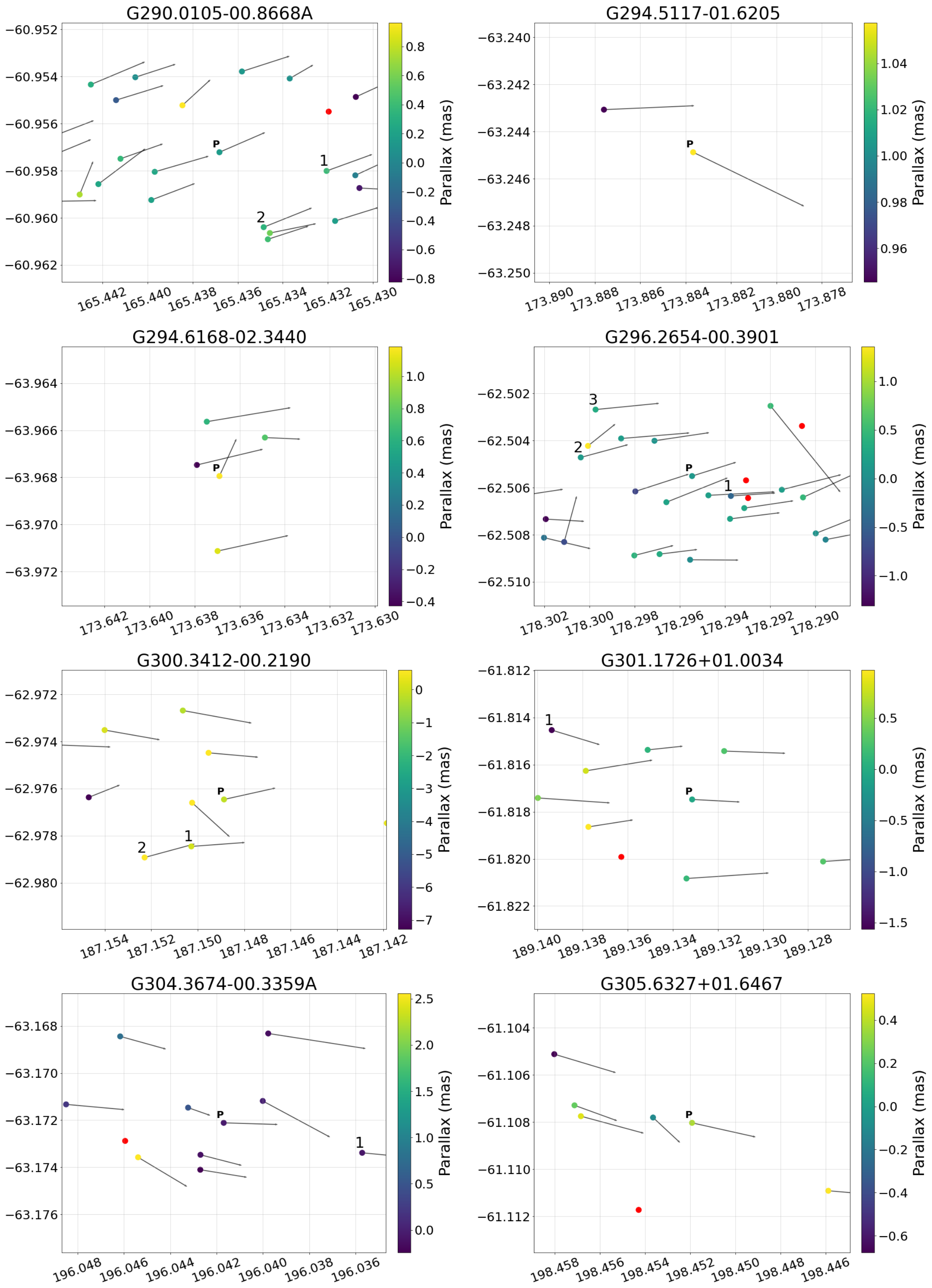

Figure D.13: Sky plots for YSOs observed in Gaia and their companions within a 15” radius. Primary YSO labelled as P. Companions labelled as numbers. RA is on the X-axis and Declination is on the Y-axis.

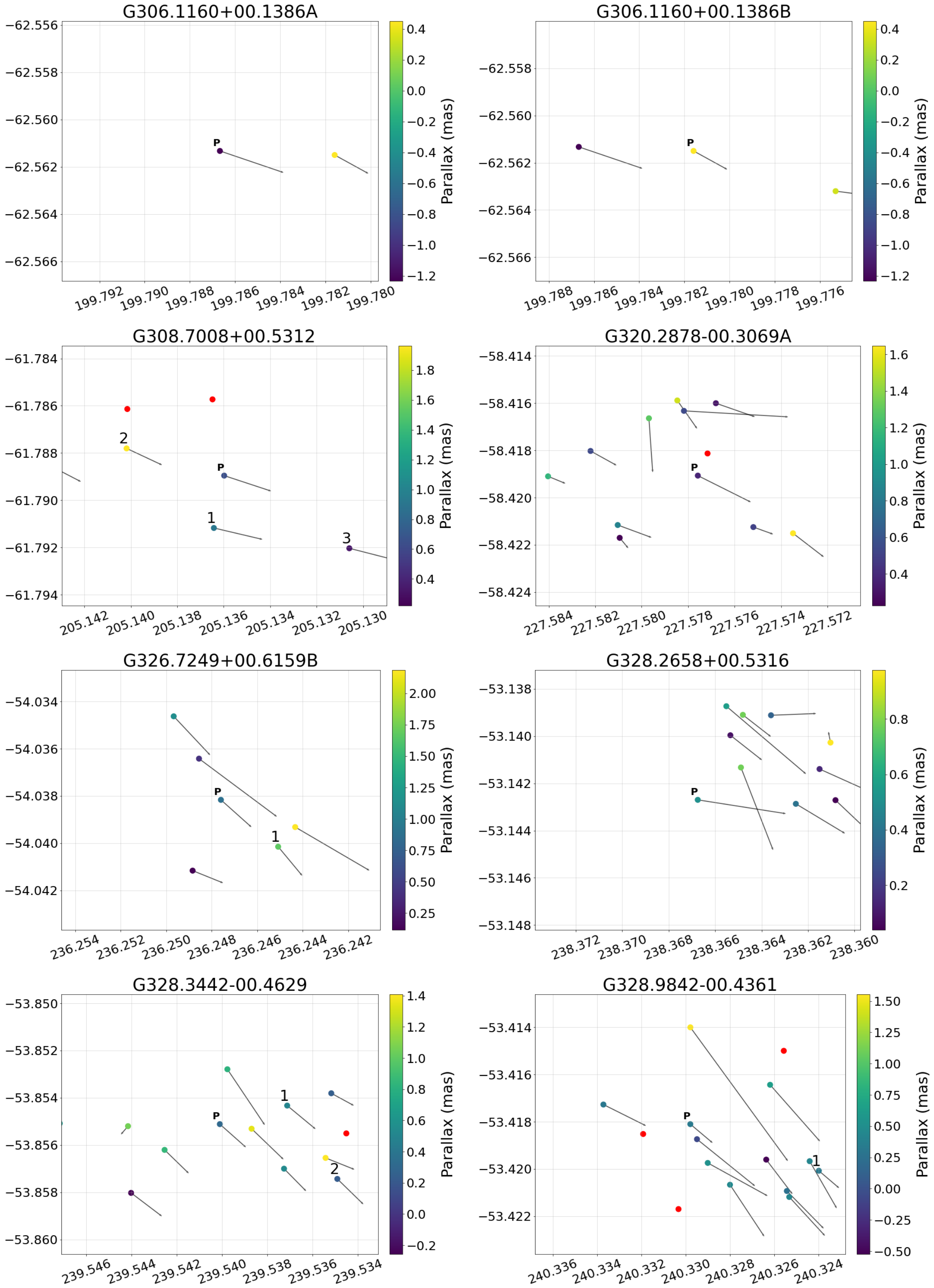

Figure D.14: Sky plots for YSOs observed in Gaia and their companions within a 15" radius. Primary YSO labelled as P. Companions labelled as numbers. RA is on the X-axis and Declination is on the Y-axis.

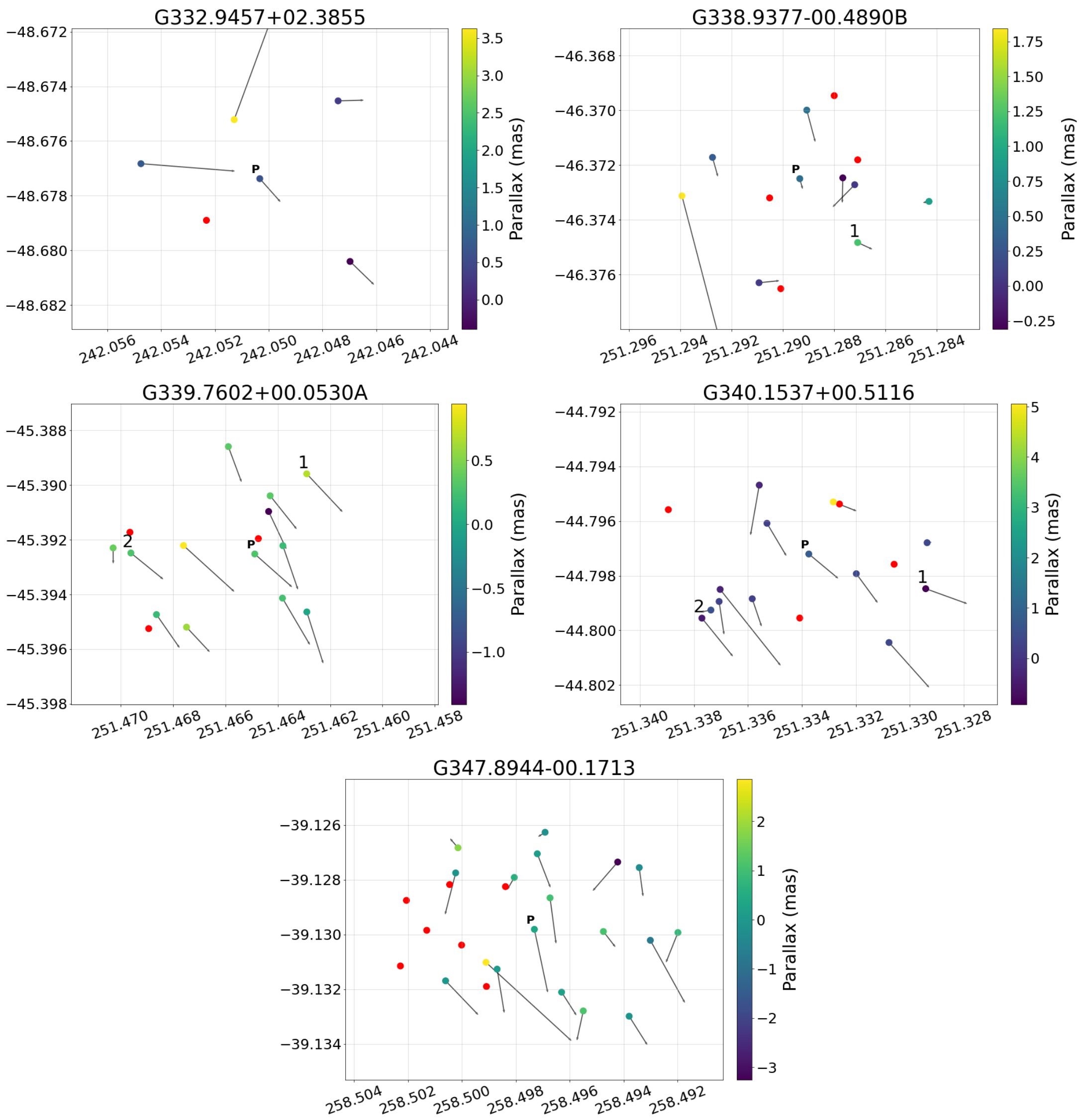

Figure D.15: Sky plots for YSOs observed in Gaia and their companions within a 15” radius. Primary YSO labelled as P. Companions labelled as numbers. RA is on the X-axis and Declination is on the Y-axis.